

A Thesis Submitted for the Degree of PhD at the University of Warwick

Permanent WRAP URL:

<http://wrap.warwick.ac.uk/91770>

Copyright and reuse:

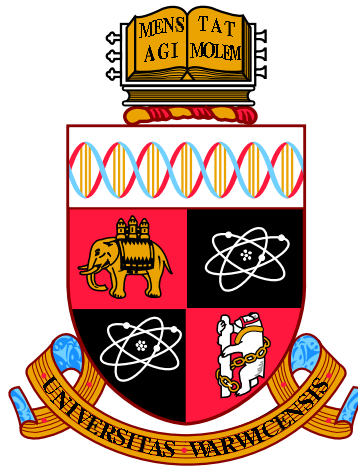
This thesis is made available online and is protected by original copyright.

Please scroll down to view the document itself.

Please refer to the repository record for this item for information to help you to cite it.

Our policy information is available from the repository home page.

For more information, please contact the WRAP Team at: wrap@warwick.ac.uk



Ultrasonics and Nanomechanics

by

Mark S Skilbeck

Thesis

Submitted to the University of Warwick

for the degree of

Doctor of Philosophy

Physics

July 2017

THE UNIVERSITY OF
WARWICK

Contents

Acknowledgments	iv
Declarations	v
Abstract	vi
Chapter 1 Introduction	1
1.1 Atomic Force Microscopy	1
1.1.1 Principle of Operation	1
1.1.2 Cantilever Mechanics	8
1.1.3 Contact Mechanics and Models	10
1.1.4 Beyond Topography	13
1.1.4.1 Measuring Mechanical Properties	14
1.1.4.1.1 Indentation and Force Curves	14
1.1.4.1.2 Tapping Mode and Mechanical Properties . .	16
1.1.4.1.3 Contact Resonance	18
1.1.4.2 Conductive AFM	19
1.1.4.3 Friction Force Microscopy	20
1.2 Ultrasonics	22
1.2.1 Ultrasound Propagation	23
1.2.1.1 Lamb Waves	25
1.2.2 Ultrasound Signal Analysis	29
1.2.3 Generation and Detection of Ultrasound	31
1.2.3.1 Piezoelectric Transducers	32
1.2.3.2 Electromagnetic Acoustic Transducers	34
1.2.3.3 Laser Ultrasonics	36
1.2.3.3.1 Laser Generation	37
1.2.3.3.2 Laser Detection	37
1.2.3.4 Source Geometry, Directivity, and Guided Waves . .	41

1.3	Scope of Thesis	41
Chapter 2	Experimental Methods	44
2.1	Force Curves	45
2.2	Calibration	46
2.2.1	Virtual Deflection	47
2.2.2	Optical Lever Sensitivity	47
2.2.3	Spring Constant and the Sader Method	48
2.2.4	Lateral Calibration	51
2.3	Automation, MacroBuilder, and Extra Hardware	54
Chapter 3	Mechanical Properties of Suspended Films	56
3.1	Introduction	56
3.2	Experimental Methods	60
3.2.1	Samples	60
3.2.2	Data Acquisition and Analysis	61
3.3	Results and Discussion	64
3.3.1	Example Result from a Single Graphene Covered Hole	64
3.3.2	Graphene and the Effect of Heating	66
3.3.3	Oxygen Functionalisation of Graphene	67
3.3.4	Differences in Membrane Puncture Behaviour	70
3.3.5	Correlating Mechanical to Structural Properties	72
3.4	Conclusions	75
Chapter 4	Ultrasonic Force Microscopy	78
4.1	Introduction	78
4.2	Theory	80
4.2.1	Analytic Model of UFM Response	80
4.2.2	Simulation of UFM Response	84
4.2.3	Superlubricity Effect	87
4.2.4	Other UFM Modes	88
4.3	Experimental Methods	88
4.3.1	Ultrasonic Force Microscopy	88
4.3.2	Samples	91
4.4	Results and Discussion	91
4.4.1	Understanding UFM	92
4.4.2	Effect of Tip Hardness	96
4.4.3	Superlubricity and “Half and Half” UFM	100

4.4.3.1	Combined friction and UFM measurements	100
4.4.3.2	Combined conductive and UFM measurements	107
4.4.3.3	Combining multiple techniques	113
4.5	Conclusions	116
Chapter 5	Ultrasonic Non Destructive Testing in an AFM	119
5.1	Introduction	119
5.1.1	NDT Techniques	119
5.1.2	Ultrasonic NDT	121
5.2	Experimental Methods	125
5.3	Results and Discussion	127
5.3.1	Out-of-Plane Displacement	127
5.3.1.1	Deflection Measurements of an Ultrasonic Pulse	128
5.3.1.2	Detection Limits	131
5.3.2	In-Plane Displacement	134
5.3.2.1	Angle of Incidence Dependence	137
5.3.3	Mapping and Features	140
5.4	Conclusions	148
Chapter 6	Conclusions and Future Work	152
6.1	Mechanical Properties of Suspended Films	152
6.2	Ultrasonic Force Microscopy	154
6.3	Ultrasonic Non Destructive Testing in an AFM	156

Acknowledgments

First, thank you to my supervisors, Dr. Rachel Edwards and Dr. Neil Wilson, for their advice and guidance throughout this work. I would also like to thank the members of both the Ultrasound and Microscopy groups for their help and company, particularly Dr. Alex Marsden and Zachary Laker for the samples and additional results they provided. My appreciation also goes to Steve Hindmarsh, the mechanical workshop, and the electronics workshop for their help in enabling many of my experiments.

A personal thank you to my family for their continued support throughout all my endeavours. Special thanks go to Dawn for her help and support throughout this, and for continually making every day better.

I also acknowledge the university and EPSRC for their funding support, and Asylum Research for their generous offerings of assistance and lent equipment.

Declarations

I declare that this thesis contains an account of my research work carried out at the Department of Physics, University of Warwick, between October 2012 and September 2016 under the supervision of Dr. R.S. Edwards and Dr. N.R. Wilson. All work presented in this thesis has been carried out by myself, except where otherwise stated. The research reported here has not been previously submitted, wholly or in part, at this or any other academic institution for admission to a higher degree.

Some of this work has been published, or is being prepared for publication, in scientific journals:

- Skilbeck, M.S., Marsden, A.J., Cao, G., et al. Multimodal microscopy using ‘half and half’ contact mode and ultrasonic force microscopy. *Nanotechnology*, 25(33):335708, 2014. [Parts of chapter 4]
- Marsden, A.J., Skilbeck, M.S., Healey, M., et al. From graphene to graphene oxide: the evolution of the atomic structure. *Preparing for submission*, 2016. [Parts of chapter 3]
- Skilbeck, M.S., Wilson, N.R., and Edwards, R.S. High resolution ultrasound detection by scanning probe microscopy: imaging surface defects, near field enhancements and vectorial displacements. *Preparing for submission*, 2016. [Parts of chapter 5]

Abstract

Since its invention, atomic force microscopy (AFM) has been a valuable tool for probing sample surfaces on the nanoscale, particularly the topography and the mechanical properties. This thesis investigates a subset of techniques focussed on measuring mechanical properties, particularly those which combine AFM with ultrasound.

First, a nanoindentation technique is used to measure the mechanical properties (2D elastic modulus and breaking load) of suspended 2D materials. Graphene grown by chemical vapour deposition (CVD) is tested and found to have similar mechanical properties to previously reported values for mechanically exfoliated graphene. The CVD grown graphene is then functionalised by exposure to atomic oxygen, significantly affecting the mechanical properties, making the sheets both softer and weaker, becoming comparable to the properties of graphene oxide. Comparison with the changes in atomic structure suggests that these changes in mechanical properties are likely caused by the creation of extended topological defects. Such 2D materials are of interest as ultrasonic nanoresonators, for which the resonant behaviour could potentially be investigated using AFM.

Ultrasonic force microscopy (UFM), a technique where the sample is oscillated at frequencies far greater than the cantilever resonance to provide a channel with contrast due to local surface stiffness, is also investigated. By combining experiment and simulation, the influence of experimental conditions on the observed response is studied and the challenges to obtaining quantitative results (e.g. the Young's modulus) are discussed. The combination of UFM with other contact mode AFM techniques, such as conductive AFM and friction force microscopy, is demonstrated for the first time, presenting an unusual ability to acquire multimodal information in a single pass. The combination is also shown to benefit from the superlubricity effect of UFM, using it to conductively image a delicate carbon nanotube network.

Finally, the use of an AFM as a detector for ultrasonic non-destructive testing, where the interaction of ultrasonic waves with sample features is used to probe a sample, is demonstrated. Test measurements are performed on a simple aluminium plate sample with a laser micro-machined slot and compared to results gathered using traditional detectors (piezoelectric transducers and laser interferometers), showing similar signal features. The advantages and disadvantages of AFM detection are discussed, with the high spatial resolution being the primary advantage. The capability to detect in-plane surface motion using the AFM's lateral channel is demonstrated, allowing for simultaneous and distinct measurement of two components (one in-plane component and the out-of-plane motion) of the surface, which is not easily achieved using traditional ultrasonic detection methods.

Chapter 1

Introduction

1.1 Atomic Force Microscopy

Atomic force microscopy (AFM) was invented in 1985 by Binnig et al. [1, 2] as a continuation of Binnig's earlier Nobel Prize [3] winning work on scanning tunnel microscopy [4, 5]. In AFM an atomically sharp, force sensitive probe is rastered across a sample surface allowing a map of the surface topography to be generated. Over the 30 years since it was first introduced AFM has seen significant development allowing for atomic resolution mapping [6] and video rate frame capture [7, 8], as well as a variety of AFM based techniques for investigation of many material properties [9].

1.1.1 Principle of Operation

AFMs achieve force sensing using a micro scale cantilever with an atomically sharp tip at one end and the other end anchored. These cantilevers behave as Hookean springs for relatively small deflections ($z_c \ll L$, the length of the cantilever) [10] and are normally rectangular or V-shaped (with the tip at the apex of the V and both legs attached to the device). The spring constant, k , of this cantilever is then determined by its size, shape, and material, allowing for a wide range of cantilevers, suitable for various applications, to be produced [9].

The deflection of this cantilever must then be measured, which was originally achieved using an STM mounted above the end of the cantilever [1, 2]. Alternative methods of deflection measurement were investigated, with position sensitive laser reflection [11, 12] becoming the standard technique today, thanks to its simplicity and low cost while still maintaining high precision and adequate bandwidth [9]. In this method, a laser is reflected off the back of the cantilever at the tip end into a position sensitive photodiode — a photodiode which is split into two or four adja-

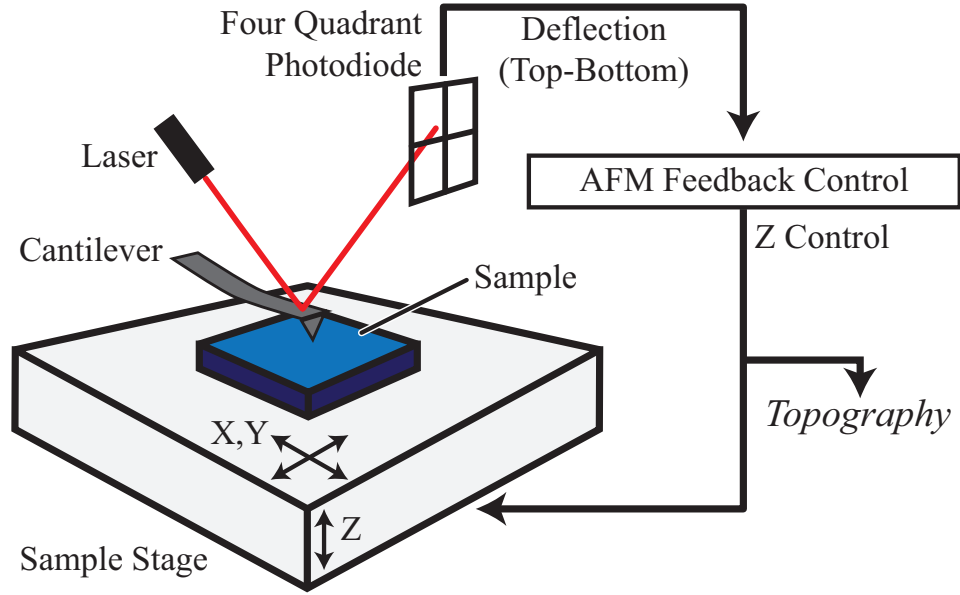


Figure 1.1: Simplified schematic of a four quadrant photodiode type AFM operating in contact mode with a sample scanning stage.

cent segments — as illustrated in figure 1.1. As the cantilever deflection increases the reflected laser moves up the photodiode, increasing the signal from the upper segments and decreasing the signal from the lower segments, meaning the difference in signal between the upper and lower segments gives a measurement of the deflection. Two segment photodiodes were originally used, though now four segment photodiodes are common allowing for detection of the lateral position of the laser spot, which moves due to torsional bending of the cantilever [13, 14]. Self sensing cantilevers are also possible, such as cantilevers with an added piezoresistive layer that changes resistance as the cantilever bends [15, 16], primarily useful for applications where compactness is desired, such as in-situ AFM in an scanning electron microscope (SEM) [17, 18].

To take advantage of the nanoscopic tip the AFM needs to be capable of moving it relative to the sample with high (sub nanometre) precision. This is achieved through the use of actuators made from piezoelectric materials, which will deform under an applied electric field (usually linearly with the field strength). These deformations are typically very small, thus allowing for very small movements to be achieved. A full AFM scanner needs to be able to move the tip relative to the sample in 3 linear axes — X and Y control the in-plane positioning of the tip over the sample surface and Z controls the height of tip. This can be achieved by attaching the scanning actuators to the cantilever (tip scanning), sample stage (sample scanning),

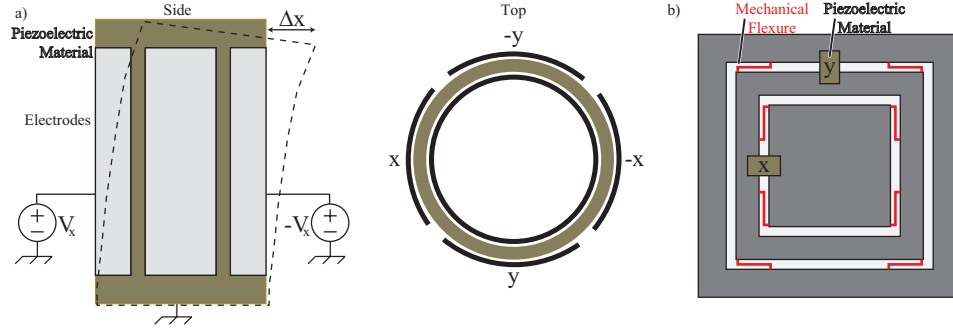


Figure 1.2: Different types of piezoelectric scanning stages; a) tube scanner, showing side and top views, adapted from [19] and b) example of a flexure stage design.

or a mix of both (e.g. X and Y attached to the sample stage and Z attached the cantilever).

One of the simplest and most common types of piezoelectric scanning stage is the tube scanner [19], illustrated in figure 1.2(a). In this, the tube is made of piezoelectric material which is designed such that an applied voltage will cause an expansion or contraction in the height of the tube, typically using shear piezoelectric actuators (i.e. the electric field is applied perpendicular to the motion, in this case along the radial direction). The tube then has electrodes applied to the outside, each covering a quarter of the circumference, with a ground electrode covering the centre of the tube. The opposite electrodes are paired together such that a positive voltage on one is a negative voltage on the other. This means that one side contracts while the other expands, causing the tube to bend towards the contracting side and moving the top of the scanner relative to the bottom, thus allowing for controlled motion in two perpendicular directions. Further, Z motion can be attained by controlling the voltage of the central “ground” electrode, causing the entire tube to expand or contract equally. While simple, this type of scanner is flawed in that the X and Y motion is done through bending and thus the scanning motion is not flat. Often this is not an issue — the angle of bending will be small and post processing of images can remove the curvature — however, it could still pose a problem if accurate height measurements are important.

An alternative scanner configuration, that does not suffer from the bending problem, is the flexure scanning stage, an example of which is illustrated in figure 1.2(b). In this the X, Y, and Z directions are all controlled through separate linear piezoelectric actuators. To allow for the X and Y motion to be actuated in a flat plane with no rotation, the stage area is attached to the surrounding system

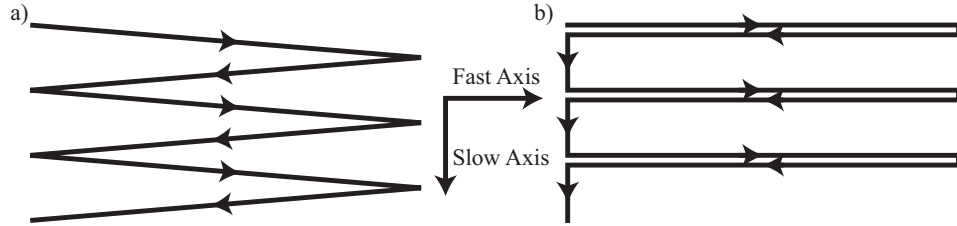


Figure 1.3: Types of AFM scanning path; a) zig-zag and b) stepwise.

through a series of flexures [20, 21]. In flexure systems the X and Y motion is often part of the sample stage, while the Z actuator is attached the cantilever. Another major advantage of flexures is that they enable the easy addition of position sensing elements.

While piezoelectric actuators allow for very precise positioning, their behaviour is often not ideal, suffering from hysteresis [22], creep (continued motion after a voltage change has finished) [23], drift (motion without any input), and rate dependent effects [24]. Many of these complications can be treated through careful calibration of a series of compensation parameters, though this can be a long and arduous process. An easier approach is to use sensors with predictable, preferably linear, behaviour, such as capacitive sensors or linear variable displacement transformers (LVDTs) [25], to measure the movement of the scanner. These sensors can be used in two ways: In open loop operation the sensor information is simply recorded with the scan and can then be used for image processing; in closed loop operation the sensor information is used to feed back onto the piezoelectric actuator drive signal to ensure accurate position while the scan is being carried out.

The X and Y motion allows for arbitrary positioning of the tip across the sample surface, which can then be used to scan the tip over the surface and map the position. This is achieved through raster scanning, which consists of different motion in the two directions: A fast axis that is scanned many times over the course of an image, creating the lines; and a slow scan axis which is scanned only once. Scanning paths can follow many designs, one of which is the zig-zag pattern illustrated in figure 1.3(a), in which the fast axis is oscillated by a triangular wave while the slow scan continually ramps in one direction. Another path is the stepwise motion illustrated in figure 1.3(b), where the slow scan axis is stepped after the fast scan axis returns to the start position, which has the advantage that the two directions of the fast scan axis should exactly correspond to each other. In both of these cases two images are produced, corresponding to the out and return directions of the fast scan axis — referred to as the “trace” and “retrace” directions, respectively. While

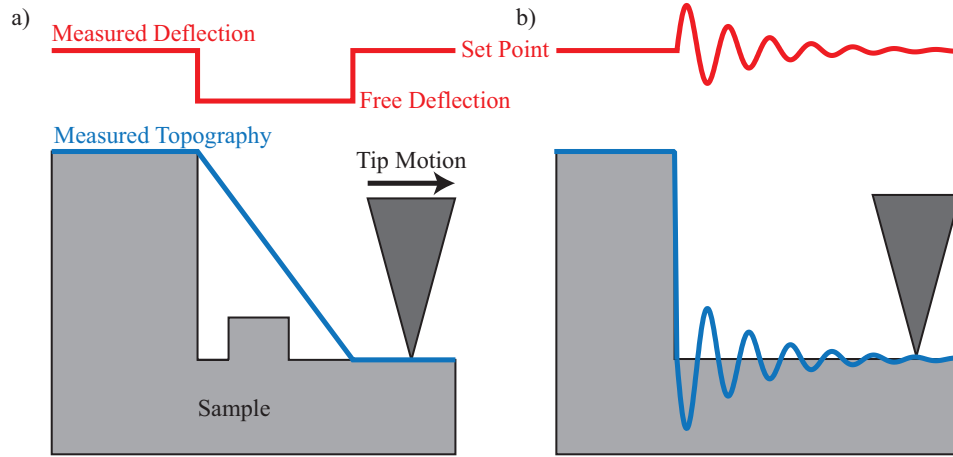


Figure 1.4: Examples of different feedback effects (shown for contact mode); a) parachuting from a low feedback sensitivity and b) ringing from a high feedback sensitivity.

the fast and slow axes will often correspond to the X and Y axes of this stage, this does not necessarily have to be the case and the two axes can be mixed together to image at an angle non orthogonal to the stage directions, which may be useful in certain cases where features of the sample are required to be at a set angle to the scan direction.

The capability to scan the nanoscopic tip across the sample with high precision can then be used to create a high resolution topographic image of the sample surface. A naïve approach to this would be to maintain the Z position of the tip-sample system while scanning in X and Y, using the measured deflection value as the topography. This, however, may result in regions where the sample is too far from the tip to be recorded and a large variation in the force applied to the sample. As such, the approach taken is to use the deflection value as a feedback on the Z positioning and taking the value of the Z position as the topographical image. This is achieved by choosing a set point value for the deflection signal (corresponding to a set loading force) and using a proportional-integral-derivative (PID) feedback loop to adjust the Z position so as to minimise the difference between the measured deflection and the set point. Of these the integral feedback is the most important (and an AFM can often be operated using only integral feedback) as proportional feedback, while faster in response, can not properly track the surface due to requiring a non-zero error value to drive it, thus resulting in a steady state error.

Careful consideration and adjustment of the feedback parameters is necessary to achieve imaging that is true to the sample's features. If the gain of the feedback

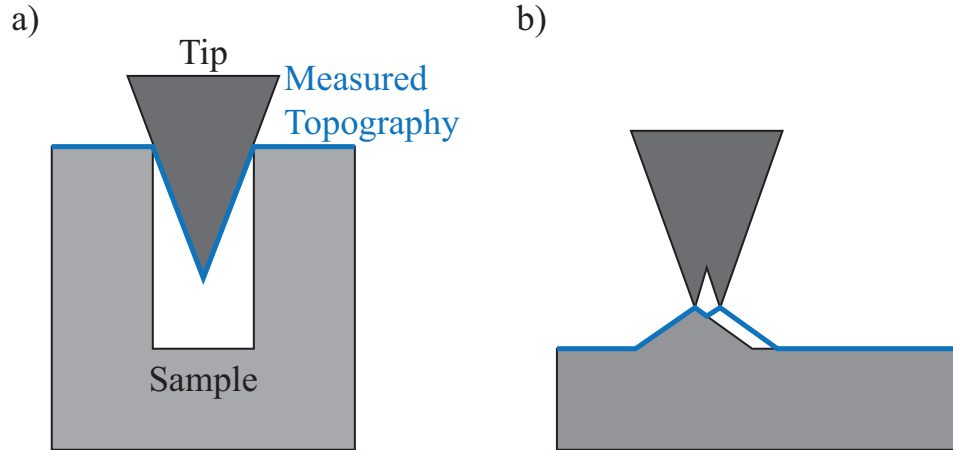


Figure 1.5: Effect of tip shape on AFM imaging; a) cone angle in deep wells and b) double imaging from two tips.

loop is too low then the tip may not be able to follow the surface when height changes are encountered, particularly at drops (as the deflection at a sharp rise will increase proportionally to the height, but at a sharp drop it can only decrease to the free deflection — the deflection value when not engaged to the sample). This leads to a parachuting effect, where the tip will approach the sample as scanning continues, resulting in any features of the surface at these points being obscured, as illustrated in figure 1.4(a). Alternatively, if the feedback gain is too high this can lead to an overshooting of the set point, resulting in a “ringing” of the cantilever, shown in figure 1.4(b). Both these effects can be readily seen in the deflection signal, which would have a constant value of the set point in the ideal case. Recording the deflection signal can therefore be useful as it provides an indication of the level of error in topography at any given point.

It is important to consider the shape of the tip when imaging as the recorded image will be a convolution of the sample topography and the tip shape [26]. This can mean that features with side slopes steeper than the tip’s cone angle will be obscured as the edge of the cone will trace the top edge of the feature, as illustrated in figure 1.5(a). It also means that it is important that the tip is a sharp single point, otherwise it will limit resolution and lead to other effects, such as a double image (figure 1.5(b)) or repeated feature (like a series of triangles with the same orientation, typically a result of a sheared tip). The tip sharpness can be reduced during operation, either by picking up parts of the sample or contaminants or through wear or breakage. As such, the tips are often treated as consumables, being replaced on a regular basis.

The operation of the AFM as described so far has been of “contact” mode AFM, in which the tip is kept in contact with the sample. This technique has drawbacks, however, in that the applied force and resultant lateral forces (from friction) can damage soft or delicate samples, such as polymers. Additionally, the constant friction can cause the tip to wear, especially if the sample surface is harder than the tip material, resulting in degraded imaging and needing to switch tips. A solution to this is the commonly used “tapping” or “AC” mode, in which the tip is oscillated to ensure intermittent contact with the surface. In this the cantilever is driven to oscillate at its resonant frequency, usually by a piezoelectric transducer located at its base, though other excitement methods, such as magnetically driven [27] or photothermal excitation with a laser [28], also exist and can be advantageous, especially for operation under liquid. The response oscillation is then measured, typically using a lock-in amplifier operating at the drive frequency on the measured deflection signal, giving an amplitude and phase measurement. When the tip is brought close to the surface the interactions will cause a reduction in amplitude and a shift in the resonant frequency (and thus a phase shift for a constant driving frequency), which can then be used for the feedback control of the height.

Two common operation modes exist for tapping mode AFM. The first, known as amplitude modulation (AM-AFM) [1], adjusts the Z position in a feedback loop to maintain a set point amplitude that is less than the free amplitude (the amplitude when the tip is far from the surface). In AM-AFM the phase (measured between the drive and oscillation signals) can be recorded as an additional information channel, corresponding to local material properties of the sample. The alternative operation mode is frequency modulation (FM-AFM) [29] in which a phase locked loop (PLL) adjusts the driving frequency based on the phase signal to keep the cantilever driven at resonance. The driving amplitude is also adjusted by feedback loop to maintain a constant oscillation amplitude. The Z height is then adjusted by a feedback loop based on the frequency shift created by the PLL, keeping the frequency shift constant. In FM-AFM the driving amplitude is recorded as an additional information channel, again corresponding to the local material properties of the sample, in this case the dissipative forces (damping effects) between the tip and sample. FM-AFM has a further advantage over AM-AFM in that the resonance frequency change in response to the surface is instant, whereas the amplitude is subject to the ring down time, which is of the order of $\frac{Q}{f_0}$. This is especially an issue in vacuum operation, where Q factors are very large and thus the response of AM-AFM can be too slow for effective scanning.

1.1.2 Cantilever Mechanics

Cantilevers are a core part of AFM operation and understanding their properties is essential. Rectangular beam cantilevers are considered here, though similar analysis also exists for other cantilever configurations. A rectangular cantilever can be considered a Hookean spring for relatively small deflections ($z_c \ll L$, the length of the cantilever) [10], with a normal spring constant given by

$$k = \frac{EWT^3}{4L^3}, \quad (1.1)$$

where L , W , and T are the length, width and thickness of the cantilever beam and E is the Young's modulus of the cantilever material [9]. Similarly, the cantilever also has a torsional spring constant, given by

$$k_T = \frac{GWT^3}{4h^2L}, \quad (1.2)$$

where h is the tip height and G is the material shear modulus, with k_T being measured in force per displacement of the end of the tip. While it is possible to measure the cantilever dimensions directly and thus calculate these constants, accurate measurement of the thickness in particular (which the constants depend on to the third power) is difficult and thus alternative methods are typically used to find them (or equivalent parameters for converting from measured signal to force). Some of these methods are detailed in sections 2.2.3 and 2.2.4 for the normal and torsional directions, respectively.

As a Hookean spring, the cantilever can be modelled as a simple harmonic oscillator (SHO) with an effective mass, m_e (the true mass is distributed over the entire cantilever while the SHO model assumes all the mass at the moving end), and a damping coefficient, c (this is dependent primarily on the fluid around the cantilever — it will be lowest for a vacuum). Driven SHOs are defined by the differential equation

$$m\ddot{z}_c + c\dot{z}_c + kz_c = F_0 \sin(\omega t), \quad (1.3)$$

where F_0 is the driving force, ω is the driving frequency (in radians per second), and t is the time. The general solution to this is given by

$$z_c(t) = A \sin(\omega t - \phi) + z_c^h(t) \quad (1.4)$$

where A is the amplitude of oscillation, ϕ is the phase lag of the tip motion behind the force and $z_c^h(t)$ is the homogeneous solution to the equation — a transient term

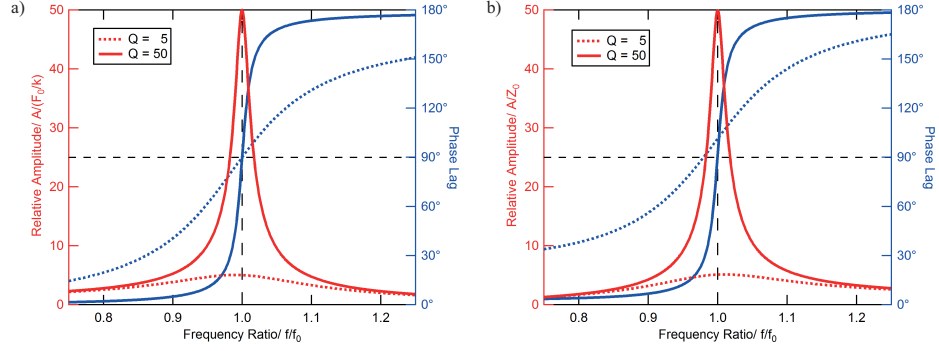


Figure 1.6: Tip response (amplitude and phase lag) for a) tip (direct) driven and b) base driven cantilever.

that quickly dies out. The values of A and ϕ are given by

$$A = \frac{F_0}{k} \sqrt{\frac{1}{(1 - \omega_r^2)^2 + \left(\frac{\omega_r}{Q}\right)^2}}; \quad (1.5)$$

$$\phi = \arctan\left(\frac{\omega_r^2}{Q(1 - \omega_r^2)}\right), \quad (1.6)$$

where $\omega_r = \frac{\omega}{\omega_0}$ is the relative frequency, ω_0 is the resonant frequency, and $Q = \frac{m\omega_0}{c}$ is the quality factor. These equations are plotted in figure 1.6(a). It can be seen that the amplitude is at a maximum just below the resonant frequency (closer with higher Q) and is dependent on the Q factor. Also the tip matches the direct driving force for $\omega \ll \omega_0$ and is completely out of phase with low amplitude for $\omega \gg \omega_0$, passing through a phase lag of 90° when on resonance.

In most AFM systems the tip is driven by motion at its base, given by $z_b(t) = Z_0 \sin(\omega t)$, where Z_0 is the oscillation drive amplitude. This means that the driving force is then provided by the cantilever itself, as the base motion is effectively changing the deflection. This results in a SHO differential equation of

$$m\ddot{z}_c + c\dot{z}_c + k(z_c - z_b) = 0. \quad (1.7)$$

However the AFM system typically measures the bending of the cantilever, and z_c is the absolute position of the tip, therefore a substitution of the relative position of the tip, $z_r = z_c - z_b$, is used, giving

$$m\ddot{z}_r + c\dot{z}_r + kz_r = -m\ddot{z}_b - c\dot{z}_b. \quad (1.8)$$

Solutions to this are then of the same form as equation 1.4 (except now for z_r and not z_c), and the values of A and ϕ become

$$A = Z_0 \frac{1 + Q^2 \omega_r^2}{\sqrt{(Q^2 - Q^2 \omega_r^2 - 1)^2 + \left(\frac{Q}{\omega_r}\right)^2}}; \quad (1.9)$$

$$\phi = \arctan\left(\frac{Q}{\omega_r(Q^2 - Q^2 \omega_r^2 - 1)}\right). \quad (1.10)$$

These solutions are plotted in figure 1.6(b), where it can be seen that the maximum amplitude is now slightly above the resonant frequency. For low frequencies, $\omega \ll \omega_0$, there is no cantilever bending (though this means the cantilever tip is still moving relative to the sample), while for high frequencies, $\omega \gg \omega_0$, the tip is out of phase with the base motion with a low amplitude. Note that, near resonance and with a high Q , $z_r \approx z_c$ as $|z_r| \gg |z_b|$.

This analysis of the tip motion is not perfect — a real cantilever is not a perfect SHO. In fact many bending modes are available for the cantilever beam, where the SHO describes only the first mode (where the deflection of each part of the cantilever is monotonic with its position along the cantilever). These higher order bending modes lead to the creation of higher harmonic oscillations [30,31].

1.1.3 Contact Mechanics and Models

Understanding the forces of interaction between the tip and sample is important for analysis of any data that relies on such interactions. For this, many models exist, of which the three most common will be covered here. Each of these models have been derived for macroscopic systems assuming a sphere of one material, here representing the tip, contacting a flat surface of another material, here representing the sample, as illustrated in figure 1.7. The models describe the relationship between three parameters — the load force, F , the indentation, d (negative values correspond to a separation), and the contact radius, r_{cont} . The system is then defined by the radius of the sphere, r_{tip} , and the material properties of the tip and sample, which are represented by a combined effective Young's modulus, E_{tot} , as given by

$$\frac{1}{E_{tot}} = \frac{3}{4} \left(\frac{1 - \nu_{tip}^2}{E_{tip}} + \frac{1 - \nu_{surf}^2}{E_{surf}} \right), \quad (1.11)$$

where E_{tip} and E_{surf} are the Young's moduli of the tip and sample, respectively, while ν_{tip} and ν_{surf} are their respective Poisson ratios.

The simplest of the models is the Hertz model [32], which assumes the sphere

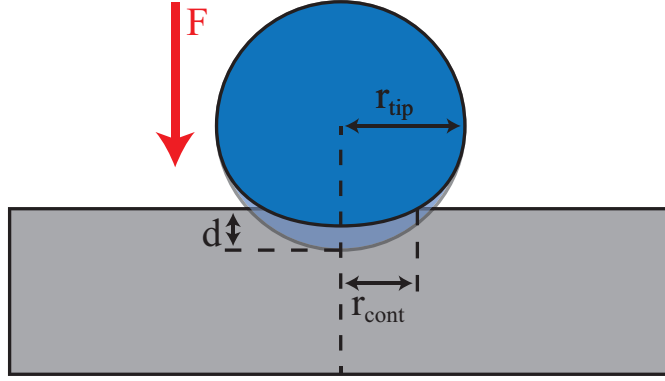


Figure 1.7: Schematic of the sphere (tip) and flat surface (sample) model used in AFM contact mechanics models.

and surface are linearly elastic and that there are no attractive forces between the two. The governing equations of the Hertz model are given by

$$\begin{aligned} r_{cont} &= \left(\frac{r_{tip} F}{E_{tot}} \right)^{\frac{1}{3}} ; \\ d &= \frac{r_{cont}^2}{r_{tip}} ; \\ F(d) &= E_{tot} \sqrt{r_{tip} d^3} . \end{aligned} \quad (1.12)$$

An example $F(d)$ curve for the Hertz model is shown in figure 1.8(a).

Without the effects of attractive forces, the Hertz model has limited applicability to many samples. One approach to add attractive forces is to consider the short range van der Waals forces, as is done in the Derjaguin-Muller-Toporov (DMT) model [33]. This modifies the indentation relationship with the addition of the adhesive force between the tip and sample, F_{ad} , and also adds consideration for the attractive forces while not in contact, resulting in governing equations given by

$$\begin{aligned} r_{cont} &= \begin{cases} \left(\frac{r_{tip}(F+F_{ad})}{E_{tot}} \right)^{\frac{1}{3}} , & \text{if } d \geq 0 \\ 0, & \text{otherwise;} \end{cases} \\ d &= \frac{r_{cont}^2}{r_{tip}} ; \\ F(d) &= \begin{cases} -F_{ad} + E_{tot} \sqrt{r_{tip} d^3}, & \text{if } d \geq 0 \\ -\frac{F_{ad} r_{atom}^2}{(r_{atom})^2 - d}, & \text{otherwise,} \end{cases} \end{aligned} \quad (1.13)$$

where r_{atom} is the interatomic spacing. Note that here the indentation has been

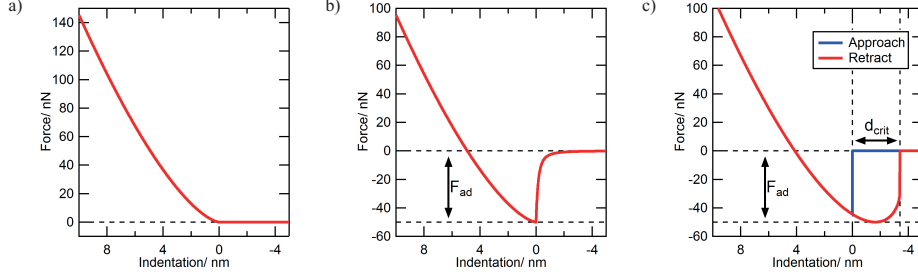


Figure 1.8: Force indentation curves for different interaction models; a) Hertz, b) DMT, and c) JKR. All curves were calculated with the same parameters; $E_{tip} = 130$ GPa, $E_{samp} = 1$ GPa, $\nu_{tip} = \nu_{samp} = 0.3$, $r_{tip} = 10$ nm, $F_{ad} = 50$ nN (DMT and JKR only), and $r_{atom} = 0.3$ nm (DMT only).

defined relative to the edge of the sample and sphere as the centreline of the atoms. An example $F(d)$ curve for the DMT model is shown in figure 1.8(b).

An alternative approach to attractive forces is to consider an adhesion when the sphere and surface are touching and that one or both of them can deform to maintain contact when pulled apart. This is the treatment of the Johnson-Kendall-Roberts (JKR) model [34], which has the governing equations

$$r_{cont} = \begin{cases} \left(\frac{r_{tip}}{E_{tot}} [\sqrt{F_{ad}} + \sqrt{F + F_{ad}}]^2 \right)^{\frac{1}{3}}, & \text{if } \begin{cases} d \geq 0, & \text{approaching} \\ d \geq d_{crit}, & \text{retracting} \end{cases} \\ 0, & \text{otherwise;} \end{cases}$$

$$d = \frac{r_{cont}^2}{r_{tip}} - \frac{4}{3} \sqrt{\frac{r_{cont} F_{ad}}{r_{tip} E_{tot}}};$$

$$d_{crit} = - \left(\frac{F_{ad}^2}{3 r_{tip} E_{tot}^2} \right)^{\frac{1}{3}}, \quad (1.14)$$

where d_{crit} is the critical indentation, calculated by minimising d with respect to r_{cont} , and is always negative and thus represents a separation. Finding a single equation for $F(d)$ is not possible due to the multiple r_{cont} terms in the equation for d , though the inverse equation ($d(F)$) can be found and an $F(d)$ dataset can be calculated numerically. Notably the JKR model exhibits hysteresis — as there are no non-contact forces present, the sphere or surface will only deform to be in contact at negative indentations while they are being pulled apart. An example $F(d)$ curve for the JKR model is shown in figure 1.8(c), including the hysteresis.

Which model to use depends on the materials of the sphere and surface as well as the forces used during experimentation. In AFM the sphere (tip) is typically a

hard material, so the surface (sample) material is the one that matters. For samples with low adhesion relative to the load forces used, the adhesion forces are negligible and can be neglected, leading to the Hertz model being suitable. For samples where adhesion cannot be neglected the DMT and JKR models are both used, with the JKR model being most suited to samples that can deform to meet the tip (i.e. soft samples with a high adhesion). The transition between the DMT and JKR can be treated using Maugis-Dugdale theory [35].

The models presented here are not perfect and represent simplifications of the real system that can provide good approximations of the real behaviour and as such only represent a subset of the models and understanding of nanoindentation [36]. For example, they presume that the sphere and the surface are both smooth relative to the tip radius, which cannot be ensured in AFM due to surface roughness. This is especially a problem for the JKR model as the possibility of multiple contact points changes the adhesive behaviour significantly. The treatment of adhesion is also limited — each model only uses one source for adhesion and doesn't necessarily account for all interactions between the tip and sample. One such effect is the formation of a thin water layer of the tip and sample when in a humid environment, leading to forces from the resulting surface tension and capillary action. Additionally, the models all assume that the tip and sample behave linearly, which is often not the case for real systems. A common treatment of the non-linearity effects in nanoindentation is the Oliver-Pharr method [37].

1.1.4 Beyond Topography

The physical probe used in AFM opens it up to be expanded to a large variety of complimentary techniques and measurements in addition to topographical imaging. The force sensitive nature of the probe makes mechanical measurements an obvious extension, as discussed in section 1.1.4.1. The addition of new data channels and specialised probes and equipment enables a variety of techniques to be explored, such as conductive AFM (cAFM, where an electrical current is measured by the tip, section 1.1.4.2) and friction force microscopy (FFM, where the lateral deflection in contact mode is used to determine surface friction, section 1.1.4.3), both of which are used in this thesis. Other techniques not used here include measuring piezoelectric material response by measuring the deflection of a cantilever in contact with a sample while an electric field is applied (piezoresponse force microscopy [38]), using a thermally sensitive probe to measure local thermal properties (scanning thermal microscopy [39]), and using microwave waveguide probes to investigate local properties such as capacitance and impedance (scanning microwave impedance

microscopy [40]). There are also dual pass lift mode techniques that measure the topography then rescan the same area at set separation and monitor the effects of long range forces, such as those from magnetic fields (magnetic force microscopy [41]) and electrical fields (electrostatic force microscopy [42, 43] and Kelvin probe force microscopy [44]).

1.1.4.1 Measuring Mechanical Properties

Materials can have a range of mechanical properties that define their behaviour when affected by forces. The simplest of these are the adhesion (attraction to other materials) and elasticity (reversible deformation under an applied force, measured by the elastic constants such as the Young’s modulus and Poisson ratio). Other mechanical properties include plasticity (permanent deformation from an applied force) and viscoelasticity (time dependent deformation under a constant force). Many of these can be measured or compared by a wide variety of AFM techniques, some of which are detailed below. In addition to these, another technique known as ultrasonic force microscopy (UFM) is covered in detail in chapter 4.

1.1.4.1.1 Indentation and Force Curves

One way of investigating mechanical properties is to directly measure the force-indentation relationship of a material and then fit it to a suitable model, such as those discussed in section 1.1.3. In AFM this is known as nanoindentation, using a technique known as force curves [45, 46]. In a force curve the deflection of the cantilever is measured as the relative Z position is changed. While the force is linearly related to deflection, the Z position has to be combined with the deflection to determine the indentation, as the Z motion is relative to the sample and cantilever base and deflection of the cantilever is relative motion between the tip and the cantilever base. Conversion of experimental data to force-indentation data and proper calibration is covered further in section 2.1.

Some of the features on a force curve are as a result of the AFM and not the sample, as illustrated in the example force curve (made using a DMT model) shown in figure 1.9. As the indentation is related to the deflection of the cantilever, the cantilever spring constant is a limit on the gradient of the force-indentation curve that can be measured — a minimum for approaching the sample and a maximum for retraction. Beyond this gradient, the change in force with indentation is less than the cantilevers change in force with deflection (and thus indentation). This leads to the jump-to-contact (approach) and pull-from-contact (retract) phenomena

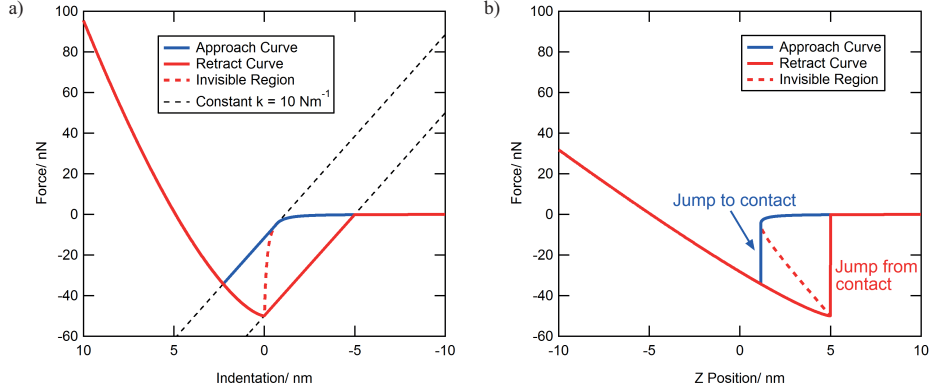


Figure 1.9: Example DMT force curve when measured with an AFM, showing the jump to/from contact effect and the resultant invisible region of the curve. a) Force against indentation, b) Force against Z position (cantilever base relative to sample — what the AFM measures). Calculations done with the parameters $E_{tip} = 130$ GPa, $E_{samp} = 1$ GPa, $\nu_{tip} = \nu_{samp} = 0.3$, $r_{tip} = 10$ nm, $F_{ad} = 50$ nN, $r_{atom} = 0.3$ nm, and $k = 10$ Nm⁻¹.

seen in figure 1.9(b), where the tip appears to be instantaneously sucked onto the surface or snaps from the surface, respectively. Therefore the minimum force (the adhesion) is never reached during approach, but can be easily measured from the retraction curve. The jumping effect also results in a region of the force-indentation relationship that cannot be probed by a conventional force curve.

Other features of force curves can also be used to provide information about the sample. For instance, hysteresis in the curve (i.e. the approach and retract curves are different beyond the jump-to-contact and pull-from-contact effects mentioned above) could be a result of poor calibration of the Z motion (hysteresis in the piezoelectric actuator motion) or indicative of a sample's plasticity [47] or viscoelasticity [48]. If the sample's properties are the cause, the retract curve will have higher indentations than the approach curve as the sample will have permanently deformed (plasticity) or be responding slower to applied forces (viscoelasticity). Viscoelasticity can also be investigated by performing a dwell — holding the force constant while indenting into the sample — and measuring the change in indentation with time [49]. Such dwells can also be useful for performing other experiments, such as current-bias (IV) sweeps in conductive AFM (see section 1.1.4.2).

Force curves are not limited to the examination of bulk mechanical properties, for example they can be used to measure the mechanical properties of 2D materials (which is investigated in chapter 3) or as a tool for pulling molecules or proteins and examining their unfolding behaviour [50,51]. They can also be combined with other

techniques to provide complimentary information for force sensitive samples, such as measuring piezoresponse at varying loads [52] or optically monitoring a biological cell as it is subjected to indentation [53,54].

Force curves are a single point method, acquiring data for only a single location on the sample. Often it is more informative to acquire data about many points over an area of the sample for comparison of different regions, or to correlate changes in mechanical properties to changes in topography. This is easily acquired as a “force-volume” map, in which force curves are acquired at individual points on a surface following a grid pattern, with the tip moving over the surface after each individual force curve. Such force-volume maps are limited, however, in their acquisition speed and thus practically attainable resolution — as a force curve must be performed at every point the total number of points that can be acquired on a map is significantly less than can be acquired from a scanned image in the same time. Newer generation AFMs have made quasi-scanning force-volume techniques available, such as Asylum Research’s Fast Force Mapping and Bruker’s PeakForce Tapping modes [55,56], which offer greatly improved speeds over conventional force mapping but are still significantly slower than the video rate imaging that these systems are often capable of [7,8]. In these quasi-scanning techniques the AFM is scanned as it would be in a standard imaging method except the Z position is oscillated at a frequency equal to the point capture rate and full time dependent data is captured. This results in a full force curve being captured at each point despite scanning operation. Topography feedback for this is typically performed using the highest deflection of each oscillation period to adjust the Z position DC offset, keeping the maximum applied force constant over a whole map. The high speed of this technique can lead to some additional difficulty in interpreting the data as some materials may respond differently to high speed indentations, e.g. due to viscoelastic effects [57,58]. Another approach to increasing spatial resolution is force slicing, in which multiple images are acquired at different set point forces [45,59], though this is sacrificing resolution in force and indentation for the spatial resolution.

1.1.4.1.2 Tapping Mode and Mechanical Properties

To understand how tapping mode can be used to measure mechanical properties it is instructive to split the tip sample forces into conservative and dissipative forces. The conservative forces only depend on the indentation of the tip into the sample (and are dependent on the elastic properties of the sample, primarily Young’s modulus), while the dissipative forces are the motion dependent deviations from the conservative forces (i.e. a measure of the hysteresis). As an example, the Hertz and DMT models

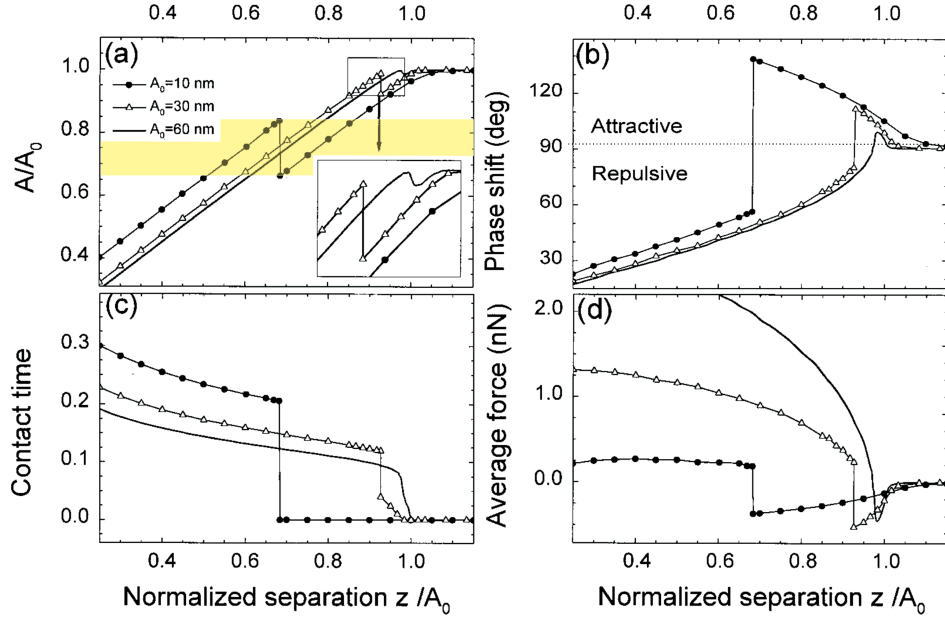


Figure 1.10: Modelled tapping mode approach curves, showing a) amplitude (bistable region for the $A_0 = 10$ nm curve highlighted in yellow), b) phase, c) contact time (as a fraction of total time), and d) average force. Figure adapted from [60].

(see section 1.1.3) are both purely conservative ($F^D = 0$), while the JKR model features some dissipative forces where $0 \leq d \leq d_{crit}$. Dissipative forces can also arise due viscoelastic effects and plastic deformations.

The effect of each of these forces is different. The conservative forces cause a frequency shift, while the dissipative forces cause a reduction in Q (effectively damping the system and reducing the amplitude) [61,62]. Note that the direction of the frequency shift is dependent on the sign of the conservative forces — if the average force during an oscillation is attractive then the resonant frequency is decreased, while if it is repulsive then the frequency will increase. Also, if the resonant frequency moves away from the drive frequency then the amplitude will decrease similarly to the effect of changing the drive frequency. The effects of this are seen in figure 1.10, noting that for $\omega \approx \omega_0$ the phase shift is linearly related to the frequency shift. In figure 1.10(a) a region in which a single amplitude corresponds to two separations is seen, called the bistable region [60,63,64]. This is a result of the switch between the attractive and repulsive regimes and is of concern when scanning in amplitude modulated tapping mode, as choosing a set point within this region allows the tip to jump between the two curves and thus cause a jump in height and phase that is not due to sample topography and properties. Imaging within the attractive regime is

possible and, as can be seen from figure 1.10(c) and (d), has significantly lower impact on the sample than imaging in the repulsive regime, which is useful for particularly delicate samples.

In amplitude modulated mode the height is adjusted to keep a constant amplitude, recording topography and phase maps. In this both the amplitude and phase change as a result of both the conservative and dissipative forces. This means that the phase gives some indication of the local mechanical properties of the sample though its exact meaning can be difficult to interpret. Frequency modulated mode partially solves this — the drive frequency is kept to the resonance using a phase locked loop and the Z height is adjusted to maintain a constant frequency shift, meaning that the topography image is a map of a constant average conservative force. The drive amplitude is adjusted to maintain a constant response amplitude, which will only be varying due the dissipative forces. This means that the drive amplitude can be used as a direct measure of the energy loss by dissipative forces [65,66].

Neither of these tapping mode methods can provide a full picture of the material properties of the surface — a natural consequence of only having two channels for three pieces of information (topography, conservative forces and dissipative forces). A solution to this is to excite the cantilever at its first and second resonances, called dual AC or AM-FM mode [67]. The first resonance is then used in AM operation to map the topography, while the second resonance is operated in FM mode with the exception that the frequency shift is measured, rather than used to control the topographic feedback. These measurements from the second resonance thus directly relate to the conservative forces (frequency shift) and the dissipative forces (drive amplitude), allowing a full picture of the material properties to be acquired. With the correct model the frequency shift can be converted into a Young's modulus [68]. Use of the second resonance also enables the measurement of stiffer materials — higher frequencies mean that the cantilever is effectively stiffer, which can be seen as the acceleration of the tip, and thus the force, is proportional to the frequency. While particularly relevant to dual AC operation, this effects all forms of oscillatory methods, with increasing frequency of operation resulting in increased sensitivity to variations in stiffer samples, though at the cost of sensitivity to softer samples.

1.1.4.1.3 Contact Resonance

Contact resonance is another way of measuring the conservative and dissipative forces between a tip and sample and can be viewed as a version of tapping mode taken in the extreme of the repulsive regime. In contact resonance mode the topographic feedback loop is as in conventional contact mode, while the cantilever is excited

at resonance. The resonance of the cantilever will be significantly above its free resonance due to the high conservative forces caused by being in contact. Changes in this resonant behaviour then correspond to the material properties of the surface. There are a variety of ways to measure these changes, the simplest of which is constant frequency excitation (similar to AM tapping mode) — the cantilever is driven at a set frequency and the amplitude and phase are measured. This is easy to perform, but the information of conservative and dissipative forces is mixed between channels. A phase locked loop can be used to track the resonant frequency (similar to the second resonance of AM-FM mode), which provides a frequency shift (for conservative forces) and amplitude (for dissipative forces), though stably tracking the resonant frequency can be difficult [69]. Two frequencies near the resonant frequency can be excited and their amplitudes and phases used to determine the frequency shift and amplitude of the resonant peak [70, 71]. The cantilever can also be excited with a range of frequencies near the resonant frequency, either by a sweep of frequencies [69, 72] or a signal containing many simultaneous frequencies [73, 74]. The response can then be Fourier analysed to determine the frequency shift and amplitude.

1.1.4.2 Conductive AFM

Conductive AFM (cAFM) is a contact mode technique which enables the measurement of the electrical properties of a sample, particularly the local conductivity [75]. A conducting tip (often a standard tip with a thin metallic coating, though solid metal [76] and doped semiconductor [77] options are also available) is used to complete an electrical circuit with the sample. Either the tip or sample is connected to ground through a high gain current amplifier (typically capable of record currents of the order of nA) while the other is attached to a controllable bias. For scanned images a set bias is chosen and the sample is imaged while also recording the measurement from the current amplifier. This results in an image of current at a set bias, giving an indication of the relative conductivity of regions on the sample surface.

Sometimes scanning is not appropriate; this can be due to having a soft or delicate sample that would be damaged by scanning, or wishing to preserve a metal coated tip as the coating at the tip apex is prone to wearing out. This leads to another form of cAFM in which it is combined with force curves (see section 1.1.4.1.1). In this a force curve is performed as normal, except at the turnaround point (i.e. the set point load, between the approach and retract curves) the position is held (either as a constant Z position or by turning feedback on, known as a dwell) and the bias is swept or oscillated while measuring the current, and then the retract curve is per-

formed. This creates a current-bias dataset (IV curve) which can then be analysed. In addition to working on soft or delicate samples, this method has the benefit of providing more information about the sample's electrical behaviour and thus can be used to determine additional electrical properties, such as the type of electrical junction formed with the tip. The electrical information can also be correlated with the mechanical information from the force curves, and the mechanical information can be used to determine a contact area in cases where it is important to the electrical measurements [78]. Naturally the force curve technique can be expanded to many points across the sample as with force mapping, a technique known as force-volume-bias-spectroscopy, sacrificing spatial resolution and speed over conventional imaging.

Some factors can complicate the acquisition of cAFM results, mostly due to difficulties in maintaining a conductive circuit with the tip. Firstly, metal coated tips can wear, leaving the apex uncoated and thus non-conductive, breaking the circuit [79, 80]. This effect is predominant in scanning operation, so can be avoided by only performing force curve type measurements. The tips (of any type) can also become coated, either with material from the sample or contaminants. Such a coating will directly affect any current measurements, depending on the properties of the coating material, and may prevent conduction entirely. Some attempts to remove the contamination without having to remove the tip may be made, such as in situ chemical cleaning or moving the tip to a metallic contact and burning the material off with a high voltage/current. Care should also be taken about the levels of current used, especially with metal coated tips — the thin metal coating may not be able to support significant current and could thus burn off, permanently breaking the conductive pathway. This is avoidable through equipment design, particularly by limiting the current to levels that are safe for the metallic tip coating.

1.1.4.3 Friction Force Microscopy

Friction force microscopy (FFM) is a contact mode technique in which the lateral deflection is acquired to measure the lateral force applied to the sample, which corresponds to the friction between the tip and the sample [13]. As the tip is scanned over the surface its motion is resisted by friction, which causes the cantilever to twist until the torsional moment balances the frictional force. The torsional twisting causes the reflected laser spot to move horizontally on the photodiode, which can be measured similarly to the normal deflection, except taking the difference of the left and right pairs of photodiodes on the four quadrant photodiode, rather than the top and bottom pairs. This requires that the fast scan axis is perpendicular to the

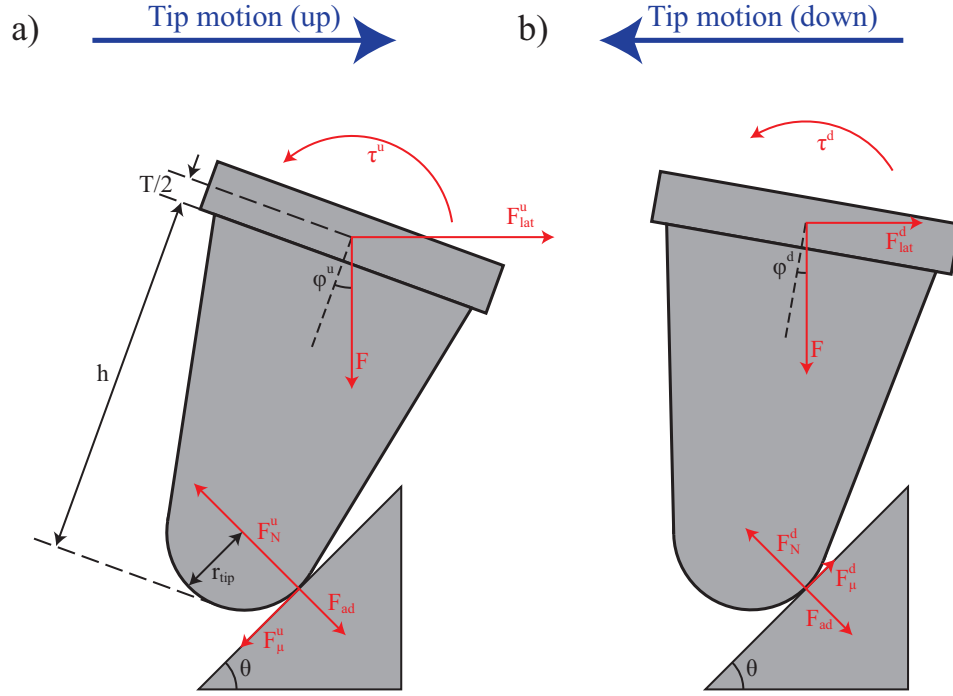


Figure 1.11: Forces acting on the tip and cantilever while the tip is travelling a) up and b) down a slope. Tip features are not drawn to scale.

length of the cantilever, as the torsion of the cantilever will only act in this direction, and the motion must be parallel to the forces from the torsion for the friction to be measured. For similar reasons contact mode AFM should never be performed with the fast scan axis parallel to the cantilever length as frictional forces could cause bending in the length, which would be read as a change in deflection and therefore the deflection signal would be coupled to the tip-sample friction forces.

It is important to consider all the forces acting on the tip during scanning, as the force on the cantilever will also depend on the gradient of the surface [81], as illustrated in figure 1.11. The forces here are the lateral (F_{lat}) and load (F) forces from the cantilever, the adhesive (F_{ad}), frictional (F_{μ}), and normal response force (F_N) between the cantilever and sample, and the torsion in the cantilever (τ). Additionally, there are the angles for the slope from flat (θ) and the twist of the cantilever (φ), and the dimensions of the tip and cantilever (r_{tip} , h , and T). The u and d superscripts refer to up and down directions, respectively, noting that the load force and adhesion do not change depending on direction. According to Amonton's Law, which is an approximation of real frictional behaviour [82, 83], the frictional force is given by $F_{\mu} = \mu F_N$, where μ is the coefficient of friction. For regular tips (i.e. not colloidal probes), $r_{tip} \ll h$, meaning the tip radius effects can be neglected.

Resolving these forces leads to force balances of

$$\begin{aligned} F_{lat}^u &= \frac{F \sin \theta + \mu(F \cos \theta + F_{ad})}{\cos \theta - \mu \sin \theta}; \\ F_{lat}^d &= \frac{F \sin \theta - \mu(F \cos \theta + F_{ad})}{\cos \theta + \mu \sin \theta}, \end{aligned} \quad (1.15)$$

for the up and down motions, respectively. This shows that the lateral force, and thus the measured lateral deflection, depends significantly on the local surface topography and not just the frictional forces. However, most samples are close to flat (i.e. θ is close to 0°), which means that equation 1.15 can be expanded as a Taylor series around $\theta = 0$ to give

$$\begin{aligned} F_{lat}^u &= +\mu(F + F_{ad}) + L\theta + \mu^2(F + F_{ad})\theta + \mathcal{O}(\theta^2); \\ F_{lat}^d &= -\mu(F + F_{ad}) + L\theta + \mu^2(F + F_{ad})\theta + \mathcal{O}(\theta^2). \end{aligned} \quad (1.16)$$

From this it can be seen that the first order effect of the slope is independent of direction and, as θ is presumed to be small, the $\mathcal{O}(\theta^2)$ can be ignored. It then follows that a measurement of the half width, given by

$$F_{lat}^W = \frac{F_{lat}^u - F_{lat}^d}{2} = \mu(F + F_{ad}), \quad (1.17)$$

results in a slope independent measurement that obeys Amonton's law. In practise this involves the measurement of the lateral signals in both the trace and retrace directions and then subtracting the retrace from the trace. Any changes in $\mu(F + F_{ad})$ will be reflected in this difference image and, as F is fixed by the set point force and changes in F_{ad} are likely to be negligible compared to $F + F_{ad}$, a map of the changing values of μ across the surface can be generated. It can, however, be beneficial to measure make local adhesion measurements to ensure that changes in adhesion are not responsible for the observed changes in friction and to get accurate measurements of μ , especially if low load forces are used [84]. To get meaningful values for the frictional forces the lateral channel needs to be calibrated, as described in section 2.2.4.

1.2 Ultrasonics

Sound waves are pressure or stress waves that travel in materials, including solids, liquids, and gasses [85]. Ultrasonic waves are sound waves with frequencies above the range of human hearing, typically around 20 kHz [86]. In this work ultrasound

is of interest both as a driving method in AFM, such as in the ultrasonic force microscopy presented in chapter 4, and for its ability to probe samples for features, used in non-destructive testing (NDT), which is investigated in chapter 5.

1.2.1 Ultrasound Propagation

There are many different modes of (ultra)sound wave, encompassing different types of particle motion within the wave. The simplest of these modes, which can travel in solids and fluids, is the bulk longitudinal wave, which travels through the bulk of a material (i.e. not adjacent to any material boundaries) [86,87]. In this wave the particles oscillate and the pressure/interaction forces between particles cause the next particles to oscillate, resulting in a wave motion along the direction of motion. Bulk shear waves, in which the particle motion is perpendicular to the wave motion, can only be sustained by solids and viscous fluids due to the necessity of direct inter-particle forces [85]. When boundaries are present (i.e. a sharp transition between two different materials) new types of waves can propagate, based on the boundary conditions [88,89]. These are classed as surface waves, with a common example being Rayleigh waves, and can have motion in directions both parallel and perpendicular to propagation. Another example of waves that arise from boundary conditions are Lamb waves, which are plate travelling waves (i.e. constrained by two parallel boundaries) and are covered further in section 1.2.1.1.

To describe the motion of the wave its properties must be known — the amplitude, frequency, f , wavelength, λ , and velocity, v , which are related by $v = f\lambda$. In isotropic solids the bulk wave velocities are dependent on the elastic properties of the material — the Young's modulus, E , and the shear modulus, G — and its mass density, ρ . The velocity of the longitudinal and shear waves are then given by

$$v_L = \sqrt{\frac{E + \frac{4}{3}G}{\rho}}, \text{ and} \quad (1.18)$$

$$v_S = \sqrt{\frac{G}{\rho}}, \quad (1.19)$$

respectively [86]. This is the simple case for non-dispersive media, however, in dispersive media there are two different velocities which must be considered, the phase velocity, v^p , and the group velocity, v^g , both of which can vary with frequency [85,89]. The phase velocity is the velocity of the phase, i.e. the velocity of a single peak of the waveform, and is related to the frequency and wavelength as before. The group velocity is the velocity of the energy of the wave, or alternatively the velocity of the

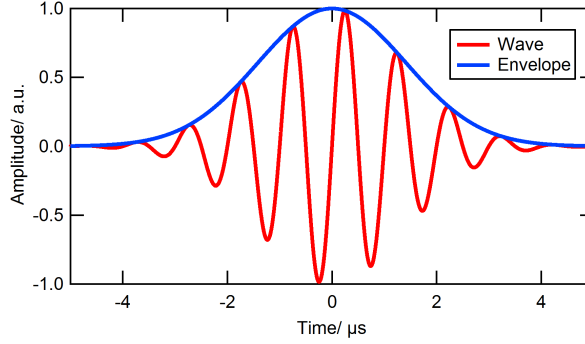


Figure 1.12: Example of a simple wave packet.

wave packet or envelope, i.e. the signal outline for a wave pulse (see figure 1.12). The group velocity is defined by $v^g = \frac{\partial \omega}{\partial k}$, where $\omega = 2\pi f$ is the angular frequency and $k = \frac{2\pi}{\lambda}$ is the wavenumber.

These waves will then interact with any boundaries they encounter. Interactions include reflection, refraction (where the wave is transmitted into the adjacent material), and mode conversion, with all of these happening in different amounts depending on the nature of the boundary. Transmission of ultrasound across a boundary is usually considered in terms of the acoustic impedance, $W = \rho v$, of each material. This can then be used to give the coefficients for the reflection,

$$R = \frac{W_B - W_A}{W_A + W_B}, \quad (1.20)$$

and transmission,

$$T = \frac{2W_B}{W_A + W_B}, \quad (1.21)$$

for a wave in material A interacting with a boundary between materials A and B [86, 89]. These coefficients relate the amplitude of the resultant (reflected or transmitted) wave to the amplitude of the incident wave. For $W_A \approx W_B$, $R \approx 0$ and $T \approx 1$, meaning that the wave is nearly fully transmitted across the boundary — these materials are considered to be acoustically matched. However, for $W_A \ll W_B$ or $W_A \gg W_B$, $|R| \approx 1$ and $T \approx 0$, meaning the wave is nearly completely reflected. As such the acoustic impedances are important when attempting to acoustically bond two materials together (e.g. attach a piezoelectric transducer to a sample) or when attempting to ensure reflections at a boundary.

Mode conversion is when a reflected/refracted wave has a different mode to the incident wave, e.g. a change from a longitudinal wave to a shear wave or a conversion between the different modes of a Lamb wave. With all these boundary

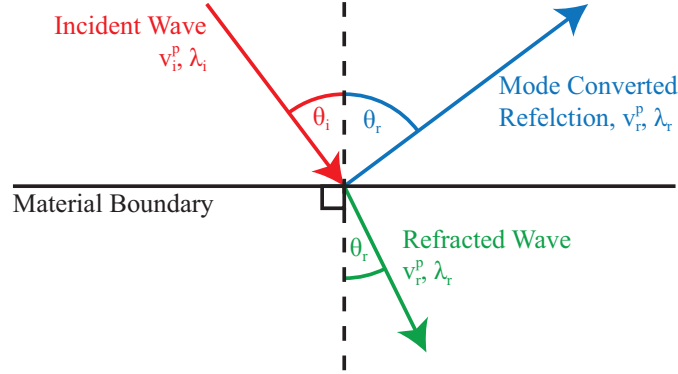


Figure 1.13: Diagram of the angles for Snell's law, showing both a mode converted reflection and a refracted wave.

interactions the frequency and separation of the wavefronts must be conserved, giving rise to Snell's law [85];

$$\lambda_i \sin(\theta_i) = \lambda_r \sin(\theta_r), \text{ or equivalently } \frac{\sin(\theta_i)}{v_i^p} = \frac{\sin(\theta_r)}{v_r^p}, \quad (1.22)$$

where θ is the angle from the normal and the i and r subscripts are for the incident and resultant wave, respectively. A diagram of these angles is shown in figure 1.13. The reflected (and mode converted) waves can also interfere with the incident waves, provided the particle motion is parallel, giving rise to interference fringes and other effects, such as near field enhancement (where the interference causes a significant increase in the total amplitude in a small region adjacent to the boundary) [90].

1.2.1.1 Lamb Waves

Lamb waves are a type of dispersive plate travelling wave, meaning that they propagate in the plane of a thin solid with material boundaries in both directions in the out-of-plane direction [91]. These occur when there are two parallel boundaries and the separation of these boundaries (the plate thickness) is comparable or less than the wavelength, while waves in plates much thicker than the wavelength can be considered as Rayleigh waves. The particle motion of a Lamb wave is both out-of-plane and in-plane, parallel to the propagation. They do not exhibit in-plane motion perpendicular to the propagation direction. The full treatment of the behaviour of Lamb waves can be found in the literature [88, 92] and the important results are presented here.

Lamb waves describe an infinite set of modes with their own motions and

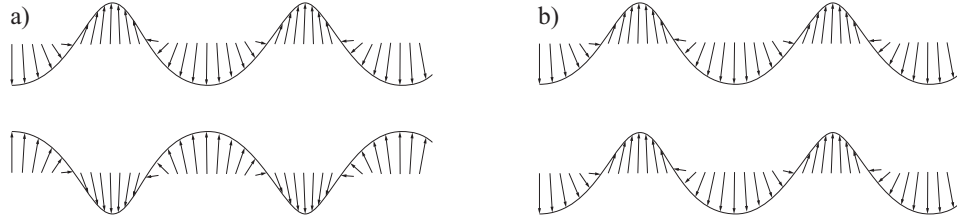


Figure 1.14: Exaggerated surface displacement profiles for Lamb wave a) symmetric and b) antisymmetric modes. Adapted from [92].

(frequency dependent) velocities. These modes can be broken down into two subsets — symmetric modes, in which the motion on the top and bottom faces is mirrored about the central plane of the plate, and antisymmetric modes in which the motion is in the same direction, as illustrated in figure 1.14. The modes are then numbered according to their order, with the lowest frequency waves (the zero-order modes) being labelled S0 and A0 for the symmetric and antisymmetric modes, respectively.

Lamb waves are defined by two equations, for each of the symmetric and antisymmetric modes, given by

$$\frac{\tan(qh)}{\tan(ph)} = -\frac{2k^2pq}{(q^2 - k^2)^2}, \text{ and} \quad (1.23)$$

$$\frac{\tan(qh)}{\tan(ph)} = -\frac{(q^2 - k^2)^2}{2k^2pq}, \quad (1.24)$$

$$(1.25)$$

respectively, where

$$p^2 = \left(\frac{\omega}{v_L}\right)^2 - k^2 \quad (1.26)$$

$$q^2 = \left(\frac{\omega}{v_S}\right)^2 - k^2, \quad (1.27)$$

$h = \frac{d}{2}$ is the half thickness of the plate [92], ω is the angular frequency of the Lamb wave, and k is its wavenumber. An infinite number of complex k solutions exist for these, though the solutions of interest are those where k has no imaginary component, as an imaginary component indicates a wave that either grows with distance (which has never been observed) or decays with distance (an evanescent wave which is not of interest here). To find the real solutions to this a frequency thickness product, fd , is substituted into one of the equations and values of v^p for the Lamb wave are tested numerically until the roots are found (more than one root can be found for each

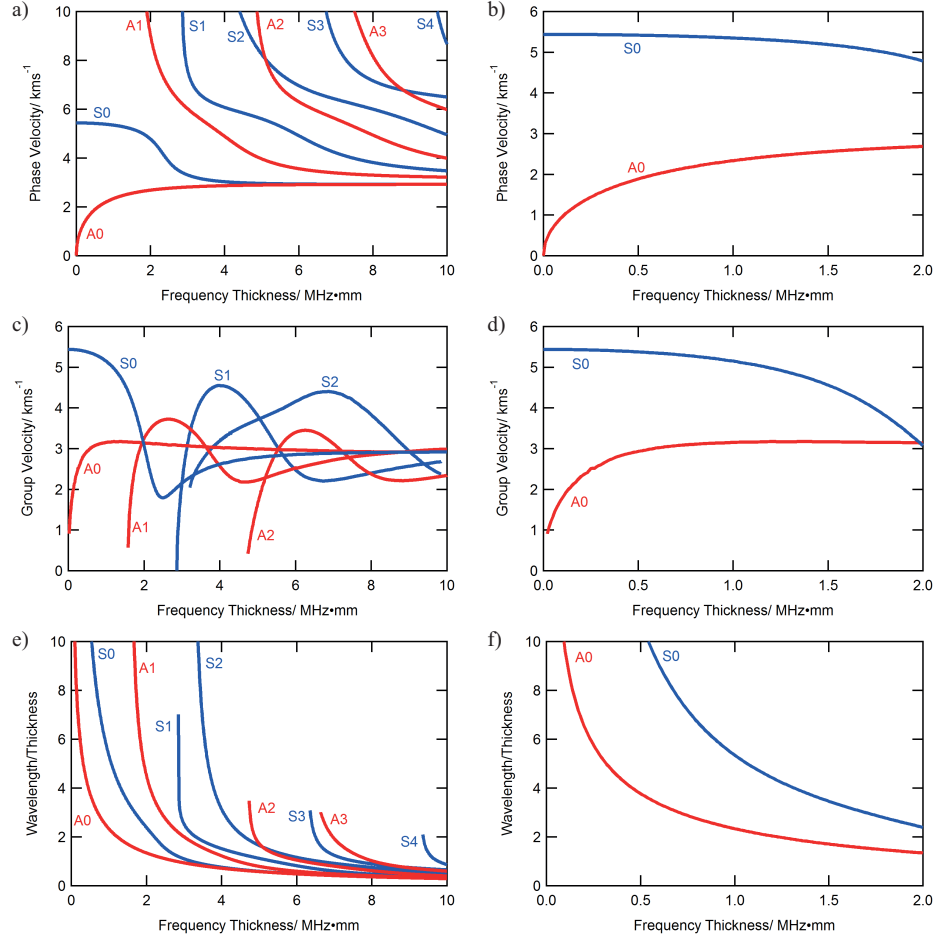


Figure 1.15: Dispersion curves for Lamb waves in aluminium; a) phase velocity, b) first modes only, c) group velocity, d) first modes only, e) wavelengths, and f) first modes only. Waves can not be maintained when the phase velocity asymptotes to infinity and this causes the cut off seen in group velocity and wavelength.

fd , corresponding to the higher order modes). This results in series of complicated dispersion curves that can be produced for Lamb waves, with an example for Lamb waves in aluminium shown in figure 1.15. Note that the x-axis of these is given as frequency-thickness, as was used in the calculation, meaning that the dispersion relationships scale with the thickness of the plate. As such, a point that corresponds to the velocity of a mode at a certain frequency and plate thickness will correspond to a lower frequency for a greater plate thickness. The phase velocity dispersion curves (figures 1.15(a) and (b)) are used to generate the wavelength (figures 1.15(e) and (f)), which gives the wavelengths for a certain frequency thickness as measured in

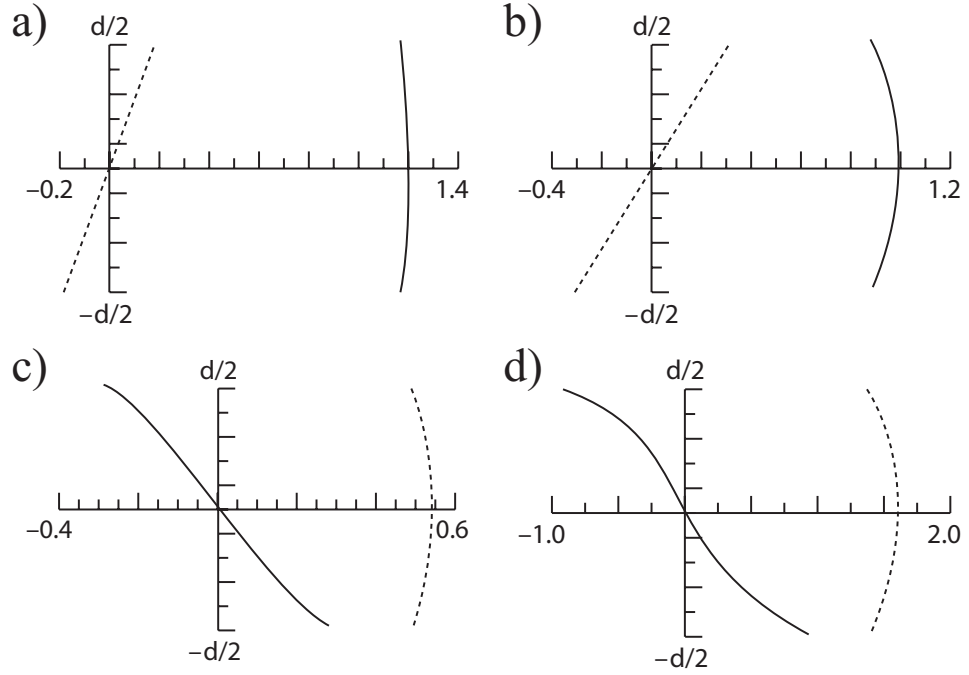


Figure 1.16: Wave structure of the low frequency S0 and A0 Lamb wave modes in aluminium. The x-axis is the velocity of the in-plane (solid line) and out-of-plane (dashed line) motion, and the y-axis is distance from the centre of the plate. a) S0, $fd = 0.5$ MHz·mm, b) S0, $fd = 1.0$ MHz·mm, c) A0, $fd = 0.5$ MHz·mm, and d) A0, $fd = 1.0$ MHz·mm. Adapted from [92].

multiples of the thickness. For all but the zero-order modes there exists a minimum frequency at which the phase velocity asymptotes to infinity, as does wavelength, indicating that these higher order modes cease to exist below certain frequencies. The experiments in chapter 5 are all performed on a plate with 0.5 mm thickness at frequencies below 500 kHz, which can be better seen in the zoomed graphs in figure 1.15. At these frequencies only the S0 and A0 mode are able to propagate. The A0 mode also appears to cut off at low frequencies, though this is a product of a numerical singularity in the method used to generate dispersion curves and not an actual cut off for the mode.

It is also possible fully describe the particle motion of the waves as a profile across the entire plate thickness in terms of the in-plane (along the direction of propagation) and out-of-plane motion [92, 93]. Examples of these profiles for the S0 and A0 modes at low frequency-thickness are given in figure 1.16. As can be seen from these, for the motion at the surface the S0 mode is primarily in-plane motion, while the A0 mode is primarily out-of-plane motion.

Lamb waves are particularly useful due to being guided by the plate bound-

aries, meaning that there can be no spreading of the wavefront in Z. Therefore, if a Lamb wave can be generated that propagates linearly rather than circularly (which can be achieved using a line source, see section 1.2.3.4) then there will be minimal spreading of the wavefront and the energy of the wave will be reduced primarily due to attenuation. This enables Lamb waves to travel over long distances, which is particularly useful for NDT where it may not be possible to place a transducer near to an area of interest. Lamb waves are used extensively in the NDT experiments done in chapter 5.

1.2.2 Ultrasound Signal Analysis

Signal analysis is an important part of any ultrasound based experiment. A simple form of signal analysis is the use of a real time lock-in amplifier, which compares an input signal, $a(t)$ to a reference signal (i.e. an oscillating signal at a set reference frequency, f_{ref}). A two phase lock-in amplifier does this at two phases of the reference signal, separated by 90° . Mathematically the lock-in amplifier operates according to

$$\begin{aligned} X(t') &= \frac{1}{t_{av}} \int_{t'-t_{av}}^{t'} \sin(2\pi f_{ref}t) a(t) dt = \frac{1}{2} A_{ref} \cos(\phi), \text{ and} \\ Y(t') &= \frac{1}{t_{av}} \int_{t'-t_{av}}^{t'} \cos(2\pi f_{ref}t) a(t) dt = \frac{1}{2} A_{ref} \sin(\phi), \end{aligned} \quad (1.28)$$

where A_{ref} is the amplitude of the signal at the reference frequency, ϕ is the phase difference between the input signal and the reference, and t_{av} is the averaging time, which needs to be much longer than the reference period to avoid noise and harmonic effects [94, 95]. The time averaging used here is a simple implementation of a low pass filter and is often instead implemented using a different filtering technique, such as a finite impulse response (FIR) filter. The amplitude and phase can be returned from these signals as

$$\begin{aligned} A_{ref} &= \sqrt{X^2 + Y^2}, \text{ and} \\ \phi &= \arctan\left(\frac{Y}{X}\right). \end{aligned} \quad (1.29)$$

This method is useful for analysing signals in real time where there is a single frequency of interest that needs to be constantly monitored. As such it is commonly used in AFM techniques, though does not provide much use for NDT techniques where pulsed ultrasound is often used, giving a broadband wave, and where the waves can be dispersive.

Another way of analysing ultrasonic signals is using a direct visualisation of them. In NDT these are often referred to as A-, B-, and C-scans [96]. An A-scan is a trace from a single or averaged collection pulse, i.e. a graph of displacement (or velocity) against time. This can be used to determine, for example, the travel time and amplitude of pulses. A B-scan considers then the spatial positioning of the test probe, either showing analysed data from an A-scan at each point (such as a time delay or amplitude) against position, or an image combining multiple A-scans, displayed as time and position axes with a colour scale corresponding to displacement (or velocity). The latter is useful as parts of the signal can be indicated to be moving in time on the image, e.g. a travelling wave will be seen as a series of diagonal lines on the B-scan, corresponding to the velocity and direction of the wave. Interference effects can also be seen in this way. Image type B-scans may become less useful when dealing with highly dispersive waves, as the different signal components can become difficult to distinguish, and over small spatial ranges the time differences of the waves will be small and thus not easy to see [97,98]. A C-scan is an extension to two dimensional spatial mapping, showing an image with a colour scale that corresponds to analysed data from the A-scans at each point. These allow for the spatial extent of defects to be visualised.

It can also be useful to look at the frequency content of a signal [99,100]. This can be achieved through a Fourier transform of the A-scan, which converts from time space to frequency space, showing the magnitude of each frequency contained within the signal [95]. The infinite time continuous Fourier transform is given by

$$\hat{a}(f) = \mathcal{F}[a(t)] = \int_{-\infty}^{\infty} a(t)e^{-2\pi ift} dt, \quad (1.30)$$

where $\hat{a}(f)$ is the frequency space representation of $a(t)$, $i = \sqrt{-1}$, and \mathcal{F} represents the Fourier transform operation. In practice, this form of the Fourier transform cannot be performed on the finite and discrete data collected experimentally. Therefore, the discrete Fourier transform (DFT) is used, given by

$$\hat{a}(f) = \mathcal{F}[a(t)] = \sum_{n=0}^{N-1} a(n\Delta t)e^{-2\pi ifn\Delta t}, \quad (1.31)$$

where N is the number of points in $a(t)$ and Δt is their separation. The DFT is typically performed computationally using the fast Fourier transform (FFT) algorithm [101–103]. While this gives some useful information about the signal, it is not particularly useful for understanding the full behaviour of the wave as it removes all time information. A solution to this is the short time Fourier transform, in which the

signal is windowed and transformed at multiple time values, producing a representation of a in time-frequency space, known as a spectrogram or sonogram [95, 104].

The windowing technique is known as the Gabor method [105]. In this a window function is defined that falls off to 0 symmetrically around $t = 0$ and is normalised (i.e. the integral over all time is equal to 1) is defined. An example of such a function, and the one used in these experiments, is the Gaussian function, given by

$$h(t) = \frac{1}{t_W \sqrt{\pi}} e^{-\left(\frac{t}{t_W}\right)^2}, \quad (1.32)$$

where t_W is the width of the window. This is then used in a Fourier transform according to

$$\hat{a}(f, t') = \mathcal{F}[h(t - t')a(t)]. \quad (1.33)$$

Typically, this result will be given as the magnitude or square of \hat{a} as the sign of the result is not always relevant. The result will then be a full breakdown of the time delay of each component of the waveform and their frequencies. Such a representation is advantageous as it allows for broadband dispersive waves to be analysed, including the overlay of dispersion curves if the sample properties and distance travelled by the pulse are known. Regions (in time and frequency) on these sonograms can then be chosen and averaged to analyse how a particular signal (frequency of a single mode and path) changes with spatial position in a B- or C-scan representation [98, 106]. One disadvantage to this technique is that resolution is inherently lost by the windowing process — a narrow window in time will, by the nature of the Fourier transform, result in very broad frequency representation. Likewise, time resolution can be sacrificed to gain frequency resolution, with the spread of the signal in time inversely related to the spread in frequency.

1.2.3 Generation and Detection of Ultrasound

There are a wide variety of techniques that can be used to generate and detect ultrasound within in a sample. In general these techniques can be separated into two categories — contact and non-contact. Contact techniques typically generate/detect ultrasound within the transducer and require the transducer to be acoustically coupled to the sample, e.g. through the use of a viscous liquid or adhesive, such that the ultrasound can pass between the sample and transducer. Non-contact techniques typically generate/detect ultrasound within the sample itself, and can therefore operate without acoustic coupling. The requirement for couplant with contact transducers can cause significant variations in the coupling efficiency (and thus generation

power/detection sensitivity) and makes them somewhat unsuitable for scanning applications and harsh environments (e.g. high temperatures causing the couplant to boil off or directly affecting the transducer). It is possible to have air coupled transducers, where the ultrasound is generated directly by the device (as in a contact technique) and then transmitted to the sample through the air (and are thus operated as a non-contact transducer), though these require careful design to optimise acoustic coupling with the air and can be prone to high attenuation at high frequencies.

1.2.3.1 Piezoelectric Transducers

Piezoelectricity is a material property in which a strain within a material generates an electric field [107]. Piezoelectric materials also display the reverse effect, in which an electric field generates a strain. As such, an oscillating voltage applied across a piezoelectric material can generate physical oscillations, and thus it can be used as a contact type ultrasonic generator. Oscillation detection can be done by measuring the voltage across the material while it is in contact with the sample surface. This makes them a simple to use transducer or actuator, and they are commonly used in a wide range of applications, including in NDT for wave detection and generation and in AFM for positioning and tapping mode oscillation. Quartz is a commonly used, naturally occurring piezoelectric material, while lead zirconium titanate (PZT — $\text{PbZr}_x\text{Ti}_{1-x}\text{O}_3$, $0 \leq x \leq 1$) is one of the most commonly used piezoelectric materials thanks to its particularly strong piezoelectric effect [108, 109]. Ongoing research includes searching for piezoelectric materials suitable for high temperature operation [110, 111] and lead-free materials with a strong piezoelectric effect for replacing PZT [112–114].

The piezoelectric effect arises in noncentrosymmetric crystals that possess an electric dipole [107]. This can be seen in the perovskite structure of PZT shown in figure 1.17. Here, it can be seen that the lead and oxygen ions form a symmetric lattice while the central, highly charged titanium or zirconium ion is off-centre (when below the material’s Curie temperature) and thus the cell is electrically polarised (a dipole). The strength of this dipole (and thus the electric field) is dependent on the size of the unit cell; a compressed cell will have a weaker dipole, and an extended cell will have a stronger dipole. The strength of the dipole then determines the strength of the electric field and thus the measured voltage. Conversely, if an electric field is applied the off centred positive ion will be attracted to the negative pole, and thus if the field is aligned with the polarisation the cell will shrink, and if it is anti-aligned the cell will grow. These two effects have the opposite direction — if a compression

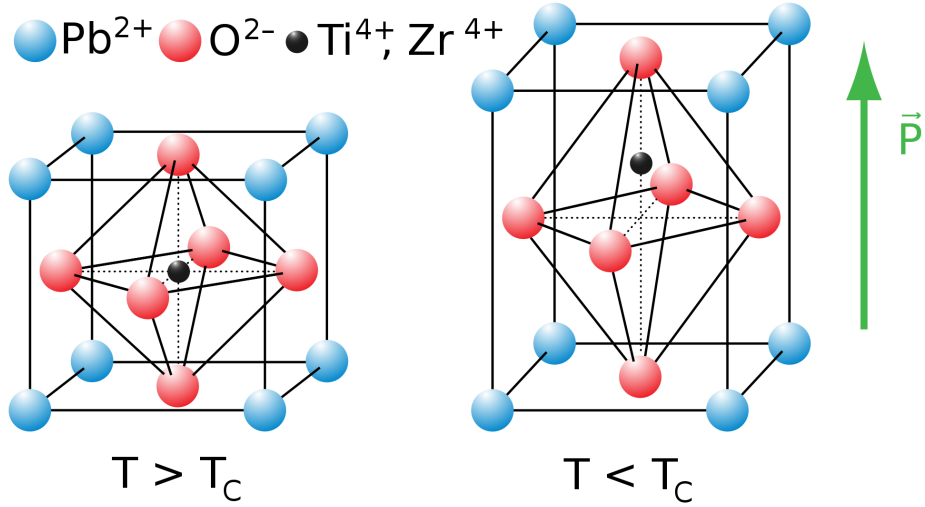


Figure 1.17: Unit cell of PZT perovskite structure, exhibiting piezoelectric properties below the Curie temperature, T_C . Reproduced from [116], similar figures are available in [109, 117].

produces a negative “top” electrode, a negative voltage applied to the “top” will cause an expansion. The piezoelectric effect described here is the longitudinal effect (where the direction of the field and strain are parallel), though the transverse effect (where the field and strain are perpendicular) and shear effect (where the field is perpendicular to a shear strain, with the opposite sides of the crystal moving in opposite directions) are also possible [115].

A macroscopic piezoelectric material, as produced, contains many unit cells, which will be naturally unaligned (polarisations in random directions). This means that the net piezoelectric effect of all the cells combined will be nullified or very small. This is solved by polarising the material, in which a very large electric field is applied to the material causing all the unit cells to align, and thus experience the same piezoelectric effect [109]. This poling is maintained due to pinning by microscopic defects within the lattice. The poling can be reversed by either poling in a new direction or by raising the temperature above the Curie temperature, at which point the dipoles are lost and will reform in random orientations when cooled to below the Curie temperature again.

Piezoelectric transducers are capable of generating and detecting many different types of ultrasound wave. For generation, the type of wave desired can necessitate the transducer being specially mounted — for example to generate Rayleigh waves a longitudinal transducer must propagate waves at an angle to the surface (not normal to the surface) and thus is mounted on a wedge acoustically coupled

to the sample. Piezoelectric transducer behaviour can also be frequency dependent, which varies with the construction of the device. Plate type transducers operating in thickness expansion mode will exhibit a resonant frequency, f_0 , corresponding to the time taken for a longitudinal wave (travelling at v_L) a full round trip through the thickness, T , of the transducer, i.e. $f_0 = \frac{v_L}{2T}$ [107].

1.2.3.2 Electromagnetic Acoustic Transducers

Electromagnetic acoustic transducers (EMATs) are a non-contact generation and detection technique. They induce ultrasound waves in electrically conductive materials through electromagnetic interactions and in ferromagnetic materials through the magnetostriction phenomenon [118]. Ferromagnetic materials are not used here, so magnetostriction is not of interest, though it can be understood as the interaction between the magnetic dipoles of a material and a magnetic field, with a more complete description available in the literature [119].

An EMAT consists of a wire coil and, in many cases, a permanent magnet. The magnet is only necessary for detection coils, though generation efficiency is improved by its presence [120], or the presence of a ferrite to strengthen the coil generated field [121]. The coil is then placed close to the surface of the electrically conducting sample, with typical lift-off heights up to a few millimetres [122,123]. For generation, the coil is then driven by a high power source, either with an alternating current at the desired ultrasonic frequency, giving a narrowband output, or with a transient source, generating broadband ultrasound. For detection the coil is attached to a high gain amplifier and the output is measured using standard methods.

Generation by EMATs is achieved through electromagnetic effects described by Maxwell's equations. Presented here is a summary of the mechanism, though a full mathematical approach can be found elsewhere [119,124]. Any wire containing a current will, according to Ampère's circuital law, have a magnetic field that encircles the current, as illustrated in figure 1.18(a). As this current is changing with time (being either AC or transient) the resultant magnetic field will also be varying with time. Thus, according to Faraday's law of induction, it will generate a current in a conductor (in this case the sample) and, according to Lenz's law, this current will act to oppose the change in magnetic field (by its own generated field). This results in a current being generated within the sample, also known as an eddy current, which mirrors the current in the coil, as illustrated in figure 1.18(b). As this is an alternating current the current density, J , is confined to the sample surface according to the skin effect,

$$J = J_s e^{\frac{-(1+i)d}{\delta}}, \quad (1.34)$$

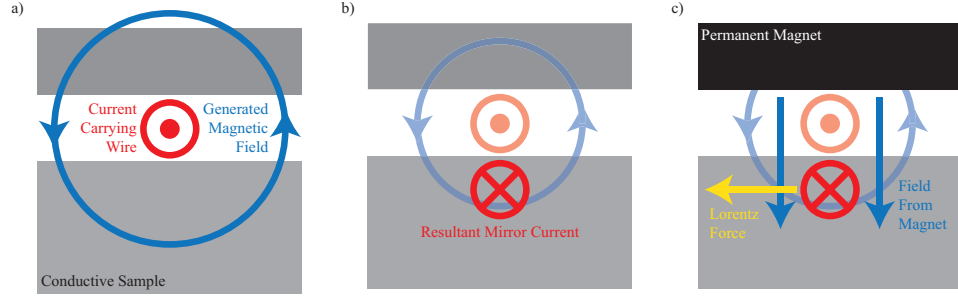


Figure 1.18: Simplified schematic for the EMAT generation mechanism. a) Field around a wire containing a changing current. b) Mirror (eddy) current caused by the changing magnetic field. c) Lorentz force from interaction between a field from a permanent wire and the mirror current.

where J_S is the current at the surface, $i = \sqrt{-1}$, d is the depth into the sample, and δ is the skin depth [119, 125]. This means that the amplitude will drop by a factor of e for each skin depth into the sample, and the imaginary component means that the phase lag is increased by 1 radian for each skin depth. For a good conductor the skin depth is given by

$$\delta = \sqrt{\frac{\rho}{\pi f \mu}}, \quad (1.35)$$

where f is the frequency, ρ is the resistivity of the sample and μ is the permeability of the sample. For aluminium, $\mu = 1.26 \times 10^{-6} \text{ m} \cdot \text{kg} \cdot \text{s}^{-2} \cdot \text{A}^{-2}$ and $\rho = 2.42 \times 10^{-8} \Omega \text{m}$ (at 0°C), for which $\delta = 0.25 \text{ mm}$ at $f = 100 \text{ kHz}$, which is much shorter than the wavelength of the ultrasound and thus the current can be considered to be contained within the surface of the sample.

The generated current means that there are moving electrons which interact with the magnetic field, \mathbf{B} , of the permanent magnet, or with the field generated by the coil, via the Lorentz force

$$\mathbf{F} = q(\mathbf{v} \times \mathbf{B}), \quad (1.36)$$

where \mathbf{v} is the velocity of the electrons and q is their charge [126]. The velocity of the electrons is related to the current density by $\mathbf{v} = \frac{\mathbf{J}}{nq}$, where n is the number density of electrons. This is illustrated in figure 1.18(c). The force is then transferred to the lattice, resulting in motion and thus generation of ultrasound. The transfer of energy from the electrons to the lattice is not an efficient process due to the difference in mass between the electron and lattice atom, and thus results in a low efficiency for EMAT generation [127]. As the Lorentz force is a cross product the generated motion will be perpendicular to both the current and the magnetic field. The current

is always constrained to be in the plane of the surface and thus the magnetic field direction will determine the motion direction — an out-of-plane field will generate in-plane motion, and an in-plane field will generate out-of-plane motion.

Detection by EMATs is the reverse of this process, though with an improved efficiency as the electrons are already moving and do not need energy to be transferred from the lattice [127]. The motion caused by the ultrasonic waves causes the electrons in the field of the permanent magnet to experience a force. This force causes motion and thus the creation of a current, which then generates a mirror current within the coil by the same process as eddy currents are created by generation EMATs. As with generation EMATs the orientation of the magnetic field determines the sensitivity to directions of motion — an out-of-plane field EMAT will be sensitive to in-plane motion, and an in-plane field EMAT will be sensitive to out-of-plane motion [128–130].

The adaptability of EMATs is a major advantage of their use — through careful consideration of the design of the EMAT, particularly the shape of the coil and direction of the permanent magnetic fields, the generation efficiency and detection sensitivity can be tuned to a variety of different wave types. Additionally, the shape of the design can easily be customised, allowing for directed waves to be generated, as discussed further in section 1.2.3.4.

1.2.3.3 Laser Ultrasonics

Laser ultrasonics covers a group of non-contact ultrasonic generation and detection techniques utilising lasers [131, 132]. Lasers are light sources that exhibit coherence both spatially (very low spreading of a beam from the source) and temporally (all waves are in phase and of a single frequency). The use of lasers means that they can be operated at a significant distance from the sample, depending on the focal length of the optics. Laser ultrasound techniques also have a significantly higher spatial resolution than single piezoelectric transducers and EMATs as they are limited by the spot size of the laser (which can be focussed to be as small as the wavelength) rather than the physical size of the probe. They do, however, pose user safety concerns associated with the use of high power light which may cause eye damage, or skin burns for particularly powerful devices, if the correct protective measures are not followed (such as protective eye wear with filters for the wavelength of the laser used). Unlike EMATs and piezoelectric transducers the mechanisms for generation and detection are significantly different.

1.2.3.3.1 Laser Generation

Laser generation of ultrasound is achieved through the use of high power lasers incident on the surface, typically in pulsed operation — very short (10s of nanoseconds) pulses of very high intensity (100s of millijoules) light. The high energy requirements for generation limit the types of laser that can be used, with Q-switched Nd:YAG and gas CO₂ lasers being common. The effect of the high incident energy on the sample causes the generation of ultrasound. The generation method can be split into two regimes; the lower energy thermoelastic regime and the higher energy ablative regime [132, 133].

In the thermoelastic regime the incident photons are absorbed by the electrons within the sample. The photons will primarily be absorbed by the electrons close to the surface, with a characteristic skin depth in metals identical to the skin depth for eddy currents, given in equation 1.35, except here the frequency is that of the incident light. For the a Nd:YAG laser with a wavelength of 1064 nm this frequency is 282 THz, which corresponds to a skin depth in aluminium of 4.7 nm, meaning that all the (non reflected) energy is absorbed in a very small region close to the surface. The absorption of energy causes a localised heating of the material and thus a localised expansion. As this expansion is over a very short time period (the pulse duration of the laser) and is confined by the cooler surrounding regions, it will cause a stress/strain field and thus generate an ultrasonic wave. The finite duration of the pulse means that the ultrasound generated will be broadband, though narrowband generation is possible through designing the laser geometry, as discussed in section 1.2.3.4,

In the ablative regime the sample surface is vaporised by the high energy of the incident wave. This results in material being ejected from the surface and thus, due to conservation of momentum, an opposite force being applied to the surface, generating ultrasound. This technique causes damage to the sample surface and is thus not suitable for samples where preservation of the surface is important.

1.2.3.3.2 Laser Detection

Laser detection of ultrasound works by reflecting a laser off the sample surface and detecting a change in the measured signal caused by motion of the surface. There are a variety of different methods by which the changes can be detected. One such method is similar to that of detecting the deflection of an AFM cantilever — a laser is reflected off the surface at an angle not normal to the surface and the position of the reflection is measured (either through use of a multi segment photodiode or a

single detector with part of the laser blocked, known as knife edge detection) [127, 132, 134]. An ultrasonic wave then causes distortions in the surface which results in the reflected laser moving. Most laser detection techniques, however, are based around interferometry, where the interference of the reflected wave with a reference wave causes a change in intensity that can be measured.

The simplest design for a reference beam interferometer is the Michelson interferometer, illustrated in figure 1.19(a) [132, 135]. The laser source is split into two arms; one which is reflected off a reference mirror at a fixed distance, and another reflected off the sample surface. These reflections are then combined and transmitted to a photodetector (such as a photodiode). If the waves are in phase at the photodetector then the constructive interference will result in a maximum measured light intensity; if they are out of phase then there destructive interference results in a minimum light intensity. A change in the position of the sample surface (of distance z , caused by an out-of-plane component of an ultrasonic wave) will cause a change in path length of twice the displacement, and thus a change in phase. As such the measured intensity can be given by

$$I = \bar{I} + I_0 \cos\left(\frac{4\pi z}{\lambda}\right), \quad (1.37)$$

where \bar{I} and I_0 are system dependent variables and λ is the wavelength of the laser. The Michelson interferometer has some drawbacks, however, as any motion of the reference arm (such as vibrations) will be coupled into the measured signal. Low frequency contributions can be reduced by moving the reference mirror with a linear actuator controlled by a low frequency feedback loop [127]. The sample surface must also have a specular reflection (i.e. a mirror surface) as differences in the wavefront geometry from a reflection from a non-polished surface will result in inaccurate measurements.

An alternative approach to combining the waves is through the use of a photorefractive crystal, as is done in a two-wave mixing interferometer, illustrated in figure 1.19(b) [136, 137]. As with the Michelson interferometer, the laser source is split into a sample arm and a reference arm, both of which reflect the laser. Rather than having both waves incident on the detector they are instead passed into a photorefractive crystal. A photorefractive crystal locally changes its refractive index in response to light intensity [138, 139], meaning that when the reference and reflected waves meet within the crystal the refractive index is changed according to their interference pattern. This results in a diffraction grating occurring within the crystal and this causes the reference beam to be diffracted such that its wavefront shape

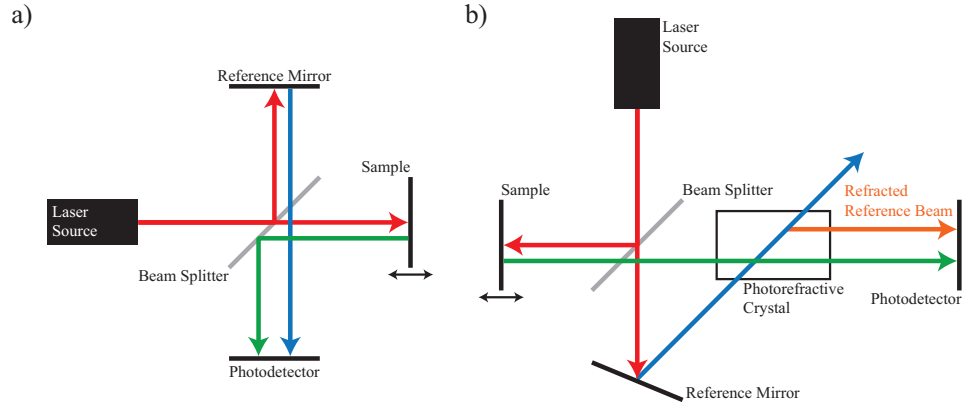


Figure 1.19: Schematics of displacement measuring interferometers; a) Michelson interferometer and b) two-wave mixing interferometer. Note that parallel laser paths are collinear in real equipment.

matches that of the reflected beam. Both beams are coincident coming out of the crystal. The two beams then interfere the same as in a Michelson interferometer and the measured intensity gives the relative displacement of the sample surface. This technique is useful as it allows for the measurement of non-specular reflections, meaning that a wider range of surfaces can be investigated without need for preparation. This type of interferometer is used in chapter 5, with the model used collecting the scattered light with a probe head. This probe head, which is connected by optical fibres to the laser source and detection electronics, has a central optical fibre for the source laser and a ring of optical fibres surrounding this for the return (non-specular) reflected lasers.

To get a map of response (e.g. the amplitude of surface oscillations) these lasers can be raster scanned across the sample surface, taking a measurement at many points. Electronic speckle pattern interferometry can also be used to map the response [132, 140, 141]. In this method the laser is spread across the surface of the sample (rather than focussed on a point). The non-specular reflections from the surface are then mixed with a wide reference beam and the resulting interference pattern is recorded by a video photodetector (i.e. a photodetector that produces spatial maps/images).

It is also possible to measure the velocity of the surface motion, instead of the displacement, by measuring the Doppler shift (the change in frequency due to a moving reflector) [132]. For motion much slower than the speed of the wave (which here is the speed of light, c , and thus this assumption will be correct) the Doppler

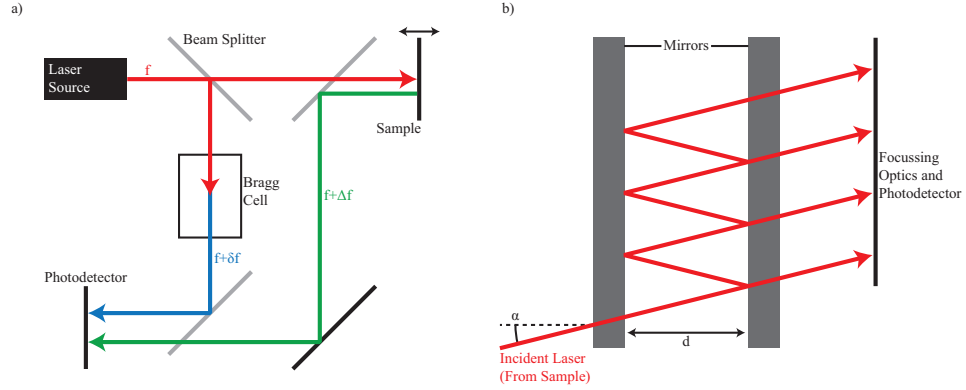


Figure 1.20: Schematics of velocity measuring interferometers; a) Doppler vibrometer and b) Fabry-Pérot interferometer.

shift is given by

$$\Delta f = \frac{2v}{c} f, \quad (1.38)$$

where v is the reflector velocity and f is the frequency of the incident light. One way to measure this is with a Doppler vibrometer, illustrated in figure 1.20(a) [132]. The design of this is similar to a Michelson interferometer, except one of the beams is directed through a Bragg cell, which introduces a frequency shift (δf , a small fraction of the wave frequency) to the wave and the sample motion adds another Doppler shift to the reflected surface wave. The reference and reflected waves will then interfere and the combined frequency shift will result in the intensity varying with a beat frequency (equal to the magnitude of the shift) as the phase alignment varies. This beat frequency can then be measured and the Doppler shift calculated, giving the surface velocity.

Another way of measuring the frequency is with a Fabry-Pérot interferometer, illustrated in figure 1.20(b) [132]. In this the reflected beam from the sample enters a chamber with mirrors on each side at a set separation. The incident wave will then interfere with its own reflections, with a maximum intensity when the optical path length of a full reflection is a multiple of the wavelength of the laser, λ , i.e. when

$$2d \cos(\alpha) = n\lambda, \quad (1.39)$$

where d is the distance between the mirrors, α is the angle of incidence of the wave, and n is an integer. As the mirrors will have a partial transmittance the intensity from the interferometer will then be maximised when equation 1.39 is satisfied. Adjustment of d or α can be performed to directly measure λ , which will have been

shifted due to the Doppler shift from the surface.

1.2.3.4 Source Geometry, Directivity, and Guided Waves

The geometry of the ultrasonic transducer used for generation plays an important role in the nature of the waves generated. The simplest geometry is the spot or point geometry, in which the transducer takes the form of a circle. In this configuration the generated ultrasound will have no preferential direction and thus the wavefronts will propagate radially. This radial propagation means that the wavefront is spreading and the intensity of the waves will decay with $\frac{1}{r^2}$ (where r is the distance travelled) for spherically spreading bulk waves, and with $\frac{1}{r}$ for circularly spreading surface and plate waves (not including attenuation from the material), making them unsuitable for long range measurements. An alternative geometry is an infinite line, which will generate straight wavefronts propagating perpendicular to the line; any propagation parallel to the line will be suppressed by the symmetry of the system — the sum of contributions from every point on the line will be zero at any point on the line. In a surface wave the wavefront will therefore not be spreading and thus there will be no decay in amplitude (ignoring attenuation from the material) and thus they can be used for long range measurements. In practise an infinite line geometry is often impractical, so instead a finite line geometry is used, which will be subject to some spreading. The finite line also means that the power of the wave is directed perpendicular to the line length, allowing the wave to be targeted.

More complex geometries of the transducer can produce additional effects. For example a curved geometry can produce waves which converge on a set focal point, dependent on the curvature, which is useful for investigating features smaller than the generator (or detector) size [142, 143]. Geometries can also be used for selective excitation of specific wavelengths — if a transducer consists of a series of lines at a set separation then only wavelengths close to a multiple of this separation will be allowed to be generated or detected, while others will be suppressed by interference [144, 145]. This effect can be achieved with an EMAT “meander coil,” which has alternating forward and return tracks that will produce opposing motion under the same magnetic field, and thus the relevant separation is the distance between two tracks of the same direction.

1.3 Scope of Thesis

In this thesis a variety of methods are used to investigate the properties of materials at the nanoscale. In particular there is a focus on looking at mechanical properties

at varying length scales using an AFM, with further focus placed on techniques that incorporate ultrasound.

In chapter 3 the mechanical properties of 2D materials are tested using nanoindentation on suspended films. This is used to measure the elastic modulus and breaking strength of chemical vapour deposition (CVD) grown graphene. Comparisons are made between as-grown graphene and graphene after different treatments — heating and oxygen functionalisation through exposure to atomic oxygen. Graphene oxide is also tested as a comparison to the oxygen functionalised CVD grown graphene results. To perform the testing, an automated method is devised to allow the acquisition of large datasets for improved statistical significance. Complementary information for x-ray photoelectron spectroscopy, Raman spectroscopy, and transmission electron microscope imaging is used to correlate the changes in mechanical properties to changes in atomic structure. These suspended 2D material sheets have an interest as ultrasonic nanoresonators, the behaviour of which could potentially be investigated using an AFM.

In chapter 4 a technique known as ultrasonic force microscopy (UFM) is investigated. This technique uses high frequency (well above the cantilever resonance) oscillations of the sample to probe the local mechanical properties of the surface, particularly the Young's modulus. The effect of various parameters (such as operation frequency and load amplitude) on the behaviour of UFM are investigated with the aid of a simulation. The effect of tip hardness on contrast in the UFM signal is also investigated. UFM is then combined with other contact mode techniques (cAFM and FFM) demonstrating simultaneous measurements of conductivity, friction, and mechanical properties. This combined approach is also used to conductively image a delicate sample (carbon nanotubes) which would normally be destroyed in contact mode imaging, taking advantage of the superlubricity phenomenon of UFM.

Finally, in chapter 5, AFM is investigated as a potential detection sensor for use in ultrasonic NDT experiments. Ultrasonic NDT is the use of ultrasonic excitation to detect cracks and other features within samples by monitoring changes in detected signals. AFM is presented as a high spatial resolution detector with high sensitivity, potentially enabling the detection of small features, such as micro-cracks. The suitability of AFM as a detector for ultrasonic NDT is demonstrated through the use of simple experiments around a laser micromachined crack in an aluminium plate, comparing AFM results to those gathered with piezoelectric transducers and an interferometer. The capability of an AFM to simultaneously and independently detect both out-of-plane and one component of in-plane motion of the sample surface is also demonstrated. This is useful for understanding the full nature of the ultra-

sound waves, such as knowing the mode content, and is not easily achieved with other common ultrasound detection techniques.

Overall conclusions and suggestions for further work are presented in chapter 6.

Chapter 2

Experimental Methods

All AFM experiments were performed using an Asylum Research MFP-3D-SA. This AFM uses laser deflection detection with a four quadrant photodiode. The photodiode is manually adjusted in the vertical axis, but the lateral axis has a fixed position. The X and Y (in-plane) motion is achieved by a flexure-based piezoelectric actuator driven stage, with LVDT nano positioning sensors for closed loop operation. The sample is mounted on this stage (sample scanning), which has a range of 90 μm in each direction and a typical sensor noise level of less than 0.5 nm and a nonlinearity of less than 0.5%. The Z (height) motion is driven by a piezoelectric actuator mounted in the head (tip motion) and also features a nano positioning sensor, though was operated in open loop mode. The extended head version of the MFP-3D was used, giving a Z range of 40 μm .

The set point for contact mode is set as an absolute value for deflection in volts. For experiments where the load force is important, the set point was set relative to the free deflection before the start of each scan. For tapping mode, the free amplitude was tuned to 1 V using the in-built auto tune feature, which performs multiple frequency passes of decreasing bandwidth around the expected resonance frequency to accurately determine the resonance for the specific cantilever. The frequency was offset to a value corresponding to an amplitude 5% lower than the amplitude at resonance on the lower frequency side of the resonance, which improves the stability of the tapping mode feedback. The setpoint for tapping mode imaging was adjusted for each sample to ensure stable imaging and was typically in the range of 600–800 mV. Scanning is performed stepwise — the AFM performs the trace (initial motion, left to right on the images) and retrace (return motion) in the fast axis at a constant speed and then steps the slow axis before performing the next line. There is some overscanning in the fast axis, meaning that the tip travels past

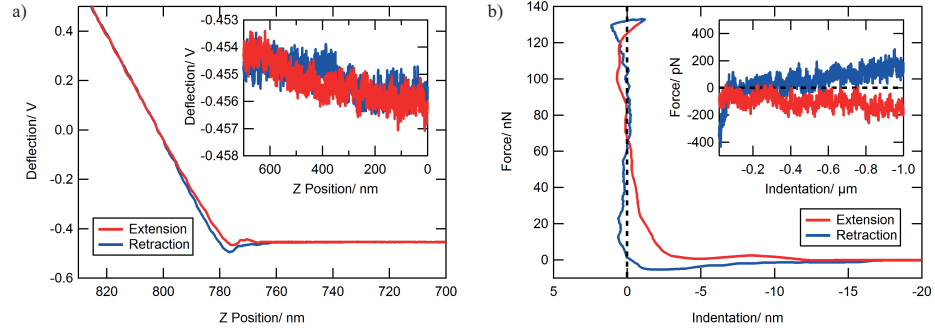


Figure 2.1: Example force curve performed on a silicon nitride sample. a) Raw data. b) Processed data. Insets show an extended view of the flat sections, with higher vertical (deflection or force) resolution.

the end of the line, to avoid artefacts associated with the turnaround.

2.1 Force Curves

Force curves, which are a measurement of force with changing Z position of the cantilever base relative to the sample at a single point, are used to measure the behaviour of samples under varying loads. The cantilever is moved towards the sample at a set rate (of the order of $1 \mu\text{ms}^{-1}$) until the cantilever deflection reaches the set point (similar operation in tapping mode using the cantilever amplitude is also possible), at which point the cantilever is retracted at the same rate to a set lift of distance (of the order of $1 \mu\text{m}$). Here, as the precise Z velocity is not important, the Z motion is performed in open loop mode using an approximated velocity to avoid noise that would be introduced by closed loop operation. The Z sensor position is still recorded as the position information. The set point here is defined as a relative value, using the deflection at the start of the measurement as the reference value, ensuring that the applied load is consistent between experiments. An example of the raw data from a force curve on a hard surface (in this case silicon), is shown in figure 2.1(a).

With an accurate cantilever calibration (see section 2.2) the raw deflection (in volts) vs Z position data (figure 2.1(a)) can be converted into force vs indentation data (figure 2.1(b)), which is necessary to perform meaningful analysis, such as with interaction models (section 1.1.3). To do this the virtual deflection (a change in the deflection signal caused by the changing position of the cantilever, but not a force, see section 2.2.1) must first be subtracted from the raw deflection signal. This is typically done in real time as the data is acquired, such that the virtual deflection does not

effect the chosen set point load. The raw deflection (in volts) is multiplied by the inverse optical cantilever sensitivity (section 2.2.2) to give the cantilever deflection in nm, z_c . This can be further converted to load force by multiplying by the cantilever spring constant, k . The Z position, Z , is then converted to indentation by

$$d = z_c - Z, \quad (2.1)$$

noting that in this case a higher Z corresponds to the cantilever base being further from the sample and a higher d corresponds to greater indentation — other sign conventions are sometimes used. The values for force and indentation are then zeroed — for force this is achieved by subtracting the value of the flat section corresponding to the tip being out of contact with the surface. Zeroing of indentation is dependent on the model used — for the Hertz model ($d = 0$ nm, $F = 0$ nN) is predicted to be a point recorded on the force curve and so is relatively easy to define, however, for the DMT and JKR models the changes in tip and sample position due to adhesive forces mean that (0,0) is not so easily defined.

2.2 Calibration

It is important for the AFM to be properly calibrated in order to get accurate data. Doing so primarily consists of calibrating the stage and the cantilever. Calibrating the stage can be done on an occasional basis, as the stage calibration should not change significantly between sessions, though should still be checked and adjusted regularly for the best results. This is achieved using samples of known parameters — grids of regularly shaped indentations with sharp features at precisely defined spacing and depth. By scanning such a sample the calibration coefficients for each axis can be determined; for a closed loop system such as was used here this typically involves a single linear constant for the sensor calibration, though this can depend on the sensors used. For open loop systems, however, the imperfect behaviour of piezoelectric transducers has to be considered, meaning that additional testing and parameters are needed to account for effects including non-linearity, scan size/speed dependence, and hysteresis.

Cantilever calibration is dependent on each individual cantilever and the positioning of the laser on them, and as such has to be done for each new cantilever used, and if the laser spot is moved. There are multiple aspects to fully calibrating a cantilever, detailed below.

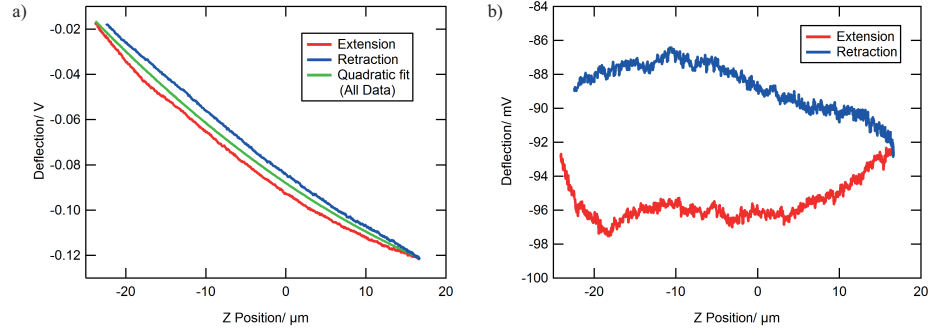


Figure 2.2: Full Z range force curves with no sample contact, showing the effect of virtual deflection. a) With no calibration, showing a quadratic fit to the data, giving first and second order constants of $-2.40 \text{ mV} \cdot \mu\text{m}^{-1}$ and $23.3 \text{ } \mu\text{V} \cdot (\mu\text{m})^{-2}$ (the offset is not important to this calibration). b) Curve performed after calibration from (a).

2.2.1 Virtual Deflection

Virtual deflection is the name given to a coupling between the measured deflection signal and the Z position, even when the tip is not in contact with the sample. The origin of this effect is not completely understood, though it is possibly due to changing optical paths as the cantilever is moved. To calibrate for this, a force curve covering the entire Z range while out of range of the surface is performed, an example of which is shown in figure 2.2(a). This is typically performed just out of range of the surface, though virtual deflection typically isn't effected by the sample at any separation, only varying with new tip mountings and laser alignments. From the force curve it can be seen that the effect is non-linear in this range, though it can be fit well with a second order polynomial. This fit (excluding the offset value, as this will change over time with drift) is then subtracted from the deflection signal, resulting in a free deflection that does not vary with Z position. This can be checked by repeating the force curve and finding a near flat curve, as shown in in figure 2.2(b). These calibration parameters are applied in real time to the measured deflection signal, allowing for accurate force application not affected by the virtual deflection, including the ability to apply very small forces, the measurement of which would otherwise be obscured by the virtual deflection.

2.2.2 Optical Lever Sensitivity

The optical lever sensitivity (OLS) is the relation between how far the cantilever deflects (in nm) and the output reading (in volts). It is typically quoted as the

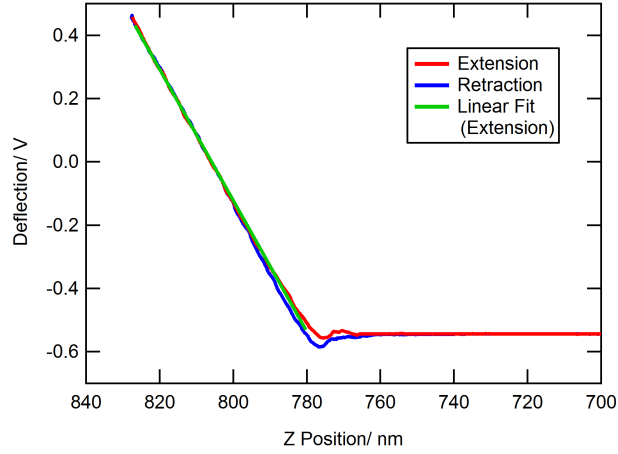


Figure 2.3: Force curve (calibrated for virtual deflection) on a silicon nitride surface. Linear fit is done on the extension section of the curve and has a gradient (corresponding to OLS) of $20.70 \text{ V} \cdot \mu\text{m}^{-1}$, which gives an inverse OLS of 48.31 nmV^{-1} .

inverse OLS (invOLS) as this is a multiplication factor for converting the reading into true deflection, with the units being nmV^{-1} . To calibrate this, a force curve is performed on a hard surface — defined as a material in which there is minimal indentation under typical applied loads. Among many suitable materials, including most metals and semiconductors, silicon is an ideal candidate for this. With a silicon sample and tip, a tip radius of 10 nm and a load force of $1 \mu\text{N}$ (much higher than is typically applied during AFM, corresponding to a typical deflection of 360 nm for the MikroMasch NSC18 cantilevers used throughout these experiments) the Hertz model (see section 1.1.3) predicts an indentation of just 2 nm.

With this force curve (example shown in figure 2.3) the cantilever deflection (in volts) increases linearly with a reducing Z position once the tip and sample are in contact. As the tip does not indent the hard sample, this increase in deflection (in nm) is equal to the change in Z position. As such, this region can be fit with a linear fit and the gradient taken as the OLS, with the inverse of this value being the one used.

2.2.3 Spring Constant and the Sader Method

The spring constant of the cantilever is the linear constant relating deflection to the load force. There are many ways of calibrating this, including use of a standard calibration cantilever [146], monitoring the resonant frequency with controlled addition of mass [147, 148], and through the amplitude of the cantilever's resonant

thermal oscillations [149]. Here, a method proposed by Sader et al. [150] (henceforth known as the “Sader method”) is used. They first noted that the spring constant of a rectangular cantilever, k , was related to the cantilever’s resonant frequency under vacuum, ω_{vac} (measured in $\text{rad}\cdot\text{s}^{-1}$), by

$$k = M_e \rho_c W T L \omega_{vac}^2, \quad (2.2)$$

where W , T , and L are the width, thickness and length of the cantilever, respectively, ρ_c is the density of the cantilever, and M_e is the normalized effective mass of the cantilever (0.2427 for $\frac{L}{W} > 5$). Application of this equation, however, is complicated by multiple factors — firstly ρ_c is not necessarily known due to a layer of material (typically aluminium or gold) being deposited onto the back of the cantilever to improve reflectivity for the laser measurement. Also, while the plan view (W and L) dimensions are simple to measure using an optical microscope, the thickness is much harder to accurately determine, and typically has relatively large manufacturing tolerances. The vacuum resonance is also not easy to measure, as AFM is typically not performed under vacuum and the presence of a fluid causes a shift in the resonant frequency due to damping.

Sader et al. [150] found that the difficulties associated with equation 2.2 could be eliminated by considering the damping effect of the fluid. With the effects of damping considered, equation 2.2 can be modified to become

$$k = 0.1906 \rho_f W^2 L Q_f \omega_f^2 \Gamma_i^f(\omega_f), \quad (2.3)$$

where ρ_f is the density of the fluid, ω_f and Q_f are the resonant frequency and quality factor of the cantilever in fluid, respectively, and Γ_i^f is the imaginary component of the hydrodynamic function for the cantilever in the fluid. Γ_i^f is defined fully in [151] and noted to only depend on the Reynolds number, given by

$$\text{Re} = \frac{\rho_f W^2 \omega}{4\eta_f}, \quad (2.4)$$

where η_f is the viscosity of the fluid. As such, equation 2.3, which is valid given $Q_f \gg 1$, is dependent on six parameters that can be readily determined — two (ρ_f , η_f) are properties of the fluid, which can be found in the literature (1.18 kgm^{-3} [152], 18.6 $\text{mg}\cdot\text{m}^{-1}\text{s}^{-1}$ [153] for air at 1 atm and 25°C), two (W , L) are dimensions of the cantilever, which can be measured prior to mounting, and two (ω_f , Q_f) are the resonant properties of the cantilever, which can be measured by the AFM. While the original version of the Sader method was only applicable to rectangular cantilevers,

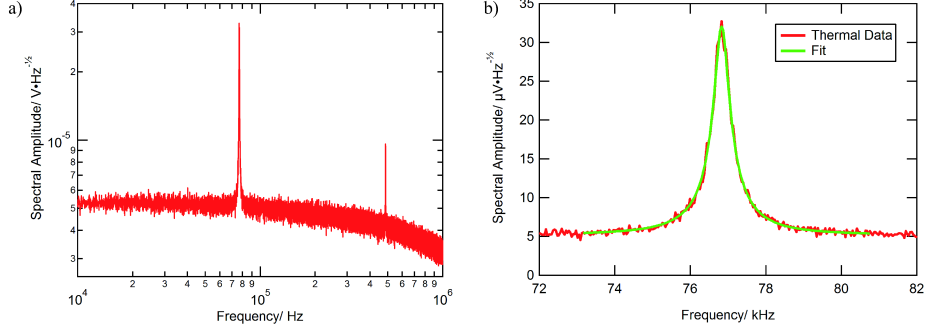


Figure 2.4: Thermal tune of the cantilever. a) Large frequency range. b) Zoomed on the first resonance peak and fit using equation 2.5, giving $f_0 = 76.83$ kHz and $Q = 187.7$, which corresponds to a spring constant of 2.76 Nm^{-1} (with cantilever plan view dimensions of $225 \text{ }\mu\text{m}$ by $35 \text{ }\mu\text{m}$).

it has since been extended to cantilevers of arbitrary shapes [154, 155].

For application of the Sader method, the plan view dimensions of the cantilevers used in these experiments were originally individually measured using a Zeiss Axioimager optical microscope before each experiment. It was found that the plan view dimensions were consistent between cantilevers within the measurement error of the microscope, and as such standard values were used for many experiments. The oscillatory behaviour of the cantilever was acquired using the thermal tune feature of the AFM while the tip was not engaged on the sample. In a thermal tune the deflection is recorded with a high sampling rate (here $\geq 1 \text{ MHz}$) for a short period of time and is then Fourier transformed, giving the amplitude spectral density, $a(f)$, in $\text{V}\cdot\text{Hz}^{-\frac{1}{2}}$ (which is the square root of the power spectral density). This was repeated a set number of times (here, 100) and the results averaged, with an example resultant spectrum shown in figure 2.4(a). The fundamental resonance peak was then fit using the inbuilt fitting function for a simple harmonic oscillator with a white noise background in a window around the peak. The fitting function uses the formula

$$a(f) = \sqrt{\frac{\left(A \frac{f_0}{f}\right)^2}{\left(\frac{f_0}{f} - \frac{f}{f_0}\right)^2 + \left(\frac{1}{Q}\right)^2} + B^2}, \quad (2.5)$$

where A and B are fitting parameters corresponding to the peak size and background level, respectively, f_0 is the fitting parameter for peak location, and Q is the fitting parameter for the quality factor. These values were used to calculate the spring constant with equation 2.3 using a calculator made available on the internet by Sader and the University of Melbourne [156].

2.2.4 Lateral Calibration

For frictional experiments the lateral force sensitivity also needs to be calibrated. As with the normal spring constant, there are many ways to achieve this, such as pushing against a known sample [157] or calibrated force sensor [158], changing oscillation frequency with the addition of mass [159], and the torsional Sader method [159,160]. Here, the improved wedge calibration method is used, in which a hard calibration sample with sloped and flat sections is scanned [161]. This gives a calibration value for converting from the raw deflection (V_{lat} , in volts) to the lateral force between the tip and sample (F_{lat} , in N), though other techniques (such as the torsional Sader method) use a two step method like the normal force calibration, with an intermediary term corresponding to either the rotation of the tip (φ , in radians) or the displacement of the tip apex (d_{lat} , in m). The relation between these terms and the torque of the cantilever due to torsion, τ , is given by

$$F_{lat} = \alpha V_{lat} = \frac{\tau}{h + \frac{T}{2}} = \beta \varphi = \frac{\beta d_{lat}}{h + \frac{T}{2}}, \quad (2.6)$$

where h is the tip height, T is the cantilever thickness and α and β are calibration factors, of which α is the one of interest here, measured in NV^{-1} .

In the wedge method the tip is scanned up and down a sloped sample, resulting in a balance of forces illustrated previously in figure 1.11 of section 1.1.4.3. With the tip travelling up the slope the measured lateral signal will have one value, V^u , while going down the slope it will have a different value, V^d . These two values can be combined to give two new values, the half-width,

$$V_W = \frac{V^u - V^d}{2}, \quad (2.7)$$

and the offset,

$$V_\Delta = \frac{V^u + V^d}{2}. \quad (2.8)$$

These values can also be calculated for the flat regions, where the up and down directions are replaced with trace and retrace directions. The width of the flat section, V_W^{flat} , is determined by the friction force (i.e. $\alpha V_W^{flat} = F_\mu$), while the offset, V_Δ^{flat} , represents any errors with the alignment of the system, such as a non-zero free lateral deflection or crosstalk from the deflection signal. As these errors affect the value on the slope equally, the slope offset is corrected to give $V'_\Delta = V_\Delta - V_\Delta^{flat}$.

The resolved forces of figure 1.11 given by equation 1.15 can then be converted

to terms of V_W and V'_Δ , giving

$$\alpha V_W = \frac{\mu(F + F_{ad} \cos \theta)}{\cos^2 \theta - \mu^2 \sin^2 \theta} \quad \text{and} \quad (2.9)$$

$$\alpha V'_\Delta = \frac{\mu^2 \sin \theta (F \cos \theta + F_{ad}) + F \sin \theta \cos \theta}{\cos^2 \theta - \mu^2 \sin^2 \theta}, \quad (2.10)$$

a full derivation of which can be seen in [161]. Equation 2.10 can then be divided by equation 2.9 to give

$$\sin \theta (F \cos \theta + F_{ad}) \mu^2 - \frac{V'_\Delta}{V_W} (F + F_{ad} \cos \theta) \mu + F \sin \theta \cos \theta = 0, \quad (2.11)$$

which is a quadratic equation for the unknown μ , consisting of measured (V_W and V'_Δ) and known values — F is the set point force, a user chosen value, F_{ad} is the adhesion, which is measured prior to the scan, and θ is the slope angle, taken from the calibration grid's manufacturer specifications or measured using the height image. Solving equation 2.11 then gives two values of μ_i , which in turn can be substituted into equation 2.9 or 2.10 to give two values of α_i . At this point one of the α_i values may be negative, in which case it can be discarded and the positive α_i is taken as the calibration coefficient, α (this can be done before substitution — a value of $\mu_i < \frac{1}{\tan \theta}$ will always yield a negative α_i). If both the values of α_i are positive then one must be selected over the other, which can be done by considering the friction on the flat regions. New friction coefficients corresponding to the flat regions are given by

$$\mu_i^{flat} = \frac{\alpha_i V_W^{flat}}{F + F_{ad}}. \quad (2.12)$$

While it is unlikely that $\mu_i = \mu_i^{flat}$, as the different crystallographic planes being scanned will have different true physical values of μ , the values should at least be similar. Thus the value of α that minimises $|\mu_i - \mu_i^{flat}|$ is chosen as the calibration coefficient, α .

Here, the wedge method was implemented by scanning a Mikromasch TGF11 trapezoidal calibration grid (with $\theta = 54.74^\circ$) in contact mode with the fast scan axis perpendicular to the length of the trapezoids. The scan size was selected such that both sides of the trapezoid were included within the scan range and both the lateral trace and retrace signals were recorded, with example images shown in figures 2.5(a–c). The two lateral images were then processed according to equations 2.7 and 2.8 and histograms of these results were produced, shown in figures 2.5(d) and (e), respectively. On the histogram of V_W the large peak at low values corresponds to

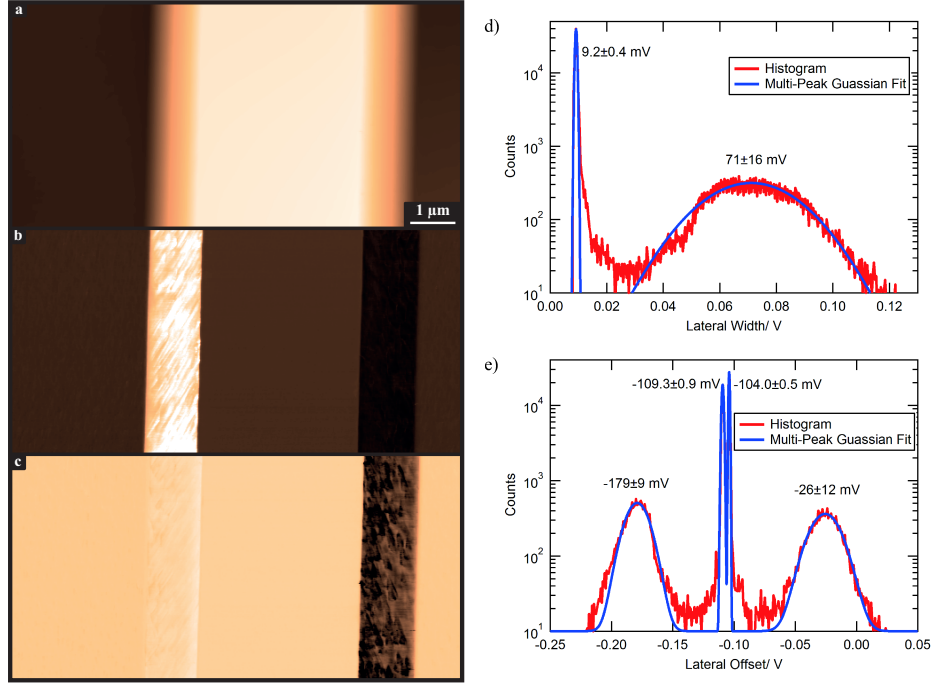


Figure 2.5: a-c) Contact mode AFM image of a TGF11 calibration grid taken with a load force of 324 nN. The channels shown and their corresponding full data scales are a) height, 2 μm , b) lateral trace, 200 mV, and c) lateral retrace, 200 mV and offset -150 mV relative to (b). d,e) Histograms of the lateral width and offset, respectively, with Gaussian fits using Igor Pro's multi-peak fitting tool, showing the peak centre and standard deviation. With an adhesion of 22 nN (measured by force curve) these values give a lateral calibration of $27 \pm 7 \mu\text{mV}^{-1}$.

V_W^{flat} and the smaller peak corresponds to V_W on the slopes. On the V_Δ histogram the large central peak corresponds to V_Δ^{flat} while the smaller side peaks correspond to V_Δ on the slopes — there are two such peaks because the force behaviour is mirrored for the second slope, effectively meaning that the direction (and thus the measured signal) is reversed relative to V_Δ^{flat} . There is also a double main peak effect on the offset histogram, which is due to differences between the plateau and valley regions of the calibration grid, possibly caused by the manufacturing process.

The histogram peaks were then fit using Gaussian curves, the central value for which is used as the appropriate value for fitting. The value of V_Δ^{flat} is the average of the two associated peaks and V'_Δ is a weighted average of the two measured peaks given by

$$V'_\Delta = \frac{\frac{1}{\sigma^a} |V_\Delta^a - V_\Delta^{flat}| + \frac{1}{\sigma^b} |V_\Delta^b - V_\Delta^{flat}|}{\frac{1}{\sigma^a} + \frac{1}{\sigma^b}}, \quad (2.13)$$

where σ is the standard deviation of each separate peak, denoted by superscript a and b . These values were then used according to the calculations previously described to give a value for α .

There are some considerations that must be made for an accurate calibration using the wedge method. Firstly, the orientation of the sample is important — if it is misaligned relative to the scan direction this will cause the effective value of θ to vary, though this can be accounted for by measuring θ in the height image as opposed to using the manufacturer specification. The sample can also be placed on a slant, which will affect both the value of θ and the measured values for the flat regions — this can be hard to accurately correct in most AFM systems, though can be monitored through the height image. Scanning over the slope causes the deflection to change, which is then corrected through the feedback loop adjusting the height position. If this feedback is not correctly tuned there can be a significant lag in the movement resulting in a different deflection, and thus load force, on the slopes. This can be corrected through careful tuning of the feedback parameters while monitoring the recorded deflection values.

2.3 Automation, MacroBuilder, and Extra Hardware

Automation was an important factor in these experiments, allowing for large datasets to be acquired without requiring significant oversight over long periods of time — many of the experiments took multiple days of continual operation to perform. This was primarily facilitated by the MacroBuilder functionality of the Asylum Research AFM control software, which sequentially executes a set of user chosen command blocks. These command blocks include the ability to control the AFM (such as performing force curves and images), changing AFM parameters (such as set point, scan size and positional offset), and flow control (such as time delays and loops). A block also existed for arbitrary code execution, which was used to perform more specialised tasks using functions written within the Igor Pro software environment. As the code was written within the same software that controlled the AFM, there was access to all the operating functions, parameters, and results of the AFM — this was used, for example, to make a function that used a reading of the deflection when the tip was not engaged to adjust the set point, ensuring that the load force was controlled and consistent despite the effects of drift. Another use was the automatic analysis of results to control the behaviour of the system, which was utilised in chapter 3 to adjust the positioning of the tip so that force curve acquisition coincided with the centre of a circular feature in a captured image.

Many of the experiments required the use additional hardware to expand the capabilities of the system, which was integrated into the software in a variety of ways. Some equipment, such as the pulse generator used to drive the EMATs in chapter 5, was controlled using triggering signals (short pulses of +5 V in an otherwise 0 V signal) generated by the digital-to-analogue converters (DACs) of the AFM controller and sent to an output BNC connector on the front of the controller. Access to these DACs was provided by the AFM software, which allowed arbitrary waves (an Igor Pro data type akin to an array) to be sent to the DACs. Other equipment, i.e. the oscilloscopes used in chapters 4 and 5 and the signal generator used in chapter 4, was controlled through the VISA command protocol over USB, which is supported by Igor Pro. For the signal generator this enabled software control of the generated wave parameters (such as frequency and amplitude), allowing for control during automated experiments and performance of the tuning sweeps. For the oscilloscopes VISA was used to pull data from the device to the computer, enabling saving of traces throughout an automated experiment in a format ready for processing and analysis. The linear actuators used in chapter 5 for long range stage positioning were controlled over USB using functions provided in a C library which were made accessible in Igor Pro using a custom made “XOP” plugin as a wrapper for the provided functions. The position sensors used for position feedback of the long range stage motion were continually monitored by an Arduino microcontroller over an I²C interface. The Arduino processed the bitwise information from the sensors into position information in mm, which was read by the computer using serial commands over USB.

Chapter 3

Mechanical Properties of Suspended Films

3.1 Introduction

2D materials are a class of materials that are spatially limited in one dimension to the extent that the properties of the material are significantly altered by this limitation and variations in the extent of the limitation can cause variations in the properties. One such group of 2D materials are 2D atomic crystals — single atomic layers with a lattice that extends only in 2 dimensions. The most well known of these is graphene, a hexagonal grid of carbon atoms that make up graphite when stacked by weak van der Waals-like coupling. Graphene was first directly observed by Geim and Novoselov, who used micromechanical cleavage to isolate flakes from a graphite sample. By placing the flakes on a silicon wafer with a SiO_2 layer, they found the monolayers could be identified by their colour due to optical interference effects [162]. Graphene has become an area of intense study due to its remarkable electrical [163], thermal [164], and mechanical properties [165]. It is also nearly transparent to visible light [166] and impermeable to nearly all fluids [167].

The first common technique for isolating graphene was simple mechanical exfoliation of graphite, either by drawing on a surface with the graphite [162] or through the repeated use of adhesive tape to separate the graphite layers [168]. These techniques produce high quality monolayer graphene flakes, though only in very small quantities along with large quantities of multi-layer flakes [163]. Newer methods of producing graphene from graphite, such as shear exfoliation [169] and sonication aided by solvents [170], allow for the production of large quantities of graphene flakes in solution. Graphene can also be grown through the use of chemi-

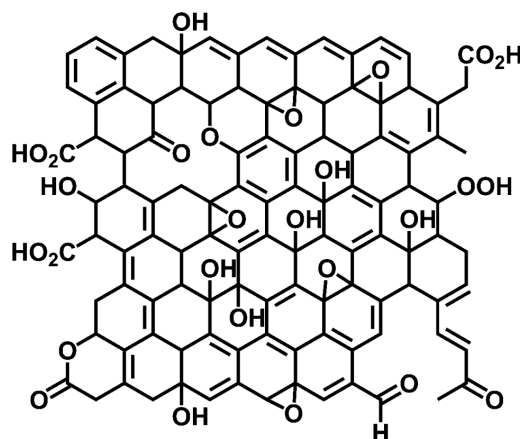


Figure 3.1: Lerf-Klinowski model of graphene oxide, showing hexagonal graphene lattice with oxygen functional groups and vacancies, reproduced from [175]. Note that this 2D representation does not show that many of the functional groups are attached in an out-of-plane direction.

cal vapour deposition (CVD) [171,172], for example through the exposure of copper to hydrogen and methane at high temperatures, with the copper substrate being removed after the growth is completed by chemical etching [173]. This produces large areas of primarily monolayer graphene, though of a polycrystalline nature and containing grain boundaries which may affect the material properties. Such a production method is highly scalable, with production of single sheets of monolayer graphene up to 750 mm in size being reported [174].

Modified versions of graphene — in which additional chemical structure is present, primarily through the addition of functional groups — also exist. The most prominent of these is graphene oxide (GO), in which oxygen functional groups are present in addition to the graphene structure. Many different models for the structure of GO exist [175], though the most common of these is the Lerf-Klinowski model [176,177] illustrated in figure 3.1. GO has multiple different oxygen groups present in the graphene structure — epoxy groups (oxygen bonded to two carbon atoms in the lattice), hydroxyl groups (-OH groups bonded to a single carbon atom), and carboxyl groups (-COOH groups bonded to a single carbon atom) all add to the structure without changing the hexagonal lattice, as well as other groups that substitute for carbons within the lattice or directly cause vacancies. These functional groups and changes to the lattice cause a significant change in the various properties of the GO when compared to graphene [178]. GO is typically synthesised directly from graphite, e.g. using the Hummers’ method [179], and can be reduced towards

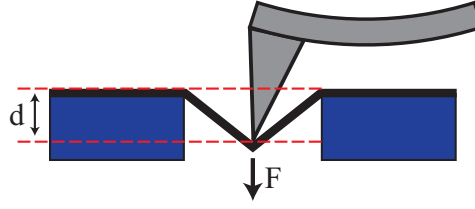


Figure 3.2: Cross section of indentation of a suspended graphene sheet (black line), not to scale.

graphene through chemical [180, 181] or heat treatment [182]. This presents another possible way to create graphene, though with concerns that the non-removable structural defects in GO reduce the quality of the produced graphene, affecting its properties. It is also possible to add these functional groups to graphene in a controlled manner, e.g. through exposure to atomic oxygen [183–185], ozone [186, 187], or oxygen plasma [188], enabling tuning of the affected properties. Many other functionalisations of graphene also exist, allowing for modification of the properties in a variety of ways [189].

Graphene’s remarkable mechanical properties have resulted in significant interest in the production of graphene-polymer nanocomposites — polymer materials containing graphene nanoplatelets or graphene derivatives (such as GO) as a strengthening additive [190–192], as well as providing additional benefits, such as thermal and electrical conductivity. These nanocomposites are already seeing commercial use in areas where high strengths and low weights are desired, such as tennis racquets [193] and bicycle wheels [194]. Functionalisation of the graphene can be used to tune the mechanical properties, improve mixing with the polymer [195], and to modify the other properties of the composite [196]. The mechanical properties are also important to understand in applications where they are not the primary motivation, for example GO is permeable to water but not most other fluids [197], thus leading it to be a candidate for use as a water filter — knowing the mechanical properties aids in the design of practical systems.

The importance of the mechanical properties of graphene, its derivatives, and other 2D materials makes measuring these properties important. Due to their 2D nature many methods used for bulk materials cannot be used, so other techniques have been developed, such as measuring the deformation of elastic substrates caused by graphene layers [198] and indenting suspended graphene sheets in beam [199] or drum [165, 200] configurations. In the drum configuration the graphene sheets are suspended over a circular hole in a stiff support and an AFM is used to indent them at the centre of the hole, as illustrated in figure 3.2. Provided the radius of the tip

is significantly smaller than the radius of the hole ($r_{tip} \ll r_{hole}$) and acting close to the centre of the hole (i.e. within $\frac{r_{hole}}{5}$) the system can be modelled as a point load acting on a clamped circular membrane of linear (i.e. no bending stiffness) isotropic elastic material. This model can be used to approximate the force-indentation (F - d) relationship as [165, 201, 202]

$$F = \sigma_0^{2D}(2\pi r_{hole}) \left(\frac{d}{2r_{hole}} \right) + E^{2D}(2q^3 r_{hole}) \left(\frac{d}{2r_{hole}} \right)^3, \quad (3.1)$$

where σ_0^{2D} is the pretension and E^{2D} is the 2D elastic modulus. E^{2D} is analogous to the Young's modulus of a 3D material and can be converted to an equivalent Young's modulus by dividing by the thickness of the sheet — in graphene this can be taken as the interplanar distance of graphite, 0.335 nm [203]. The dimensionless parameter, q , is given by

$$q = \frac{1}{1.05 - 0.15\nu - 0.16\nu^2}, \quad (3.2)$$

where ν is the Poisson ratio. For graphene the Poisson ratio can be taken as the in-plane Poisson ratio for graphite, 0.165 [204], giving $q = 1.02$. This indentation technique can also be used to determine the strength of the sheets from the load at which the tip causes the membrane to fail — such breaking loads are dependent on the tip radius [165] and defects and grain boundaries within the suspended area [205, 206].

There has been some research into the mechanical properties of graphene derivatives. Previous studies of graphene oxide (GO) have found it to be significantly softer and weaker than pristine graphene [207]. Similarly, the effects of controlled defect addition and partial oxygen functionalisation have been studied by exposing pristine graphene sheets to oxygen plasma, again finding a significant decrease in stiffness and strength as the level of functionalisation is increased [206]. In both cases this change in properties has been attributed to the increased presence of defects within the sheet.

Despite the importance of the mechanical properties of these materials, there is considerable variation in reported values. For example, values for the 2D elastic modulus of graphene oxide range from $110 \pm 17 \text{ Nm}^{-1}$ [207] to $269 \pm 21 \text{ Nm}^{-1}$ [208]. Accurate measurements of their mechanical properties, and an understanding of how they change with functionalisation, is essential to the application of these materials.

Here the nanomechanical properties of graphene and chemically modified graphene were probed by nanomechanical indentation. A method of automating

the indentation of films suspended over circular holes was developed to allow easy acquisition of large datasets, improving the statistical significance of the results and enabling comparison between different samples. This was used to test CVD grown graphene, the effect of heating, the effect of functionalisation through exposure to atomic oxygen, and graphene oxide. These results are then compared by their elastic moduli and breaking loads.

3.2 Experimental Methods

All AFM images and force curves were acquired using an Asylum Research MFP-3D-SA AFM. The tips used were MikroMasch NSC18 tips (silicon tip with nominal normal spring constant of 2.8 Nm^{-1} , resonance frequency of 75 kHz, and tip radius of 8 nm), which were calibrated using the Sader method (see section 2.2.3).

3.2.1 Samples

The graphene samples were supplied and prepared by A. Marsden of the Warwick Microscopy Group. Graphene on copper was grown by low pressure chemical vapour deposition (LP-CVD) [173] on copper foils (99.5% purity, 0.025 mm thick, Alfa Aesar product number 46365), as described in [209]. The process started with an electropolish of the copper foils in a solution of orthophosphoric acid and urea (60 s at 5 V, $\sim 2.6 \text{ A}$) [210]. The foils were then placed in a quartz tube under vacuum (10^{-3} mbar) with a 20 sccm flow of hydrogen and heated to 1000°C at a rate of 15°Cmin^{-1} then annealed at this temperature for 20 minutes. To start the growth, methane was introduced at 20 sccm for 20 minutes while still held at 1000°C . The methane and hydrogen were kept on during cooling to 600°C , after which the methane was turned off.

The graphene samples were transferred to silicon nitride TEM support grids for testing. The grids are produced by Silson and consist of a thin film — the thickness of this is nominally 100 nm but not controlled — suspended over a 1 mm square window, with the central 0.5 mm square containing an array of regularly spaced holes with diameters of $3.25 \mu\text{m}$ and centre-centre distances of $6.5 \mu\text{m}$. Graphene transfer was achieved by spin coating the foils with formvar (in solution with chloroform) to act as a transfer support for the graphene and then etching the copper foils away by placing them on an ammonia persulphate solution. The graphene and formvar sheets were then transferred to deionised water 5 times to remove the residual etchant. The cleaned sheets were then scooped onto the support grids, such that the graphene was in between the support grid and the formvar layer. The formvar was then cleaned off

by soaking the grids in chloroform for 5 minutes, followed by acetone for a further 5 minutes and then dried in a critical point dryer using liquid CO₂, necessary to avoid damage from surface tension to the graphene covering the holes in the support grid. For comparison, a sample was also heated (after the chemical cleaning) on a hotplate in air at 200°C for 1.5 hours, a common technique for further removing the polymer residue.

To dose the graphene with oxygen the graphene on support grid samples were placed under UHV ($< 10^{-8}$ mbar) and exposed to atomic species of oxygen (O•). These species were introduced using an Oxford Applied Research TC50 gas cracker (50 W) with oxygen gas. This was done on two separate samples with 2 and 4 minute exposure times, measured for the time the cracker was running at 50 W with an oxygen pressure of 6×10^{-6} mbar. Some additional exposure to molecular oxygen also occurred, though this is known not to affect the graphene [185].

The graphene oxide samples were supplied by H. Thomas of the Rourke group, Warwick Chemistry, and prepared by A. Marsden. They were produced using a modified Hummers' method [211,212], dissolved in deionized water and diluted to approximately 0.01 mg·mL⁻¹. The support grids were coated with a thin carbon layer using a carbon evaporator (for 1.5 s) and then plasma cleaned (at 100 W for 1 minute) — this increases the surface's hydrophilic properties for improved wetting and better dispersion of the GO flakes — before a single drop of the GO solution was drop cast onto the surface and left to dry in air.

3.2.2 Data Acquisition and Analysis

A tapping mode scan of a 15 μm sided square at the centre of the testing area (a region within the holey region of the SiN grid) was taken and used to determine the vectors and offset of the grid of holes. This information was then used to find the centre of all holes within the desired area, here an 80 μm square (chosen to fit within the 90 μm stage range of the AFM with some additional space for scanning and drift correction). Using a small (15 μm) scan avoided the issue where scanning over uncovered holes would cause the sample to shift — due to the tip entering an uncovered hole and then pushing the sample once the other side was reached — thus causing the scan to be unusable. In total there were 175–185 holes within the 80 μm square area, depending on the orientation and position of the sample.

The known locations of the holes were then individually tested in turn. First, a 6 μm tapping mode scan centred on the expected hole location was acquired (see figure 3.3 for an example). The phase image (figure 3.3(c)), chosen due to its clear contrast between the hole and the surrounding area, was then thresholded with Igor

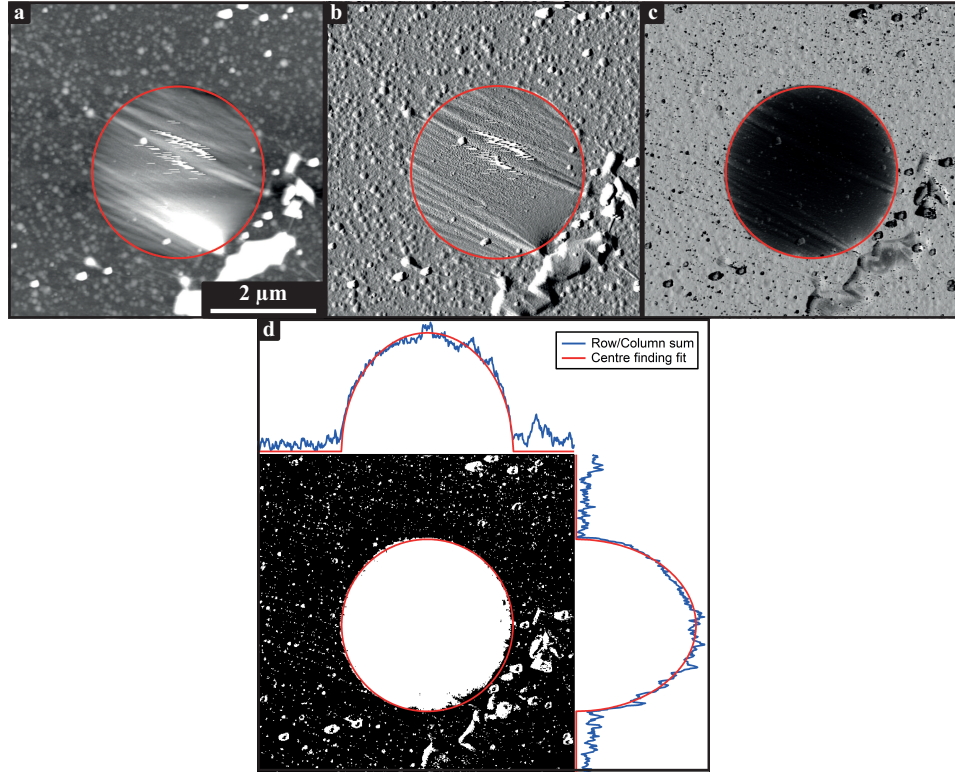


Figure 3.3: Tapping mode AFM image of a graphene covered hole. The channels and their corresponding data scales are a) height, 35 nm, b) amplitude, 5 nm with a minimum value of 35 nm, c) phase, 60° with a minimum value of 75° . d) Thresholded version of (c) with summed rows and columns and fits to these using equation 3.3. The location of the hole as found by the fitting is highlighted by a red circle in all images.

Pro's *ImageThreshold* function (using the iterative method option) to give a new image consisting of two arbitrary values (0 and 255). The contrast in the phase image ensured that the covered hole mostly assumed one value and the support mostly assumed the other. The average value of the thresholded image was checked to see if it was < 127.5 (less than half the pixels had a value of 255), otherwise the values were flipped to ensure that the hole had the value of 255, which made fitting of the location more robust. The thresholded image, $T(x, y)$, was then summed separately along the rows and columns to give two lines (see figure 3.3(d) for an

example), which were then fitted according to the equations

$$\begin{aligned} \sum_y T(x, y) &= \begin{cases} A_x \sqrt{r_{hole}^2 - (x - x_c)^2} + B_x, & \text{if } |x - x_c| < r_{hole} \\ B_x, & \text{otherwise, and} \end{cases} \\ \sum_x T(x, y) &= \begin{cases} A_y \sqrt{r_{hole}^2 - (y - y_c)^2} + B_y, & \text{if } |y - y_c| < r_{hole} \\ B_y, & \text{otherwise,} \end{cases} \end{aligned} \quad (3.3)$$

where A_x , A_y , B_x , and B_y are fitting parameters, r_{hole} is the radius of the hole and can be used as a fitting parameter, though the fitting is more robust if it is pre-defined, and x_c and y_c are fitting parameters corresponding to the coordinates of the centre of the hole. A_x and A_y were initialised to 255 times the radius of the hole in pixels, while B_x and B_y were initialised to 0 and allow for background “noise” in the thresholded image. The centre coordinates were used to shift the expected locations of the remaining holes, compensating for drift and sample shifting. This compensation was done in the manner of a feedback loop to prevent errors from the imaging or centre finding procedure from causing the positions to be shifted too far in the wrong direction.

Using the coordinates of the hole centre found from the image, successive force curves were performed on the centre of the suspended sheet at increasing loads. The first force curve was performed with a relative set point of 1 V, with subsequent force curves increasing by 1 V up to 10 V, with each volt typically corresponding to an increase in load of 120–140 nN, depending on the cantilever. Taking multiple curves at steadily increasing loads meant that that a usable curve was recorded at each point even if the film broke.

For analysis, the detection of the hole location was manually checked for each hole and the force curves were manually inspected to select the curve in which the film initially broke (identified by a smooth curve followed by a sharp drop and then a non smooth increase), or the curve from the highest load if the film never broke. The breaking load was then determined from the highest load reached before breaking. The curve from the approach direction up to the breaking point was then modified to be of force versus indentation (see section 2.2 for more details) and the force offset was corrected. This curve was then fit using equation 3.1 with an additional offset for the indentation values as a fitting parameter, giving the elastic modulus and pretension of the membrane.

The total time to acquire a full set of results (of 175–185 holes) was 24–36 hours, which could be left unattended after the initial setup. After analysis there were typically 50–100 holes with usable data, depending on the sample. Unusable

data was typically caused by uncovered or partially covered holes, failure of the hole finding fit resulting in force curves not at the centre of the hole, and failures when fitting to the acquired force curves. The averages and standard deviations for both E^{2D} and breaking load were calculated for each set, as was the normalised correlation coefficient between these (where applicable — results for which the film did not break were ignored). The error on the average was calculated as $\frac{\sigma}{\sqrt{N}}$, where σ is the standard deviation and N is the number of results.

Some considerations need to be made to perform this experiment. Firstly the support must be stiff enough that it does not deflect under the forces applied, which was tested by performing a force curve with a 10 V set point on the support and finding that there was no indentation. It is for this reason that the silicon nitride support grids were used — holey carbon films were tried first but found to be too soft. Secondly, the spring constant of the cantilever also needs to be considered — a cantilever that is too stiff will not deflect sufficiently for a good measurement, while a soft cantilever will not cause sufficient indentation of the suspended film. Here, cantilevers with a nominal spring constant of 2.8 Nm^{-1} were used, which are ideal for the softer functionalised membranes, but slightly too soft for the pristine graphene sheets, increasing uncertainty.

3.3 Results and Discussion

First, an example result from a suspended CVD graphene sheet is shown to demonstrate the acquisition and analysis process for each data point. This process is then used to investigate the effects of heating, which is used in the transfer of CVD grown graphene to remove polymer residue, on the mechanical properties of graphene. Oxygen functionalisation of graphene is also investigated, comparing the mechanical properties of graphene oxide with CVD grown graphene dosed with varying levels of O^\bullet , using the same process.

3.3.1 Example Result from a Single Graphene Covered Hole

Figures 3.3(a–c) show a tapping mode image taken of a single graphene covered hole on the grid. The location of the covered hole is clearly visible in all three images, with the suspended graphene having a significantly different texture in the height and amplitude images and a completely different value in the phase image when compared to the surrounding graphene supported by the silicon nitride grid. A few artefacts can be seen within the suspended region, and similar effects were seen on many images in greater quantities — these are likely a tip sticking effect that has a

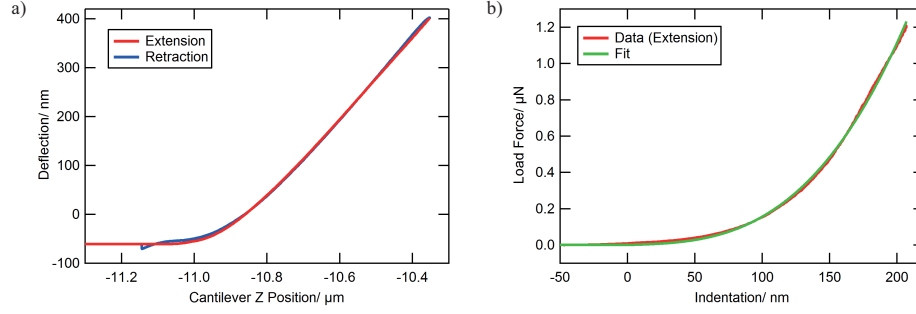


Figure 3.4: Example force curve from a graphene covered hole. a) Deflection versus z position of the cantilever. b) Force versus indentation, with fitting of equation 3.1. The force was zeroed using the flat section of the curves (which extends far to the left of both (a) and (b)) before fitting and the indentation was zeroed after fitting using the fitted offset parameter.

large impact due to the graphene being able to deflect upwards, staying with the tip as it retracts. As the phase image is the one with the best contrast, it is used for finding the centre of the suspended graphene membrane, as explained in section 3.2.2. This image is an example of one of the clearest taken, however the technique was reliable in dealing with images that were off centre or with poorer contrast.

The location of the hole, acquired from figure 3.3(d), was used to perform force curves in the centre of the hole. The force curve with the maximum load force used is shown in figure 3.4(a), where it can be seen that the graphene did not break under this load. Some slight hysteresis is visible in the retract curve, as is a slight jump from contact after a downwards curve at the minimum force — this downwards tick is of a similar shape to the increasing curve, which is expected as the graphene sheet will behave the same in both indenting and pulling directions. The force curve was then processed (section 3.2.2) and fitted using equation 3.1, as shown in figure 3.4. From this fit the 2D elastic constant (E^{2D}) of this film is 332 Nm^{-1} , corresponding to an effective Young's Modulus of 1.0 TPa, assuming a thickness of 0.335 nm, the interplanar distance of graphite [203]. The pretension from the fitted curve is found to be 0.07 Nm^{-1} , which can similarly be converted into an effective pre-stress of 210 MPa. This pretension is very low compared to the elastic properties of the membrane, indicating that the sample was relaxed when transferred to the support grids. Low pretension was found to be the case in the rest of the experiments here and therefore is not reported further.

3.3.2 Graphene and the Effect of Heating

Early experiments on CVD grown graphene by Ruiz-Vargas et al. found it to have much lower elastic constants and breaking strength when compared to exfoliated graphene [213]. This was originally attributed to the polycrystalline nature of the CVD grown sheets and the presence of grain boundaries and other defects. Later it was suggested that the poor mechanical properties of CVD grown graphene were a result of the transfer methods used, notably the chemical etchant used to remove the copper substrate and the act of heating to remove the polymer used as a support. By changing the etchant used and avoiding heating after transfer, Lee et al. showed that CVD grown graphene can have similar mechanical properties to exfoliated graphene [214]. Here, CVD grown graphene was transferred using an ammonia persulphate etchant, as was used in [214], and the effect of heating (at 200°C for 1.5 hours on a hot plate) after transfer was investigated. It is likely that the unheated sample still had remnants of the formvar polymer used to support the films during transfer that were not fully removed by the chloroform solvent, though this should have minimal effect on the results due to its significantly lower elastic constants when compared to graphene.

Histograms of results from the unheated and heated graphene are shown in figures 3.5(a) and (b) respectively. The vast majority of tests for both of these didn't break under the maximum applied load of 1.2 μN , which is in line with the strength recorded for exfoliated graphene sheets [165]. The breaking strength is dependent on the tip radius, with sharper tips causing breaks at lower forces — the tip radius here was not measured, but is given by the manufacturer as 8 nm, which is sharper than those used in [165], though this experiment does not go to the breaking forces seen there. These loads are, however, much higher than the breaking forces observed in the early experiments by Ruiz-Vargas et al. [213], indicating that the reduction in strength they observed was likely caused by reactions with the chemical etchant, though heating may have had some effect outside the range of load forces used here. Some sheets do break and this may be due to defects present within the suspended region, such as grain boundaries or small pre existing tears and holes.

The elastic moduli of the as-cleaned and heated graphene sheets (figures 3.5(a) and (b) respectively) showed significant differences. The as-cleaned graphene had an average 2D elastic modulus (E^{2D}) of $398 \pm 16 \text{ Nm}^{-1}$ with a standard deviation of 136 Nm^{-1} . This is slightly higher though within a standard deviation of previously reported values for both pristine exfoliated graphene ($342 \pm 30 \text{ Nm}^{-1}$ [165]) and Lee et al.'s results for CVD grown graphene ($328 \pm 15 \text{ Nm}^{-1}$ [214]). The high value and variance seen in the experiments here may be attributed to the relatively

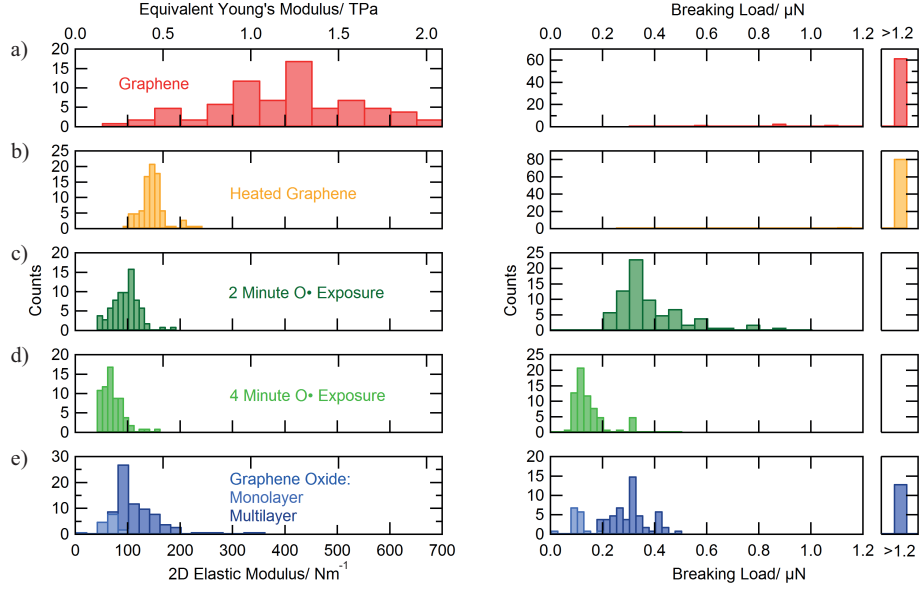


Figure 3.5: Histograms of elastic constant (left) and breaking load (right) of a) CVD grown graphene, b) CVD grown graphene heated for 1.5 hours at 200° , graphene exposed to O^{\bullet} for c) 2 minutes, d) 4 minutes, and e) graphene oxide. The GO results correspond to a single dataset and have been separated into monolayer and multilayer based on their grouping in figure 3.6. The equivalent Young's modulus is calculated assuming a 0.335 nm film thickness, corresponding to graphene.

low spring constant of the cantilevers used — the stiff graphene sheet is less compliant than the cantilever, meaning that the indentation calculation has a higher error due to measurement uncertainties, as well as there being an increased effect of systematic calibration error. The heated graphene had an average E^{2D} of $146 \pm 3\text{ Nm}^{-1}$ with a standard deviation of 25 Nm^{-1} , significantly lower than that of pristine graphene though still higher than the values reported by Ruiz-Vargas et al. ($55 \pm 21\text{ Nm}^{-1}$ [213]). This indicates that both heating and the etchant have a significant effect on the elastic properties of graphene sheets. The mechanism by which the elastic modulus is reduced by heating is unknown, as it has been previously reported that graphene is stable in air up to 200°C [215], the temperature to which this sample was heated.

3.3.3 Oxygen Functionalisation of Graphene

The effect of oxygen functionalisation was also studied. Here, both GO produced using the modified Hummers' method and CVD grown graphene functionalised through

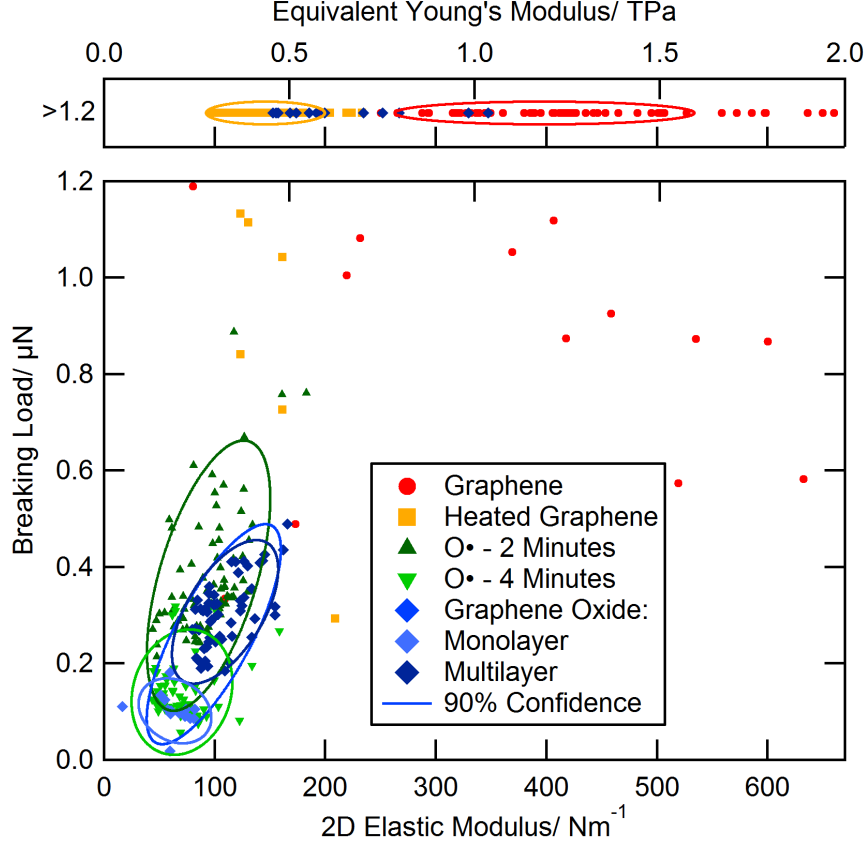


Figure 3.6: Scatter plot of all the breaking loads and elastic moduli of the tested graphene and graphene derivative samples. The 90% confidence ellipses ignore the breaking strength for the graphene and heated graphene results, while the ellipsis for the GO results ignores all the points that were unbroken. The GO results correspond to a single dataset and have been separated into monolayer and multilayer based on their grouping. The equivalent Young's modulus is calculated assuming a 0.335 nm film thickness, corresponding to graphene.

exposure to atomic oxygen have been tested to make a direct comparison. Histograms of the results from this are shown in figures 3.5(c-e), with a scatterplot of every measurement shown in figure 3.6.

From the histograms (figure 3.5(c,d)), there is a clear and significant reduction in both E^{2D} and breaking strength with increasing levels of oxygen dosing on CVD grown graphene. The average E^{2D} values of $95 \pm 3 \text{ Nm}^{-1}$ and $70 \pm 3 \text{ Nm}^{-1}$ for 2 minutes and 4 minutes of O^\bullet exposure, respectively, correspond to reductions by a factor of 4.2 and 5.7 relative to the as-cleaned CVD grown graphene value of

$398 \pm 16 \text{ Nm}^{-1}$. Similarly, the breaking loads reduced to $382 \pm 15 \text{ nN}$ and $140 \pm 7 \text{ nN}$ for the 2 minute and 4 minute exposures respectively, both significantly below the forces in excess of $1.2 \text{ }\mu\text{N}$ required to break the CVD grown graphene. These reductions demonstrate a relationship between level of functionalisation and the mechanical properties which is similar to the results seen for graphene exposed to an oxygen plasma [206]. These results are not directly comparable due to the different techniques used, with the plasma being more destructive and thus introducing more defects while the $\text{O}\bullet$ exposure creates more functional groups.

The GO results (figure 3.5(e)) show an average E^{2D} and breaking load of $99 \pm 3 \text{ Nm}^{-1}$ and $261 \pm 13 \text{ nN}$, respectively. However, from the scatterplot of the results shown in figure 3.6, it is clear that the GO is split into two distinct regions — one which is concurrent with the 4 minute oxygen exposure result and one at higher values of E^{2D} and breaking load, shifting the average result. These higher valued results are due to the difficulty in creating monolayer coverage of GO using the drop casting method and corresponds to holes with two layers of GO. This was confirmed by examining the sample’s diffraction patterns in a transmission electron microscope (TEM) and finding that the sample consisted of primarily (approximately 80%) bilayer regions, with the remainder as monolayer regions and a small number of higher layer count regions. Direct measurement of the number of layers for each hole was not possible — performing the TEM measurements first would potentially modify the GO, while performing it after is not possible due to the AFM breaking the sheets. TEM examination was performed by Z. Laker.

Using the scatterplot (figure 3.6) the GO results were broken down into the two groups, which have been assumed to be monolayer and multilayer. These groups were then analysed, finding average E^{2D} values of $64 \pm 4 \text{ Nm}^{-1}$ and $109 \pm 3 \text{ Nm}^{-1}$ for the monolayer and multilayer groups, respectively, and breaking loads of $102 \pm 8 \text{ nN}$ and $307 \pm 9 \text{ nN}$. The results for the assumed monolayer sheets are similar to those seen for the 4 minutes of $\text{O}\bullet$ exposure, indicating that they are mechanically similar and therefore similar in composition. The multilayer results have double the 2D elastic modulus of the monolayer results, which is expected for a primarily bilayer group. The breaking load triples, which is compatible with the breaking being primarily propagated by defects — with two layers the weak areas of one layer may be covered by a stronger area of the other layer, and thus prevent the propagation of breaks, and thus the breaking strength increases by a factor more than the number of layers. A more thorough analysis of different layer numbers would be needed to draw strong conclusions about the affect of increased layer count on breaking strength, however.

Figure 3.6 also shows the correlation between E^{2D} and breaking load. For the

GO results there is a strong correlation between E^{2D} and breaking load (correlation coefficient of 0.77), which is expected for property variations primarily caused by differing number of layers. When broken into two groups, the results for monolayer GO shows a weak negative correlation (-0.22), though the multilayer GO results have a moderate correlation (0.59). This may indicate that the multilayer results have partial multilayer coverage with an average of two layers or that there is an effect from the stacking and local properties of the layers that affects E^{2D} and breaking load in a similar manner. The 2 minute O• exposure results also have a moderate correlation (0.57), which may be as a result of differing levels of functionalisation between the individual testing holes. The 4 minute O• exposure results, however, have a weak correlation (0.15) which, along with their concurrence with the monolayer GO results, indicates that the shift in mechanical properties has been fully completed by this level of exposure, either due to becoming equivalent to GO or further changes not having a significant effect on the mechanical properties.

3.3.4 Differences in Membrane Puncture Behaviour

During these experiments it was noted that after the breaking point was reached the deflection dropped sharply before increasing again, with the minimum value still being greater than the free deflection value, meaning that the film is still supporting the tip after the break. Examples of this for each of the four states of oxygen functionalisation tested here are shown in figure 3.7(a). This provides some information about the nature of the failures — as the membrane is still acting on the tip this means that part of the sheet must still be touching the tip cone, as illustrated in figure 3.7(b). The side of the tip is not touching the side of the hole in the silicon nitride grid as the width of the tip at this point is much less than the diameter of the hole ($3\text{ }\mu\text{m}$), as determined by the full cone angle (specified by the manufacture as 40°) and the indentation after breaking ($< 1\text{ }\mu\text{m}$). Also, the cantilever is not touching the edge of the silicon nitride grid as the tip height (specified by the manufacture as $12\text{--}18\text{ }\mu\text{m}$) is much greater than the indentation after breaking. Therefore it can be inferred that the magnitude of the drop after the membrane breaks indicates the extent of the breaking, with smaller drops (as seen with the GO and high levels of oxygen functionalisation) corresponding to smaller, more localised failures. Such localisation is consistent with the failures being primarily caused by the weaker defects within the lattice and such defects being more common in the highly functionalised materials.

An estimation of the size of the initial hole created after failure is possible by making the following assumptions:

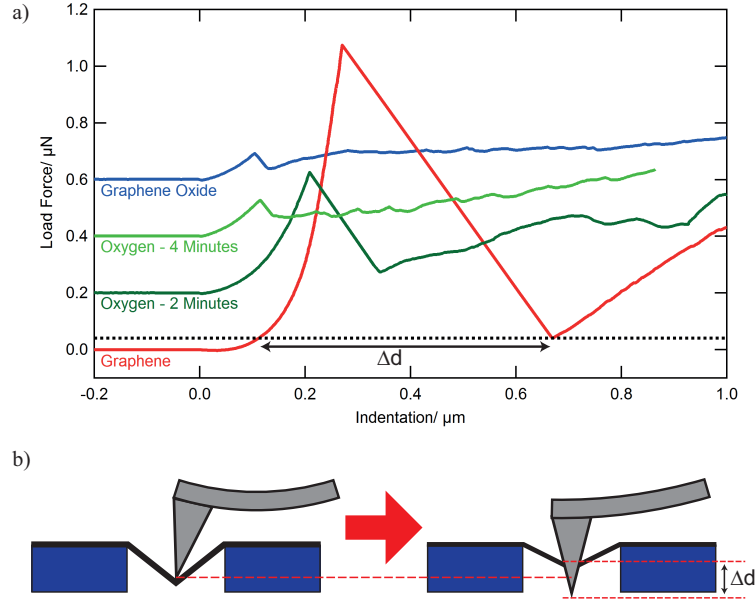


Figure 3.7: a) Force versus indentation curves for different levels of oxygen functionalisation, showing the differences in the breaking behaviour. The curves have been offset to make them easier to distinguish — the left flat section of each corresponds to a load force of 0 N. b) Example of a break event as seen from the side in a cross section view, showing the change in indentation, Δd . Schematic is not to scale.

1. The hole is symmetrical around the tip and interacts with the sides of the tip.
2. The tip is a cone shape with a set angle between sides, θ_{cone} (here 40°).
3. The film relaxes such that the indentation of the film after the failure is the same as the indentation before the failure at the same applied force.

These assumptions are approximations of the real system, particularly (1) and (3) for larger breaks, but can still be used to give an idea of the extent of the failure. Using these assumptions, the diameter of the hole immediately after failure is given by

$$D_{break} = 2\Delta d \tan\left(\frac{\theta_{cone}}{2}\right) \quad (3.4)$$

where Δd is the difference in indentation between the value at the minimum force after the failure and the value at the same force from before the failure. For the curves shown in figure 3.7(a), these results are given in table 3.1. From this it can be seen that the as-grown graphene break is 8–10 times larger than the break for the highly functionalised sheets, while the 2 minute oxygen exposure has a break of intermediate size, further supporting that the failures are mediated by defects within the lattice and that they are more common in the highly functionalised samples. Note

Sample	Δd (nm)	D_{break} (nm)
Graphene	560	410
2 minute oxygen exposure	240	180
4 minute oxygen exposure	60	40
Graphene oxide	70	50

Table 3.1: Estimated sizes of the holes created by the failure of the films tested in figure 3.7(a).

that the graphene sheet used here is weaker than most of the sheets tested (as they did not break) which may indicate that it had more defects than typical and the size of the break is therefore not representative of the rest of the graphene, which may have significantly larger failures.

3.3.5 Correlating Mechanical to Structural Properties

Other experiments, investigating the physical and chemical structure of these samples, were carried out by A. Marsden and are presented here as complimentary information. The first of these is the X-ray photoelectron spectroscopy (XPS) data shown in figure 3.8(a), which shows abundances of functional groups within the sample. The rightmost (lowest binding energy) peak in the C1s spectra, seen for every sample, corresponds to the graphitic carbon structure of pristine graphene. As the O• exposure is increased a new peak grows to the left of the graphitic peak, which indicates the presence of epoxy groups [184]. Further functionalisation (exposure times of over 8-minutes) causes another peak to appear at higher binding energy, corresponding to carbonyl (C=O) and carboxyl (C(O)OH) groups, which cannot be distinguished due to the peak broadness. These high dose samples also exhibit lower total C1s intensities, meaning that carbon has been removed from the surface, indicating significant damage to the graphene lattice and possibly the creation of extended holes within the sheet. In contrast, previous work on GO has found XPS spectra similar to that exhibited by the 4 minute O• exposure sample [217].

Raman spectroscopy, which indicates the characteristic phonon energies and thus the physical structure of the material, was also performed, here using a Renishaw InVia system with a HeNe 633 nm laser. Results from this are shown in figure 3.8(b). Three peaks, which are characteristic for graphene, are visible. The G peak is present for all graphene samples, while the D and D' peaks are normally forbidden due to symmetry — their appearance indicates the presence of topological defects, such as changing a 6 atom ring to a 5 or 7 atom ring [218, 219]. The D peak can be seen

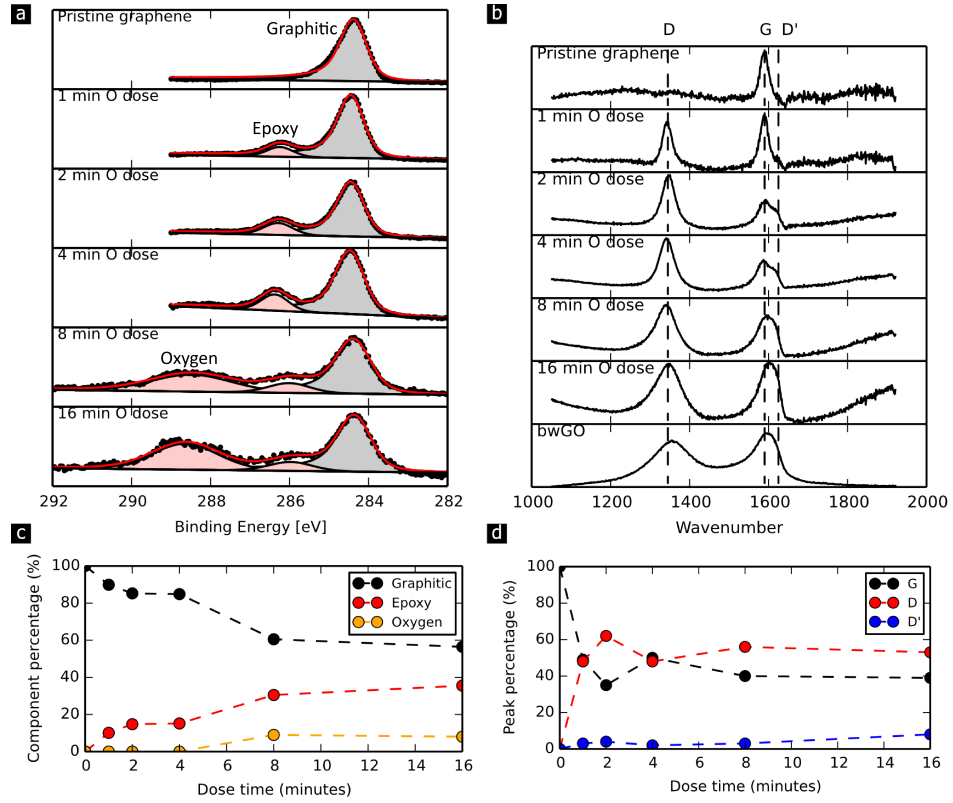


Figure 3.8: a) C1s XPS spectra for graphene with different times of exposure to O^\bullet . b) Raman spectra. c) Change in component proportions with increasing O^\bullet exposure times, determined from the XPS spectra. d) Change in Raman peak intensities. Reproduced from [216].

in all functionalised samples and increases in intensity relative to the G peak with increasing O^\bullet exposure times, indicating an increasing disorder. The D' peak can also be seen at higher exposure times, though is merged with the G peak due to resolution. For comparison a base-washed GO (bwGO) sample is also included — base-washing is the process of removing oxidative debris (small, highly functionalised material on the surface of the GO) by washing the GO in sodium hydroxide — showing a spectra that is consistent with a highly disordered sheet of graphene. The 2D peak is not included in these results due to the range of the spectrometer.

Transmission electron microscope (TEM) images were captured using a JEOL ARM 200F operating at 80 kV, with care taken to reduce beam damage. Example images are shown in figure 3.9. The graphene sample (figure 3.9(a)) shows a continuous hexagonal lattice with no visible defects. After exposure to O^\bullet (figure 3.9(b)) some defects can be seen, consistent with the increased disorder seen from the Raman results. However, as epoxy groups are expected to be the predominant functional-

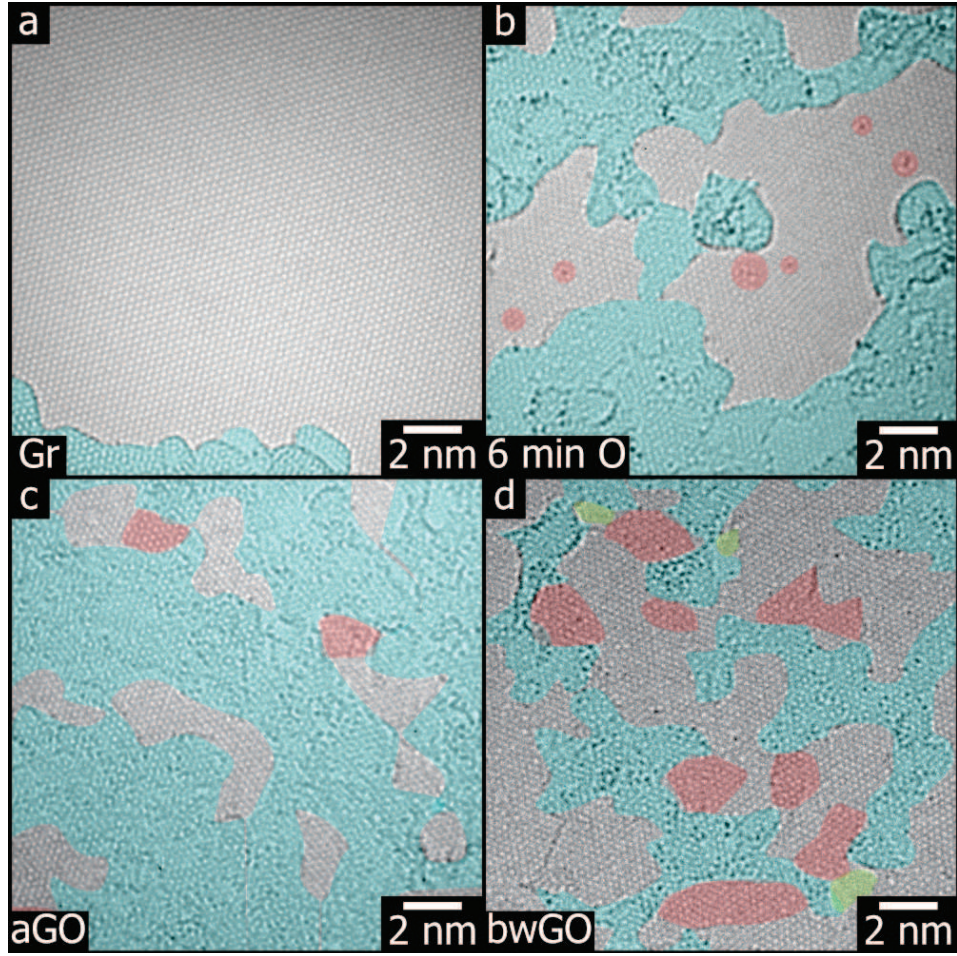


Figure 3.9: High resolution TEM images of a) pristine graphene, b) graphene after a 6 minute $O\bullet$ exposure, c) as-produced GO, and d) bwGO. Blue highlighting indicates amorphous regions — transfer polymer residue in (a) and (b) and oxidative debris in (c) and (d). Red highlighting indicates defects in the graphene lattice and green highlighting indicates holes in the lattice. Reproduced from [216].

isation group for this sample it is possible that the number of defects is under-represented as such groups are thought to move quickly under or be removed by the electron beam [185]. Note that the increased amount of amorphous material, attributed to residue from the polymer used for transferring the sample, is likely due to variations in contamination across the samples and not as a result of the functionalisation. The as-produced GO image (figure 3.9(c)) is largely obscured by the oxidative debris, which is significantly reduced in the bwGO image (figure 3.9(d)). On this bwGO image several large regions of topological defects can be seen as well

as the presence of small holes within the lattice.

Combined, these results show that the oxygen functionalisation of graphene results in the addition of topological defects to the graphene lattice. These topological defects are likely the cause of the reduced mechanical properties seen from AFM probing, which is consistent with results seen for from introducing defects through other methods (e.g. exposure to plasma [206], while here it was done chemically). Interestingly, the changes in mechanical properties appear to reach a limit, seen here after 4 minutes of O• exposure, despite much greater quantities of topological defects being possible through higher levels of functionalisation or in GO. This suggests that the mechanical effect of such defects may extend much further than the region of the defect itself.

3.4 Conclusions

Indentation measurements of suspended graphene and graphene derivative sheets were acquired. These indentation measurements gave information about the mechanical properties of these 2D materials, with a summary of results given in table 3.2. These results give new insight into the effects of functionalisation on the mechanical properties of graphene. The CVD grown graphene tested here was shown to have a high stiffness and breaking strength, in line with previous work on mechanically exfoliated pristine graphene sheets [165]. It was found that heating this graphene caused a significant drop in the stiffness, which supports that the relatively poor mechanical properties of CVD grown graphene previously reported [213] were actually a result of the transfer method and not the growth itself [214]. Oxygen functionalisation of CVD grown graphene was achieved through exposure to atomic oxygen in UHV and was found to cause a significant drop in both stiffness and breaking strength, with longer exposures bringing the mechanical properties in line with GO produced using a modified Hummers' method, for the results that are presumed to be from monolayer coverage. Comparison with TEM, Raman, and XPS measurements shows that the decrease in stiffness and strength are correlated to the formation of extended topological defects. This is further supported by the estimations of the size of the initial puncture of the suspended films, suggesting that the highly functionalised samples had much more localised breaks and so were highly defect limited. Observations of these defects, and similar mechanical properties from both wet chemical oxidation and soft gas phase oxidation by atomic oxygen suggests that they are a generic feature of extended covalent functionalisation of graphene. The dramatic decrease in stiffness associated with these changes has enormous significance for the

Sample	Datapoints	Average E^{2D} (Nm⁻¹)	E^{2D} Std. Dev. (Nm⁻¹)	Assumed Thickness (nm)	Avg. Effective Young's Modulus (GPa)	Avg. Breaking Load (nN)	Breaking Load Std. Dev. (nN)	Correlation Coefficient	Typical Break Size (nm)
Graphene	75	398±16	136	0.335	1190±50	>1200	N/A	N/A	410
Heated graphene	87	146±3	25	0.335	436±9	>1200	N/A	N/A	N/A
2 mins O• exposure	75	95±3	25	N/A	N/A	382±15	131	0.57	180
4 mins O• exposure	67	70±3	21	N/A	N/A	140±7	61	0.15	40
GO (all)	71	99±3	28	0.700	141±4	261±13	106	0.77	N/A
GO (monolayer)	16	64±4	15	0.700	91±6	102±8	31	-0.22	50
GO (multilayer)	55	109±3	22	1.400	79±2	307±9	69	0.59	N/A

Table 3.2: Summary of results from the indentation of suspended films. Average values are given with their uncertainty as well as the separate standard deviations. The effective Young's modulus is calculated by dividing E^{2D} by the film thickness. For graphene this is the interplanar spacing of graphite, but for GO a thickness of 0.7 nm per layer is more accurate [207, 220], with the multilayer results assumed to be dominated by bilayer regions, with the quantities of these levels of coverage in line with TEM measurements. The correlation coefficient is between E^{2D} and the breaking load. The results for GO that did not break under the maximum load were ignored for the values given here.

application of functionalised graphene in composites.

To acquire statistically significant results an automated approach was essential. This automated technique makes mechanical testing of new samples simple, and thus could be applied to a range of samples. One such sample is reduced graphene oxide, where the GO has been reduced towards graphene by either chemical [180,181] or heat treatment [182], to see if graphene with the expected mechanical properties could be attained through this method, or if the lattice defects would cause the films to be softer and weaker. Some early tests were carried out comparing GO and reduced GO and suggested that the mechanical properties were not improved by reduction, though problems with attaining a consistent coverage on the grids used here meant that the results were unreliable. Reductions of oxygen functionalised graphene could also be studied, to see if there is a level of functionalisation beyond which there is a transition from reversible to irreversible changes in mechanical properties. In addition to oxygen functionalised graphene, there are many other functionalised forms of graphene [195,221,222] that should also be measured. Other 2D materials could also be studied, such as hexagonal boron nitride (a hexagonal lattice of alternating boron and nitrogen atoms, which has had theoretical predictions [223,224] and some experimental study [225] of the mechanical properties), and many others [226–228]. The methodology developed could thus be applied to the nanomechanical analysis of a wide range of membranes of varying stiffness (by varying membrane diameter and cantilever spring constant), with the key advantage of obtaining statistically significant results in a relatively short time.

Chapter 4

Ultrasonic Force Microscopy

4.1 Introduction

Ultrasonic force microscopy (UFM) is an AFM technique developed in the early 1990s that uses ultrasonic vibrations, typically in the 2–10 MHz range, to probe mechanical properties of sample surfaces [229–231]. The ultrasound is usually applied via a piezoelectric transducer bonded to the bottom of the sample, though it has also been done using high-order cantilever oscillation modes [232] and cantilever guided very high frequency excitations, i.e. above 10 MHz [233]. UFM has previously been applied to a variety of systems, such as investigating stress induced mechanical property variations in hard samples like semiconductor nanodots [234, 235], damascene structures [236], and crystalline domains in thin films [237], as well as softer samples such as carbon fibres in an epoxy matrix [238] and rubber inclusions in PMMA [239]. It has also been shown to be sensitive to subsurface defects, including surface film delaminations [240] and lattice defects [241].

Other AFM techniques for examining the mechanical properties of sample surfaces do exist, the most common of these being with traditional tapping mode AFM (see section 1.1.4.1.2). In amplitude modulated tapping mode the phase signal is related to the material properties of the sample surface, as is the amplitude in frequency modulated operation [242–244]. The relations between these, however, depend on a variety of factors and are not simple to interpret in terms of material properties. Improvements to tapping mode for material characterisation have been made by using dual frequency excitation of the first two cantilever eigenmodes, allowing the first to be used for topographical feedback and the second for material contrast, allowing for quantitative results with careful calibration of interaction model parameters [67].

Perhaps the simplest method of obtaining mechanical information from AFM is to perform force-indentation curves, as discussed in section 1.1.4.1.1. These curves can be fitted to models of tip-sample interaction giving quantitative information about the material elastic properties [46]. The range of sample stiffnesses accessible by this technique is largely limited by the cantilever stiffness — the cantilever must be stiff enough to cause measurable sample indentation, but soft enough that there is measurable deflection. Individual force curves can be performed across a surface in a grid pattern, allowing these properties to be mapped as an image. However, doing this is significantly slower or much lower resolution than scanning techniques due to the need to perform a full force curve at each point. Newer generation AFMs have greatly increased the speed of this technique through use of quasi-scanning techniques, such as Asylum Research’s Fast Force Mapping and Bruker’s PeakForce Tapping modes [55,56], though these are still significantly slower than other scanning techniques on the same systems.

Contact resonance AFM (see section 1.1.4.1.3) is another technique for finding mechanical information about the sample surface. In this the cantilever is held in contact with the surface and then the behaviour of the cantilever’s resonant oscillations are monitored, the frequency of which is greatly increased due to contact with the surface and dependent on the surface properties [245,246]. This allows quantitative information about the surface properties to be acquired, though the setup for doing this is complicated by the need to drive the sample at resonance, requiring specialised transducers with a flat response over a large frequency range.

UFM sets itself as an alternative to these techniques, having advantages and disadvantages when compared to each. Its results, while not quantitative, provide simple to interpret depictions of relative surface stiffness across a sample. Performing such experiments is also simple, requiring only small additions to a typical commercial AFM, and can be done in conventional scanning operation at typical speeds.

Here, the set up of a UFM experiment on a silicon sample is investigated, examining the effects of various experimental parameters on the cantilever response and discussing the considerations to be made when choosing these parameters. These results are also compared to simulated results, demonstrating differences between the real and expected response and thus the challenges that affect the possibility of quantifying UFM results. Consideration of tip material in UFM is also presented, showing how contrast can be affected by this choice. Finally, the combination of UFM with other contact mode techniques, such as friction force microscopy and conductive AFM, is demonstrated, presenting UFM as an option for multifunctional examination of a surface. This combined scanning mode is also shown to allow

for multifunctional scanning of samples too delicate to be scanned in conventional contact mode AFM, such as carbon nanotubes.

4.2 Theory

In UFM, the sample is oscillated such that vibrations are out-of-plane (perpendicular to the surface) at frequencies well above the resonance frequency of the cantilever, for which the cantilever is unable to respond and effectively becomes stationary over the oscillation period [247–250]. This causes the tip to be periodically indented into and retracted from the sample surface as the sample oscillates. Due to the shape of the non-linear tip-sample force indentation relationship, this causes the time averaged force on the cantilever to increase relative to the static case, and thus the deflection of the cantilever increases as well. The amount the time-averaged force increases by depends on the slope of the force indentation relationship; the steeper slope of stiffer samples results in a higher force. This additional deflection is then decoupled from the deflection caused by sample topography by amplitude modulating the ultrasound such that it is only on for half of the time. The frequency of modulation is chosen to be well below the cantilever resonance, such that the motion is largely equivalent to the effect of static forces, while also being high enough that there are several cycles of ultrasound on/ultrasound off at each pixel of the image. The UFM signal is then read as the amplitude output of a lock-in amplifier, operating on the deflection signal at the modulation frequency. The time averaged — or low pass filtered — deflection signal is used as the feedback control as in standard contact mode AFM.

4.2.1 Analytic Model of UFM Response

A simple model for the tip surface system that can be used to understand UFM is the two spring model, in which the sample is modelled as a spring, with stiffness s , and the tip is a mass on the end of another spring, the cantilever, with a stiffness of k , as illustrated in figure 4.1 [249]. For a static force, displacing the base of the sample from the rest length of the system by a distance, z_s , the deflection of the cantilever, z_c , is given by

$$\begin{aligned} kz_c &= s(z_s - z_c) \\ z_c &= \frac{z_s}{1 + \frac{k}{s}}. \end{aligned} \tag{4.1}$$

For hard samples the surface is much stiffer than the cantilever, $k \ll s$, and the deflection of the cantilever becomes approximately equal to the displacement of the

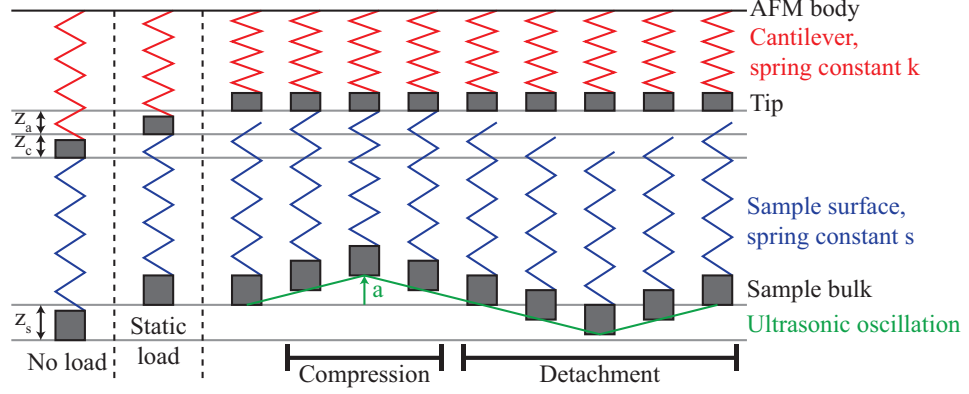


Figure 4.1: Schematic diagram of the two spring model used to create an analytic model of UFM response.

sample, therefore making it hard to distinguish between similarly hard surfaces.

When the sample is ultrasonically oscillated with an amplitude, a , this induces an additional cantilever deflection, z_a . The time dependent position of the sample surface is given by $A(t)$, and there are two regimes to consider; $A(t) > a_{cont}$, where the tip is in contact with the surface, and $A(t) < a_{cont}$, where it is detached. In this a_{cont} is defined by the free length of the surface spring, given by

$$a_{cont} = z_a + z_c - z_s. \quad (4.2)$$

This can be used to calculate the average force, F_{av} , exerted by the spring over one oscillation period of duration T , given by

$$F_{av} = \frac{1}{T} \int_0^T F(t) dt, \quad (4.3)$$

$$\text{where } F(t) = \begin{cases} s[A(t) - a_{cont}], & \text{if } A(t) > a_{cont} \\ 0, & \text{otherwise.} \end{cases} \quad (4.4)$$

Under an $A(t)$ which is symmetric in time around $t = \frac{T}{2}$ and monotonic between $t = 0$ and $t = \frac{T}{2}$ (e.g. a cosine wave) this can then be simplified to give

$$F_{av} = \frac{2s}{T} \int_{t_{cont}}^{\frac{T}{2}} (A(t) - a_{cont}) dt, \quad (4.5)$$

where t_{cont} is the time corresponding to $A(t_{cont}) = a_{cont}$ within this time period.

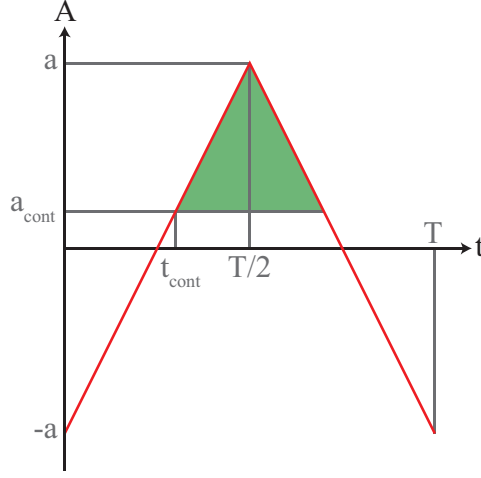


Figure 4.2: Schematic of $A(t)$ (red line) for a triangular waveform, showing the period of contact and region of non-zero force for which the area is calculated (green shading).

A simple model for $A(t)$ is that of a triangular wave, as shown in figure 4.2. From this, the integral in equation 4.5 is equivalent to the area of the shaded triangle, which results in the solution given by equation 4.6;

$$\begin{aligned}
 F_{av} &= \frac{2s}{T} \left[\frac{1}{2} \left(\frac{T}{2} - t_{cont} \right) (a - a_{cont}) \right], \\
 \text{where } t_{cont} &= \frac{T}{4a} (a + a_{cont}); \\
 F_{av} &= \frac{s}{4a} (a - a_{cont})^2.
 \end{aligned} \tag{4.6}$$

Removing a_{cont} using equation 4.2, then z_s using equation 4.1 and balancing with the force due to the compression of the cantilever spring gives

$$k(z_c + z_a) = \frac{s}{4a} \left(a - z_a + \frac{k}{s} z_c \right)^2, \tag{4.7}$$

which can be rearranged to give a quadratic in z_a ;

$$0 = z_a^2 - 2 \left(a + 2 \frac{k}{s} z_c + 2a \frac{k}{s} \right) z_a + \left(a^2 + \left(\frac{k}{s} z_c \right)^2 - 2a \frac{k}{s} z_c \right). \tag{4.8}$$

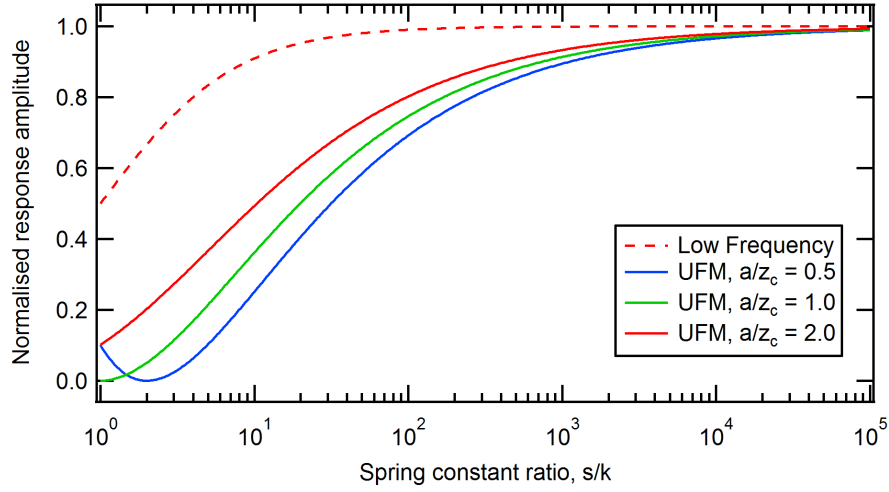


Figure 4.3: Cantilever response to sample oscillations with varying sample surface stiffness, normalised to the amplitude of the surface oscillations. Low frequency oscillation response (dashed line) was calculated using equation 4.1, and the response amplitude is the amplitude of cantilever oscillation. Ultrasonic oscillation responses (solid lines) were calculated using the analytic model with triangular oscillations (equation 4.9), where the response amplitude is the additional deflection, z_a , normalised by the driving amplitude, a . Different colours are for different oscillation amplitudes relative to the set point deflection ($\frac{a}{z_c}$).

The solution to this is

$$z_a = z_c \left[\frac{k}{s} + \frac{a}{z_c} + 2 \frac{ka}{sz_c} - 2 \sqrt{\frac{ka}{sz_c} \left(\frac{k}{s} + 1 \right) \left(\frac{a}{z_c} + 1 \right)} \right], \quad (4.9)$$

where only the negative root is used to avoid the unphysical $z_a > a$.

Response curves for equation 4.9, as well as a comparison to the static and low frequency case of equation 4.1, are given in figure 4.3. From this it is clear that contrast in the response with changing sample stiffness falls off for conventional AFM around $s \sim 100k$, whereas for UFM it falls off around $s \sim 10000k$, allowing for the investigation of samples with much higher stiffnesses. However, at values of s comparable to k the UFM response becomes negligible, making the technique unsuitable for soft samples, though a cantilever with a lower spring constant would increase the response. For the ultrasonic response with an amplitude $\frac{a}{z_c} = 0.5$ (blue curve) an up turn in response is seen below $\frac{s}{k} < 2$, which can be substituted into

equation 4.1 to give

$$z_c = \frac{z_s}{1 + (> 0.5)} ;$$

$$z_s > 1.5z_c ,$$

which can further be substituted into equation 4.2 with the assumption that $z_a = 0$, corresponding to the deflection before the ultrasound is started, giving

$$a_{cont} < -0.5z_c = -a .$$

This means that the point at which contact is broken, a_{cont} is outside of the oscillation range and thus the assumptions for UFM operation are broken, meaning the up turn is unphysical and would not be seen in experiments.

4.2.2 Simulation of UFM Response

The analytic model, while useful to demonstrate the principle of UFM, does not provide an accurate representation of a real system. This is primarily due to the modelling of the surface as a spring, which is an oversimplification, and better models exist, as discussed in section 1.1.3. The complexity of these models prevents the use of analytical techniques to derive the cantilever response in real systems, so instead an iterative simulation technique is used.

Parameters for the simulation are defined first, including the material properties (Young's modulus and Poisson ratio) for the sample and the tip, the tip radius, the adhesive force between the tip and the surface, the cantilever spring constant, k , the set point deflection (with no oscillation) of the cantilever, z_c , and the ultrasonic oscillation amplitude of the surface, a . The interaction model (e.g DMT, see section 1.1.3) is also selected and used to create a force versus indentation dataset, $F(d)$, for a range of indentations, d , which are significantly larger than the oscillation amplitude. This dataset is used as a lookup table throughout the simulation.

The initial indentation, d_0 , is found by finding the set point force on the lookup dataset, i.e. where $F(d_0) = kz_c$. A single oscillation in indentation is created, with the central value being the initial indentation and the oscillation, typically a sine wave, having the ultrasonic oscillation amplitude. These indentations are converted into forces using the lookup dataset, as shown in figure 4.4, and an average is taken to find the average force during this oscillation, given by

$$F_0 = \frac{1}{2\pi} \int_0^{2\pi} F(d_0 + a \sin(t)) dt . \quad (4.10)$$

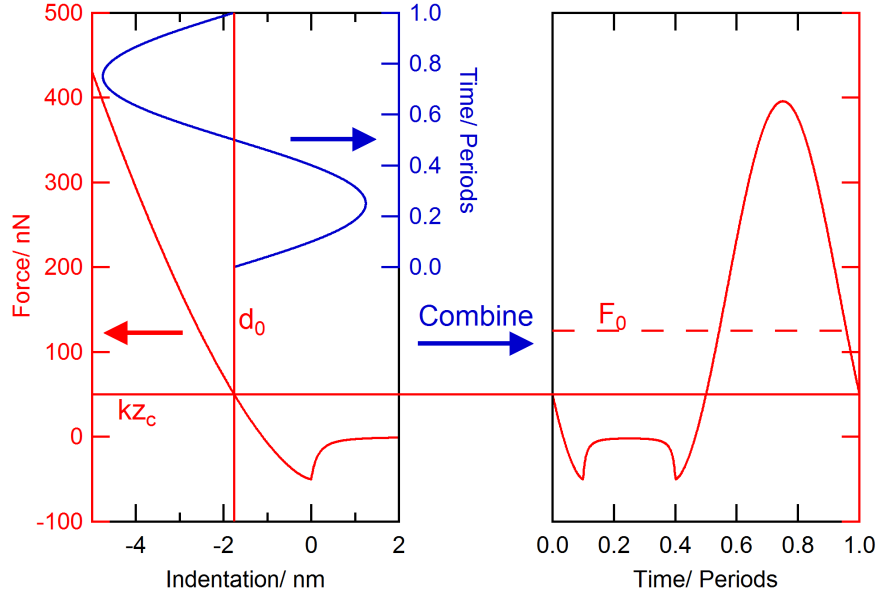


Figure 4.4: Example of the first force calculation step in the simulation. The left graph shows a DMT model force curve (red curve), from which the set point force is used to find the initial indentation (red lines). An oscillation is made around this indentation (blue curve), which is then converted to the force versus time curve shown on the right by converting each indentation point on the oscillation wave to a force using the DMT curve. Once this is done, an average of the force versus time wave is taken, here displayed as a red dashed line.

Special care is taken to the direction of motion when using hysteretic models, such as the JKR model. Due to the positive curvature of the interaction models, this average force is always higher than the set point force.

This higher force causes an additional cantilever deflection which corresponds to increasing the average tip sample separation and thus reduces the indentation at the centre of oscillation, i.e. $d_{F_0} = d_0 + \frac{F_0}{k} - z_c$. An oscillation with this new indentation as a central point results in an average force lower than F_0 , again due to the shape of the force curve, which means that the new deflection, and thus force from the cantilever, is too high when compared to the force exerted by the oscillating surface. The correct additional deflection is therefore the value at which the force due to the deflection of the cantilever balances with the average force over the oscillation period. This can be found using the bisection method on the central indentation value, using the static case indentation, d_0 , as the initial upper bound, d_{max} , and the indentation due to the additional deflection from the average

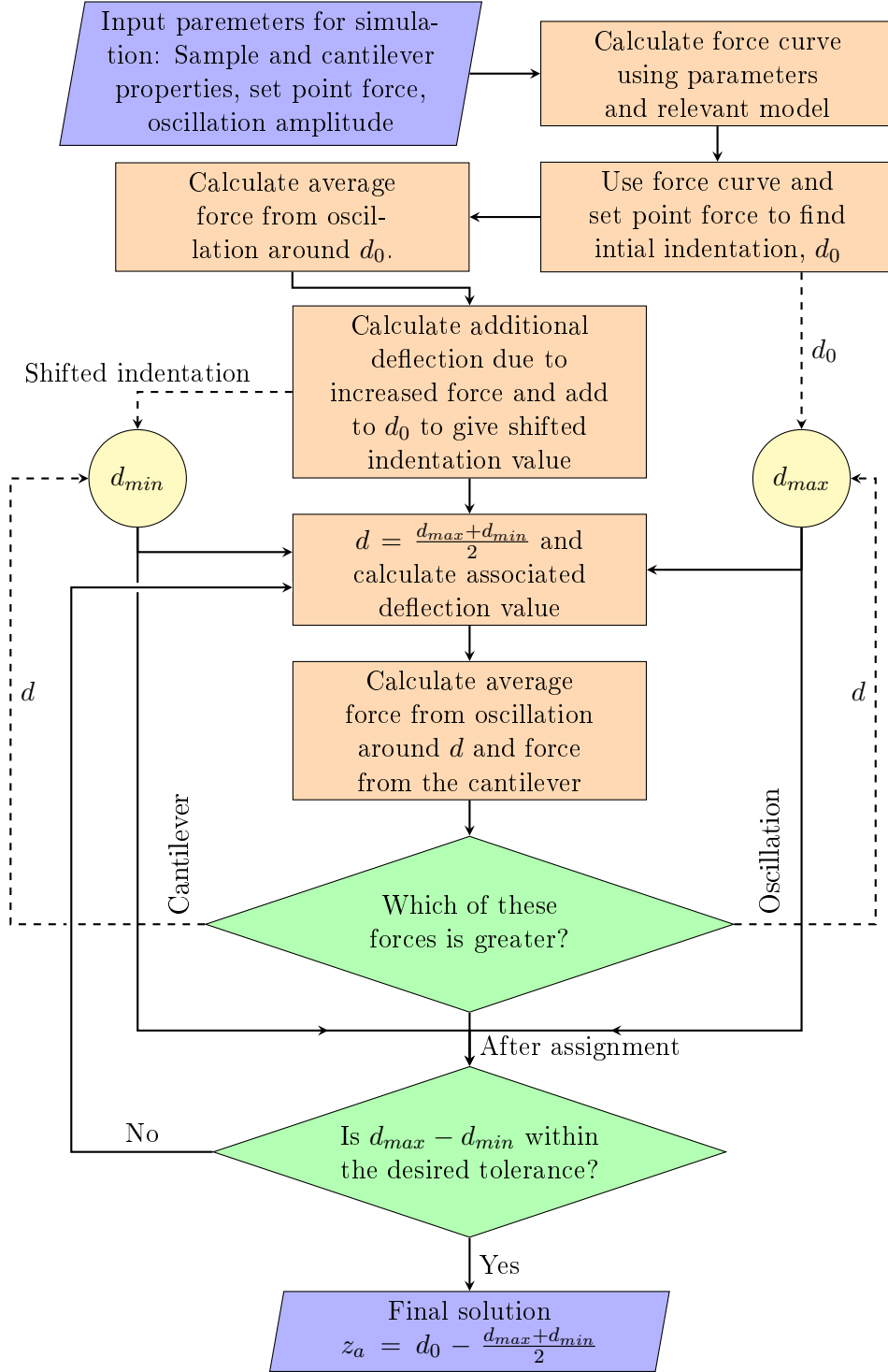


Figure 4.5: Flow chart of the simulation process. Dashed lines indicate assignments to reused variables.

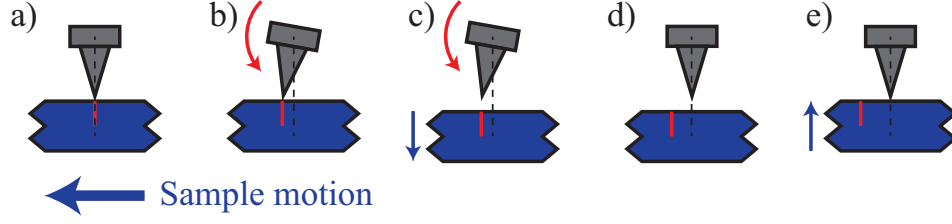


Figure 4.6: Schematic of the cause of superlubricity in UFM operation, showing one cycle of ultrasonic sample vibration. The red line marks a constant position on the sample's (blue) surface. a) Sample starts in contact with tip. b) Motion of the sample causes cantilever to twist creating torsion (red arrow). c) Sample retracts from tip. d) Torsion restores tip to central position. e) Sample re-engages with tip in new location.

force due to oscillation, d_{F_0} , as the initial lower bound, d_{min} . The force balance equation between the force from the cantilever deflection and the average force from the sample during an oscillation, given by

$$k(d_0 - d + z_c) \stackrel{?}{=} \frac{1}{2\pi} \int_0^{2\pi} F(d + a \sin(t)) dt, \quad (4.11)$$

is then evaluated for $d = \frac{d_{max} + d_{min}}{2}$. If the left hand side (the force from the cantilever) is greater than the right hand side (the average force from the sample during an oscillation) the value of d becomes the new d_{min} ; if the left hand side is less than the right hand side, the value of d becomes the new d_{max} . This process is repeated until an accuracy tolerance is achieved, which is defined as $d_{max} - d_{min} < d_{tol}$, at which point $d = \frac{d_{max} + d_{min}}{2}$ becomes the final value of indentation and the additional deflection due to the ultrasonic oscillations is $z_a = d_0 - d$. The full process is shown as a flow chart in figure 4.5.

4.2.3 Superlubricity Effect

Application of ultrasonic vibrations results in a reduction of friction between two objects, which is known as the superlubricity phenomenon [251–253]. In UFM this is observed as an ability to scan fragile samples that are typically destroyed by contact mode operation, despite the higher normal forces during parts of the ultrasonic vibration. The origin of this reduced friction is attributed to periodic detachment between the two objects — in the case of UFM the tip periodically detaches completely from the surface, given an oscillation amplitude that exceeds the distance between the average indentation and the pull-off point. The periodic detachment allows for the cantilever to restore to the central lateral position, i.e. zero torsional force, thus

ensuring that the tip is applying no lateral forces to the sample, as illustrated in figure 4.6. The short period of detachment is sufficient as the torsion induced during the period of contact is limited by the duration of the contact and the movement speed of the sample, allowing for only a small deviation from the central position.

4.2.4 Other UFM Modes

The form of UFM described here, in which the sample is actuated at ultrasonic frequencies, is the most basic version of UFM, however two other techniques exist in the UFM family; waveguide UFM (wUFM) and heterodyne force microscopy (HFM) [249]. Waveguide UFM works similarly to conventional UFM except the ultrasound is applied to the cantilever, which acts as a mechanical waveguide to bring the oscillations to the tip [233,254]. This has two advantages over conventional UFM: It does not require special preparation of the sample (i.e. mounting to an ultrasonic actuator) and it is only sensitive to the local surface properties of the sample — subsurface heterogeneities which would effect the transmission of ultrasound in conventional UFM have no effect in wUFM. In HFM both UFM and wUFM are combined while operating at slightly different frequencies [255]. The response is then measured at the beat frequency, i.e. the difference between the two exciting frequencies. The amplitude of this beat frequency will give contrast similar to UFM and wUFM. Differences in relaxation times of the surface (e.g. as a result of changing viscoelastic properties) will result in a delay of the surface oscillation, manifesting as a change in the phase of the beat signal (measured relative to the mixed driving signals). As such, the phase channel of HFM provides additional information about the viscoelastic properties of the sample surface.

4.3 Experimental Methods

4.3.1 Ultrasonic Force Microscopy

All AFM images were acquired with an Asylum Research MFP-3D-SA AFM, with a schematic of the UFM specific setup given in figure 4.7. For ultrasonic excitation a disk piezoelectric transducer (made by PI Ceramic using material PIC255) operating in thickness expansion mode with a nominal resonance frequency of 8 MHz was used. To ensure acoustic coupling, the samples were bonded to this using salol (phenyl salicylate). The transducer was driven using a Tektronix AFG3022B arbitrary function generator and the UFM driving frequency was tuned to give the biggest cantilever response, which corresponds to the transducer resonance. The

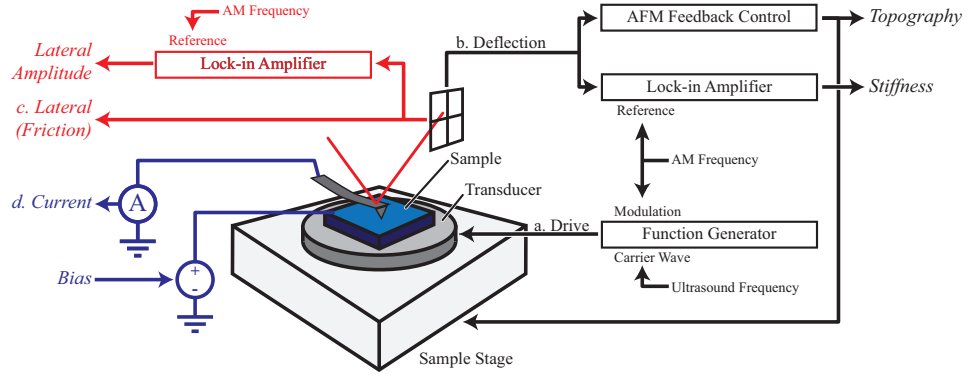


Figure 4.7: Schematic of the UFM setup. The right hand side of the image shows the standard UFM setup and the left hand side corresponds to the addition of simultaneous friction and conductivity measurement techniques used in section 4.4.3. Signals labelled with letters correspond to the signals in figures 4.8, 4.16, and 4.20.

amplitude modulation took a half sine shape, as illustrated in figure 4.8, with a frequency of 4 kHz and maximum amplitude for the signal generator, i.e. $20 V_{pp}$ before the 50Ω output impedance, giving typical surface amplitudes of approximately 1 to 10 nm (determined by assuming the surface amplitude is larger but of similar magnitude to the UFM response amplitude). The modulation was achieved using the modulation input on the signal generator, driven by a sine wave at the modulation frequency from the AFM controller. The signal generator takes modulation inputs of less than -1 V to have a modulation output of 0%, scaling linearly up to 100% at 1 V, therefore the output from the controller had an amplitude of $4 V_{pp}$ and a DC offset of -1 V, to achieve the desired half-sine wave modulation as shown in figure 4.8(a). UFM response was normally measured using the internal lock-in amplifier of the AFM controller, which uses the modulation output signal as a reference. For results with a lateral amplitude channel (amplitude of change in lateral signal due to modulation of ultrasound, as discussed in section 4.4.3.1), the lateral amplitude was acquired with the internal lock-in amplifier while the UFM signal was acquired with an external Stanford Research Systems SR830 lock-in amplifier, both running at the modulation frequency. All oscilloscope traces were captured using a Tektronix TDS 1001B oscilloscope.

For most measurements the tips used were MikroMasch NSC18 tips (silicon tip with nominal normal spring constant 2.8 Nm^{-1} , resonance frequency of 75 kHz, and tip radius 8 nm), which were calibrated when necessary using the Sader method (see section 2.2.3) for the normal spring constant and the wedge calibration method (see section 2.2.4) on a MikroMasch TGF11 trapezoidal calibration grid for the

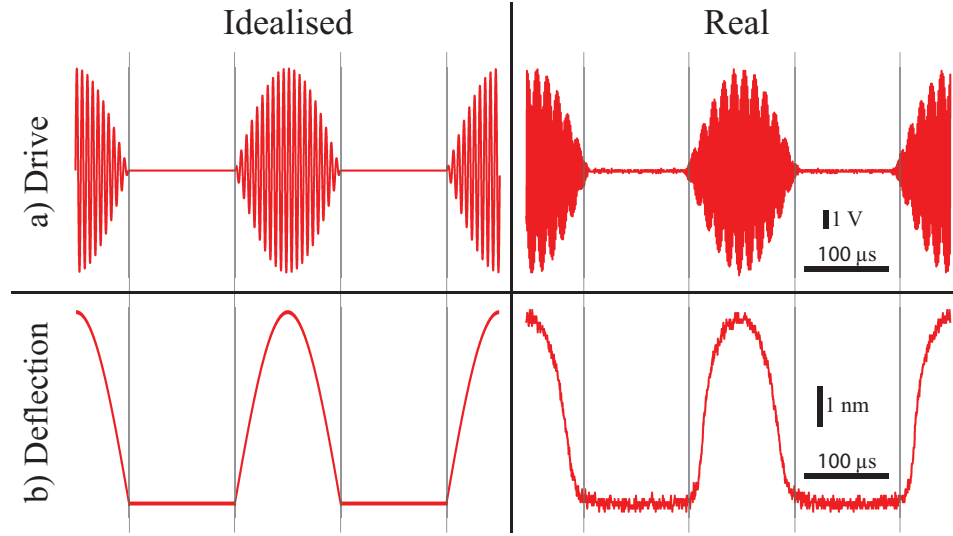


Figure 4.8: Idealised and captured oscilloscope traces of the signals generated during UFM operation. The idealised traces are simplified to show the basic structure of each signal. The idealised drive signal is represented with a much lower ultrasonic frequency than is typically used, for the purposes of visibility. In the real drive signal the high ultrasonic frequency causes the fringes seen on the envelope of the signal due to a lack of time resolution in the oscilloscope. The traces are lined up such that their modulation phase matches. (a) and (b) Corresponds to the outputs labelled in figure 4.7.

lateral spring constant. For the comparison of tip materials in section 4.4.2, Mikro-Masch NSC14/Hard tips (silicon tip with diamond like carbon (DLC) coating with nominal normal spring constant 5 Nm^{-1} , resonance frequency 160 kHz, and tip radius 8 nm before coating) were used as the harder tip for comparisons between tip materials.

For the conductive measurements an Asylum Research ORCA tip holder was used for current amplification; for the single walled carbon nanotube (SWNT) results a dual gain ORCA with gains of 10^6 VA^{-1} and 10^9 VA^{-1} was used whilst for the graphene nanoplatelet epoxy composite results a standard ORCA with a gain of $5 \times 10^6 \text{ VA}^{-1}$ was used. The tips used were platinum coated NSC18 (specifications as above) for the nanotube sample and platinum coated MikroMasch CSC37 tips (longest cantilever, nominal normal spring constant 0.3 Nm^{-1} , resonance frequency 20 kHz and tip radius 8 nm) for the graphene nanoplatelet epoxy composite sample. The bias voltage was applied to a gold contact on the nanotube sample and directly to the top surface of the composite sample.

4.3.2 Samples

For testing UFM parameters and comparisons to simulations a piece of silicon cleaved from a silicon wafer was used. The gold on silicon sample, used to test contrast and the effect of tip materials, was created by sputtering a 50 nm layer of gold onto another piece of silicon wafer and then scratching a small area off down to the silicon. To test the capabilities of UFM as a multifunctional technique a variety of carbon nanomaterial samples were used.

The graphene on copper foil samples were supplied by A. Marsden from the Warwick Microscopy Group. They were grown using the LP-CVD method previously described in section 3.2.1 with some modifications; the electropolish was for 10 s at 5 V (~ 1.5 A), the quartz tube was held at 10^{-1} mbar, and the methane flow was 2 sccm. The samples were examined on the copper they were grown on, so no transfer was performed.

The single walled carbon nanotube (SWNT) samples were supplied by N. Wilson in the Warwick Microscopy Group. The nanotubes were grown on a silicon oxide on silicon substrate by catalysed chemical vapour deposition (cCVD) using an iron catalyst and methane as feedstock, as described in [256].

The graphene nanoplatelet epoxy composite was supplied by G. Cao, I. Kinloch, and R. Young from the University of Manchester. It was made using xGnP graphene nanoplatelets from XG Sciences, grade M25 (average particle diameter and thickness of 25 μm and 6 nm, respectively, according to manufacturer information) in Araldite LY 556 epoxy with hardener XB 3473, with 8% graphene by weight. The graphene nanoplatelets were stirred into the epoxy using an IKA EUROSTAR shear mixer for 1 hour at 2000 rpm. The hardener was then added (at a weight ratio of 23:100 to the epoxy) and stirred for a further 10 minutes at 2000 rpm. The mixture was sonicated at 37 kHz for 10 minutes, followed by vacuum degassing in an oven at 60°C for 10 minutes. The mixture was poured into a mold and cured at 140°C for 12 hours. Once cooled to room temperature the sample was removed from the mould and cut to size. The images presented here are taken on a cut face.

4.4 Results and Discussion

Here, the results start with simple experiments on silicon, showing the steps taken during setup of the UFM system and the effect of varying parameters such as the drive frequencies and the load force. These results are also compared to simulations, with an aim to understand the differences between the real and simulated systems and to investigate the possibility of using simulations to quantify the results. A

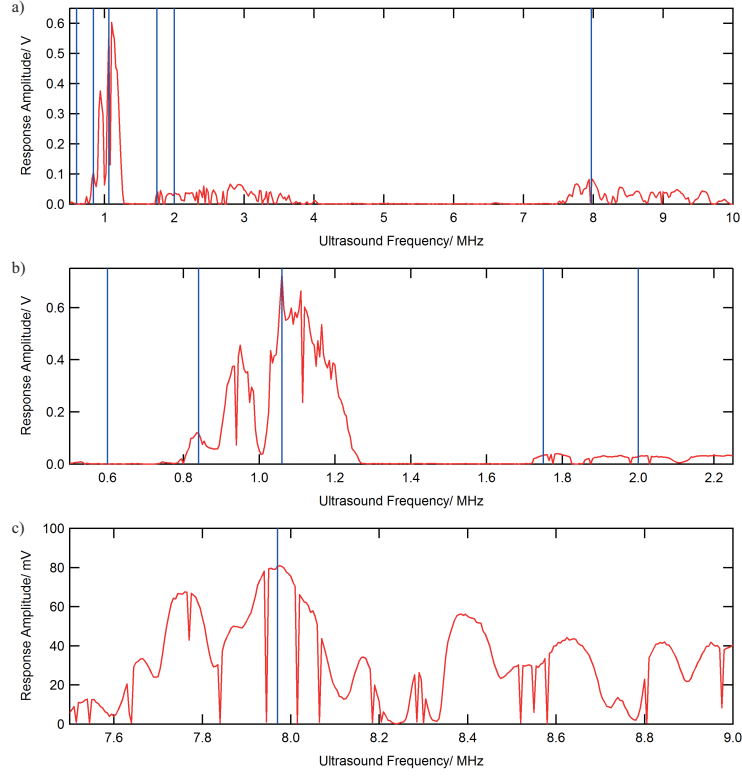


Figure 4.9: UFM response amplitude with varying ultrasound frequency, performed on a silicon sample with a modulation frequency of 4 kHz, the maximum drive amplitude possible, and a set point force of 100 nN. a) Full range sweep. b,c) Reduced range sweeps with higher frequency resolution. Blue lines correspond to traces shown in figure 4.10.

comparison of UFM contrast between a silicon and diamond like carbon coated tip on a gold and silicon sample was also performed, to demonstrate the effect of tip material on UFM imaging. Finally, combining UFM with other contact mode techniques is demonstrated by using friction force microscopy and conductive AFM simultaneously with UFM, performed on a variety of carbon nanomaterial samples.

4.4.1 Understanding UFM

When starting a UFM experiment the frequency of the ultrasonic oscillations must be tuned to ensure that the frequency is sufficient to enter the UFM regime and that there is a significant response amplitude [257]. An example of this tuning on a silicon sample is shown in figure 4.9(a). Naïvely it could be expected that peak amplitude response at 1.06 MHz would make it the best frequency to use, however, this is not the case due to the response of the cantilever at this frequency not being fully in

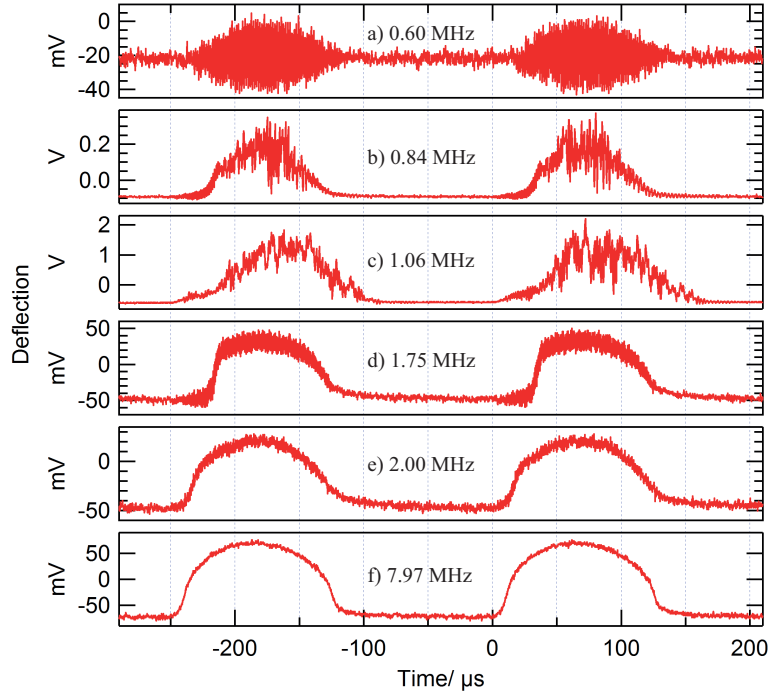


Figure 4.10: Traces of cantilever deflection at different ultrasound frequencies, performed on a silicon sample with a modulation frequency of 4 kHz, the maximum drive amplitude possible, and a set point force of 100 nN.

the UFM regime and instead partially following the high frequency oscillations. The cantilever response as frequency is increased, as shown in figure 4.10, demonstrates that there is a transition between conventional cantilever response at 0.60 MHz (figure 4.10(a)), where the cantilever follows the ultrasonic oscillations of the sample, and UFM behaviour at 2 MHz and above (figures 4.10(e,f)), where the cantilever deflects due to the ultrasonic oscillations but does not follow them. Between the two regimes the cantilever deflects partially in the UFM regime and partially follows the oscillations, resulting in the deflection traces appearing distorted and noisy. It is possible that other effects, particularly the response time of the AFM's four quadrant photodiode, are responsible for the apparent lack of following of the ultrasonic oscillations, but the lack of distortion from the expected curve (figure 4.8(b)) present in the 2.00 and 7.97 MHz traces, unlike the 1.75 MHz trace (figure 4.10(d)), implies that the expected UFM behaviour is dominant. In this example, an ultrasonic frequency of 7.97 MHz was chosen, corresponding both to the expected resonance of the piezoelectric transducer and the highest response amplitude within the UFM regime.

The modulation frequency can also be tuned, the result of which is shown

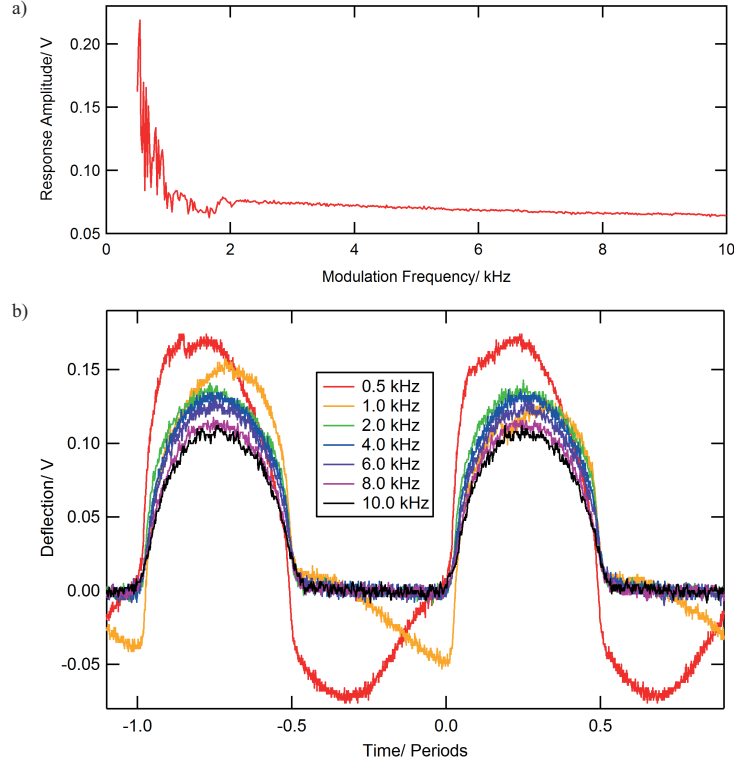


Figure 4.11: Effect of modulation frequency on UFM response, performed on a silicon sample with an ultrasound frequency of 7.97 MHz, the maximum drive amplitude possible, and a set point force of 100 nN. a) Sweep of response amplitude against modulation frequency. b) Oscilloscope captured traces at different modulation frequencies.

in figure 4.11(a). The response is mostly flat except at low modulation frequencies, where the response amplitude inconsistently increases with decreasing frequency. This is caused by the feedback loop used for engaging the tip, which uses the deflection signal after being low pass filtered at 1 kHz, responding to the additional deflection caused by the UFM operation. This can be seen in the traces in figure 4.11(b) which display distortion from the expected signal for the 0.5 and 1.0 kHz signals, especially in the region where ultrasound is off and the deflection should be flat. There is a small reduction in amplitude with increasing modulation frequency, which is matched by a decrease in peak amplitude visible in the 2 to 10 kHz traces shown in figure 4.11(b). The cause of this reduction is unclear, it may be due to the driving electronics, a small change in the responsiveness of the piezoelectric transducer, or the behaviour of the cantilever at these frequencies. When picking a modulation frequency the scanning pixel rate must also be considered; the modula-

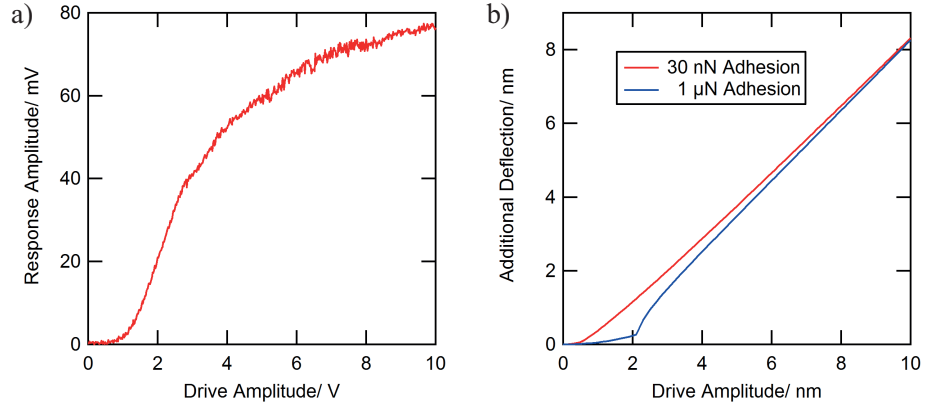


Figure 4.12: Response amplitude of UFM on silicon with varying drive amplitude. a) Real result, with ultrasonic frequency of 7.97 MHz, modulation frequency of 4 kHz, and a set point force of 100 nN. b) Simulated response using the DMT model with a cantilever spring constant of 2.65 Nm^{-1} (as measured for the real system), set point force of 100 nN, a tip radius of 10 nm (estimated value of the real system), and both the tip and sample with the elastic properties of silicon (130 GPa Young's modulus, 0.28 Poisson ratio [258,259]). Two lines are shown for different values of adhesion, where 30 nN is the measured value for the real system.

tion frequency must be high enough that at least one cycle of modulation, though preferably more, occurs at every pixel within a scan, otherwise there will not be enough time at each pixel to give accurate data, leading to mixed information between the UFM response and topography signals. In most experiments a modulation frequency of 4 kHz was used as this is above both the feedback filter frequency and the pixel scanning rate, while still maximising the output amplitude, though the loss of amplitude is not significant enough to avoid using higher frequencies for higher resolution or faster images.

It is also interesting to look at how the response amplitude changes with drive amplitude, shown in figure 4.12(a). The response increases slowly up to a certain drive amplitude, at which point there is brief rapid increase in amplitude followed by a steady slower increase. This behaviour is not seen in the simulations when using the measured and expected parameters of the system (figure 4.12(b)), though can be seen when using a much greater adhesion value, although the effect is still not near the same magnitude. Additionally, the simulations show the response generally increasing almost linearly with drive amplitude, whereas the real result shows a slight tapering off in response; this could be due to a non-linear response from the transducer. This implies that the simulation is flawed, possibly in the model used

for tip-surface interaction, which may be altered by the frequency of oscillation, or with the assumptions made about the motion of the system. It is possible that the cantilever is still partially following the surface during the oscillations but not being detected due to the relatively slow photodiode response; this would cause a significant change in behaviour at the point at which the amplitude is great enough to cause detachment from the surface and thus change the behaviour of the tip following the surface. This could explain the similarity in shape to the large adhesion simulations, where the high adhesion creates a region that strongly affects the UFM response due to the shape of the tip-sample interaction model.

UFM response also varies with the applied normal force, demonstrated by the force curve results shown in figure 4.13(a). As the normal force increases the UFM response decreases, which is as expected from the simulations shown in figure 4.13(b) and from the understanding that UFM response is as a result of the curvature of the tip sample interaction force, which is straighter at higher load forces. The magnitude of this decrease is consistent with the simulations for a drive amplitude of about 4 nm, noting that the simulation does not extend to negative forces, as seen in the retract curve. A small increase at high load forces is visible in the real results, but not in the simulations, however, this increase in amplitude is not seen in the oscilloscope traces captured at different set points (figure 4.13(c), implying that the increase is either due to inconsistent behaviour from the lock-in amplifier or due to the dynamic nature of the force curve capture, neither of which would effect the oscilloscope traces or be accounted for in the simulation. From these results it is clear that using a lower set point can improve the UFM response signal, which can help in cases where response is lowered, such as softer samples and samples with poor transmission of ultrasound. A higher set point force reduces the susceptibility of the response to changing forces, which can be caused by drift in the free deflection, thus making the results more reliable.

4.4.2 Effect of Tip Hardness

UFM can have problems with reduced contrast if the tip material is of similar or lower stiffness than the surface being probed. Intuitively, the softer of two objects interacting will be the most affected by the compression force, making a relatively soft tip material the dominant contribution to the interaction. Mathematically, this is evident from the combined Young's modulus, E_{tot} , as given by

$$\frac{1}{E_{tot}} = \frac{3}{4} \left(\frac{1 - \nu_{tip}^2}{E_{tip}} + \frac{1 - \nu_{surf}^2}{E_{surf}} \right), \quad (4.12)$$

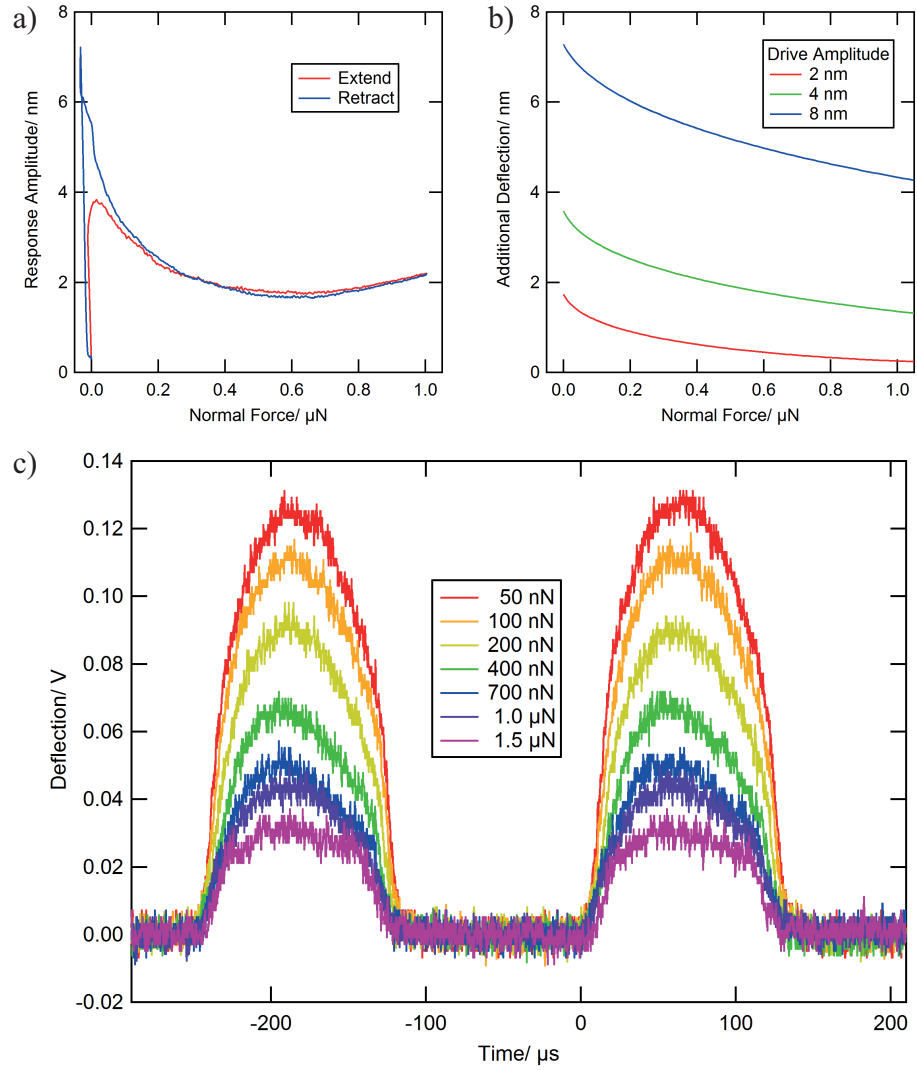


Figure 4.13: Effect of varying load force on UFM response with a silicon sample. a) Real result, using a force curve technique to vary force, for an ultrasonic frequency of 7.97 MHz, modulation frequency of 4 kHz, and the maximum possible drive amplitude. b) Simulated response using DMT model with a cantilever spring constant of 2.65 Nm^{-1} (as measured for the real system), a tip radius of 10 nm (estimated value of the real system), and both the tip and sample with the elastic properties of silicon (130 GPa Young's modulus, 0.28 Poisson ratio), with different drive (surface) amplitudes. c) Oscilloscope traces of the deflection signal at different set point forces, captured under the same conditions as (a) except using static normal forces.

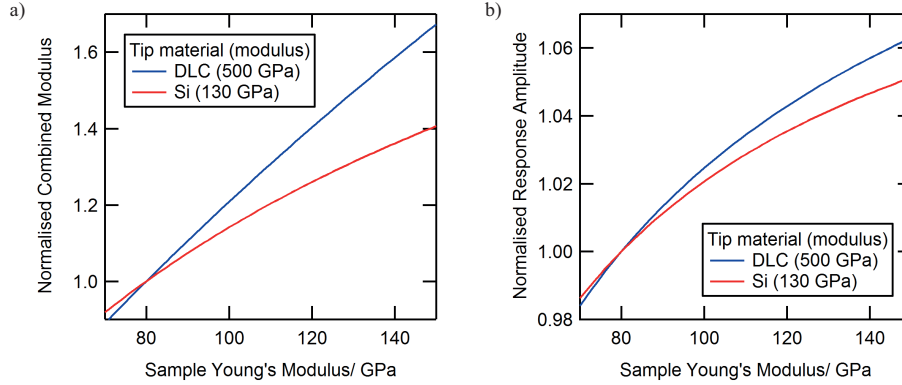


Figure 4.14: Effect of tip hardness on UFM response with varying sample Young's modulus. a) Change in the combined Young's modulus with tip and sample Poisson ratios of 0.3. b) Change in the simulated response (simulation parameters of 50 nN adhesive force, 10 nm tip radius, tip and sample Poisson ratios of 0.3, 100 nN set point force, 5 nm drive amplitude and a cantilever spring constant of 3 Nm^{-1} using the DMT model). On both, curves are given for tip materials of silicon and diamond-like carbon (DLC). All graphs have been normalised by their value at a sample Young's modulus of 80 GPa, corresponding to gold [260].

where E_{tip} and E_{surf} are the Young's moduli of the tip and surface materials respectively and ν_{tip} and ν_{surf} are their Poisson ratios. E_{tot} is a parameter common to all the tip-sample interaction models, as discussed in section 1.1.3. In this, for materials with similar Poisson ratios, the smaller of the values between E_{tip} and E_{surf} will have the most significant contribution to the final value, and if one is significantly smaller than the other the larger value will become mostly irrelevant to E_{tot} . This can be seen in the graph plotted in figure 4.14(a), where the combined modulus has a significantly higher slope for the harder tip, and therefore the contrast is improved when comparing similar sample moduli. The effect this has on the simulated response is given in figure 4.14(b), where the harder tip is again shown to have greater change in response for the same change in sample modulus. This reduction in contrast when using a relatively soft tip material is further complicated by variations in secondary contributors to UFM response, particularly the adhesion, having an effect on contrast comparable to the reduced effect of sample stiffness, possibly even resulting in inverted contrast — a stiffer material can give a lower response.

The solution to this is to use a tip made of a harder material, as demonstrated in figure 4.15, where a sample of silicon (Young's modulus of 130 GPa [259]) partially covered by a 50 nm gold layer (Young's modulus of 80 GPa [260]) by sputter coating is imaged with two different tips, one made of silicon, and one with a diamond-like

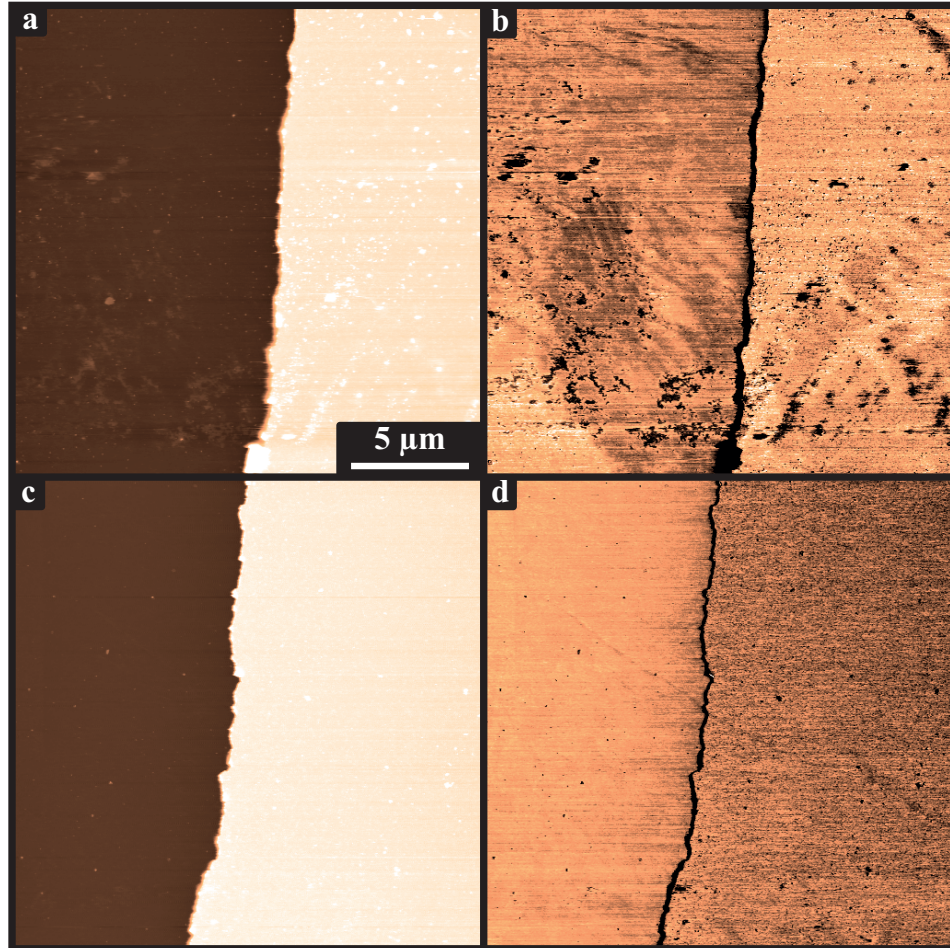


Figure 4.15: UFM results of a gold on silicon sample using two tips with different hardness. a,b) Silicon tip, height and UFM response respectively. c,d) Diamond-like carbon coated tip, height and UFM response respectively. Both height images have a data full scale of 70 nm. The UFM response images have a scale extending 30% in each direction from central values of 0.55 nm and 1.00 nm for the silicon and DLC coated tip respectively, ensuring that the relative responses give consistent contrast. There is an overlap of approximately $7\ \mu\text{m}$ between the different tips, corresponding to the bottom of the silicon tip images and the top of the DLC coated tip images.

carbon (DLC) coating (Young’s Modulus of 500 GPa [261]). In both cases the raised gold section is on the right and is seen to have a different UFM response to the silicon on the left side, with a line of very low response separating them — an artefact caused by the local topography’s effect on the tip-sample contact. The contrast can be evaluated using the average values of the regions: For each UFM response image an average is taken in the leftmost (silicon) and rightmost (gold) 5 μm , giving a response of 0.54 ± 0.06 nm and 0.57 ± 0.06 nm respectively for the silicon tip and 1.05 ± 0.04 nm and 0.88 ± 0.06 nm respectively for the DLC coated tip. The contrast between these is then given as the increase in response for the silicon over the gold, which is -5 ± 14 % for the silicon tip and 19 ± 9 % for the DLC coated tip, showing that the silicon tip produces a low inverted contrast, whereas the DLC coated tip produces strong contrast in the expected direction. This improvement in contrast is significantly greater than that predicted by the simulations in figure 4.14(b), though this does not account for the inverted contrast seen when using the silicon tip. The inverted contrast when using the silicon tip strongly implies that other interaction factors, such as adhesion, are having a strong effect on the UFM response. The strength of this effect being relatively diminished when using the DLC coated tip is supported by the increased contribution from the combined Young’s modulus, as seen in figure 4.14(a), though the change in tip material could also affect the secondary contributors, particularly the adhesion. It is possible that this improvement in contrast has contributions from other factors, such as the different spring constants, but simulations of these and previous experiments [257] show little effect on the expected contrast, especially compared to the effect of changing the tip hardness.

4.4.3 Superlubricity and “Half and Half” UFM

The modulation of the ultrasonic excitation signal leads to a “half and half” operation of the AFM, where half of the time it is in contact mode and the other half it is in ultrasonic force mode. As the period at which it is alternately in UFM or contact AFM mode is less than the time between pixels, this means that signals usually acquired during contact mode scanning, such as in friction force microscopy (see section 1.1.4.3) and conductive AFM (see section 1.1.4.2), can be acquired simultaneously with UFM stiffness information.

4.4.3.1 Combined friction and UFM measurements

Figure 4.16(c) shows the lateral forces measured when scanning in modulated UFM mode. Comparing the lateral force, figure 4.16(c), with the ultrasonic excitation, it

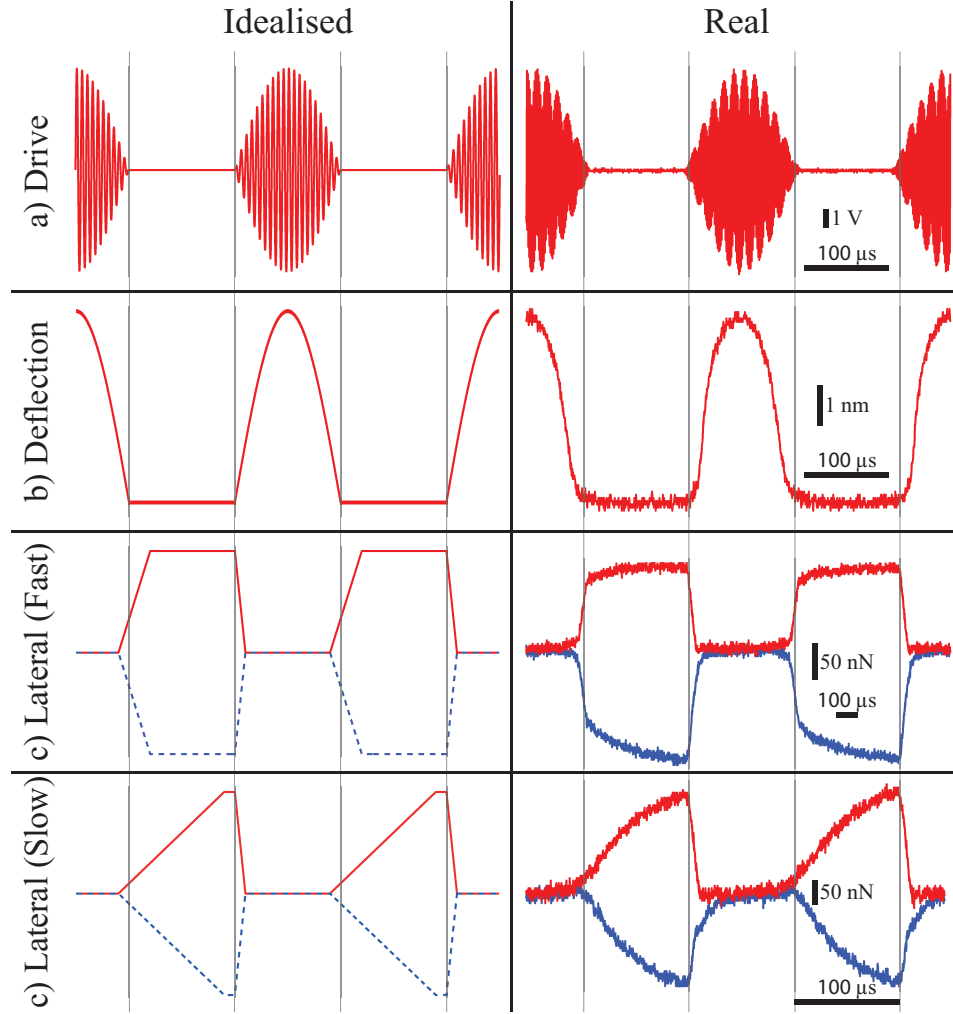


Figure 4.16: Expanded version of figure 4.8 showing idealised and captured oscilloscope traces of signals generated during UFM operation, with additional lateral signals. All the traces are lined up such that their modulation phase matches. On the lateral traces, the two lines (red and blue) correspond to the trace and retrace scan directions, and “slow” and “fast” refer to the tip velocities of $25 \mu\text{ms}^{-1}$ and $125 \mu\text{ms}^{-1}$ respectively, though the modulation frequencies are also different, resulting in the fast trace having a tip motion 25 times faster relative to the modulation phase. Lettering corresponds to the outputs labelled in figure 4.7.

can be seen that the friction force disappears (the trace and retrace signals overlap) when the ultrasonic excitation exceeds a critical value. This is the origin of the superlubricity in UFM, as discussed in section 4.2.3. However, when the ultrasonic amplitude is reduced below this threshold the tip is in continuous contact with the sample, and friction can start to torsionally bend the cantilever and hence induce a lateral deflection. The time taken for this lateral deflection to reach its steady state value depends on the scanning speed and the torsional stiffness of the cantilever. The value reached depends on the normal force and coefficient of friction. Hence, initially, an almost linearly increasing lateral force is observed, becoming constant once the torsion reaches the friction limit. The gradient of the initial slope is dependent on the scanning speed, as can be seen through comparison between the fast and slow scanning speed traces shown in figure 4.16(c). When the ultrasound turns on again, the cantilever torsion rapidly decreases until the superlubricity threshold is reached, at which point the lateral force becomes zero again. The tip thus moves across the surface in a stick-slip motion, presenting the opportunity to measure friction simultaneously with UFM. These results appear similar to results seen in acoustic friction force microscopy [262] and ultrasonic friction force microscopy [263], however, these both rely on the use of shear ultrasound wavemodes, as opposed to the longitudinal ultrasound wavemodes used here. Significant coupling between the longitudinal and shear modes is unlikely, i.e. the longitudinal mode will be the dominant mode, and the results are consistent with previously published work regarding ultrasonic out-of-plane surface oscillations [252].

To further investigate the effect of scanning speed on the slope observed in lateral measurements during UFM operation oscilloscope traces of the lateral signal were taken at different tip velocities, as shown in figure 4.17(a). Some cross talk with the deflection signal is seen here as an additional sharp jump as the ultrasound is turned on/off, which is ignored in the further analysis. The initial slope on these were fitted, giving a gradient measured in Vs^{-1} , which are compared to the tip velocities in figure 4.17(b). The measured gradient is proportional to the velocity with a proportionality constant of $(5.49 \pm 0.03) \text{ V} \cdot \mu\text{m}^{-1}$. This proportionality supports that the linear slope is as a result of the finite motion required to cause cantilever motion, and can therefore be used as the lateral optical lever sensitivity, more commonly given as the inverse value of $(182 \pm 1) \text{ nmV}^{-1}$. This calibration is not directly useful in friction force microscopy, where the lateral force is of interest rather than the displacement. However, it has uses elsewhere, particularly if doing force curve experiments, similar to those in chapter 3, on a lateral axis, where the displacement of the tip is required for the purposes of correctly giving an “indentation” value.

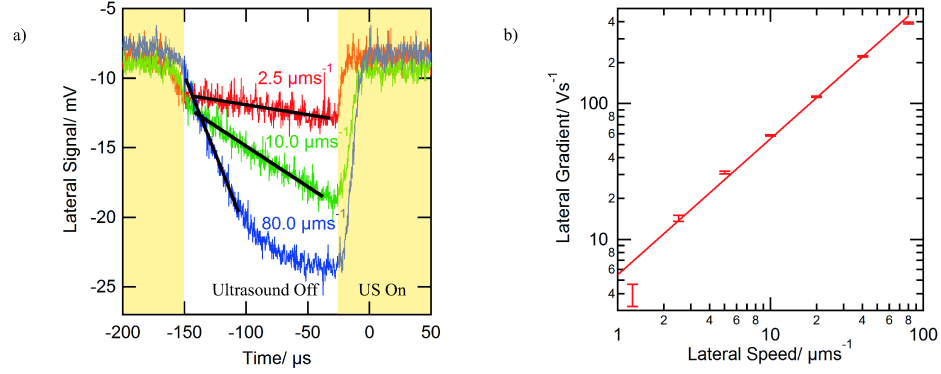


Figure 4.17: Effect of scanning speed on lateral signal in UFM operation. a) Lateral signal traces captured at different scanning speeds on silicon. Black lines are fits for the initial gradient. Some crosstalk from the deflection channel is visible at the start and end of the signal region, which is ignored for fitting. b) Initial gradients versus scanning speed for a range of scanning speeds, with a linear fit.

These calibrations are possible in other ways, such as by performing friction loops and using the stick-slip behaviour of the tip [264,265], or by pinning the tip against an object on the sample surface [160], but the UFM method presents a simple and reliable alternative.

The nature of this slope effect also presents an additional consideration when performing frictional measurements with UFM and gives a natural limit on the resolution possible. To see any contrast in the friction signal the lateral signal must reach its maximum value, i.e. the point at which the lateral force equals the maximum friction between tip and sample, during the half period of the modulation in which the ultrasound is off. This requires that the scanning speed to be over a threshold for a certain modulation frequency, with the two being proportional. However, the pixel acquisition rate must also be below the modulation frequency, otherwise the the UFM and topography will be coupled. With the examples shown in figure 4.17 the lateral signal was only seen reaching a maximum with a scanning speed above $40 \mu\text{ms}^{-1}$ at a modulation frequency of 4 kHz, giving an absolute minimum pixel size of 10 nm at one pixel per modulation period. This resolution can be improved by lowering the maximum lateral force between tip and sample, which can be achieved through lowering the load force, or by ensuring this maximum lateral force is reached quicker, primarily accomplished through using a shorter tip (making the same lateral motion result in more cantilever torsion) or using a cantilever with a higher torsional spring constant.

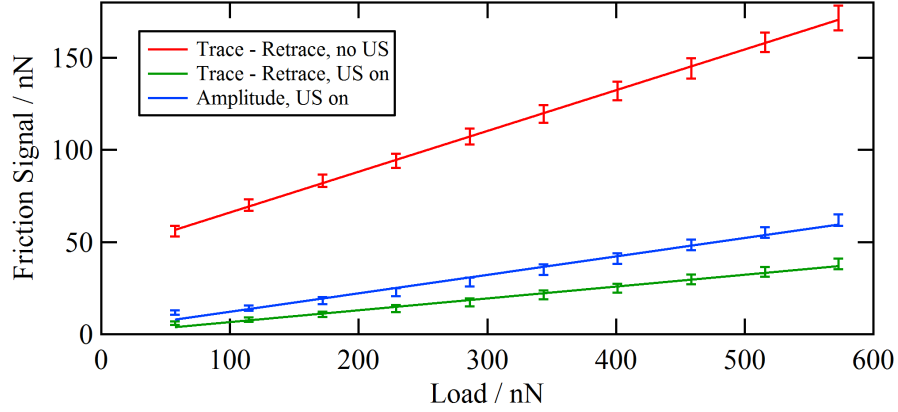


Figure 4.18: Variation in friction signal with varying loads on a silicon sample under different UFM conditions, with a linear best fit for each.

As the friction still affects the lateral signal for part of the time, friction can be recorded during UFM operation. This can be done in the same way as traditional friction force microscopy, where the average lateral trace and retrace values are taken at each pixel. However, the modulation of the lateral force signal due to the ultrasound being turned on and off leads naturally to an alternative approach; using a lock-in amplifier to measure the oscillation in the lateral force signal, which is proportional to the friction force. This lateral amplitude value has a significant advantage in that, unlike conventional friction force microscopy, it is independent of the topography as the topographical influence on the lateral signal is a DC offset.

Figure 4.18 demonstrates the differences in quantitative measurements of friction caused by applying UFM, showing the dependence of the measured friction in relation to the load force. The first observation is that the difference between the lateral trace and retrace values during modulated UFM operation depends linearly on the load and therefore still obeys Amontons's law, as in conventional friction force microscopy [82]. The lateral amplitude signal has a slight deviation from linearity, though this could be due to noise or crosstalk from the deflection channel having a noticeable effect at low load forces. The dimensionless gradients for the linear fits are 0.221 ± 0.002 for the result without ultrasound, 0.064 ± 0.002 for the trace minus retrace result with ultrasound, and 0.100 ± 0.004 for the amplitude measurement. The difference between the amplitude and trace minus retrace gradients for the results with ultrasound enabled can be attributed to the behaviour of the lock in amplifier. The non-ultrasound trace minus retrace result has a gradient 3.45 times greater than that of the result with ultrasound on. A factor of at least 2 is expected due to

the averaging between the superlubricity section and the friction section, with lower scanning speeds causing this factor to increase because the average value will decrease as the waveform becomes less square (e.g. going from the fast to the slow traces of figure 4.16(c)). These factors would need calibrating for true quantitative friction results during UFM, though this demonstrates that quantitative results are possible. The intercept of the linear fits for both the amplitude and the lateral trace minus retrace with UFM on are close to zero, however, for the case without ultrasound applied the intercept on the friction axis is 44 ± 1 nN, implying that the adhesion in the ultrasound case is minimal, as this is what causes the zero load friction. Typically adhesion in AFM is dominated by the effects of a water meniscus forming around the tip-sample contact. This meniscus may be dispersed by the ultrasonic operations and would therefore need to reform during the no ultrasound period. However, the formation time of the water meniscus in AFM has been shown to be on the order of milliseconds [266], which is longer than the typical modulation period, resulting in there potentially being no meniscus present during UFM operation.

Figure 4.19 shows an example of simultaneously measured topography, UFM and friction force maps. The sample is graphene grown on copper foil by chemical vapour deposition (CVD) [173]; the growth was halted before a complete monolayer of graphene was formed, such that the surface is partially covered in single atom thick graphene islands a few micrometres in diameter. The graphene islands are not directly visible in the topography image, figure 4.19(a), which is dominated by the fact that the copper surface is rough with large undulations from the cold rolling process used to make the foil [209,210]. In the UFM response, figure 4.19(b), contrast due to the graphene islands can be seen. The graphene is darker in contrast than the surrounding bare copper surface, indicating a lower UFM response and hence softer surface. Force curves showed that the adhesion was unchanged across the sample, and previous work has shown that if graphene is fully delaminated from a surface the ultrasound signal completely disappears [267]. This is consistent with graphite’s out-of-plane Young’s modulus (~ 40 GPa [268]) being lower than copper’s (130 GPa [152]), though could also be due to a comparatively soft interface between the graphene and copper, consistent with the graphene being decoupled from the copper (but not delaminated) and only weakly physisorbed to it [209]. The lateral force, figure 4.19(c), also clearly resolves the graphene islands due to their low friction [269] (note that due to the scan direction, the colour scale is inverted and lighter contrast corresponds to higher friction). All of the images in figure 4.19 were taken simultaneously in a single pass and in one scan direction; as expected, the lateral force image, figure 4.19(c), shows large cross-talk with the topography. The

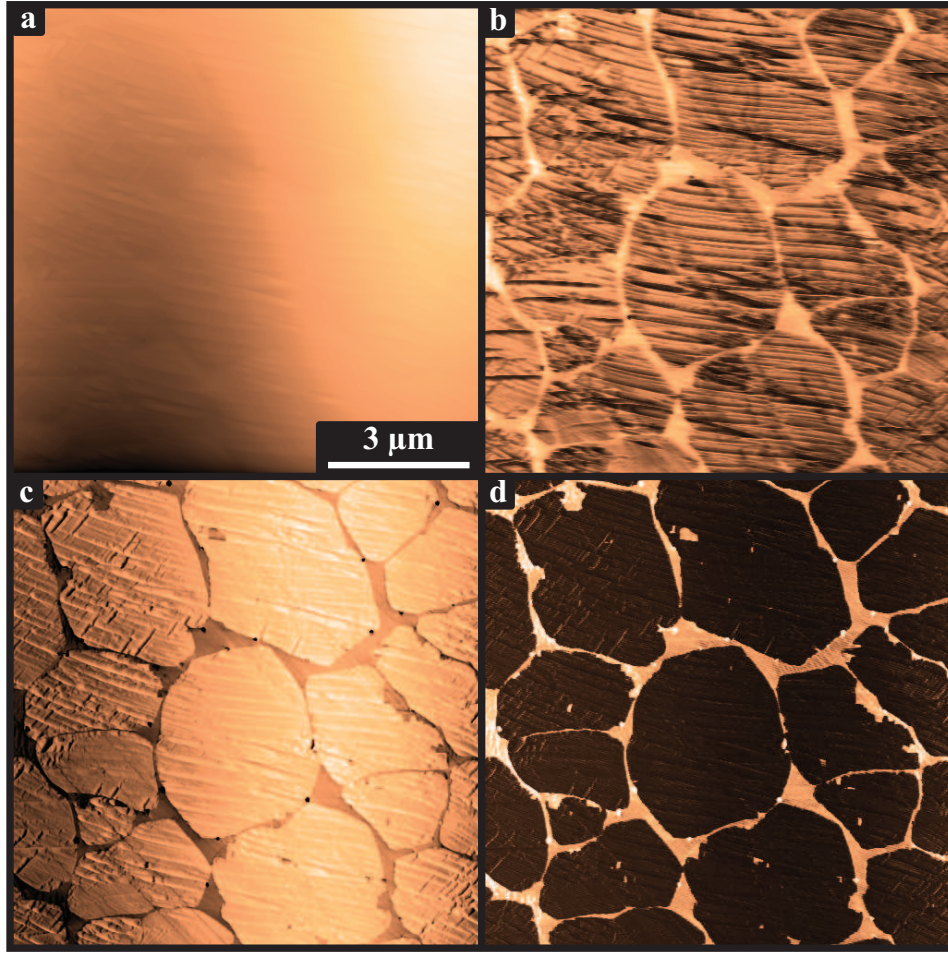


Figure 4.19: Simultaneously captured images of copper foil with graphene islands. The channels shown and their corresponding full data scales are a) height, 600 nm, b) UFM response, 10 nm, c) lateral force (cantilever torsion), 400 nN, and d) lateral amplitude (amplitude of the lateral signal at the modulation frequency), 50 nN. All are taken in the retrace direction.

lateral amplitude, figure 4.19(d), shows similar clear frictional contrast (here darker contrast is lower friction), but with no topographical cross-talk. This demonstrates that the lateral amplitude signal can be used directly as a measure of the local friction on the surface, without the need to subtract the trace from the retrace signals. Some horizontal lines are also visible, particularly in the UFM channel. From the height image it can be seen these are striations, which are due to the copper's original surface. These likely manifest in the UFM image due to changes in contact shape and area between the tip and sample due to the local topography, while appearing in the lateral image due to the local gradients. As before with the

cold rolling undulations, the effects of the local gradient due to the striations are largely removed in the lateral amplitude image.

The ability to directly measure multiple material properties simultaneously in one pass is extremely useful, as this allows exact spatial correlation and minimises the effect of changing tip geometry. It is particularly advantageous for AFM scanners not operated under closed loop conditions or for samples with large drift (i.e. when it is not possible to accurately compare points from the two scan directions). This is often apparent when subtracting trace and retrace lateral force images to form a friction image, where a small misalignment in points between the scan directions results in blurring and a loss of resolution. Therefore, the ability to capture frictional images in a single scan direction without topographical cross talk can allow for easier frictional imaging on open loop systems. Furthermore, with some consideration of additional factors, the friction values obtained during UFM should be usable in a quantitative manner.

4.4.3.2 Combined conductive and UFM measurements

Another contact mode technique that can be combined with UFM is conductive AFM (cAFM), where a conductive tip is used to form a circuit with a sample over which a bias is applied and a current is measured. Figure 4.20(d) shows the measured current between tip and surface as the ultrasonic excitation is modulated. The current flows during the period in which ultrasound is off and hence the tip is in contact with the surface. No current is measured when the ultrasound is on, with the onset of zero current correlating to the onset of superlubricity, when the tip is periodically retracted from the surface, though some noise-like signals are seen which may indicate the unreliable presence of current. It is unclear why the observed current falls to zero, as the tip does periodically contact the sample whilst the ultrasound is applied; speculatively, this could be due to the virtual earth amplifier used to measure the current, or possibly due to a temporal component in the formation of electrical contact between the tip and sample that is longer than the period of contact. However, the measured presence of current during the contact period indicates that conductivity mapping can be performed simultaneously to UFM, with the additional advantage of superlubricity to reduce tip and sample damage. This is of particular importance for cAFM, as the integrity of the metal coating on the tips is critical for current flow between tip and sample.

Figure 4.21 shows combined UFM and cAFM of a SWNT network on an insulating silicon oxide substrate. The SWNTs were grown directly onto the substrate by catalysed chemical vapour deposition (cCVD) [256]. Such networks are of interest

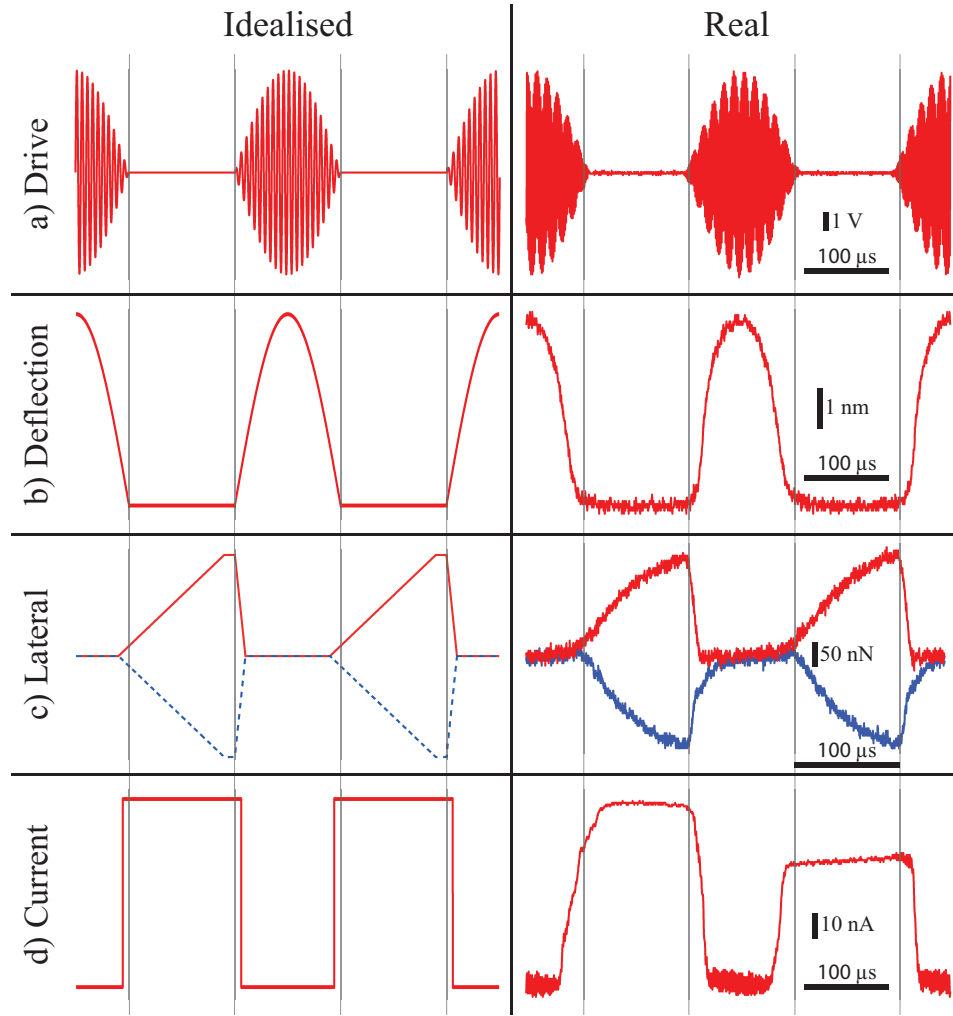


Figure 4.20: Expanded version of figures 4.8 and 4.16 showing idealised and captured oscilloscope traces of signals generated during UFM operation, with added current signals. All the traces are lined up such that their modulation phase matches. Lettering corresponds to the outputs labelled in figure 4.7.

for applications such as flexible electronics [270], for example transparent conductors and sensors [271]. The cCVD growth process results in random growth of metallic and semiconducting SWNTs; for sensor applications the current flow should be dominated by the semiconducting SWNT (whose conductance is highly dependent on the environment), whilst for transparent conductors the more highly conductive metallic SWNTs should dominate. For both applications, understanding conduction through the contacts between nanotubes is imperative, as these usually dictate the electrical response. The high spatial resolution of cAFM is thus, in principle, ideal for studying such networks. Although there have been some prior reports, e.g. [272], cAFM

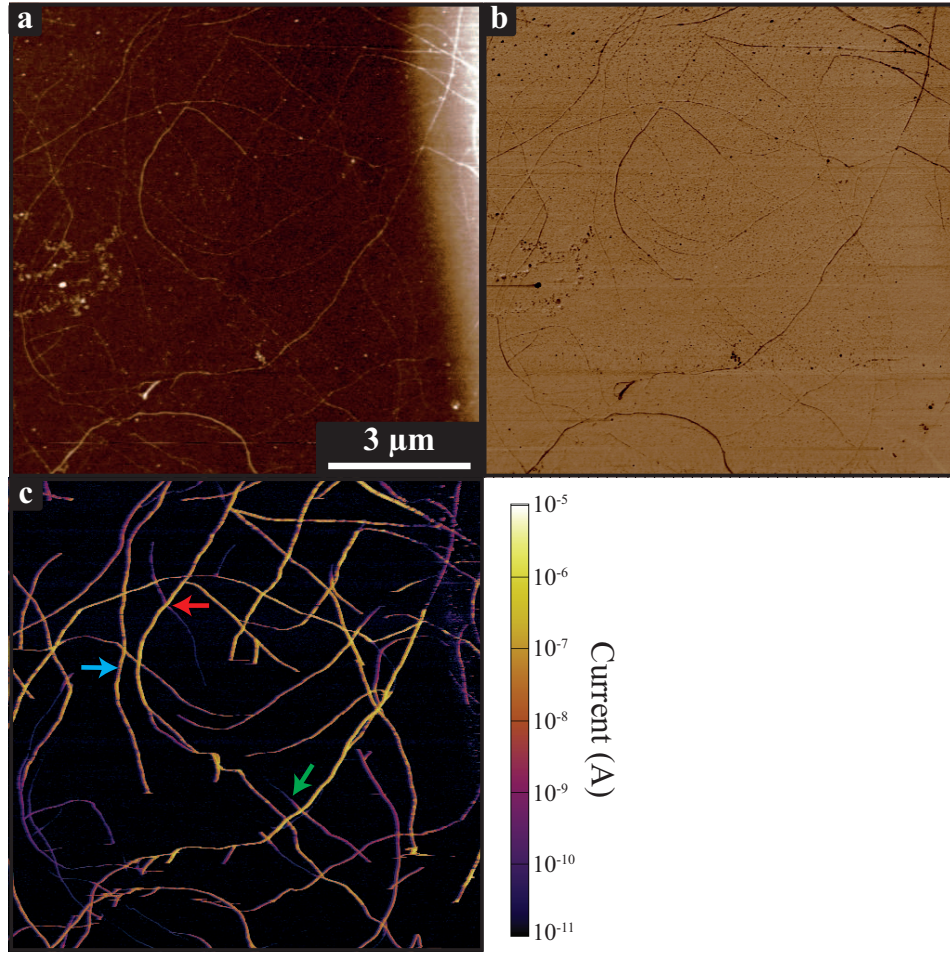


Figure 4.21: Simultaneously captured images of carbon nanotubes on a silicon substrate. The nanotube network is connected to a gold pad to the right of the image, which is held at a 2 V bias. The channels shown and their corresponding full data scales are a) height, 6 nm, b) UFM response, 1 nm, and c) logarithmic current, scale given on the image. The arrows indicate different types of nanotubes with line profiles shown in 4.23.

analysis of the networks is usually complicated by the fact that the nanotubes are easily damaged by contact mode AFM scanning and hence alternatives to conventional contact mode cAFM have to be used [273]. However, due to the superlubricity induced by UFM, it is straightforward to map the conductivity of the SWNT network with minimal damage by combined UFM and cAFM, and this is performed here. Measurements were repeated many times without any major damage to the SWNTs, unlike when scanning in conventional contact mode. Figure 4.22 demonstrates the difference in effect of scanning a nanotube network in UFM mode and

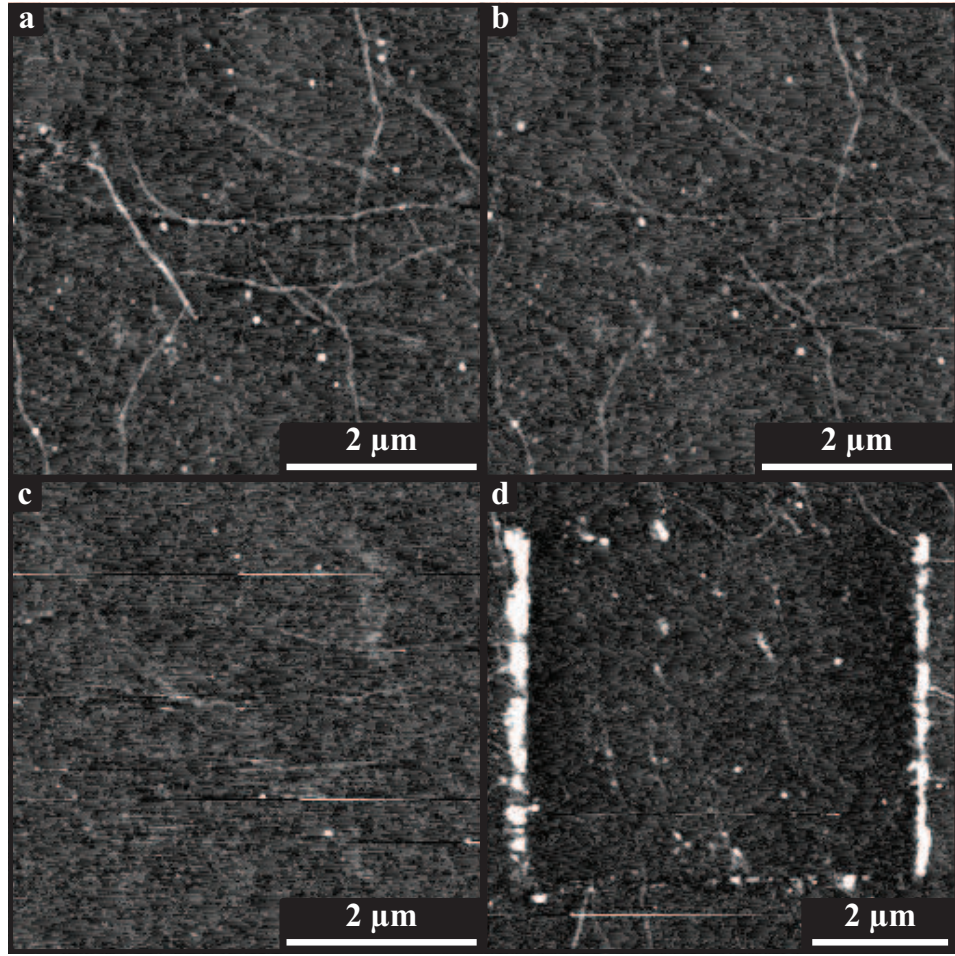


Figure 4.22: Sequential topographical images of nanotubes on silicon oxide. a) First 5 μm scan in UFM mode, b) fourth 5 μm scan in UFM mode, c) first 5 μm scan in contact mode, taken immediately after (b), and d) 7 μm UFM mode scan taken after two 5 μm contact mode scans.

conventional contact mode. Parts (a) and (b) show the minimal damage caused by repeated UFM mode scans — the only significant change is the loss of a nanotube left of the centre of the image, which was likely very loosely adhered to the surface (supported by its higher profile compared to the rest of the network). Part (c) shows the significant damage caused by a single contact mode scan. When scanned in contact mode the nanotubes are pushed to the side by the AFM tip, as seen in figure 4.22(d) by the raised ridges at the edge of the central 5 μm area that was previously scanned.

The topography image for the conductive scan, figure 4.21(a), shows the intersecting network of SWNTs, each typically 1–2 nm in height. The raised region

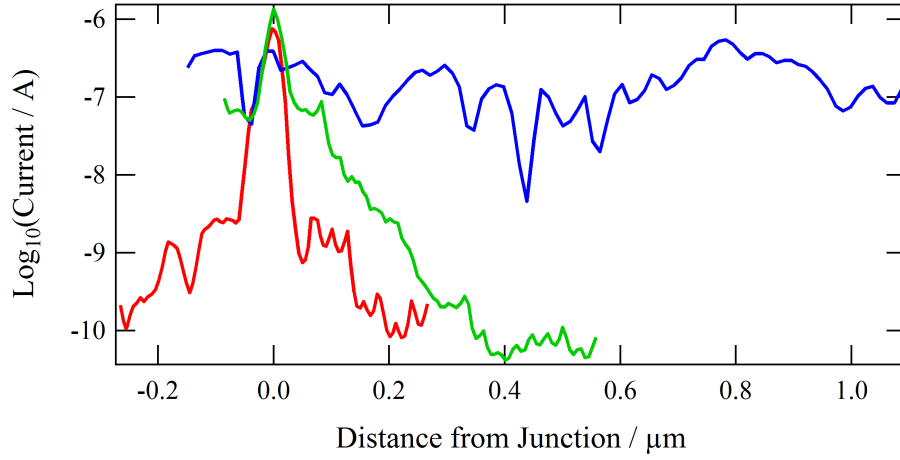


Figure 4.23: Sections along the nanotubes highlighted in figure 4(c) of the main text, averaged over a 2 pixel width. The red curve is for a high contact resistance between nanotubes, the blue curve is a metallic nanotube with low contact resistance, and the green curve is a semiconducting nanotube.

in the top right of the image is a residue of the lithographic process used to deposit the gold, which also reduces the conductivity. In the UFM response, figure 4.21(b), the SWNTs appear to be softer (darker contrast) than the silicon oxide substrate; this could be due to the modified contact shape of the tip on the nanotube or due to the lower radial stiffness of the nanotubes. However, the conductivity map, figure 4.21(c), clearly reveals the conductive pathways through the SWNT network. Note that the colour scale is logarithmic with respect to current, such that the measured currents vary over more than five orders of magnitude.

From figure 4.21(c) it is possible to identify the metallic and semiconducting nanotubes and the differences in contact resistances between them. Figure 4.23 shows the current along different types of nanotubes present in the nanotube network, and across the contacts they form. Each curve corresponds to the nanotube indicated by the arrows in figure 4.21(c); the blue curve is nearly flat, indicating that it is limited by resistances in the network closer to the electrode, and similar to the neighbouring SWNTs, suggesting a low resistance at the junction and the nanotube being metallic in nature. The red curve clearly shows an immediate drop in current by over three orders of magnitude within 50 nm of the junction, indicating a high resistance in the contact between the two nanotubes. The green curve shows a steep linear decrease with distance on this log scale, indicating an exponential decay in current, which is consistent with semiconducting nanotubes. Due to the multiple connections to each nanotube in this network, it is not easy here to quantitatively extract contact

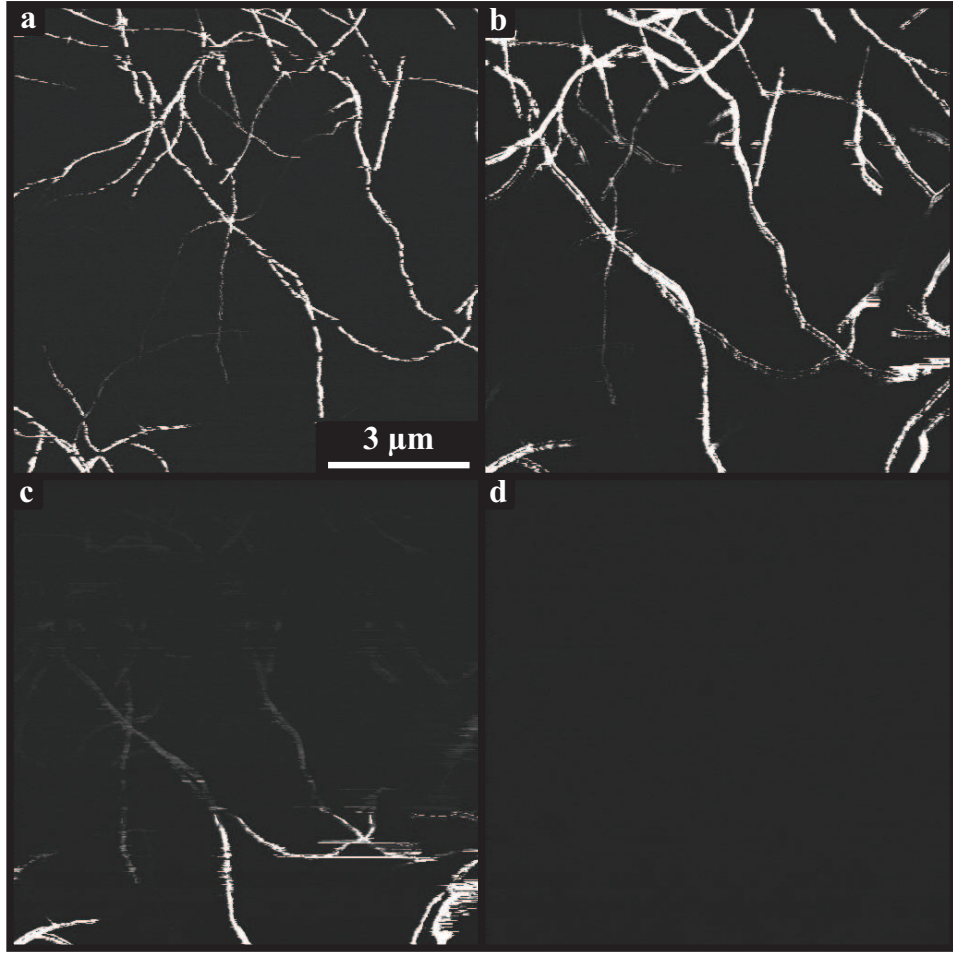


Figure 4.24: Four conductive scans of nanotubes on silicon oxide, connected to a gold contact held at a 0.5 V bias, all with a scale of 500 pA (white areas are saturated). a) First scan in UFM mode, b) fifth scan in UFM mode, c) first contact mode scan, immediately following (b), and d) second contact mode scan.

resistances and the resistivity of individual SWNTs. However, this would be possible on lower density networks.

Figure 4.24 further demonstrates the difference between scanning nanotubes in UFM mode and contact mode. It can be seen that repeated UFM scans provide reliable measurements of the current, presenting little damage to either the sample or the conductivity of the tip, though in this case the tip picked up some debris from the sample leading to the double tip artefact seen in figure 4.24(b). Once switched to contact mode (i.e. turning off the ultrasound), the conductive imaging failed within half a scan frame, as seen in figure 4.24(c), and did not recover. The

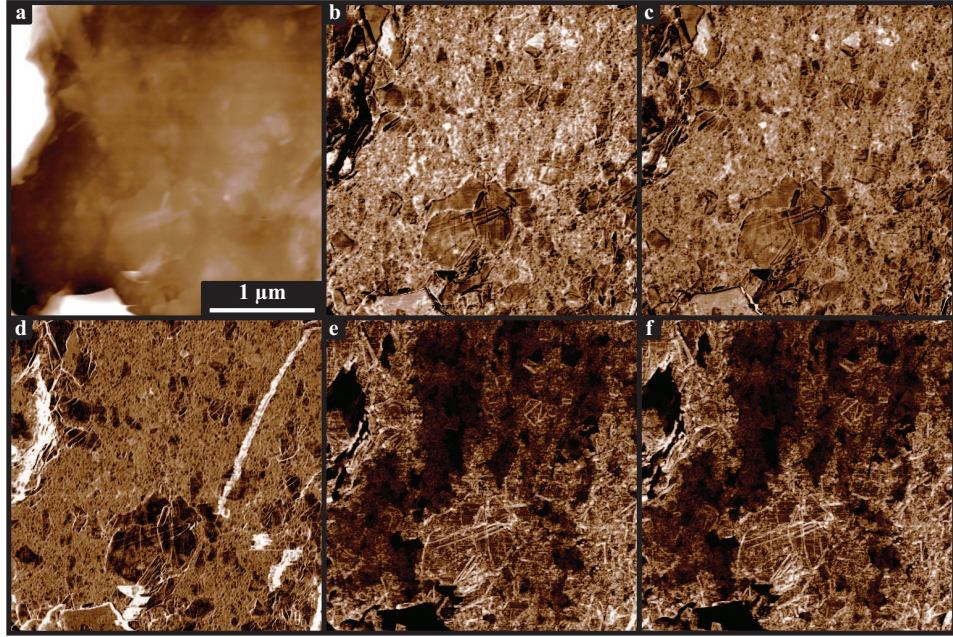


Figure 4.25: Simultaneously captured images of a graphene nanoplatelet epoxy composite. The top of the sample is connected to a wire which is held at a 0.5 V bias. The channels shown and their corresponding full data scales are a) height trace, 150 nm, b,c) UFM response trace and retrace respectively, 0.5 nm with a minimum value of 0.5 nm, d) lateral trace minus retrace, 4 mV, and e,f) current trace and retrace respectively, 2 μ A.

conductivity measurements were remarkably consistent, both across a single image and after multiple scans, which is surprising considering that metal coatings of tips, such as the Pt coating used here, are prone to wear [79]. This indicates that UFM not only reduces damage to the sample but also reduces damage to the tip.

4.4.3.3 Combining multiple techniques

The half and half approach enables multiple contact mode techniques to be acquired simultaneously with UFM. Figure 4.25 shows combined UFM, friction, and cAFM measurements on a graphene nanoplatelet epoxy composite. The composite is made from multi-layer graphene nanoplatelets with flakes of nominal average diameter 25 μ m and thickness 6 nm, randomly dispersed at comparatively high loading fraction (8% by weight) in an epoxy matrix (see section 4.3.2 for more details). The sample was cut for UFM analysis to study the dispersion and connectivity of the graphene nanoplatelets within the matrix. The height image, figure 4.25(a), shows features that look like they could be due to graphene nanoplatelets but as the sample is

comparatively rough it is difficult to identify them with any confidence. The UFM response, figures 4.25(b) and (c), shows much more detail with clear variations in the sample stiffness. Both the trace and retrace images are shown, figures 4.25(b) and (c) respectively, demonstrating the exact reproducibility of the result. The friction image, formed from subtracting the lateral deflection signal in the trace and retrace directions and shown in figure 4.25(d), gives interesting complementary information to the UFM image. There is a strong correlation between the regions of lower friction and the regions of lower UFM amplitude, and thus these are identified as regions where graphene is present at the surface, an assignment reinforced by the topography image. Note that this is highlighting graphene nanoplatelets directly at the surface and it is likely that they also extend below the surface, however, it does seem to indicate that there has been some fragmentation of the xGnP graphene nanoplatelets during shear mixing or from the when the sample was cut, as evidenced by the much smaller than expected sizes of the nanoplatelets.

It is interesting that the graphene nanoplatelets show a lower UFM response, implying that they are softer than the surrounding epoxy matrix. This was consistent across many measurements with several different tips (see figure 4.26 for a further example). The c-axis, i.e. out-of-plane, Young's modulus of graphite (~ 40 GPa [268]) is higher than epoxy (typically < 5 GPa [274]), so in this instance we would naïvely expect the graphene to show greater UFM amplitude, i.e. lighter contrast. As with the graphene on copper sample, delamination of the graphene nanoplatelets is not seen as the UFM signal does not fall to zero. The lower UFM response could be due to poor acoustic coupling between the nanoplatelets at the surface and the epoxy which would reduce the surface ultrasonic amplitude. Alternatively it could be due to a weak interface between the graphene and epoxy, softer than the interplanar interface of graphite and also softer than bulk epoxy, resulting in reduced out-of-plane stiffness.

Further information can be seen in the current images, figures 4.25(e) and (f). Again both the trace and retrace image are shown, demonstrating the reproducibility of the result. The sample could be scanned for several hours under these conditions without degradation of the sample or tip and maintaining reproducibility of the current image. The correlation between features in the current image and the other image channels is again strong, but it also reveals new information. As expected, there is higher current around the exposed graphene nanoplatelets seen in figures 4.25(e) and (f). Additionally, further structure can be seen in these current images, with larger positional scale variations visible in the current image, which is likely due to the local network structure of the graphene nanoplatelets resulting in

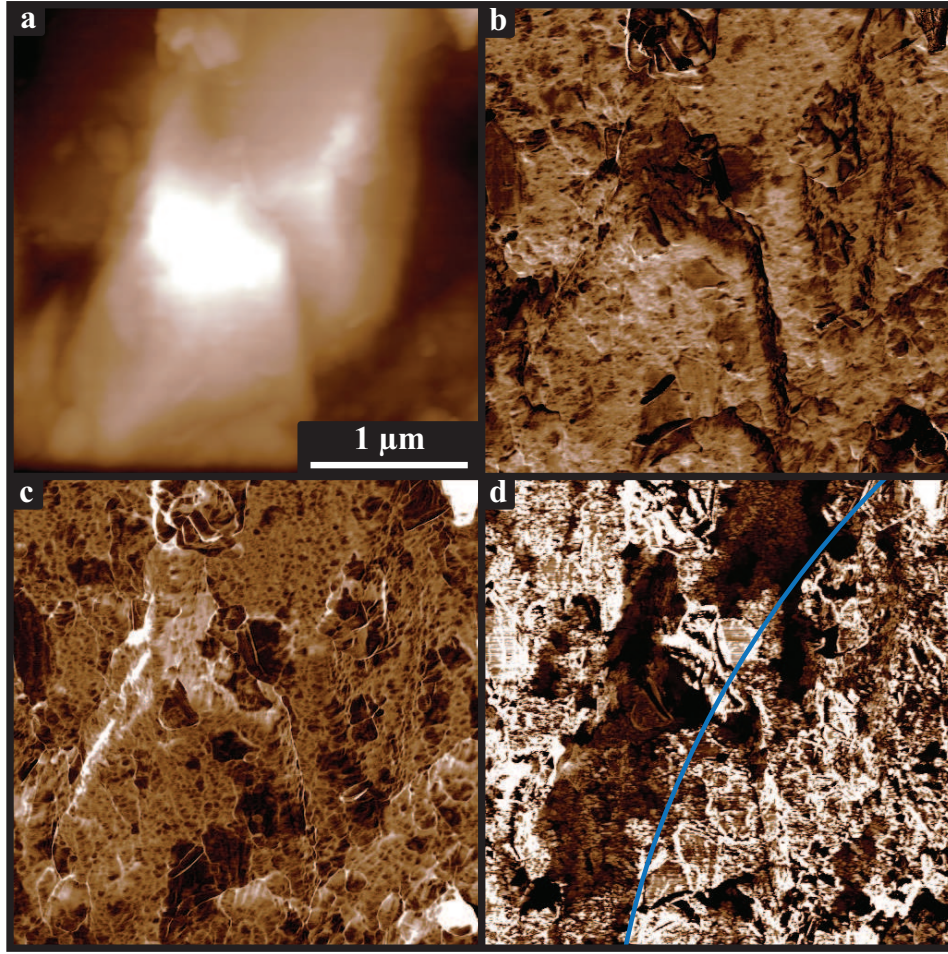


Figure 4.26: Simultaneously captured images of a graphene nanoplatelet epoxy composite. The top of the sample is connected to a wire which is held at a 0.5 V bias. The channels shown and their corresponding data scales are a) height, 300 nm, b) UFM response, 1.5 nm, c) lateral trace minus retrace, 8 mV, and d) current, 600 nA. The blue line on part (d) is the possible edge of a subsurface flake, seen as the region of surface flakes with high conductivity.

some surface sheets having poorer conductive pathways to the bulk. This is further supported by additional imaging in other areas of the sample, such as in figure 4.26, where the regions of high conductivity are consistent with a significantly larger flake below the surface forming these conductive pathways, as seen in figure 4.26(d). These larger flakes are expected to exist as the sample was made with an average flake size of $25\ \mu\text{m}$. The edges of many of the platelets appear to have enhanced current flow, though this is correlated to changes in topography, making it likely that these features are due to a tip effect. The loading fraction of graphene here is high, substantially

greater than the percolation threshold [275], which is consistent with the high level of conductivity seen across the image. Combined, these multiple channels give rich information on the dispersion and percolation of the graphene nanoplatelet epoxy composite, showing both the flakes visible at the surface corroborated by multiple data channels and the larger subsurface flakes implied by the current channel.

4.5 Conclusions

The effects of the control parameters, such as the driving and modulation frequencies, on UFM response were investigated. Here, the transition between traditional AFM and UFM regimes was shown by sweeping the driving frequency. A transitional region, in which the tip stopped following the surface, was found between 0.5 MHz and 2.0 MHz for the cantilever used (nominal free resonance of 75 kHz), indicating the minimum required driving frequency for UFM operation. This suggests that using cantilevers with low or moderate (<100 kHz) resonant frequencies is ideal, though it is more important to use a driving frequency that is significantly above this resonance to ensure true UFM operation (here the transitional region ended at about 25 times the free air resonance). An oscilloscope was used to check that the behaviour matched the expected UFM behaviour, though it can be assumed that UFM behaviour is followed provided the driving frequency is significantly higher than the cantilever resonance. The modulation frequency was also tested, finding that it has minimal effect on the response provided that the frequency used is above the filter frequency for the topography feedback loop. A simulation of UFM response was created, which was compared to experimental results where the drive amplitude and load force were varied, showing similar behaviour, though with differences in the magnitude of the features and unexpected behaviour in the experimental results at extreme loads.

One of the primary deficiencies with UFM is the lack of quantifiable results in terms of common physical parameters, such as the Young's modulus. This is primarily due to the complicated relationship between the sample mechanical properties and the UFM response with further difficulties arising due to secondary parameters, such as tip radius, adhesion, and drive amplitude. Assuming that the secondary parameters are constant and known, a simulation based response to quantify the sample properties from the UFM response amplitude would seem to be possible. However, the results from section 4.4.1 indicate that the simulation, based on traditional models of tip-surface interaction and an assumption of no cantilever motion during a single ultrasonic oscillation, does not accurately depict the behaviour of the

UFM system and thus cannot be used to accurately determine the expected response due to sample properties, and therefore cannot be used for accurate quantification. Further investigation into the behaviour of this system at the high frequencies used may allow improvements to the assumptions made in the simulations, potentially resulting in more reliable comparisons between them and real results.

Another possible approach to quantification would be the use of calibration samples, with multiple regions of known physical properties to give reference points for sample parameters resulting in certain response amplitudes, allowing estimations based on the expected monotonic relationship between sample Young's modulus and UFM response amplitude. The accuracy of such a calibration technique would be limited by the non-linear relationship between the elastic properties and the response amplitude and care would have to be taken over the secondary factors, particularly the set point force and the oscillation amplitude. While the set point force is simple to control to a set value, maintaining oscillation amplitudes between the calibration sample and the sample being investigated would be difficult. This is because they may have different levels of ultrasonic coupling with the transducer and different ultrasonic transmittance through the sample. Thus additional calibration of the surface amplitude would be required, either by use of an interferometer to directly measure the surface oscillation amplitude or by ensuring there is a region on the investigated sample of known parameters that can be used as a reference point.

UFM is particularly useful for investigating hard samples, such as semiconductors, though care has to be taken with samples where the tip material properties are comparable to those of the sample as this can cause a reduction in contrast between areas of different Young's modulus, as seen in section 4.4.2. This can result in samples where there are significant material property variations displaying insignificant levels of contrast between regions, or even inverted contrast due to secondary contributing factors to the UFM response. The contrast was shown to improve by using a tip made of or coated with a material with a much higher Young's modulus than is expected for the sample materials.

The nature of UFM as a primarily contact mode technique can be used to perform other traditional contact mode techniques simultaneously, as shown in section 4.4.3. This allows single pass acquisition of sample elastic properties and other property channels, such as friction and electrical current, enabling easy correlation between these channels. Other AFM elastic property measurement techniques typically rely on intermittent contact and thus cannot be easily combined with such contact mode techniques in a single pass, thus presenting a significant benefit to UFM. This is especially true for friction force microscopy as it requires sustained

contact with the sample surface during scanning to enable torsional bending of the cantilever. One area where this is useful is the ongoing development of multifunctional nanostructured materials, where multiple material properties are enhanced through control of material at the nanometre scale. For example, fillers such as graphene or nanotubes can be added to composites to enhance mechanical properties and at the same time increase thermal and electrical conductivity [276,277], so being able to measure these properties simultaneously could help improve the speed of measurement, and therefore development, and understanding of how the properties are linked. Similarly, in phase-change materials, changes in functional properties such as conductivity are induced by changes in structural, and hence mechanical, properties [278], meaning simultaneous measurements of these properties could help the understanding and development of these materials.

Additionally, the ability to combine UFM with these contact mode techniques allows them to be performed with the benefit of the superlubricity phenomenon seen in UFM operation. This phenomenon means that no long term lateral forces are applied to the sample, enabling imaging of delicate samples. This was demonstrated with the conductive imaging of nanotubes (section 4.4.3.2), where the image was acquired with minimal damage to the delicate nanotubes. Capturing this image only required a simple set up and little additional tuning of scanning parameters, such as set point force, showing that UFM is a simple to perform and reliable technique.

Chapter 5

Ultrasonic Non Destructive Testing in an AFM

5.1 Introduction

Non destructive testing (NDT) covers a range of techniques used to examine the structural integrity of materials without affecting their physical condition [279–281]. It can be used both to ensure the quality of products during manufacturing and to monitor the condition of components throughout their life cycle, especially those with high uptime and that operate under high stresses, such as power plants [282], pipelines [283], rail tracks [284], and jet engines [285]. This allows maintenance to be carried out or replacements provided only when necessary, reducing down time and operating costs while still ensuring safe operation. Many NDT techniques can be carried out in-situ, further reducing the need for down time and potentially allowing for continual automated monitoring of the system [286]. One type of NDT uses ultrasonic waves to probe a material, and is investigated here with the use of an AFM based pickup sensor, potentially allowing for high spatial resolution testing.

5.1.1 NDT Techniques

The simplest and oldest form of NDT is visual inspection — examining a material either by eye or with the use of remote viewing tools, such as endoscopes and cameras, to look for the visual signs of damage, including corrosion, cracking, or stress [279, 281, 287]. This can be improved through use of magnifying optics or by using dye penetrant testing in which a dye accumulates in cracks and highlights them in one of many ways, such as having a high visual (colour) contrast or being reactive to UV light [288]. Such techniques can be quick to perform and can easily cover large areas,

but require direct access to the component of interest, are only sensitive to surface defects, do not provide much information about the extent or severity of the defects, and are prone to human error [289]. As such, visual inspection is typically used as a basic inspection or as a precursor to more rigorous techniques [290]. Typically visual inspection can detect defects that are millimetres in size, with higher resolution possible using magnifying optics, at the cost of speed of inspection or the size of the area covered.

Internal inspection of a material can be achieved through the use of penetrative radiation, such as electromagnetic waves (e.g. x-rays [291,292] and gamma rays [293]) or neutrons [294]. The radiation is directed at the component of interest and detected on the far side, with the material causing attenuation and scattering of the radiation. Cracks and inclusions within the material will change the interactions and thus result in a difference in the detected signal. Some radiographic techniques use information from Compton scattering, which allows for the detector to be placed on the same side of the sample as the source for detecting backscattered radiation, meaning that it can work even in situations with limited access to the sample [292,295]. Contrast for surface features can be increased by using a contrast agent — a substance that strongly interacts with the radiation being used and thus has a high visibility in scans and images — in the same way that dyes can be used to improve visual inspection [296]. It is also possible to build a 3D image of the internal sample structure by combining images from multiple angles, a technique known as computed tomography [297–299]. These techniques, however, have a high cost associated with the sources and detectors, and can pose a risk to anyone in the vicinity of testing due to radiation exposure. Additionally, in-situ testing is often impractical due to the required source and detector positioning. Radiation testing can be done with high resolution, capable of detecting defects sizes on the order of micrometres.

Electrical methods can also be used to find defects within electrically conductive samples by measuring an induced current flow. Cracks will cause increased path lengths for the current within a sample and thus increase the effective resistance of the sample. These measurements can be performed directly, requiring contact with the sample and prior calibration of the expected measurement [300,301], or indirectly through the use of induced currents, known as eddy current testing [301,302]. In eddy current testing an alternating current is passed through a coil, creating a magnetic field that induces eddy currents with a conductive sample, which then create their own magnetic field, which can be measured using a magnetic field sensor (such as a Hall effect [303] probe or a giant magnetoresistance [304,305] sensor) or

by measuring current generated within the original coil. This resultant current will have its amplitude and phase affected by defects in the material. Alternating currents have the property that they are limited to a region close to the surface of a conductor, known as the skin depth. This skin depth is dependent on the frequency of the current, and thus electrical techniques are surface sensitive with a variable depth of sensitivity, allowing for information about the depth of defects to be gathered [306,307]. Electrical techniques are capable of detecting defects with sizes of the order of hundreds of micrometres.

The above techniques represent a subset of the available NDT techniques, while many others, including the examination of magnetic fields around magnetic samples [308] and imaging the thermal distribution across a heated sample and looking for abnormal gradients or features [309], also exist. Here, the use of ultrasonic waves in NDT is of interest.

5.1.2 Ultrasonic NDT

Ultrasonic NDT is a widely used technique that utilises high frequency (typically >20 kHz) sound waves to inspect samples [96,310]. As an ultrasonic wave propagates through a sample it will interact with features within the sample, such as cracks, defects, and material boundaries, causing reflections, diffraction, reduction in transmission, and conversion of the mode content of the wave package [85,92,311]. By investigating the temporally resolved amplitude and frequency content of a generated wave package, information about these cracks, such as their size and location, can be inferred. Typically, this is accomplished through the use of one or more ultrasound transducers (generators and sensors coupled to the sample) [312], with common examples being piezoelectric transducers, electromagnetic acoustic transducers (EMATs) [119] and lasers (high power pulsed lasers for generation and laser interferometers for sensing) [132], which are discussed in detail in section 1.2.3.

The simplest form of ultrasonic NDT is a single transducer used as both a generator and a detector in a pulse-echo configuration, illustrated in figure 5.1. A short pulse of ultrasound — typically narrowband (small range of frequencies generated) to prevent dispersion — is generated and then propagates through the sample. When the wave reaches a feature, such as the opposite face of the sample, it will be reflected back towards the transducer and detected as a pulse. The time between the generated pulse and the detected pulse, t , can be measured, which can be combined with the known wave velocity, v_p , to give the distance the wave has travelled, $d = v_p t$ (which is twice the distance to the feature) [96]. This is often used for thickness gauging, as a control for manufactured sheets or to monitor losses in

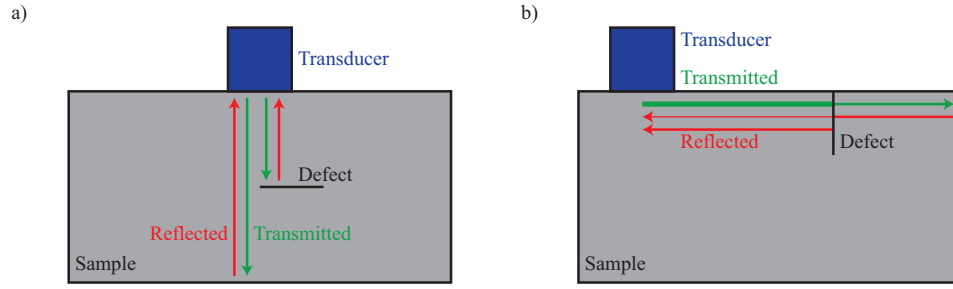


Figure 5.1: Example wave paths for a single transducer pulse-echo ultrasonic NDT configuration for a) bulk waves and b) (guided) surface waves. For surface waves, the amount of wave reflected and transmitted by a defect depends on the defect depth and the wavelength.

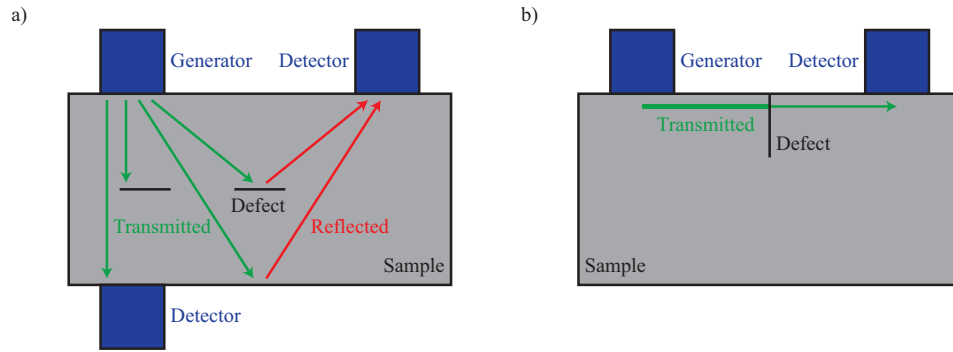


Figure 5.2: Example wave paths for a dual transducer pitch-catch ultrasonic NDT configuration for a) bulk waves and b) (guided) surface waves.

wall thickness due to e.g. corrosion. Alternatively, if the distance is known this can be used to calculate the wave velocity.

If a defect is present within the path of the ultrasound propagation it will reflect the wave, giving another detected pulse with a time delay dependent on the distance to the crack. The reflected pulse from the sample edge will also be reduced in amplitude due to the crack. By moving the transducer and monitoring the amplitude of the reflections the spatial extent of the defect can be evaluated — the edge of a crack can be defined by the “6 db drop”, i.e. the point at which the reflected pulse has half the amplitude due to only being half within the wave beam [96]. This technique is limited as it can only detect features that are perpendicular to the wave propagation direction as other reflections will not return to the transducer, though the presence of a non perpendicular crack may be inferred from a drop in amplitude of an edge reflection if one is present.

A more flexible approach is to use two separate transducers, one for generation

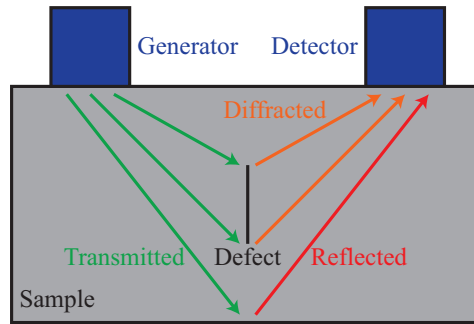


Figure 5.3: Example wave paths for a time of flight diffraction ultrasonic NDT experiments.

and the other for detection, in a pitch-catch configuration, illustrated in figure 5.2. A pulse is emitted by the generator and travels to the detector and if a defect exists between these two transducers the amplitude of the detected wave will be reduced as a result. Thus, by moving the pair of transducers around the sample, either held at a set separation or only moving one, and monitoring the detected signal defect can be located [96,310]. Additional effects may also be present, such as reflected signals off features not directly between the transducers and enhancement in amplitude when one of the transducers is close to a feature due to interference from the reflected waves [90,98,313].

The diffraction of waves by defects is also something that can be considered [314–316]. When an ultrasonic wave interacts with the edge of a feature it is diffracted in many directions, meaning that a crack that is not perpendicular to the wave propagation direction may still be detected, as illustrated in figure 5.3. The time delay of such a diffracted signal will be minimised when the crack is equidistant from both transducers, and the distance to the crack can be calculated from this time delay and the known wave velocity. As the crack edge causes this signal, additional diffraction signals from other edges of the crack can be used to infer the extent of the crack. This technique is known as time of flight diffraction.

Wave velocity measurements can also be used to examine various material properties. Lamb waves in plates, for example, have a velocity dependent on the frequency thickness product, meaning that a measured velocity for a set frequency can be used to determine the plate thickness [97,317]. This can be used in place of through wave pulse-echo measurements, which is especially useful for thinner plates where pulse-echo measurements are complicated by the short travel time. Velocity is related to the elastic properties of the sample, allowing measurements of the elastic moduli [318–320]. Wave velocity can also be used to provide information about

the composition [319], orientation of grains in anisotropic materials [321], or the stress and strain within the sample [322]. Mapping of the grain structure can be achieved through measuring the velocity across different paths through the sample in a tomography like technique [323], and by measuring local velocity across an entire sample. Local velocity measurements can be performed using spacing controlled laser generation and detection to determine the optimal wavelength (and thus velocity for a set frequency) [324–326].

Ongoing research in ultrasonics covers a wide range of areas. This includes the development of transducers that can operate in the harsh environments often present in industrial environments, such as high temperatures in power plants [327,328] and for use on constantly moving samples to inspect railway tracks [284]. Improvements to the accuracy and specificity of information about cracks is being made using transducer arrays, that allow for control over wave direction, and use of advanced analysis such as time-reversal and beamforming algorithms for high resolutions [100, 329–332].

Resolution of ultrasonic NDT is often limited by the physical transducer size or the wavelength of the ultrasonic waves, resulting in resolutions of the order of millimetres. Higher resolutions, down to the order of micrometres, can be achieved through the use of laser ultrasonics or transducer arrays. High resolutions are particularly useful for investigating micro-cracks, which are of interest as they can significantly affect material properties [333–336] and be a precursor to cracking on a larger scale [337–339]. Semiconductor devices are affected by defects within them, with micro-cracks being a significant problem for yield and performance [340,341]. Such micro-crack detection requires high spatial resolution and sensitivity and is typically carried out using laser ultrasonics [342] — transducer arrays could also be used to do this, though they are expensive and many samples in which micro-cracking is of interest are too small to be used with arrays. These requirements are also fulfilled by AFMs, which routinely achieve spatial resolutions of the order of nanometres and sensitivities of the order of tens of picometres. In this chapter the use of AFM as an ultrasonic detector for NDT experiments is investigated, demonstrating its suitability. This is achieved by detecting EMAT generated Lamb waves in macroscopic aluminium plate samples. The ability for an AFM to simultaneously and independently detect out-of-plane motion and one component of in-plane motion, which is useful for understanding the mode content of waves, is also demonstrated.

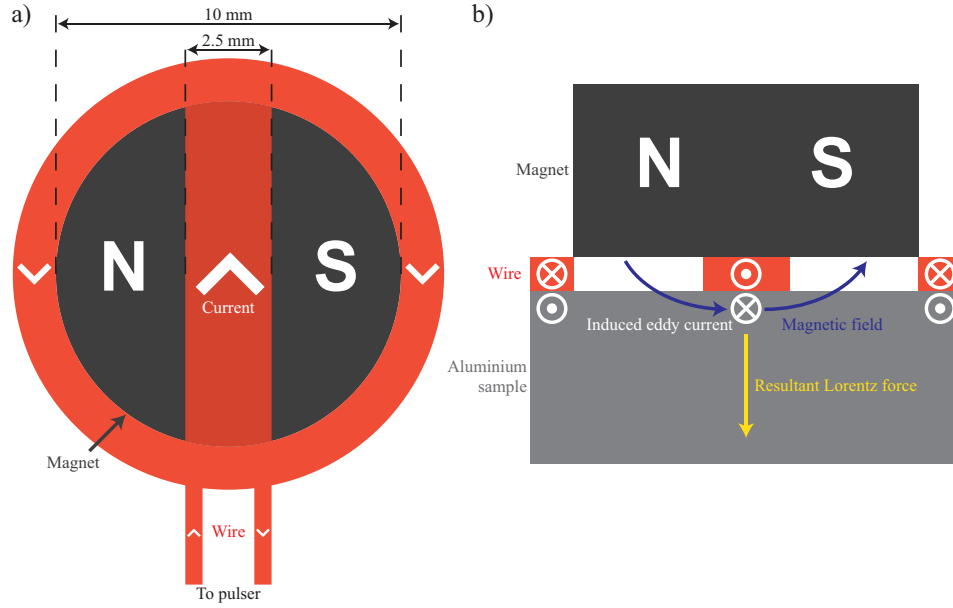


Figure 5.4: The design of the EMAT used to generate ultrasound. a) View from underneath, the wire path consists of 8 wires, with each of the outside return paths having 4 wires. b) Cross sectional view through the horizontal centreline of (a), showing the magnetic field, induced current and the resultant Lorentz force within the aluminium sample. The wire height and aluminium thickness is not to scale.

5.2 Experimental Methods

All experiments were performed on 0.5 mm thick plates of aluminium, with the exact configuration (size, features, and transducer locations) illustrated for each experiment in the results. Slots in the aluminium were cut using an Oxford Lasers E-355 laser cutter (diode pumped solid state Nd:YAG class 4 laser operating at 355 nm). Ultrasound was generated in the plate using an EMAT made with 0.28 mm diameter enamel coated copper wire supported by Kapton tape, held underneath a cylindrical neodymium-iron-boron magnet from Supermagnete (material N52, 10 mm diameter, 5 mm thickness, diametrically magnetised, with an epoxy resin coating). The design of the EMAT is shown in figure 5.4. The magnetic field and induced eddy current within the sample are both in-plane and perpendicular to each other, resulting in the force being out-of-plane (see section 1.2.3.2 for more details on EMAT theory). The EMAT was driven using an in-house built high voltage pulser box that has previously been used in other EMAT-based ultrasound experiments [343,344]. This pulser charges a 1 μF capacitor to 700 V and then discharges it through a thyristor, resulting in a large transient signal across the EMAT. A powerful broadband (ap-

proximately 50–500 kHz) ultrasound wave is generated by the EMAT at a repetition (pulse) rate of a few Hertz. The generated ultrasound will be primarily Lamb waves, as discussed in section 1.2.1.1, in the thin aluminium plates used, with the first antisymmetric (A0) mode being preferentially generated due to its predominantly out-of-plane motion, corresponding to the main forces. The symmetry of the line source style EMAT means that generated waves will be strongest with a propagation direction perpendicular to the wire direction and weakest parallel to the wire direction. Some in-plane motion will also be generated (as will the first symmetric (S0) mode), with particle motion parallel to the propagation direction. Some additional ultrasound may be generated by the return tracks of the wire, though these are likely to be significantly weaker than the main waves and difficult to distinguish due to the small physical spacing.

For AFM-based detection an Asylum Research MFP-3D-SA was used with a NanoWorld Arrow UHF tip (nominal normal spring constant of 6 Nm^{-1} and a nominal resonant frequency of 850 kHz). Some additional information was gathered using MikroMasch NSC18 tips (nominal normal spring constant of 2.8 Nm^{-1} and a nominal resonant frequency of 75 kHz). All experiments were performed in contact mode with a set point of 0.5 V, corresponding to a deflection of 10–20 nm. The signals (both the “AC deflection” — the deflection signal after a 1 kHz cut-off high pass filter — and the lateral deflection) were then passed to a Tektronix DPO 2012 oscilloscope along with the trigger signal from the pulser, recording the signal averaged over 8 pulses (to reduce the measured noise levels). The normal optical lever sensitivity was also calibrated (see section 2.2.2) and used to convert the AC deflection into absolute displacement, while the lateral signal was left in its raw form. To acquire results in many locations over a line or region, the long range (relative to the piezoelectric actuator driven sample stage) X and Y motion of the AFM was automated by replacing the in built micrometers with Physik Instrumente N-470 PiezoMike linear actuators. Position sensing was achieved using ams NSE-5310 magnetic linear position sensors, with a precision of $0.5 \text{ }\mu\text{m}$. Positioning was performed with a $5 \text{ }\mu\text{m}$ tolerance.

To compare the AFM based results with more traditional methods, piezoelectric transducers and an interferometer were used as alternative detectors. The two piezoelectric transducer used were a CTS VP-1.5 pinducer (10 MHz bandwidth and 1.5 mm crystal diameter) and a transducer with 5 MHz nominal frequency and 10 mm crystal diameter. The interferometer used was an Intelligent Optical Systems AIR-1550-TWM with 125 MHz bandwidth, measuring out-of-plane displacement. For the line measurements using the interferometer sample positioning was achieved

using a stepper motor based stage.

All the results were processed using Wavemetrics Igor Pro software. The individual results were first filtered using the in-built *FilterFIR* operation as a high pass filter with a filter frequency of 50 kHz, to remove low frequency signals that would dominate the resultant sonograms and obscure features of interest, and 5000 filter coefficients, which ensured quick processing time without sacrificing significant signal quality. For the sonograms (time windowed Fourier transforms giving a measure of the amplitude in time-frequency space — see section 1.2.2 for more information) the *SG_sonogram* function, included in the sonogram package that comes with Igor Pro, was used. The sonogram used Gabor windowing and a 25 kHz frequency resolution, chosen to give an appropriate balance between the time and frequency resolution of the produced sonograms.

5.3 Results and Discussion

Here, the applicability of using AFM as a detector of ultrasound for NDT has been tested. Firstly, out-of-plane detection is demonstrated through detection of EMAT generated pulses using the deflection channel of the AFM. This is then compared to similar measurements using piezoelectric transducers to demonstrate that the signals seen using the AFM are similar to those from other techniques and thus valid. The performance of AFM detection is also explored, comparing its sensitivity, bandwidth and resolution to detection with piezoelectric transducers, EMATs, and interferometers. Secondly, detection of in-plane motion using the lateral channel is tested, first by looking at the lateral signal for a single result and then examining the effect of changing the angle between the wave travel direction and cantilever orientation. Finally, the ability to find sample features, such as defects — in this case simulated by a narrow slot passing through the entire plate thickness — is tested by performing many readings in both a line and rastered square pattern, mapping changes in amplitude of prominent features seen in the sonograms.

5.3.1 Out-of-Plane Displacement

The motion of an ultrasound wave can be made of components both in and out-of-plane, with relative amplitudes depending on the wavemode content and frequency of the wave, as discussed in section 1.2.1.1. AFM lends itself naturally to the detection of the out-of-plane displacement of a sample surface — in contact mode the tip will directly follow any motion of a hard surface, provided that the oscillation frequency is not too high (as is the case in UFM, chapter 4). This motion will be detected as

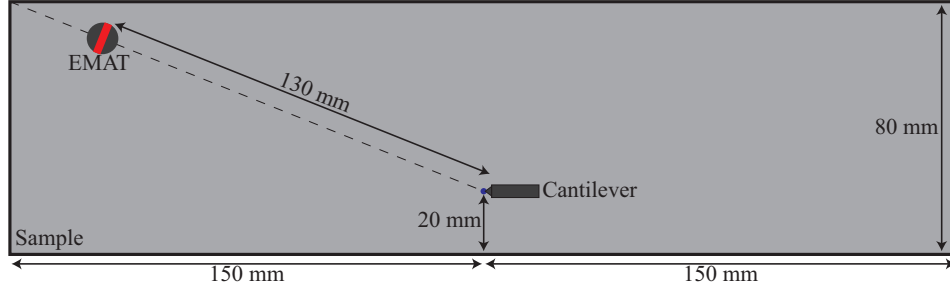


Figure 5.5: Top down view of the sample and transducer configuration for the point pulse experiments. The sample is a 0.5 mm thick aluminium sheet. Orientation of the EMAT coil is represented by the red line, indicating the position of the central wires (see figure 5.4). The cantilever and tip (here shown not to scale, but in the correct orientation) are in contact at the location of the blue dot. For the piezoelectric transducer experiments the cantilever is replaced with the transducers, centred on the blue dot.

a change in the deflection signal which would typically result in the AFM feedback loop adjusting the z position of the cantilever to restore this to a set point value. However, the deflection signal is passed through a low pass filter before the feedback loop, here with a cut-off frequency of 1.5 kHz. As this frequency is much lower than those typically used in ultrasonic NDT, the motion does not cause a feedback response and the signal of interest can be measured by recording the unfiltered deflection signal with suitable time resolution. This deflection signal can also be easily converted into absolute displacement (in metres) through calibration of the optical lever sensitivity (see section 2.2.2).

5.3.1.1 Deflection Measurements of an Ultrasonic Pulse

An example of ultrasonic detection using an AFM, taken using the sample configuration shown in figure 5.5, is given in figure 5.6, showing a trace of the AC deflection channel after the pulse and a sonogram of this result. The position of the EMAT and cantilever were chosen such that the path between them was not parallel to the side walls of the plate, which reduces the effect of reflections. The overlaid dispersion curves show the first symmetric (S_0 , non dispersive in this frequency range) and antisymmetric (A_0 , dispersive) modes, with higher order modes existing outside the frequency and time range shown here. There is a weak S_0 signal present, mostly visible from the trace as the scale suppresses the signal in the sonogram, and a strong A_0 signal matching closely with the dispersion curve. The A_0 signal is expected to be dominant as, for the frequencies and plate thickness here, the majority

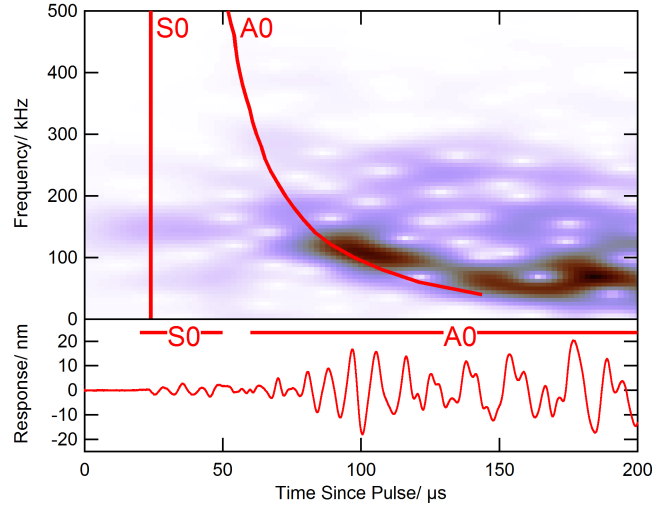


Figure 5.6: Time trace (bottom) and sonogram (top) of the AFM deflection signal using the configuration in figure 5.5. The sonogram colour scale is in arbitrary units, where darker indicates a greater response. The red lines on the sonogram correspond to the primary S0 (left, non-dispersive) and A0 (right, dispersive) modes of Lamb waves in a 0.5 mm thick aluminium plate.

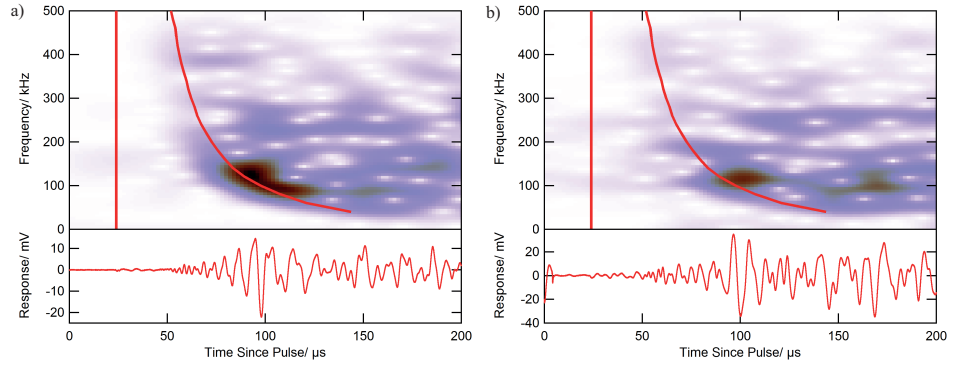


Figure 5.7: Time trace (bottom) and sonogram (top) of the response from piezoelectric transducers using the configuration in figure 5.5 — a) 1.5 mm diameter transducer, b) 10 mm diameter transducer. The sonogram colour scale is in arbitrary units, where darker indicates a greater response. The red lines on the sonograms correspond to the primary S0 (left, non-dispersive) and A0 (right, dispersive) modes of Lamb waves in a 0.5 mm thick aluminium plate.

of motion at the surface in the S0 mode is in-plane, whereas it is mostly out-of-plane in the A0 mode [92] and the deflection channel of the AFM detects out-of-plane motion. Additionally, the design of the EMAT creates primarily out-of-plane forces, which would lead to a stronger A0 mode for the same reasons. The signal is seen to cut off above frequencies of about 350 kHz, which corresponds to the approximate bandwidth of the EMAT used — the width of the current path in the centre of the EMAT was 2.5 mm which is close to the wavelength of the A0 wave at the maximum frequency seen (3.5 mm at 350 kHz). The finite size of the EMAT limits the ability to generate (or detect) waves with a comparable wavelength to the width, with the generated amplitude dropping to about third for this wavelength to EMAT width ratio, relative to long wavelengths [345]. This implies that the cut off frequency seen here is primarily caused by the bandwidth of the EMAT, though there are possibly weak higher frequency signals that are suppressed by the AFM’s bandwidth. Some additional signals are seen after the A0 dispersion curve, which are likely due to reflections from the edges of the sample.

This experiment was repeated using piezoelectric transducers as the sensors, with results shown in figure 5.7. These results show a marked similarity with the AFM results in figure 5.6, with a weak S0 pulse visible and a much stronger A0 signal, as well as additional signals visible after the A0 dispersion curve, which are attributed to reflections. Of particular interest is the feature on the sonograms around 100 μ s and 100 kHz, which is the strongest region in both the piezoelectric transducer results and the AFM results. This implies that the feature is a true ultrasound signal generated by the EMAT and is not a result of high sensitivity at that frequency by the AFM, strengthening the validity of the AFM results.

Some signal in the piezoelectric transducer results is visible at higher frequencies than in the AFM results, particularly the leading A0 signal at 400 kHz and 60 μ s, which is easily seen in both the piezoelectric transducer traces and sonograms and barely seen in the AFM sonogram. The frequency rolloff (reduction in amplitude above a certain frequency) here is due to the EMAT width effect and confirms that the rolloff seen in the AFM result is atleast partially due to the frequency sensitivity of the AFM detection, which will be discussed in section 5.3.1.2. While all the signals have content in the time following the initial A0 signal, the sonograms in this region look significantly different for both the piezoelectric transducer results and the AFM result. These differences have a variety of causes: firstly, the position of the piezoelectric transducers and AFM tip on the sample will not be exactly the same, which would cause significant differences in signals from reflections due to the more complicated paths from the EMAT to the sensor and due to the spatially dependent

effects of interference between different wave paths. Secondly the size of the sensor can have an effect — the AFM tip will only have contributions from the area around the tip, which is assumed to have a radius of about 10 nm, while the piezoelectric transducers will have contributions from their entire area (with diameters of 1.5 mm and 10 mm) and thus have additional paths and interferences resulting in the final seen signal.

5.3.1.2 Detection Limits

It is important to understand the limits affecting the use of AFM as an ultrasonic sensor and how these compare to other ultrasonic detection methods. The first limit of interest is the sensitivity, i.e. the minimum amplitude that can be measured by a system, as defined by the noise level, which can be frequency dependent. In AFM the noise level is primarily caused by the thermal oscillations of the cantilever and the electrical noise from the photodiode and electrical circuit. The combined effect of these was measured by taking the standard deviation of the output voltage and converting it to distance using the optical level sensitivity. For the Arrow UHF tips used here, it was found to be 110 pm, reduced to 44 pm when the the signal was an average of 8 readings. There are various ways to increase the sensitivity of the AFM — using averaged output signals (as done here) is the simplest, although the choice of cantilever can also have an impact, with stiffer cantilevers having lower thermal noise [346], and through use of better shielding and lower noise photodiodes and electronics.

For comparison to the piezoelectric transducer response, the amplitude of the negative peak seen at 100 μ s on figures 5.6 and 5.7 was divided by the standard deviation of the signal recorded before 0 μ s for the same experimental setup. This was found to be 310 for the AFM, 350 for the 10 mm transducer, and 360 for the pinducer, showing that the sensitivity of the AFM is similar to these transducers. Interferometers have had reported sensitivities down to 1-10 pm [132,347,348], which is better than the AFM sensitivity here, though the AFM used is not necessarily optimised for detection sensitivity. Overall the sensitivity of AFM is comparable to the sensitivities of other ultrasonic detection techniques.

Another important limit is the frequency sensitivity; the ability of the sensor to detect oscillations at different frequencies. In AFM there are two primary factors that limit the maximum frequency that is detectable: the system electronics and the cantilever properties. The main bottleneck in the system electronics is the four quadrant photodiode, which will have a response time, often cited as the rise time, T_r , which will lead to maximum bandwidth of $f_{BW} = \frac{0.35}{T_r}$. A thermal noise spectrum (a

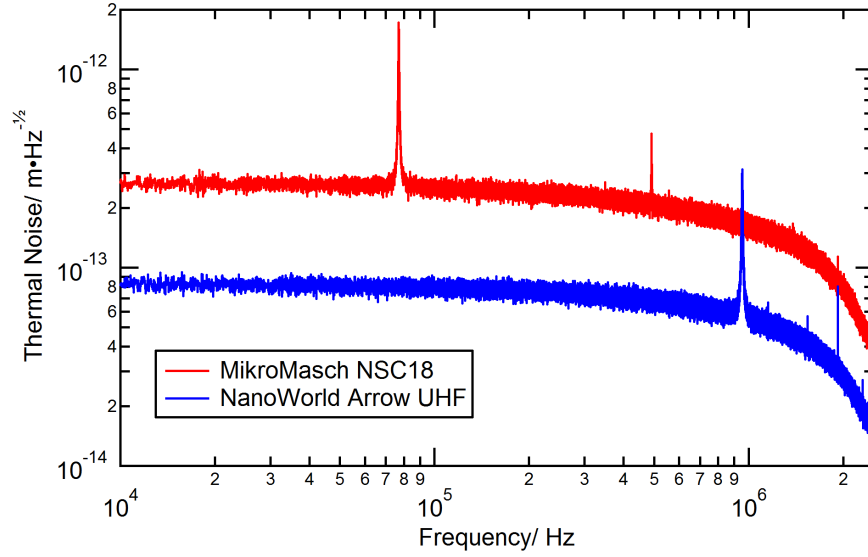


Figure 5.8: Thermal noise spectra of two different AFM cantilevers.

Fourier transform of the raw deflection signal without any driving oscillations on the cantilever) can indicate the frequency at which the photodetector response rolls off. An example for the system used here is shown in figure 5.8, demonstrating a reduction in sensitivity above 1 MHz. The peaks on this thermal noise spectra correspond to the free air resonances of the cantilevers. Higher speed four quadrant photodiodes are available, with rise times in the region of 1–10 ns, corresponding to bandwidths in excess of 35 MHz. The frequency capability of the analogue to digital converters (ADCs) within the AFM may also be a concern, though an external oscilloscope can be used in place of these, as has been done in these experiments, provided there is an unfiltered analogue output of the photodiode response available.

The cantilever also sets an upper limit for the frequency response based on its resonance frequency; as seen in UFM (chapter 4), the cantilever will stop following the surface at frequencies significantly above this frequency. Tip design can be altered to increase this frequency, with resonant frequencies upwards of 1 MHz commercially available. Note also that the resonance of the cantilever is modified by contact with the surface, as shown by the comparisons between driven tuning curves seen in figure 5.9, where contact with the surface increased the frequency of the primary resonance by nearly a factor of 5. As seen earlier in the ultrasound frequency testing for UFM (section 4.4.1), the cantilever (which is the same type as in figure 5.9) does respond to surface oscillations at frequencies above even this increased resonance (oscillations seen at 600 kHz in figure 4.10(a)), suggesting that the stated resonance

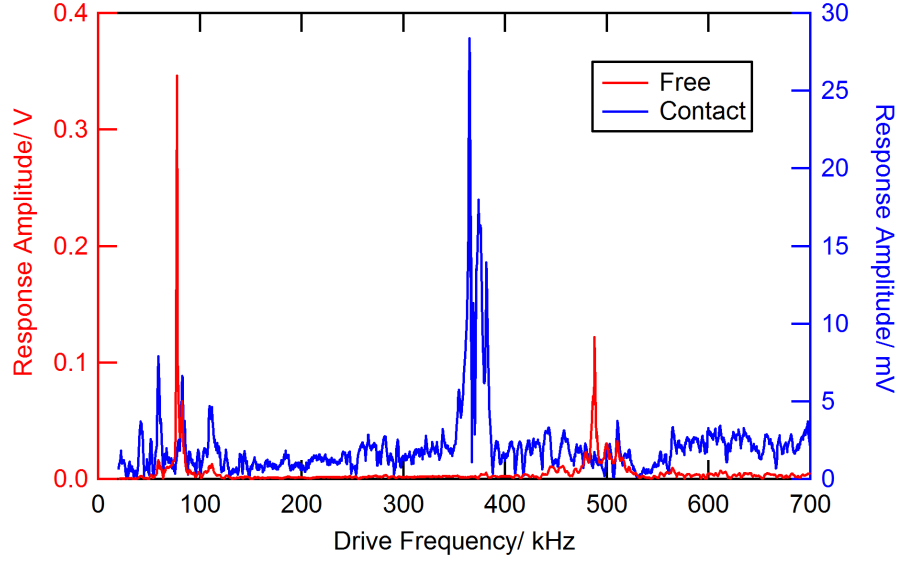


Figure 5.9: Tuning curves for a MikroMasch NSC18 tip, take in free air and in contact with an aluminium sheet. The set point for the contact measurement was 1 V, which corresponds to a force of 100–150 nN for these tips.

of the cantilever is not the limit on its ability to respond to surface oscillations, but does still provide an indication of the possible bandwidth.

The bandwidth of EMATs is primarily limited by their size, with sensitivity to wavelengths greater than the width of the coil (current pathway) [345]. The minimum size for a coil is limited by the minimum width of the wire used to make the coil — for a wire thickness of 0.1 mm and a typical wave velocity in aluminium of 3000 ms^{-1} the bandwidth limit is therefore 30 MHz. However, only having one turn of wire will reduce the detection sensitivity (or output power for a generation coil) of the EMAT, so there is a trade-off between sensitivity and frequency. The frequency bandwidth of piezoelectric transducers is again related to their physical dimensions, where the resonant frequency, is inversely proportional to their thickness. The frequency response of piezoelectric transducers can be variable based on design, though often there is a usable region of frequencies below the resonant frequency. Typical piezoelectric transducers have resonant frequencies up to 10s of MHz, though new techniques allowing them to be produced with thicknesses of the order of 10s of μm enable resonant frequencies up to 1 GHz [349]. Interferometer bandwidth is limited by the rise time of the light detection system, typically a photodiode. The single photodiodes used for interferometry detection (as opposed to the quadrant detectors

used in AFM) can have bandwidths in excess of 1 GHz [350, 351], enabling such bandwidths for interferometry. This places the practical limit of AFM detection bandwidth (of the order of 10 MHz) at the low end of bandwidth when compared to other techniques, though with significant improvement possible through design specialised for ultrasound detection.

The spatial resolution of the AFM should be a significant advantage over other techniques. The resolution of the AFM is usually limited by the radius of the tip, which is typically about 10 nm for standard tips, although sharper tips are available for atomic resolutions (~ 1 nm). Other techniques have limits much higher than this, with piezoelectric transducers and EMATs being limited by their size (typically over a millimetre) and interferometers having an absolute maximum resolution defined by diffraction limited optics, which results in a resolution of the order of the wavelength of light used, which is typically 400–1000 nm [132], though with practical designs having larger spot sizes. This high resolution, however, is not necessarily useful as the resolution can be dependent on the wavelength of the ultrasound. While small features can still create measurable signals with sensitive enough equipment, the ability to resolve two nearby features can also be of importance. In the far field (i.e. where the detector is far from the feature relative to its size) the resolution is typically of the order of the wavelength, though can be improved through the use of analysis of many results with different detector and source locations (possibly using arrays of transducers) [331]. This means that the practical resolution can be limited by the frequency bandwidth of the detector — for the case of Lamb waves in aluminium (typical velocity of 3000 ms^{-1}) and AFM detection (with a maximum bandwidth of 10 MHz) this results in a practical resolution of 0.3 mm, better than EMATs and piezoelectric transducers but worse than interferometry. In the experiments here the frequency is typically around 100 kHz which, when combined with the A0 phase velocity at this frequency of 700 ms^{-1} , gives a practical resolution of 7 mm. In the near field (detector close to the feature) the resolution is greatly improved as the signals from separate features may not have combined at this range. Wavelength can still be an important consideration in the near field, however, as features could be hidden by the near field signals, such as near field enhancements.

5.3.2 In-Plane Displacement

The deflection channel is not the only data channel available in the AFM; the torsional bending of the cantilever is also detected as a separate lateral deflection channel. Signals in this channel correspond to the tip moving perpendicular to the centreline of the cantilever, which will be caused by in-plane motion of the surface in

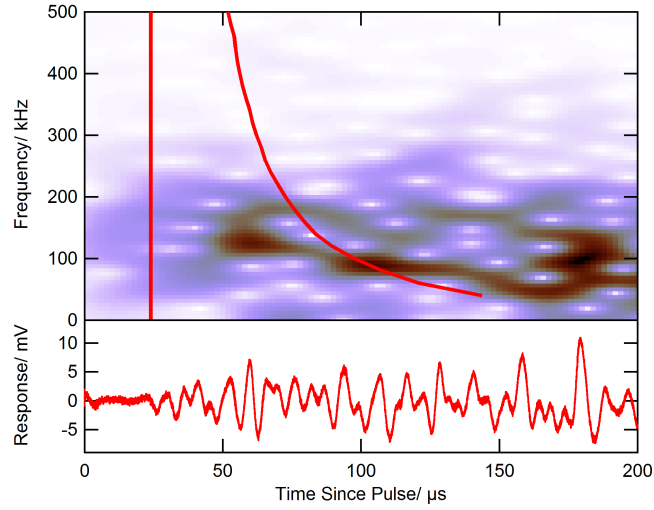


Figure 5.10: Time trace (bottom) and sonogram (top) of the lateral deflection signal using the configuration in figure 5.5, taken simultaneously with the results in figure 5.6. The sonogram colour scale is in arbitrary units, where darker indicates a greater response. The red lines on the sonogram correspond to the primary S0 (left, non-dispersive) and A0 (right, dispersive) modes of Lamb waves in a 0.5 mm thick aluminium plate.

the same direction. This allows for simultaneous and distinct detection of two out of three of the possible surface motion components at a single point, which is useful for determining the mode content of waveforms. Such combined measurements are not typically possible with other techniques. With EMATs and piezoelectric transducers it is possible to design them such that they will pick up in-plane motion, though this cannot be done simultaneously with a distinct out-of-plane measurement at the same location. It is possible to use laser detectors to measure in-plane motion, such as with knife edge detection [132], electronic speckle pattern interferometry [352–354], and heterodyne interferometry [355]. These techniques can be combined with out-of-plane detection, but doing so has significant difficulties associated with the alignment of multiple systems.

An example of a measurement of the in-plane displacement using the lateral channel, taken simultaneously with the out-of-plane results shown in figure 5.6, is shown in figure 5.10. In this the S0 signal is still weaker than the A0 signal, though much more visible in the time trace than it was for the out-of-plane result; this agrees with the expectation that the lateral measurement is sensitive to the in-plane motion but the EMAT used is primarily generating the A0 mode due to its design. Note that, due to the orientation of the sample, the direction of measurement is 68° to

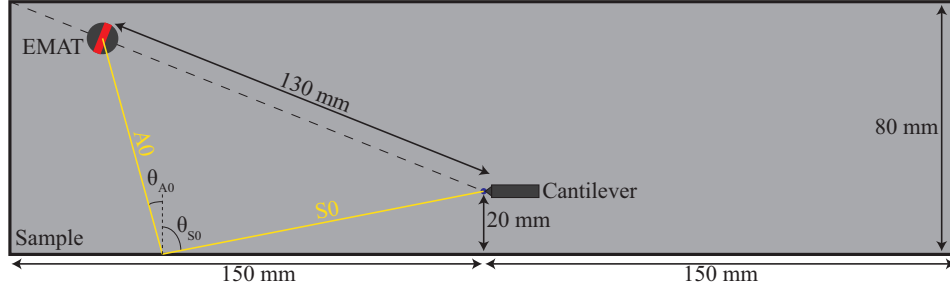


Figure 5.11: Top down view of the point detection experiment (from figure 5.5) with orange lines indicating a possible reflection and mode conversion pathway to explain a particular sonogram feature in the lateral detection results (figure 5.10).

the direction of travel for the waves from the EMAT — this could also reduce the S0 signal as the EMAT design produces in-plane motion primarily along the direction of travel, and thus there will only be a small component in the measurement direction. This is explored further in section 5.3.2.1.

A feature on the sonogram in figure 5.10 is seen at around $60 \mu\text{s}$ and 125 kHz , which does not correspond to either of the primary S0 and A0 waves, marked by red lines. This feature is likely a reflection, and due to its strength relative to the other signals it could be from mode conversion from the out-of-plane A0 mode, which is a majority of the EMAT output, to the in-plane S0 mode that can be detected by the lateral deflection of the cantilever. A diagram showing a possible reflection path is shown in figure 5.11. In this the angle of incidence of the A0 wave, θ_{A0} , and the angle of reflection of the S0 wave, θ_{S0} , are governed by Snell's law, which is discussed in more detail in section 1.2.1;

$$\frac{\sin(\theta_{A0})}{v_{A0}^p} = \frac{\sin(\theta_{S0})}{v_{S0}^p}, \quad (5.1)$$

where v_{A0}^p and v_{S0}^p are the phase velocities of the A0 and S0 waves respectively, which depend on the frequency and sample thickness. By considering the geometry of the system (figure 5.11) and Snell's law with the phase velocities of the waves at the frequency of interest (125 kHz in a 0.5 mm plate; $v_{A0}^p = 640 \text{ ms}^{-1}$, $v_{S0}^p = 5440 \text{ ms}^{-1}$) the angles can be calculated as 7° and 80° for θ_{A0} and θ_{S0} respectively. These angles can then be used to calculate the distance travelled of each of the A0 and S0 segments and used with the group velocities of these modes ($v_{A0}^g = 1450 \text{ ms}^{-1}$, $v_{S0}^g = 5440 \text{ ms}^{-1}$) to give a total travel time for this wave mode of $68 \mu\text{s}$. This is slightly later than seen in the sonogram, though this could be explained by errors in

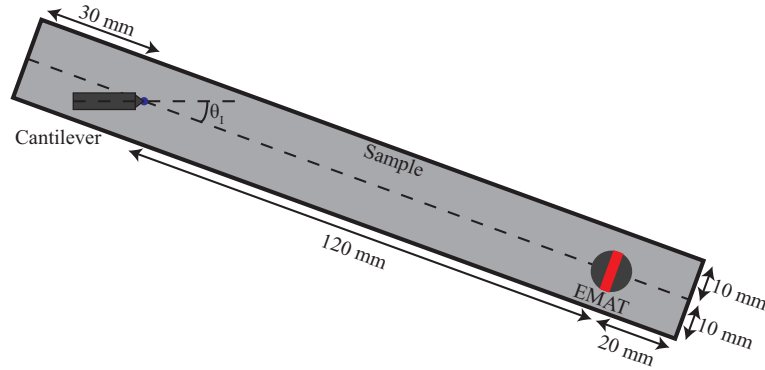


Figure 5.12: Top down view of the sample and transducer configuration for the angular dependence experiments. The sample is a 0.5 mm thick aluminium sheet. Orientation of the EMAT coil is represented by the red line, indicating the position of the central wires (see figure 5.4). The cantilever and tip (here shown not to scale, but in the correct orientation) are in contact at the location of the blue dot. The aluminium sample is placed at different angles, θ_I , relative to the cantilever orientation.

the size and shape of the aluminium sheet, and the positioning of the EMAT and the tip on it. This S0 reflection is travelling nearly parallel to the cantilever direction (11° difference), which means that the strength is not due to better alignment of the surface with the cantilever (which is discussed further in section 5.3.2.1) but due to the relative strength of the A0 wave, making the mode converted S0 wave stronger than the directly produced S0 wave. A similar reflection off the top edge of the aluminium sample is also possible, and would be present at $32 \mu\text{s}$ at the same frequency, but is not seen on the sonogram. The reason such a feature is not seen is likely due to the directionality of the EMAT — it is designed such that waves will propagate strongest in a direction perpendicular to the wire direction, and this propagation direction was chosen to be in line with the AFM tip. For the bottom reflection the A0 wave from the EMAT is emitted at 62° to the propagation direction, whereas the A0 wave for the top reflection would be emitted from the EMAT at 105° to the propagation direction (75° from the backwards propagation direction, which should display similar behaviour due to the coil symmetry).

5.3.2.1 Angle of Incidence Dependence

If the lateral deflection is detecting one direction of in-plane motion and the in-plane motion is primarily in one direction (as is the case with Lamb waves), the lateral signal should have significant variation when changing the angle between these two directions. In this case the surface motion is parallel to the propagation

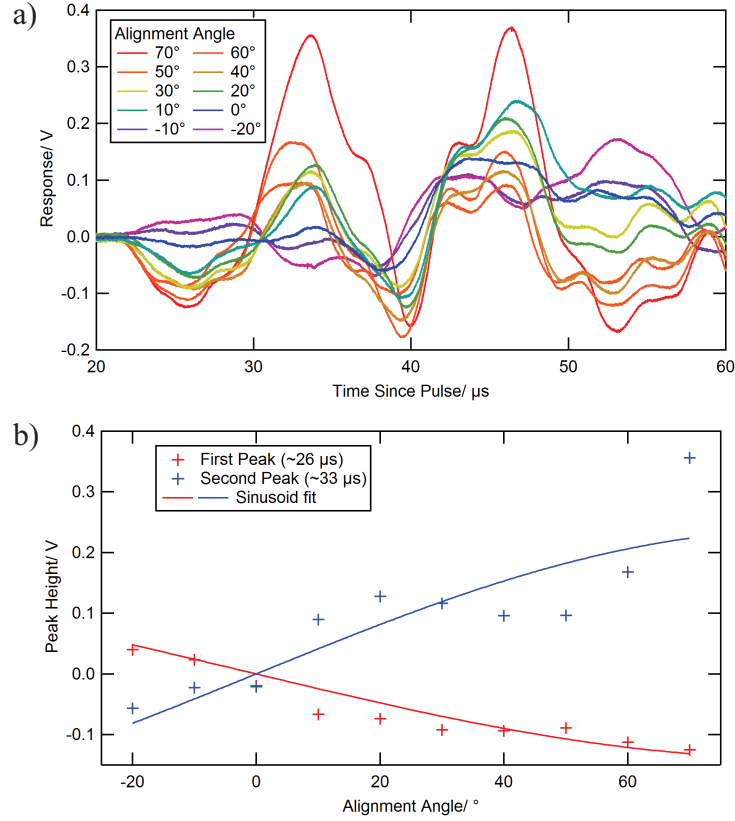


Figure 5.13: Changes in response of lateral deflection with varying angle of alignment between the cantilever and wave travel direction. a) Traces of response, zoomed in to focus on the primary S0 wave. b) Peak height of the first two peaks shown in (a).

direction and the cantilever detection direction is perpendicular to the length of the cantilever — as such the signal should be minimised when the wave is propagating parallel to the length of the cantilever. This was tested by using a narrow strip of aluminium with the EMAT generation directed along the centreline, as illustrated in figure 5.12. In this case a narrow sample was used to allow the greatest range of angles to be tested, as limited by the “legs” of the AFM. This strip of metal was oriented in the AFM such that the angle between the cantilever length and wave propagation direction was varied in 10° intervals from -20° to 70° , measured between the direction of propagation and the length of the cantilever (perpendicular to the detection direction of the lateral channel), labelled as θ_I in figure 5.12 (with the angle shown being above 0°).

The results of this experiment are shown in figure 5.13(a), which is zoomed in on the S0 region of the traces. The first two peaks show a clear dependence on

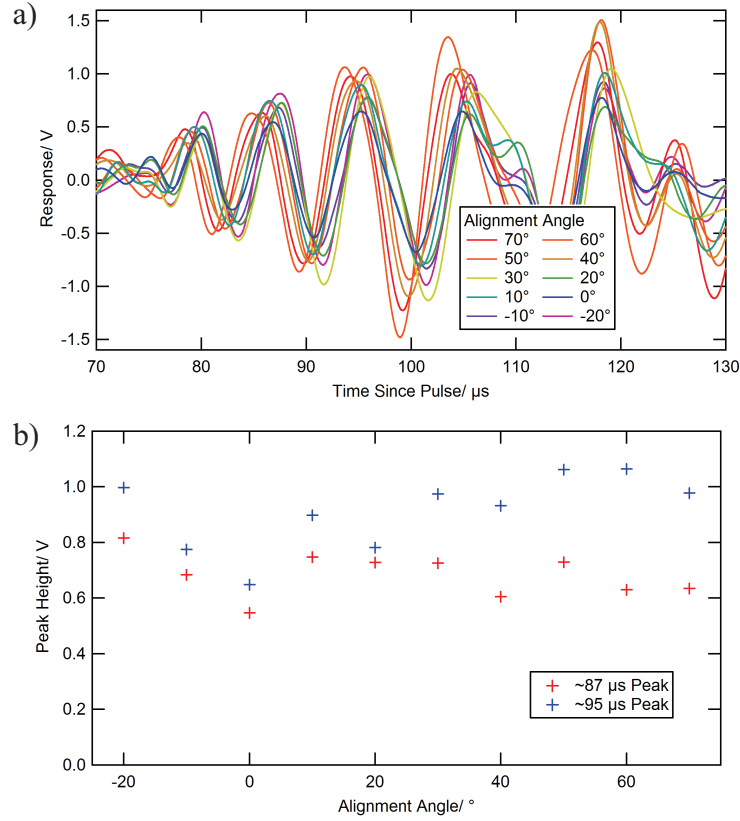


Figure 5.14: Changes in response of deflection with varying angle of alignment between the cantilever and wave travel direction. a) Traces of response, zoomed in to focus on the start of the primary A0 wave. b) Peak height of two peaks shown in (a).

angle, having a minimum/maximum value at the angle at which the direction of propagation is most aligned with the detection direction of the cantilever and an inversion in signal direction at 0° . This is the predicted behaviour for this system. Further peaks do not show such a strong dependence on angle, which could be due to contributions from reflections off the sides of the aluminium strip. The slight changes in timing can be attributed to small errors in the manual positioning of the sample.

For additional analysis of the results in figure 5.13(a) the value of the maximum magnitude for each angle was taken for the first and second peak and plotted against angle in figure 5.13(b). In both cases there is unexpected behaviour in the $30\text{--}50^\circ$ range, where the amplitude doesn't grow significantly with increasing angle. The design of the AFM sample stage meant that a magnetic material was underneath the EMAT for these angles, resulting in the EMAT clamping down on the

sample, an effect which could reduce the strength of the generated Lamb waves. For the assumptions made regarding detection and motion direction, the amplitude would be expected to follow a sine dependence on angle, which has been fitted on figure 5.13(b). The behaviour does loosely follow the expected dependence, though a larger data range would be required to make a strong conclusion. Overall the angular dependence shown here strongly supports that the lateral channel is detecting in-plane motion.

The simultaneous deflection (out-of-plane) signals were also recorded, as shown in figure 5.14(a). As with the lateral results small variations in the time delay of each signal are visible, which can be accounted for by the imperfect positioning of the sample resulting in small variations in distance between the EMAT and the AFM tip. The peak heights for the peaks near $87 \mu\text{s}$ and $95 \mu\text{s}$ are shown in figure 5.13(b). Variations in the signal amplitude can be seen, though there is no correlation with the angle, which is the expected result as the out-of-plane detection should not be dependent on tip orientation. The random variations in amplitude can be attributed to small changes in the positioning of the sample under the tip and changes in the sample environment affecting the generation and propagation. This further supports that the results in figure 5.13 — change in lateral response with changing angle — are due to the change in angle and not due to other changes with the system.

5.3.3 Mapping and Features

Scanning a sample to look for features (such as defects) by examining changes in the ultrasonic signal is a common practise in ultrasonic NDT. Such experiments were first carried out here by doing readings at regularly spaced intervals along a line crossing a narrow laser cut slot in the aluminium sheet sample, as illustrated in figure 5.15. This line scan has a total of 300 points at $20 \mu\text{m}$ separation, for a total length of 6 mm. Figures 5.16(a) and (b) show sonograms for the deflection (out-of-plane) traces of the first (nearest to the EMAT, before the slot) and last (furthest from the EMAT, after the slot) results from this set respectively. These results are similar to those seen in section 5.3.1.1, with a strong A0 signal, a weaker S0 signal and frequencies primarily in the 100 kHz region. The signal measured after the slot is significantly weaker than the signal measured before the slot, which is expected as the slot will block propagation of the wave. Additional signals are visible after the primary A0 signal, which can be attributed to reflections from the sample edges.

A video of all the sonograms was produced and used to determine regions of high signal strength. These regions (shown by the boxes on figures 5.16(a) and (b))

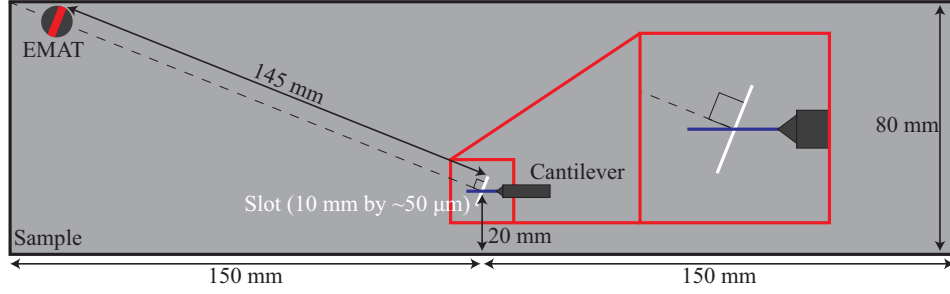


Figure 5.15: Top down view of the sample and transducer configuration for the line scan experiments. The sample is a 0.5 mm thick aluminium sheet. Orientation of the EMAT coil is represented by the red line, indicating the position of the central wires (see figure 5.4). The cantilever and tip (here shown not to scale, but in the correct orientation) are brought into contact at regularly spaced positions along the blue line. The red box inset is a threefold zoom of the area of interest.

were then averaged for each sonogram and plotted against distance in figure 5.16(c). From this the location of the slot, which has been arbitrarily set as the $x = 0$ mm point on the figure, is clear — there is a sudden drop in the amplitude of all signals at this location due to the slot blocking the transmission of the waves. The A0 signals show significant enhancement in amplitude as the slot is approached, with a minimum value being seen at a distance of 1.1 mm from the slot for the signal in the 100 kHz region (blue trace) and 1.8 mm for the signal in the 40 kHz region (red trace) — the ratio of these to the wavelengths for the A0 signals at these frequencies (6.9 mm for 100 kHz and 11.0 mm for 40 kHz) are the same for both frequencies at 0.16. This near-field enhancement of ultrasound has been previously seen for both detection [90,313,356,357] (as is the case here) and generation [358] near to cracks and is attributed to interference between the incident wave and reflected and mode converted waves.

The S0 signal shows little variation with position other than the reduction caused by the slot and a single point of strong signal on the edge of the slot, which may be an enhancement effect or a result of the interaction between the tip and the geometry at the slot edge. The S0 signal also appears significantly stronger than would be expected and has been seen in the previous results (section 5.3.1.1) for out-of-plane detection — this implies that the “S0” signal may be an A0 wave, mode converted from the primary S0 wave at the slot and thus appearing at very close to the time expected of an S0 wave. This mode conversion would also explain the lack of enhancement of the signal as the A0 mode will dominate the detected signal and not interfere with the incoming S0 wave.

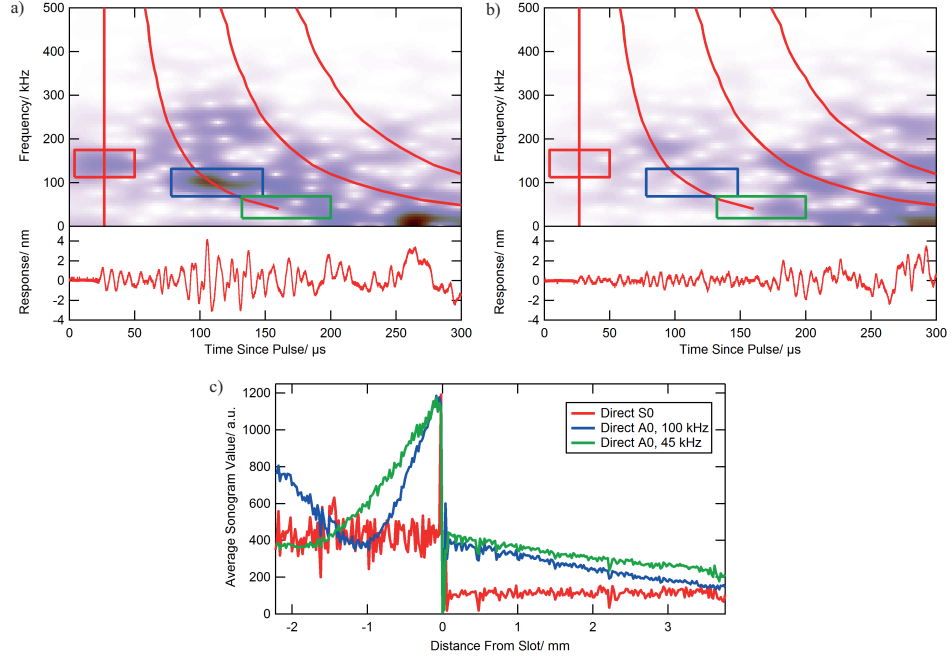


Figure 5.16: a,b) Time trace (bottom) and sonogram (top) of the deflection signal using the configuration in figure 5.15 — a) first point of the scan, closest to the EMAT, b) last point, furthest from the EMAT. The sonogram colour scale is in arbitrary units, where darker indicates a greater response, and the same scale is used for both (a) and (b). The red lines on the sonogram correspond to the primary S0 (left, non-dispersive) mode and A0 modes for the primary path, plus double and triple length path A0 modes (right, dispersive, in order). c) Averages of the sonograms within the corresponding coloured squares in (a,b), with the x axis zeroed to the location of the slot.

For comparison this experiment was repeated using an interferometer for detection in place of the AFM. 100 measurements were done every $62.5 \mu\text{m}$ for a total length of 6.25 mm. The first (nearest to the EMAT, before the slot) and last (furthest from the EMAT, after the slot) traces from this set of results are shown with corresponding sonograms in figures 5.17(a) and (b) respectively. These are very similar to the AFM results in figure 5.16, showing a clear A0 signal and a significant reduction in amplitude in the result from after the slot, though with some notable differences; firstly, the S0 signal is barely visible and has a much lower amplitude relative to the A0 signal than was seen with the AFM. It is possible that the S0 signal has been masked by the higher noise of the interferometer. There is also a higher frequency part of the A0 signal visible in both the trace and the sonogram, having a 400 kHz oscillation arriving at $60 \mu\text{s}$ — this further demonstrates that

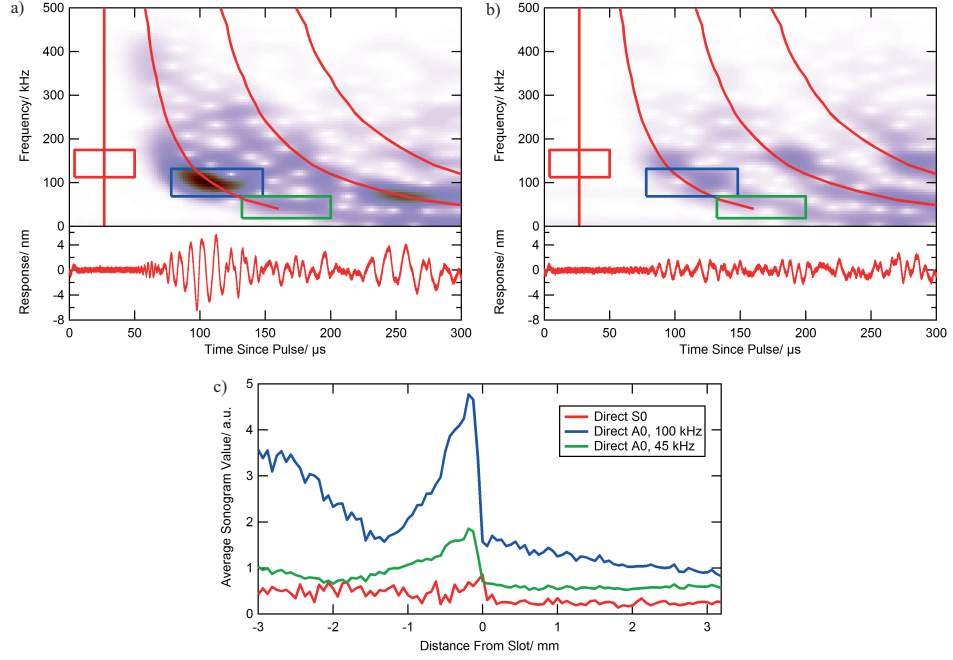


Figure 5.17: a,b) Time trace (bottom) and sonogram (top) of the interferometer signal using the configuration in figure 5.15 — a) first point of the scan, closest to the EMAT, b) last point, furthest from the EMAT. The sonogram colour scale is in arbitrary units, where darker indicates a greater response, and the same scale is used for both (a) and (b). The red lines on the sonogram correspond to the primary S0 (left, non-dispersive) mode and A0 modes for the primary path, plus double and triple length path A0 modes (right, dispersive, in order). c) Averages of the sonograms within the corresponding coloured squares in (a,b), with the x axis zeroed to the location of the slot. The regions averaged here are the same as in figure 5.16. The line corresponding to the S0 signal (red) has been multiplied by a factor of 10 for visibility.

the bandwidth rolloff seen in the AFM results is due to the AFM and not purely the EMAT, and that the AFM bandwidth is not as high as might be expected based on the cantilever resonance. Finally, the signals seen after the primary A0 signal are much more defined in the interferometer result than in the AFM; such a difference could be explained by cantilever ringing (where the cantilever continues to oscillate after it has been excited regardless of the surface motion at the time). Interestingly these additional signals correspond to A0 signals for double and triple the EMAT–detector separation, which is unexpected due to the lack of symmetry in the sample setup. The signal for triple distance may be explained by reflection off the short side of the aluminium furthest from the EMAT, though no single or double

reflection exists with a total path length of double the EMAT–detector separation. The interferometer results also display a much higher noise level than the AFM results, highlighting the routinely high sensitivity of the AFM.

The same regions of the sonogram used for amplitude analysis of the AFM results (figure 5.16) were used for analysing the interferometer results, with averages of the chosen sonogram regions taken at every point and plotted against distance in figure 5.17(c). These results are overall very similar to those from the AFM (figure 5.16(c)) — significant enhancement is seen for both A0 signals near to the slot, with a sudden drop at the slot. The distance from the slot of the minimum values for the A0 signals also matches those of the AFM results (1.1 mm and 1.8 mm for the higher and lower frequency regions, respectively), as does the enhancement factor (the ratio of the maximum value to the minimum value for each averaged signal), which is approximately 3 for both the A0 signals with both detection methods. Some differences do exist, notably the two A0 signals were of similar amplitudes in the AFM result, whereas the higher frequency signal is much stronger in the interferometer results. This may be due to a non flat frequency result of one of the systems, most likely the AFM.

The lateral channel was recorded simultaneously with the results from figure 5.16, with figures 5.18(a,b) showing traces and sonograms for the first (closest to the EMAT, before the slot) and last (furthest from the EMAT, after the slot) positions respectively. These sonograms are similar to the one for the sample without a slot (figure 5.10), where the main feature is seen at around 120 kHz and 60 μ s, which is attributed to a mode converted (A0 to S0) reflection off the bottom edge of the sample (figure 5.11). Weaker signals corresponding to the direct S0 and A0 waves are also visible, as is a signal corresponding to an A0 signal at double the separation, as was seen in the out-of-plane and interferometer results of this experiment. As before, features on these sonograms were identified using a video of all sonograms, with regions selected around these features (boxes on figures 5.18(a) and (b)) and averaged at every position, with the averages plotted against position in figure 5.18(c). While there is some variation in signal strength with distance before the slot, none of these results display the near slot enhancement seen for the A0 waves in figures 5.16 and 5.17. This indicates that, for the A0 signals, the measured response is a result of mode conversion from A0 to S0 at the slot and thus not interfering with the incident wave. For the S0 signal it is possible that, due to the orientation of the cantilever, the signal is dominated by a reflected wave with in-plane motion perpendicular to the propagation direction, which would not interfere with the incident wave with motion parallel to the propagation direction. An increase in signal

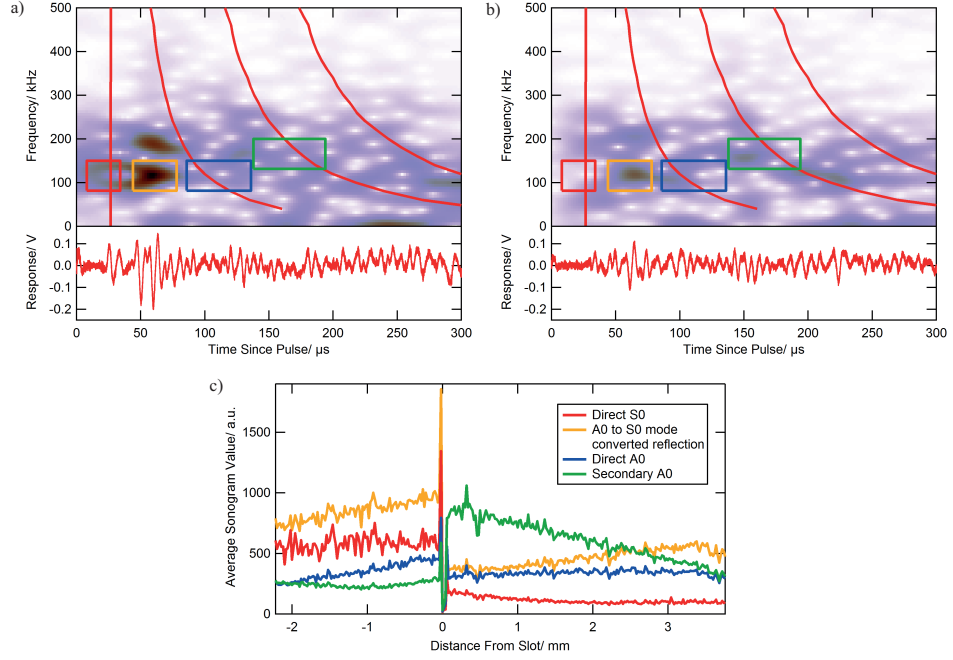


Figure 5.18: a,b) Time trace (bottom) and sonogram (top) of the lateral deflection using the configuration in figure 5.15, taken simultaneously with the results in figure 5.16 — a) first point of the scan, closest to the EMAT, b) last point, furthest from the EMAT. The sonogram colour scale is in arbitrary units, where darker indicates a greater response, and the same scale is used for both (a) and (b). The red lines on the sonogram correspond to the direct S0 (left, non-dispersive) and A0 modes, plus double and triple length path A0 modes (right, dispersive, in order). c) Averages of the sonograms within the corresponding coloured squares in (a,b), with the x axis zeroed to the location of the slot.

is seen for all the signals on the last point before the slot, though this may be due to the local geometry of the sample surface at this point. The primary S0 and A0 waves, as well as the mode converted S0 reflected wave, all display a drop in signal past the slot as expected. The double distance A0 wave, however, shows an increase in amplitude past the slot, which indicates that the path for this signal goes around the slot.

A scan of a sample can also be done in two dimensions to provide further information about the spatial extent of a feature of interest. This is performed by rastering the capture points over the 2D area in a stepwise pattern, similar to an AFM scan. To save time the slow axis is stepped at the end of each line and the return motion is used to capture a new line of points. Here, the same sample as used for the line scans was investigated, mapping the area around the end of the

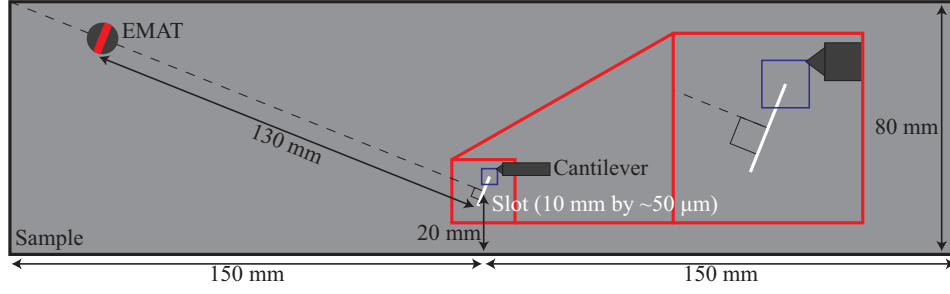


Figure 5.19: Top down view of the sample and transducer configuration for the mapping experiments. The rectangle is a 0.5 mm thick aluminium sheet. Orientation of the EMAT is represented by the red line, indicating the position of the central wires (underneath the magnet — see figure 5.4). The cantilever and tip (here shown not to scale, but in the correct orientation) are brought into contact at regularly spaced positions within the blue square, forming a grid of points. The red box inset is a threefold zoom of the area of interest.

slot in a 50 by 50 point map with $100\ \mu\text{m}$ point separation, covering a total area 5 mm by 5 mm, as shown in the schematic in figure 5.19. A sonogram for the deflection channel (for out-of-plane motion) from the point closest to the EMAT is shown in figure 5.20 and displays features discussed previously — a strong A0 signal, particularly below 150 kHz, a weak S0 signal, and a variety of signals after the A0 signal that can be attributed to reflections.

Areas of interest on the sonogram (figure 5.20(a)), again found by looking for strong features on a video of sonograms of all points, are highlighted by boxes on the figure. Averages in these areas were taken at each point and mapped against position, shown in figures 5.20(b–e). The location of the slot is clearly visible in all of these, extending from the bottom edge to the centre of the maps, displaying a sudden, significant change in response amplitude. The S0 signal (figure 5.20(b)) shows two distinct regions — a consistent amplitude covering the majority of the image, and a stronger region directly between the EMAT and the slot. This is similar to the line results (figure 5.16) and supports the S0 seen by the deflection channel primarily being a result of a mode converted reflection at the slot. All of the A0 regions measured (figures 5.20(c–e)) display similar behaviour to each other — a dip in amplitude followed by an enhancement as the slot is approached from the EMAT (as discussed previously) and a region of lower response on the side of the slot away from the EMAT. These are particularly prominent on the highest frequency signal (figure 5.20(c)); two minima are visible parallel to the slot (at distances of approximately 0.15 and 0.5 wavelengths from the slot), with significant enhancement

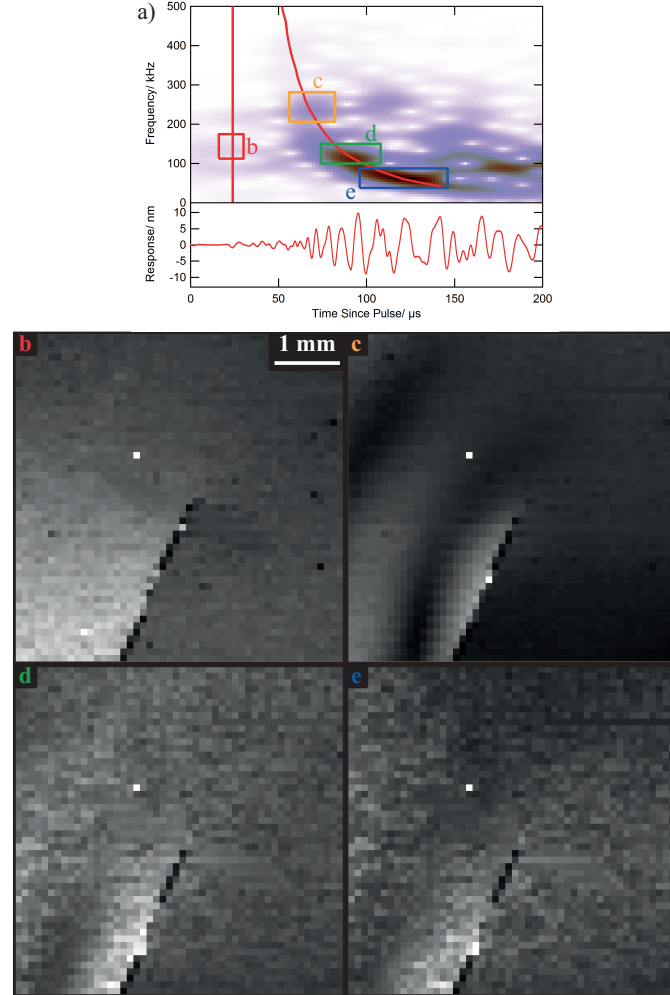


Figure 5.20: a) Time trace (bottom) and sonogram (top) of the deflection signal using the configuration in figure 5.19, showing the result from the point closest to the EMAT. The sonogram colour scale is in arbitrary units, where darker indicates a greater response. The red lines on the sonogram correspond to the primary S0 (left, non-dispersive) and A0 (right, dispersive) modes of Lamb waves in a 0.5 mm thick aluminium plate. The coloured boxes correspond to the regions averaged to give the maps shown in (b–e), which are all orientated to match figure 5.19 and have arbitrary colour scales where white corresponds to the highest response and black corresponds to zero.

at the slot and a smaller increase between the minima. This double minima effect is not visible on the two other A0 results (figures 5.20(d) and (e)), however, the minima visible on these is further from the slot and thus the second minima would be too far from the slot to be seen within the scan range here. These longer distances are consistent with the longer wavelengths of these lower frequency waves.

As before, the lateral channel was also recorded simultaneously with the results from figure 5.20. A trace and sonogram from the point closest to the EMAT are shown in figure 5.21(a). Regions selected from the sonogram, as marked, have been averaged and the results mapped in figures 5.21(b–e). All the signals attributed to S0 waves (figures 5.21(b–d)) show a clear shadow region on the side of the slot away from the EMAT and a small increase on the near side of the slot, which could be due to contributions from reflected waves, though no near slot enhancement is seen. It would be expected that the shadow region for the mode converted S0 wave (figure 5.21(d)) resulting from the reflection of an A0 wave off the bottom edge of the sample (as previously discussed in section 5.3.2) would be at a different angle to that of the direct S0 waves (figures 5.21(b,c)) due to the different angle of incidence of the waves. However, the shadow does not have a defined edge, making such a comparison difficult in these results. The A0 signal is strongest in the area adjacent to the slot on the side closest to the EMAT, with reduced signal elsewhere. This supports that the signal detected here is mode converted reflections from the slot rather than the incident A0 wave (which is primarily out-of-plane and thus should not be detected by the lateral channel). This is further supported by the lack of the near crack enhancement that was seen in the out-of-plane results (figures 5.20(c–e)) as this implies that the wave being measured in-plane is of a different origin to the ones measured out-of-plane.

5.4 Conclusions

The use of AFM as a detector for ultrasonic NDT has been demonstrated. This was first shown by detecting broadband Lamb waves within an aluminium sheet and comparing the measured waves to those measured using piezoelectric transducers. These results were similar for the different detection methods and matched the expected dispersion curves for Lamb waves. The AFM was then scanned over a manufactured slot in the sheet and changes in the amplitude of detection of various features in time-frequency space were examined. The behaviour here was again as expected, finding that the AFM correctly detected a drop in amplitude in the shadow region behind the slot as well as significant near-field enhancement as the slot was

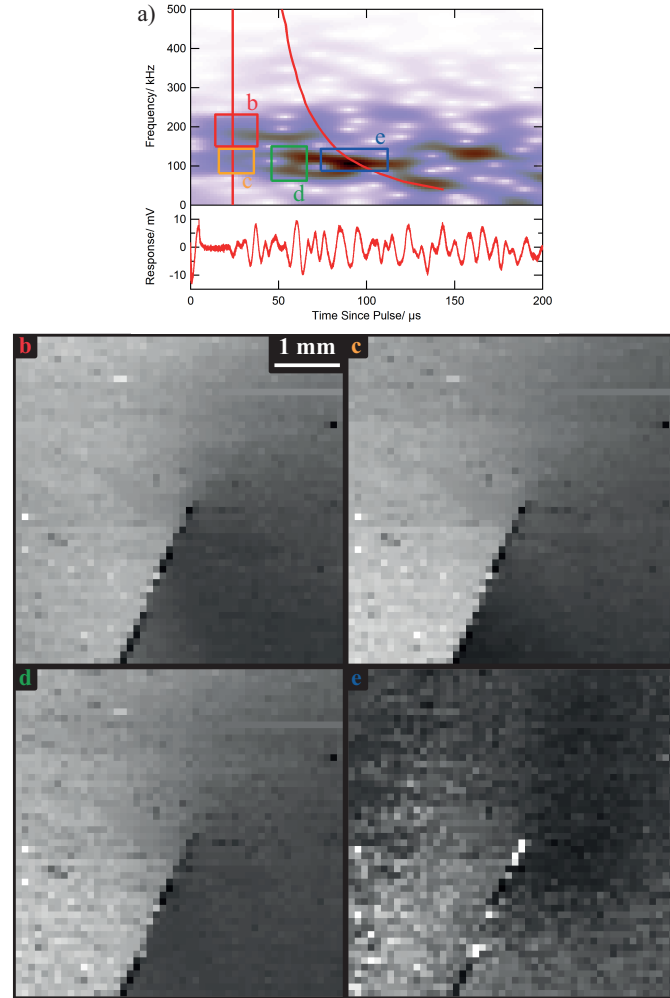


Figure 5.21: a) Time trace (bottom) and sonogram (top) of the lateral deflection signal using the configuration in figure 5.19, showing the result from the point closest to the EMAT and taken simultaneously to the results in figure 5.20. The sonogram colour scale is in arbitrary units, where darker indicates a greater response. The red lines on the sonogram correspond to the primary S0 (left, non-dispersive) and A0 (right, dispersive) modes of Lamb waves in a 0.5 mm thick aluminium plate. The coloured boxes correspond to the regions averaged to give the maps shown in (b–e), which are all orientated to match figure 5.19 and have arbitrary colour scales where white corresponds to the highest response and black corresponds to zero.

approached from the side closest to the generation source. This matched the results seen when using an interferometer as the detector, further showing that the AFM can be used instead of other detection methods and provide similar behaviour, while potentially benefiting from the AFM's high sensitivity and resolution.

The limits of AFM as an ultrasound detector were discussed and compared to other detection techniques, i.e. piezoelectric transducers, EMATs, and laser interferometers. It was found that the sensitivity of the AFM was comparable to the other techniques and that the spatial resolution was significantly better than them, especially the piezoelectric transducers and EMATs. Frequency bandwidth was lower in the AFM than with other techniques, though significant improvement should be possible through use of different equipment, primarily by using photodiodes and cantilevers designed for higher frequency operation. The low frequency bandwidth also presents an issue for the practical spatial resolution of the ultrasonic NDT as features significantly smaller than the wavelength of the ultrasound used may have weak interaction with the ultrasound waves (making them harder to detect) and features much closer than the wavelength may be hard to individually resolve.

Detection of in-plane wave motion through use of the lateral deflection channel was demonstrated, showing that it was possible to detect the in-plane waves simultaneously with (but independent from) out-of-plane detection. The lateral deflection was shown to be a measure of in-plane motion by the higher relative amplitude of the S0 mode (with primarily in-plane motion) compared to the A0 mode (with primarily out-of-plane motion) while the A0 mode dominated in the normal deflection channel, as expected. This was further confirmed by comparing signals taken where the incidence angle of the wave relative to the cantilever was changed, finding that there was a strong dependence on angle, including an inversion in direction as the centreline was passed, as was expected. Such ability to detect in-plane motion simultaneously (in both time and position) with, but as a distinct signal from, out-of-plane motion represents a significant advantage over piezoelectric transducer and EMAT based detection, where this is not possible, and laser based detection, where this is possible though requires a significantly more complicated set up. This in-plane detection was, however, limited to only a single axis, meaning that complete information about the surface motion is not available. Therefore, in experiments using AFM for in-plane detection, care should be taken to ensure the cantilever is oriented such that the length of the cantilever is perpendicular to the direction of in-plane motion that is of interest.

Using a commercial AFM resulted in some limitations on samples that could be tested. While the Asylum Research MFP-3D has a large and open scanning stage

and a manually adjustable height, allowing for larger samples to be used than in a typical AFM, it still posed significant restrictions on what can be used. Firstly, the separation of the legs that hold the head up mean that the samples must have one dimension no larger than 8 cm and samples close to this size must be particularly oriented (as was the case in many of the experiments here). Secondly, the height of the head is not infinitely adjustable, resulting in a maximum sample thickness of a few centimetres. Additionally, the lack of any automated long range height control of the tip means that the samples must be flat and smooth such that the variation in height over a scanned area is less than the range of motion of the Z piezoelectric actuator, which is 40 μm for this equipment. The scanning stage design also meant that lateral motion of the sample was limited to about a 5 mm square, preventing any longer range measurements from being taken.

The limitations of this AFM in regards to both bandwidth and sample size mean that there are two primary directions that AFM based ultrasonic NDT could be taken. The first of these is to custom build an AFM-like detector that is more suitable for ultrasonic NDT measurements. This would entail using a four quadrant photodiode based measurement system with the photodiode and electronics chosen for higher frequency operation. A piezoelectric actuator would need to be present on the Z axis for engaging, though further motion would be achieved by mounting this to a standard stepper motor based stage with three axes of motion. This would allow for scanning of large areas of samples with fewer restrictions on size, as well as the ability to adjust the height of the detector to allow for rougher or uneven samples. This would primarily be useful for the simultaneous detection of two directions of wave motion.

An alternative direction would be to focus on microscopic detection, which could be done using a commercial AFM, with modern high speed AFMs being preferable for their higher bandwidth capabilities. For this, laser generation of ultrasound would be the ideal source due to the ability to generate close to the cantilever without creating a physical obstruction within the AFM, with the bandwidth capability and small spatial extent of the generation point also being beneficial. Such experiments could be used to look at micro-cracking in small samples, such as silicon wafers, taking advantage of the AFM's high spatial resolution and sensitivity. Some difficulty may be encountered in aligning the generation laser within the confines of the AFM system. Care would also have to be taken to ensure that the high power laser would not interfere with the AFM operation (e.g. by saturating the photodiode with scatter reflections) or even damaging parts of the AFM (such as the photodiode or the often present digital camera).

Chapter 6

Conclusions and Future Work

This thesis details the development and application of AFM based techniques for probing nanomechanical properties, with the focus for much of the work being the combination of AFM with ultrasound. As shown, the AFM can probe materials in many ways and although most of the existing literature on AFM probes low frequency interactions between tip and surface, advances in hardware and understanding mean that in the future higher frequency, in particular ultrasonic, interactions will surely become more important. To conclude, this chapter summarises the conclusions of the work presented here and outlines interesting potential future work.

6.1 Mechanical Properties of Suspended Films

In chapter 3 the mechanical properties of 2D materials were investigated through indentation measurements. These were used to measure the elastic moduli and breaking strengths of CVD grown graphene and graphene derived materials. First, CVD grown graphene was tested and it was found that it had properties in line with those previously reported for pristine graphene (e.g. from exfoliation of graphite). The CVD grown graphene was also heated, a common step in the transfer procedure of CVD grown graphene to remove polymer residue from the sample, and this was found to cause a significant drop in the stiffness. This drop is similar to that seen in previous research on CVD grown graphene, implying that the relatively poor mechanical properties found in that research were a result of the transfer process and not the growth method.

The CVD grown graphene was also functionalised by exposure to atomic oxygen in UHV. This was found to significantly reduce both the stiffness and breaking strength, with longer exposures (and thus higher functionalisation) resulting in

greater reductions. After a certain duration (here 4 minutes, though this is variable with functionalisation method) the properties appeared to stop changing and were in line with the properties of graphene oxide (GO) sheets (produced directly using the Hummers' method) measured in the same way, suggesting that there is a limit to the effect of functionalisation on mechanical properties. TEM, Raman, and XPS measurements were also acquired, showing that the changes in mechanical properties correlated to the formation of extended topological defects. The sizes of the holes created at the breaking point were estimated by analysis of the force curves recorded at the breaking point, finding that higher functionalisation resulted in smaller holes. This supports the theory that the breaking is limited by the defects. Furthermore, similar results reported in the literature for a reduction in mechanical properties from defects created through plasma exposure suggests that the reduction is a generic feature of these topological defects.

The results were acquired through the creation of an automated technique that enabled the measurement of many holes on a grid without need for user interaction, thus enabling the collection of large datasets and statistically significant results. This method therefore provides a way to test many different samples easily, which may help in the development of materials with tunable properties, including uses such as composites. With regards to the work here on functionalised graphene, GO that has been reduced towards graphene would be interesting to investigate to see whether the mechanical properties of graphene could be recovered or if the continued presence of the topological defects would maintain the reduced mechanical properties of GO. Some early testing was done on this, suggesting that the reduction did not improve the mechanical properties, though problems encountered in achieving monolayer coverage of GO on the grids used made these results unreliable, though further experimentation could improve this. Some recent work [359] has also suggested that very low defect counts in graphene can increase the stiffness, which warrants further investigation using different defect creation techniques. There are a wide variety of other 2D materials that could also be investigated using this method, such as other functionalised forms of graphene, hexagonal boron nitride, and many others.

One area of interest with suspended graphene is its potential as a resonator for use in nanoelectromechanical systems (NEMS), for applications such as highly sensitive mass and temperature detection [360,361]. The oscillatory behaviour depends on the mechanical properties of the graphene, as has been measured here, but it is useful to directly measure the resonance behaviour (particularly the frequency and Q factor). Such measurements have been done using laser interferometry [362],

including spatial mapping of the resonance modes [363]. However, laser interferometers have a limited spatial resolution compared to the scale of a typical nanoresonator ($\sim 1 \mu\text{m}$ across), hence an AFM might be able to provide higher resolution measurements. This may be possible through the use of an electrostatic force microscopy (EFM) like technique, in which the tip is scanned at a set height over the sample (known from a previous scan of the sample) while oscillating at resonance. Any long range forces from the sample will cause a shift of the cantilever's resonance frequency, which can be tracked with a phase locked loop. By applying a potential difference between the tip and the sample a capacitive force is set up. The measured frequency shift is then proportional to the force gradient [43], which will vary based on the separation and thus oscillations of the resonator. Typical resonator frequencies are much higher than cantilever resonant frequencies, so the change in force gradient will be an average over a membrane oscillation and, as the force gradient is not proportional to distance, this will be different for different amplitude oscillations. A possible limitation is that the presence of the tip may affect the oscillation of the membrane due to the reciprocal force, and the tip has a much higher mass than the membrane, though the resonance shift technique is very sensitive and thus this force can be minimised.

6.2 Ultrasonic Force Microscopy

In chapter 4 the ultrasonic force microscopy (UFM) technique, in which the sample is oscillated at high frequencies to image contrast in the surface's mechanical properties, was investigated. First the parameters of UFM operation were tested. The ultrasonic driving frequency was shown to be a very important consideration — here there was a transitional region from frequencies for normal AFM operation up to the UFM regime that extended in frequency to about 25 times the cantilever's free air resonance frequency. The ultrasonic signal is also amplitude modulated at a frequency below the cantilever resonance and it was found that variations on this modulation frequency had little effect on the response signal, provided that it was above the filtering frequency for topographical feedback. A simulation of UFM response was also created and compared to experimental results for varying drive amplitude and load force. It was found that the simulation qualitatively predicted the behaviour, though some features seen in the experimental results at extreme loads were not seen in the simulation.

The simulation results highlighted one of the areas in which UFM is weak — the difficulty in quantitative analysis of common physical parameters, such as

the Young's modulus. This is partially due to the complicated dependence of the response on many factors as well as the sample properties, such as tip radius and drive amplitude, though even with these being presumed constant throughout the experiment the simulation results did not fully align with experimental results. Further investigation into the behaviour of the UFM system is necessary to fully model the response and thus give reliable quantitative results. An alternative approach to quantification is the use of calibration samples, using results from regions of known mechanical properties to calibrate the expected response amplitudes. This would still not be ideal, however, as the secondary factors (such as adhesion) could easily change between calibration sample and measured sample. Also, if the calibration sample was separate to the experimental sample (i.e. there were no calibration regions on the experimental sample) then the drive amplitude would also have to be calibrated between the two samples (e.g. using an interferometer), as the ultrasonic coupling between the transducer and samples could vary.

The behaviour of UFM when investigating samples with Young's moduli similar to the tip was also tested using a gold on silicon sample. It was found that samples with similar or greater Young's moduli than the tip result in reduced contrast due to the deformation contribution from the tip being significant. This could even cause contrast inversion (where a harder region appears softer according to the UFM image) due to contributions from secondary factors (such as adhesion). Further testing with a much harder tip (coated in diamond-like carbon rather than bare silicon nitride) showed a significant improvement in contrast.

UFM is unusual among mechanical measurement techniques in AFM as it only operates half of the time, with the other half of the time being regular contact mode AFM, with both halves occurring at every pixel of the scan. This was used to implement other contact mode techniques (here conductive AFM and friction force microscopy) simultaneously with UFM. This makes UFM unique in its capability for single pass multifunctional imaging of samples, including a mechanical property channel. UFM also displays a superlubricity phenomenon, in which no long term lateral forces are applied to the sample, enabling the imaging of delicate samples. In combination with the "half and half" functionality this means that contact mode techniques can be applied to samples that are typically damaged by regular contact mode scanning, as was done here with conductive imaging of a carbon nanotube network [364].

The "half and half" operation of the UFM mode could be used to study a variety of samples with correlated multifunctional properties. For example, graphene and nanotube fillers are being used to modify the properties of composites, includ-

ing mechanical properties and thermal and electrical conductivity. Simultaneous measurement of these properties on the nanoscale will aid understanding and development of these materials. In other materials, changes in functional properties can be related to changes in mechanical properties. For example in phase change materials functional property changes are caused by modifications to the structure. The capability to scan delicate samples expands the range of materials that can be investigated, such as soft polymer samples which are difficult to scan in contact mode though often have useful electrical properties. Some difficulties may be encountered in scanning polymers with UFM, however, as their low elastic moduli will mean that the cantilever response could be reduced and may not be high enough to enter UFM operation, thus not benefiting from the superlubricity effect.

6.3 Ultrasonic Non Destructive Testing in an AFM

Finally, in chapter 5, the use of AFM as a detector for ultrasonic non-destructive testing (NDT) was demonstrated. This was achieved by a series of measurements of electromagnetic acoustic transducer (EMAT) generated Lamb waves in an aluminium plate, demonstrating that the measured signals using an AFM were the same as expected from the known dispersion curves for Lamb waves. These results were also compared to results from piezoelectric transducer and interferometer detection, finding that the AFM produced results similar to these common techniques but with a higher spatial resolution. A slot was laser machined into the aluminium and changes in response around this were measured, finding the expected loss in amplitude beyond the slot and near-field enhancement effects before the slot, further confirming that the AFM is a suitable detector in ultrasonic NDT experiments.

The limitations and benefits of AFM detection were also discussed. It was found that the AFM had a comparable sensitivity to other techniques, though the bandwidth was limited to frequencies below about 300 kHz. Frequency bandwidth could potentially be improved by design of a system purpose built for high frequency detection, particularly through use of a faster photodiode and higher frequency cantilevers. The spatial resolution of the AFM is significantly better than other techniques, capable of measurements across nanometres, comparing favourably to the micrometres possible when using interferometers and millimetres with piezoelectric transducers and EMATs. The frequency limitations do pose some issues for the spatial resolution, however, as features significantly smaller than the wavelength may have weak interactions with the ultrasonic wave and features with separations significantly shorter than the wavelength may be difficult to resolve. These problems

are diminished in the near-field of the features, where the immediate effects (such as enhancement and reduced transmission) can be seen, and improvement to frequency bandwidth would also help significantly here.

It was also demonstrated that the lateral deflection channel could be used to detect one component of the surface's in-plane motion, by detecting changes in the signal as the angle between the cantilever and sample was changed. This could be done simultaneously with the out-of-plane detection using the normal deflection channel, while both signals are independent. Such simultaneous and independent measurements are significantly more difficult to do using the conventional techniques, presenting a significant advantage to AFM detection. Such capabilities would be particularly useful for interpreting the mode content of the signals, as different modes have different distributions between the motions, allowing for further understanding of the origin of the seen signals and thus interpretation of their causes.

Further work in this area would be focussed on moving past the limitations imposed by the commercial AFM system used for the experiments here. One such limitation is the sample size — samples tested must be smaller than the sample stage (here the limit was mainly a maximum dimension of 8 cm due to the AFM head's "legs") and have surface feature heights smaller than the Z range of the AFM (here 40 μm). Testing area was also limited by the sample stage, with even the "long range" modifications limited to a 5 mm square on the equipment used here. The solution to this would be to build a custom detector system that worked similarly to an AFM — a cantilever with a laser reflection four quadrant photodiode detection system, plus a fine Z approach piezoelectric actuator. This could then be mounted in place of a conventional detector on a 3-axis stepper motor stage, allowing for long distance motion in 3D and the scanning of large arbitrarily shaped samples. The main advantage to this approach is the simultaneous in-plane and out-of-plane detection, and significantly improved spatial resolution over EMATs and piezoelectric transducers (though the precision of the stepper motors means interferometers with a small spot size would likely have a similar spatial resolution).

Further use of commercial systems could also be a possibility, with the higher bandwidth of newer generation AFMs having significant benefit. Here the focus would be on microscopic detection, where the limitations of the sample stage would not be a factor. The main barrier to this would be the localised generation of ultrasonic waves necessary for ultrasonic NDT as EMATs and piezoelectric transducers can be bulky and hard to mount effectively on small samples. The solution would be to use laser generation, for which most of the equipment can be separate from the sample, requiring only a light path to use. Some concerns about the effect of the

high powered generation laser on the AFM would have to be considered, such as the possibility that the scattered reflections may saturate the photodiode. This set up would be ideal for looking at microcracking on small samples and would primarily benefit from the high spatial resolution and detection sensitivity the AFM offers.

Bibliography

- [1] Binnig, G., Quate, C., and Gerber, C. Atomic force microscope. *Physical Review Letters*, 56(9):930–933, 1986.
- [2] Binnig, G.K. Atomic-force microscopy. *Physica Scripta*, T19:53–54, 1987.
- [3] Binnig, G. and Rohrer, H. Scanning tunneling microscopy - from birth to adolescence. *Nobel Lecture*, 1986.
- [4] Binnig, G., Rohrer, H., Gerber, C., and Weibel, E. Tunneling through a controllable vacuum gap. *Applied Physics Letters*, 40(2):178–180, 1982.
- [5] Binnig, G. and Rohrer, H. Scanning tunneling microscopy. *Surface Science*, 126(1-3):236–244, 1983.
- [6] Giessibl, F.J. AFM’s path to atomic resolution. *Materials Today*, 8(5):32–41, 2005.
- [7] Picco, L., Bozec, L., Ulcinas, A., et al. Breaking the speed limit with atomic force microscopy. *Nanotechnology*, 18(4):044030, 2007.
- [8] Schitter, G. and Rost, M.J. Scanning probe microscopy at video-rate. *Materials Today*, 11:40–48, 2008.
- [9] Meyer, E., Hug, H.J., and Bennewitz, R. *Scanning Probe Microscopy: The Lab on a Tip*. Springer, 2003.
- [10] Beléndez, T., Neipp, C., and Beléndez, A. Large and small deflections of a cantilever beam. *European Journal of Physics*, 23(3):371–379, 2002.
- [11] Meyer, G. and Amer, N. Novel optical approach to atomic force microscopy. *Applied Physics Letters*, 53(12):1045, 1988.
- [12] Alexander, S., Hellemans, L., Marti, O., et al. An atomic-resolution atomic-force microscope implemented using an optical lever. *Journal of Applied Physics*, 65(1):164–167, 1989.

- [13] Marti, O., Colchero, J., and Mlynek, J. Combined scanning force and friction microscopy of mica. *Nanotechnology*, 1(2):141–144, 1990.
- [14] Hipp, M., Bielefeldt, H., Colchero, J., Marti, O., and Mlynek, J. A stand-alone scanning force and friction microscope. *Ultramicroscopy*, 42-44:1498–1503, 1992.
- [15] Thaysen, J., Boisen, A., Hansen, O., and Bouwstra, S. Atomic force microscopy probe with piezoresistive read-out and a highly symmetrical Wheatstone bridge arrangement. *Sensors and Actuators, A*, 83(1):47–53, 2000.
- [16] Dukic, M., Adams, J.D., and Fantner, G.E. Piezoresistive AFM cantilevers surpassing standard optical beam deflection in low noise topography imaging. *Scientific Reports*, 5(November):16393, 2015.
- [17] Stahl, U., Yuan, C.W., De Lozanne, A.L., and Tortonese, M. Atomic force microscope using piezoresistive cantilevers and combined with a scanning electron microscope. *Applied Physics Letters*, 65(22):2878–2880, 1994.
- [18] Mick, U., Eichhorn, V., Wortmann, T., Diederichs, C., and Fatikow, S. Combined nanorobotic AFM/SEM system as novel toolbox for automated hybrid analysis and manipulation of nanoscale objects. In *2010 IEEE International Conference on Robotics and Automation*, pages 4088–4093. IEEE, 2010.
- [19] Moheimani, S.O.R. Invited Review Article: Accurate and fast nanopositioning with piezoelectric tube scanners: Emerging trends and future challenges. *Review of Scientific Instruments*, 79(7):071101, 2008.
- [20] Huy Hoang Pham, and I-Ming Chen, . Kinematics, workspace and static analyses of 2-DOF flexure parallel mechanism. In *7th International Conference on Control, Automation, Robotics and Vision, 2002. ICARCV 2002.*, volume 2, pages 968–973. Nanyang Technological Univ, 2002.
- [21] Yao, Q., Dong, J., and Ferreira, P.M. Design, analysis, fabrication and testing of a parallel-kinematic micropositioning XY stage. *International Journal of Machine Tools and Manufacture*, 47(6):946–961, 2007.
- [22] Damjanovic, D. Hysteresis in piezoelectric and ferroelectric materials. In *The Science of Hysteresis*, volume 3, chapter 4, pages 337–465. Elsevier, 2006.
- [23] Jung, H. and Gweon, D.g. Creep characteristics of piezoelectric actuators. *Review of Scientific Instruments*, 71(4):1896–1900, 2000.

- [24] Delibas, B., Arockiarajan, A., and Seemann, W. Rate dependent properties of perovskite type tetragonal piezoelectric materials using micromechanical model. *International Journal of Solids and Structures*, 43(3-4):697–712, 2006.
- [25] Fleming, A.J. A review of nanometer resolution position sensors: Operation and performance. *Sensors and Actuators, A*, 190:106–126, 2013.
- [26] Ricci, D. and Braga, P.C. Recognizing and Avoiding Artifacts in AFM Imaging. In *Atomic Force Microscopy*, volume 242, chapter 3, pages 25–38. Humana Press, New Jersey, 2004.
- [27] Han, W.H., Lindsay, S.M., and Jing, T.W. A magnetically driven oscillating probe microscope for operation in liquids. *Applied Physics Letters*, 69(26):4111–4113, 1996.
- [28] Labuda, A., Cleveland, J., Geisse, N., et al. Photothermal excitation for improved cantilever drive performance in tapping mode atomic force microscopy. *Microscopy and Analysis*, 28(3):23–27, 2014.
- [29] Albrecht, T.R., Gruütter, P., Horne, D., and Rugar, D. Frequency modulation detection using high-Q cantilevers for enhanced force microscope sensitivity. *Journal of Applied Physics*, 69(2):668–673, 1991.
- [30] Lozano, J.R. and Garcia, R. Theory of multifrequency atomic force microscopy. *Physical Review Letters*, 100(7):076102, 2008.
- [31] Marinello, F., Passeri, D., and Savio, E. *Acoustic Scanning Probe Microscopy*. Springer, 2012.
- [32] Huber, M.T. Zur Theorie der berührung fester elastischer körper. *Annalen der Physik*, 319(6):153–163, 1904.
- [33] Derjaguin, B.V., Muller, V.M., and Toporov, Y.P. Effect of contact deformations on the adhesion of particles. *Journal of Colloid and Interface Science*, 53(2):314–326, 1975.
- [34] Johnson, K.L., Kendall, K., and Roberts, A.D. Surface Energy and the Contact of Elastic Solids. *Proceedings of the Royal Society A: Mathematical, Physical and Engineering Sciences*, 324(1558):301–313, 1971.
- [35] Maugis, D. Adhesion of spheres: The JKR-DMT transition using a Dugdale model. *Journal of Colloid And Interface Science*, 150(1):243–269, 1992.

- [36] Fischer-Cripps, A.C. *Nanoindentation*, 2nd edition. Springer-Verlag, 2004.
- [37] Oliver, W.C. and Pharr, G.M. An improved technique for determining hardness and elastic modulus using load and displacement sensing indentation experiments. *Journal of Materials Research*, 7(6):1564–1583, 1992.
- [38] Güthner, P. and Dransfeld, K. Local poling of ferroelectric polymers by scanning force microscopy. *Applied Physics Letters*, 61(9):1137–1139, 1992.
- [39] Majumdar, A., Carrejo, J.P., and Lai, J. Thermal imaging using the atomic force microscope. *Applied Physics Letters*, 62(20):2501–2503, 1993.
- [40] Lai, K., Kundhikanjana, W., Kelly, M., and Shen, Z.X. Modeling and characterization of a cantilever-based near-field scanning microwave impedance microscope. *Review of Scientific Instruments*, 79(6):063703, 2008.
- [41] Martin, Y. and Wickramasinghe, H.K. Magnetic imaging by “force microscopy” with 1000 Å resolution. *Applied Physics Letters*, 50(20):1455–1457, 1987.
- [42] Martin, Y., Abraham, D.W., and Wickramasinghe, H.K. High-resolution capacitance measurement and potentiometry by force microscopy. *Applied Physics Letters*, 52(13):1103–1105, 1988.
- [43] Girard, P. Electrostatic force microscopy: principles and some applications to semiconductors. *Nanotechnology*, 12(4):485–490, 2001.
- [44] Nonnenmacher, M., O’Boyle, M.P., and Wickramasinghe, H.K. Kelvin probe force microscopy. *Applied Physics Letters*, 58(25):2921–2923, 1991.
- [45] Cappella, B. and Dietler, G. Force-distance curves by atomic force microscopy. *Surface Science Reports*, 34(1-3):1–104, 1999.
- [46] Butt, H.J., Cappella, B., and Kappl, M. Force measurements with the atomic force microscope: Technique, interpretation and applications. *Surface Science Reports*, 59(1-6):1–152, 2005.
- [47] Burnham, N.A., Colton, R.J., and Pollock, H.M. Interpretation of force curves in force microscopy. *Nanotechnology*, 4(2):64–80, 1999.
- [48] Tripathy, S. and Berger, E.J. Measuring viscoelasticity of soft samples using atomic force microscopy. *Journal of Biomechanical Engineering*, 131(9):094507, 2009.

- [49] Attard, P. Measurement and interpretation of elastic and viscoelastic properties with the atomic force microscope. *Journal of Physics: Condensed Matter*, 19(47):473201, 2007.
- [50] Rief, M. Reversible unfolding of individual titin immunoglobulin domains by AFM. *Science*, 276(5315):1109–1112, 1997.
- [51] Neuman, K.K.C. and Nagy, A. Single-molecule force spectroscopy: optical tweezers, magnetic tweezers and atomic force microscopy. *Nature Methods*, 5(6):491–505, 2008.
- [52] Kalinin, S.V., Rar, A., and Jesse, S. A decade of piezoresponse force microscopy: Progress, challenges, and opportunities. *IEEE Transactions on Ultrasonics, Ferroelectrics, and Frequency Control*, 53(12):2226–2251, 2006.
- [53] Trache, A. and Meininger, G.A. Atomic force-multi-optical imaging integrated microscope for monitoring molecular dynamics in live cells. *Journal of Biomedical Optics*, 10(6):064023, 2005.
- [54] Trache, A. and Lim, S.M. Live cell response to mechanical stimulation studied by integrated optical and atomic force microscopy. *Journal of Visualized Experiments*, 44:4–7, 2010.
- [55] Sweers, K., van der Werf, K., Bennink, M., and Subramaniam, V. Nanomechanical properties of a-synuclein amyloid fibrils: a comparative study by nanoindentation, harmonic force microscopy and Peakforce QNM. *Nanoscale Research Letters*, 6:270–279, 2011.
- [56] Young, T.J., Monclus, M.A., Burnett, T.L., et al. The use of the PeakForce quantitative nanomechanical mapping AFM-based method for high-resolution Young’s modulus measurement of polymers. *Measurement Science and Technology*, 22(12):125703, 2011.
- [57] Kim, K.S., Lin, Z., Shrotriya, P., Sundararajan, S., and Zou, Q. Iterative control approach to high-speed force-distance curve measurement using AFM: Time-dependent response of PDMS example. *Ultramicroscopy*, 108(9):911–920, 2008.
- [58] Kim, Y., Yang, Y.I., Choi, I., and Yi, J. Dependence of approaching velocity on the force-distance curve in AFM analysis. *Korean Journal of Chemical Engineering*, 27(1):324–327, 2010.

- [59] Cappella, B., Baschieri, P., Frediani, C., Miccoli, P., and Ascoli, C. Improvements in AFM imaging of the spatial variation of force-distance curves: on-line images. *Nanotechnology*, 8(2):82–87, 1999.
- [60] García, R. and San Paulo, A. Attractive and repulsive tip-sample interaction regimes in tapping-mode atomic force microscopy. *Physical Review B*, 60(7):4961–4967, 1999.
- [61] Paulo, Á. and García, R. Tip-surface forces, amplitude, and energy dissipation in amplitude-modulation (tapping mode) force microscopy. *Physical Review B*, 64(19):1–4, 2001.
- [62] Sader, J.E., Uchihashi, T., Higgins, M.J., et al. Quantitative force measurements using frequency modulation atomic force microscopy — theoretical foundations. *Nanotechnology*, 16(3):S94–S101, 2005.
- [63] Paulo, Á.S. and García, R. Unifying theory of tapping-mode atomic-force microscopy. *Physical Review B*, 66(4):041406, 2002.
- [64] Raman, A., Melcher, J., and Tung, R. Cantilever dynamics in atomic force microscopy. *Review Literature And Arts Of The Americas*, 3(1):20–27, 2008.
- [65] Cleveland, J.P., Anczykowski, B., Schmid, A.E., and Elings, V.B. Energy dissipation in tapping-mode atomic force microscopy. *Applied Physics Letters*, 72(20):2613–2615, 1998.
- [66] Anczykowski, B., Gotsmann, B., Fuchs, H., Cleveland, J., and Elings, V. How to measure energy dissipation in dynamic mode atomic force microscopy. *Applied Surface Science*, 140(3-4):376–382, 1999.
- [67] Hurley, D., Kocun, M., Revenko, I., Ohler, B., and Proksch, R. Fast, quantitative AFM nanomechanical measurements using AM-FM viscoelastic mapping mode. *Microscopy and Analysis*, SPM Supple(April):9–13, 2015.
- [68] Garcia, R. and Proksch, R. Nanomechanical mapping of soft matter by bimodal force microscopy. *European Polymer Journal*, 49(8):1897–1906, 2013.
- [69] Yamanaka, K., Maruyama, Y., Tsuji, T., and Nakamoto, K. Resonance frequency and Q factor mapping by ultrasonic atomic force microscopy. *Applied Physics Letters*, 78(13):1939–1941, 2001.

- [70] Rodriguez, B.J., Callahan, C., Kalinin, S.V., and Proksch, R. Dual-frequency resonance-tracking atomic force microscopy. *Nanotechnology*, 18(47):475504, 2007.
- [71] Gannepalli, A., Yablon, D.G., Tsou, A.H., and Proksch, R. Mapping nanoscale elasticity and dissipation using dual frequency contact resonance AFM. *Nanotechnology*, 22(35):355705, 2011.
- [72] Rabe, U., Kopycinska, M., Hirsekorn, S., et al. High-resolution characterization of piezoelectric ceramics by ultrasonic scanning force microscopy techniques G A Schneider and W Arnold. *Journal of Physics D: Applied Physics*, 35:2621–2635, 2002.
- [73] Jesse, S., Kalinin, S.V., Proksch, R., Baddorf, A.P., and Rodriguez, B.J. The band excitation method in scanning probe microscopy for rapid mapping of energy dissipation on the nanoscale. *Nanotechnology*, 18:435503, 2007.
- [74] Yablon, D.G., Gannepalli, A., Proksch, R., et al. Quantitative viscoelastic mapping of polyolefin blends with contact resonance atomic force microscopy. *Macromolecules*, 45(10):4363–4370, 2012.
- [75] Kelley, T.W., Granstrom, E., and Frisbie, C.D. Conducting probe atomic force microscopy: A characterization tool for molecular electronics. *Advanced Materials*, 11(3):261–264, 1999.
- [76] Zou, J., Wang, X.F., Bullen, D., et al. A mould-and-transfer technology for fabricating scanning probe microscopy probes. *Journal Of Micromechanics And Microengineering*, 14(2):204–211, 2004.
- [77] Niedermann, P. Chemical vapor deposition diamond for tips in nanoprobe experiments. *Journal of Vacuum Science & Technology A*, 14(3):1233–1236, 1996.
- [78] Wood, D., Hancox, I., Jones, T.S., and Wilson, N.R. Quantitative nanoscale mapping with temperature dependence of the mechanical and electrical properties of poly(3-hexylthiophene) by conductive atomic force microscopy. *The Journal of Physical Chemistry C*, 119(21):11459–11467, 2015.
- [79] Palacio, M. and Bhushan, B. Nanomechanical and nanotribological characterization of noble metal-coated AFM tips for probe-based ferroelectric data recording. *Nanotechnology*, 19(10):105705, 2008.

- [80] Chung, K.H. Wear characteristics of atomic force microscopy tips: A reivew. *International Journal of Precision Engineering and Manufacturing*, 15(10):2219–2230, 2014.
- [81] Sundararajan, S. and Bhushan, B. Topography-induced contributions to friction forces measured using an atomic force/friction force microscope. *Journal of Applied Physics*, 88(8):4825–4831, 2000.
- [82] Gao, J., Luedtke, W.D., Gourdon, D., et al. Frictional forces and Amontons’ law: From the molecular to the macroscopic scale. *The Journal of Physical Chemistry B*, 108(11):3410–3425, 2004.
- [83] Braun, O.M. Bridging the gap between the atomic-scale and macroscopic modeling of friction. *Tribology Letters*, 39(3):283–293, 2010.
- [84] Bennewitz, R. Friction force microscopy. In Gnecco, E. and Meyer, E., editors, *Fundamentals of Friction and Wear*, chapter 1, pages 3–16. Springer International Publishing, Cham, 2007.
- [85] Kinsler, L.E., Frey, A.R., Coppens, A.B., and Sanders, J.V. *Fundamentals of Acoustics*, 4th edition. John Wiley & Sons, Inc., 2000.
- [86] Cracknell, A.P. *Ultrasonics*. Wykeham Publications, 1980.
- [87] Cheeke, J.D.N. *Fundamentals and Applications of Ultrasonic Waves*, 2nd edition. CRC Press, 2012.
- [88] Viktorov, I.A. *Rayleigh and Lamb Waves*. Plenum Press, 1967.
- [89] Rose, J.L. *Ultrasonic Waves in Solid Media*. Cambridge University Press, 2004.
- [90] Dutton, B., Clough, A.R., and Edwards, R.S. Near field enhancements from angled surface defects; a domparison of scanning laser source and scanning laser detection techniques. *Journal of Nondestructive Evaluation*, 30(2):64–70, 2011.
- [91] Lamb, H. On waves in an elastic plate. *Proceedings of the Royal Society A: Mathematical, Physical and Engineering Sciences*, 93(648):114–128, 1917.
- [92] Rose, J.L. *Ultrasonic Guided Waves in Solid Media*. Cambridge University Press, 2014.

- [93] Auld, B.A. *Acoustic Fields and Waves in Solids, Volume 2*. Krieger Publishing Company, 1990.
- [94] Horn, A. *Ultra-Fast Material Metrology*. Wiley-VCH, 2009.
- [95] Byrne, C.L. *Signal Processing: A Mathematical Approach*, 2nd edition. Taylor & Francis, 2014.
- [96] Blitz, J. and Simpson, G. *Ultrasonic Methods of Non-destructive Testing*. Chapman & Hall, 1995.
- [97] McAughey, K.L., Edwards, R.S., Potter, M.D.G., and Dixon, S. Ultrasonic thickness measurements of sub-millimetre thickness sheets. In *18th World Conference on Nondestructive Testing*, 2012.
- [98] Clough, A.R. and Edwards, R.S. Characterisation of hidden defects using the near-field ultrasonic enhancement of Lamb waves. *Ultrasonics*, 59:64–71, 2015.
- [99] Edwards, R.S., Dixon, S., and Jian, X. Depth gauging of defects using low frequency wideband Rayleigh waves. *Ultrasonics*, 44(1):93–98, 2006.
- [100] Hill, S. and Dixon, S. Localisation of defects with time and frequency measurements using pulsed arrays. *NDT & E International*, 67:24–30, 2014.
- [101] Cooley, J.W. and Tukey, J.W. An algorithm for the machine calculation of complex Fourier Series. *Mathematics of Computation*, 19(90):297–301, 1965.
- [102] Heideman, M.T., Johnson, D.H., and Burrus, C.S. Gauss and the history of the fast Fourier transform. *IEEE ASSP Magazine*, 1(4):14–21, 1984.
- [103] Cooley, J.W. The re-discovery of the fast Fourier transform algorithm. *Mikrochimica Acta*, 93(1-6):33–45, 1987.
- [104] Stanković, L., Daković, M., and Thayaparan, T. *Time-Frequency Signal Analysis with Applications*. Artech House, 2014.
- [105] Gabor, D. Theory of communication. Part 3: Frequency compression and expansion. *Journal of the Institution of Electrical Engineers - Part III: Radio and Communication Engineering*, 93(26):445–457, 1946.
- [106] Clough, A.R. and Edwards, R.S. Scanning laser source Lamb wave enhancements for defect characterisation. *NDT & E International*, 62:99–105, 2014.

- [107] Nelson, W.G. *Piezoelectric Materials: Structure, Properties, and Applications*. Nova Science Publishers, 2010.
- [108] Van Randeraat, J. and Setterington, R.E. *Piezoelectric Ceramics*, 2nd edition. Mullard, 1974.
- [109] Jaffe, B. *Piezoelectric Ceramics*. Academic Press, 1971.
- [110] Damjanovic, D. Materials for high temperature piezoelectric transducers. *Current Opinion in Solid State and Materials Science*, 3(5):469–473, 1998.
- [111] Burrows, S.E., McAughey, K.L., Edwards, R.S., and Dixon, S. Sol-gel prepared bismuth titanate for high temperature ultrasound transducers. *RSC Advances*, 2(9):3678–3683, 2012.
- [112] Panda, P.K. Review: Environmental friendly lead-free piezoelectric materials. *Journal of Materials Science*, 44(19):5049–5062, 2009.
- [113] Rödel, J., Jo, W., Seifert, K.T.P., et al. Perspective on the development of lead-free piezoceramics. *Journal of the American Ceramic Society*, 92(6):1153–1177, 2009.
- [114] Aksel, E. and Jones, J.L. Advances in lead-free piezoelectric materials for sensors and actuators. *Sensors*, 10(3):1935–1954, 2010.
- [115] Kholkin, A.L., Pertsev, N.A., and Goltsev, A.V. Piezoelectricity and Crystal Symmetry. In *Piezoelectric and Acoustic Materials for Transducer Applications*, pages 17–38. Springer US, Boston, MA, 2008.
- [116] Perovskite Structure of PZT. <https://commons.wikimedia.org/wiki/File:Perovskite.svg>. Accessed 2016-09-29.
- [117] Izyumskaya, N., Alivov, Y.I., Cho, S.J., et al. Processing, structure, properties, and applications of PZT thin films. *Critical Reviews in Solid State and Materials Sciences*, 32(3):111–202, 2007.
- [118] Ribichini, R., Nagy, P.B., and Ogi, H. The impact of magnetostriction on the transduction of normal bias field EMATs. *NDT & E International*, 51:8–15, 2012.
- [119] Hirao, M. and Ogi, H. *EMATs for Science and Industry: Noncontacting Ultrasonic Measurements*. Springer, 2003.

- [120] Dixon, S. and Palmer, S.B. Wideband low frequency generation and detection of Lamb and Rayleigh waves using electromagnetic acoustic transducers (EMATs). *Ultrasonics*, 42(10):1129–1136, 2004.
- [121] Dixon, S. and Jian, X. Eddy current generation enhancement using ferrite for electromagnetic acoustic transduction. *Applied Physics Letters*, 89(19):193503, 2006.
- [122] Dutton, B., Boonsang, S., and Dewhurst, R.J. A new magnetic configuration for a small in-plane electromagnetic acoustic transducer applied to laser-ultrasound measurements: Modelling and validation. *Sensors and Actuators A*, 125(2):249–259, 2006.
- [123] Morrison, J.P., Dixon, S., Potter, M.D.G., and Jian, X. Lift-off compensation for improved accuracy in ultrasonic lamb wave velocity measurements using electromagnetic acoustic transducers (EMATs). *Ultrasonics*, 44:e1401–e1404, 2006.
- [124] Ribichini, R. *Modelling of Electromagnetic Acoustic Transducers*. Phd thesis, Imperial College London, 2011.
- [125] Blitz, J. *Electrical and Magnetic Methods of Non-destructive Testing*, second edition. Chapman & Hall, 2012.
- [126] Jian, X., Dixon, S., and Edwards, R.S. Ultrasonic field modelling for arbitrary non-contact transducer source. In Lopez, J.F., Quan, C., Chau, F.S., et al., editors, *Proceedings of SPIE*, volume 5852, pages 515–519, 2005.
- [127] Palmer, S.B. and Dixon, S. Industrially viable non-contact ultrasound. *Insight: Non-Destructive Testing and Condition Monitoring*, 45(3):211–217, 2003.
- [128] Jian, X., Dixon, S., Grattan, K.T.V., and Edwards, R.S. A model for pulsed Rayleigh wave and optimal EMAT design. *Sensors and Actuators, A*, 128(2):296–304, 2006.
- [129] Ribichini, R., Cegla, F., Nagy, P.B., and Cawley, P. Study and comparison of different EMAT configurations for SH wave inspection. *IEEE Transactions on Ultrasonics, Ferroelectrics, and Frequency Control*, 58(12):2571–2581, 2011.
- [130] Rosli, M.H., Edwards, R.S., and Fan, Y. In-plane and out-of-plane measurements of Rayleigh waves using EMATs for characterising surface cracks. *NDT & E International*, 49:1–9, 2012.

- [131] Scruby, C.B. Some applications of laser ultrasound. *Ultrasonics*, 27(4):195–209, 1989.
- [132] Scruby, C.B. and Drain, L.E. *Laser Ultrasonics Techniques and Applications*. CRC Press, 1990.
- [133] Davies, S.J., Edwards, C., Taylor, G.S., and Palmer, S.B. Laser-generated ultrasound: its properties, mechanisms and multifarious applications. *Journal of Physics D: Applied Physics*, 26(3):329–348, 1993.
- [134] Sharples, S.D., Light, R.A., Achamfuo-Yeboah, S.O., Clark, M., and Somekh, M.G. The SKED: speckle knife edge detector. *Journal of Physics: Conference Series*, 520(1):012004, 2014.
- [135] Michelson, A.A. and Morley, E.W. On the relative motion of the Earth and the luminiferous ether. *American Journal of Science*, s3-34(203):333–345, 1887.
- [136] Klein, M.B., Bacher, G.D., Grunnet-Jepsen, A., Wright, D., and Moerner, W.E. Homodyne detection of ultrasonic surface displacements using two-wave mixing in photorefractive polymers. *Optics Communications*, 162(1):79–84, 1999.
- [137] Kamshilin, A.A., Päiväsaari, K., Klein, M., and Pouet, B. Adaptive interferometer using self-induced electro-optic modulation. *Applied Physics Letters*, 77(25):4098–4100, 2000.
- [138] Ashkin, A., Boyd, G.D., Dziedzic, J.M., et al. Optically-induced refractive index inhomogeneities in LiNbO_3 and LiTaO_3 . *Applied Physics Letters*, 9(1):72–74, 1966.
- [139] Hall, T.J., Jaura, R., Connors, L.M., and Foote, P.D. The photorefractive effect-a review. *Progress in Quantum Electronics*, 10(2):77–146, 1985.
- [140] Leendertz, J.A. Interferometric displacement measurement on scattering surfaces utilizing speckle effect. *Journal of Physics E: Scientific Instruments*, 3(3):214–218, 1970.
- [141] Jacquot, P. Speckle interferometry: A review of the principal methods in use for experimental mechanics applications. *Strain*, 44(1):57–69, 2008.
- [142] Kim, B., Lee, J., and Lee, S. New design and analysis for point-focusing of surface waves in contact testing. *IEEE Transactions on Ultrasonics, Ferroelectrics and Frequency Control*, 40(2):162–166, 1993.

- [143] Thring, C.B., Fan, Y., and Edwards, R.S. Focused Rayleigh wave EMAT for characterisation of surface-breaking defects. *NDT & E International*, 81:20–27, 2016.
- [144] Guo, Z., Achenbach, J.D., and Krishnaswamy, S. EMAT generation and laser detection of single lamb wave modes. *Ultrasonics*, 35(6):423–429, 1997.
- [145] Stratoudaki, T., Hernandez, J.A., Clark, M., et al. Cheap optical transducers (CHOTs) for narrowband ultrasonic applications. *Measurement Science and Technology*, 18(3):843–851, 2007.
- [146] Torii, A., Sasaki, M., Hane, K., and Okuma, S. A method for determining the spring constant of cantilevers for atomic force microscopy. *Measurement Science and Technology*, 7(2):179–184, 1999.
- [147] Cleveland, J.P., Manne, S., Bocek, D., and Hansma, P.K. A nondestructive method for determining the spring constant of cantilevers for scanning force microscopy. *Review of Scientific Instruments*, 64(2):403–405, 1993.
- [148] Sader, J.E., Larson, I., Mulvaney, P., and White, L.R. Method for the calibration of atomic force microscope cantilevers. *Review of Scientific Instruments*, 66(7):3789–3798, 1995.
- [149] Hutter, J.L. and Bechhoefer, J. Calibration of atomic-force microscope tips. *Review of Scientific Instruments*, 64(7):1868–1873, 1993.
- [150] Sader, J.E., Chon, J.W.M., and Mulvaney, P. Calibration of rectangular atomic force microscope cantilevers. *Review of Scientific Instruments*, 70(10):3967–3969, 1999.
- [151] Sader, J.E. Frequency response of cantilever beams immersed in viscous fluids with applications to the atomic force microscope. *Journal of Applied Physics*, 84(1):64–76, 1998.
- [152] Kaye, G.W.C. and Laby, T.H. *Tables of Physical and Chemical Constants*, 16th edition. Longman, 1995.
- [153] Kadoya, K., Matsunaga, N., and Nagashima, A. Viscosity and Thermal Conductivity of Dry Air in the Gaseous Phase. *Journal of Physical and Chemical Reference Data*, 14(4):947–970, 1985.

- [154] Sader, J.E., Pacifico, J., Green, C.P., and Mulvaney, P. General scaling law for stiffness measurement of small bodies with applications to the atomic force microscope. *Journal of Applied Physics*, 97(12):124903, 2005.
- [155] Sader, J.E., Sanelli, J.A., Adamson, B.D., et al. Spring constant calibration of atomic force microscope cantilevers of arbitrary shape. *Review of Scientific Instruments*, 83(10):103705, 2012.
- [156] Sader, J.E. Atomic Force Microscope Cantilevers (Calibration method of Sader). <http://www.ampc.ms.unimelb.edu.au/afm/calibration.html>. Accessed 2016-08-26.
- [157] Liu, W., Bonin, K., and Guthold, M. Easy and direct method for calibrating atomic force microscopy lateral force measurements. *Review of Scientific Instruments*, 78(6):063707, 2007.
- [158] Xie, H., Vitard, J., Haliyo, S., Régnier, S., and Boukallel, M. Calibration of lateral force measurements in atomic force microscopy with a piezoresistive force sensor. *Review of Scientific Instruments*, 79(3):033708, 2008.
- [159] Green, C.P., Lioe, H., Cleveland, J.P., et al. Normal and torsional spring constants of atomic force microscope cantilevers. *Review of Scientific Instruments*, 75(6):1988–1996, 2004.
- [160] Cannara, R.J., Eglin, M., and Carpick, R.W. Lateral force calibration in atomic force microscopy: A new lateral force calibration method and general guidelines for optimization. *Review of Scientific Instruments*, 77(5):053701, 2006.
- [161] Varenberg, M., Etsion, I., and Halperin, G. An improved wedge calibration method for lateral force in atomic force microscopy. *Review of Scientific Instruments*, 74(7):3362–3367, 2003.
- [162] Novoselov, K.S., Jiang, D., Schedin, F., et al. Two-dimensional atomic crystals. *Proceedings of the National Academy of Sciences of the United States of America*, 102(30):10451–10453, 2005.
- [163] Geim, A.K. and Novoselov, K.S. The rise of graphene. *Nature Materials*, 6(3):183–191, 2007.
- [164] Balandin, A.A. Thermal properties of graphene and nanostructured carbon materials. *Nature Materials*, 10(8):569–581, 2011.

- [165] Lee, C., Wei, X., Kysar, J.W., and Hone, J. Measurement of the elastic properties and intrinsic strength of monolayer graphene. *Science*, 321(5887):385–388, 2008.
- [166] Falkovsky, L.A. Optical properties of graphene. *Journal of Physics: Conference Series*, 129:012004, 2008.
- [167] Bunch, J.S., Verbridge, S.S., Alden, J.S., et al. Impermeable atomic membranes from graphene sheets. *Nano Letters*, 8(8):2458–2462, 2008.
- [168] Novoselov, K.S., Geim, A.K., Morozov, S., et al. Electric field effect in atomically thin carbon films. *Science*, 306(5696):666–669, 2004.
- [169] Paton, K.R., Varrla, E., Backes, C., et al. Scalable production of large quantities of defect-free few-layer graphene by shear exfoliation in liquids. *Nature Materials*, 13(6):624–630, 2014.
- [170] Hernandez, Y., Nicolosi, V., Lotya, M., et al. High yield production of graphene by liquid phase exfoliation of graphite. *Nature Nanotechnology*, 3(9):563–8, 2008.
- [171] Reina, A., Jia, X., Ho, J., et al. Large area, few-layer graphene films on arbitrary substrates by chemical vapor deposition. *Nano Letters*, 9(1):30–35, 2009.
- [172] Kim, K.S.K.S., Zhao, Y., Jang, H., et al. Large-scale pattern growth of graphene films for stretchable transparent electrodes. *Nature*, 457(7230):706–710, 2009.
- [173] Li, X., Cai, W., An, J., et al. Large-area synthesis of high-quality and uniform graphene films on copper foils. *Science*, 324(5932):1312–4, 2009.
- [174] Bae, S., Kim, H., Lee, Y., et al. Roll-to-roll production of 30-inch graphene films for transparent electrodes. *Nature Nanotechnology*, 5(8):574–578, 2010.
- [175] Dreyer, D.R., Todd, A.D., and Bielawski, C.W. Harnessing the chemistry of graphene oxide. *Chemical Society Reviews*, 43(15):5288–301, 2014.
- [176] Lerf, A., He, H., Forster, M., and Klinowski, J. Structure of graphite oxide revisited. *Journal of Physical Chemistry B*, 102(23):4477–4482, 1998.
- [177] He, H.Y., Klinowski, J., Forster, M., and Lerf, A. A new structural model for graphite oxide. *Chemical Physics Letters*, 287(1-2):53–56, 1998.

- [178] Zhu, Y., Murali, S., Cai, W., et al. Graphene and graphene oxide: Synthesis, properties, and applications. *Advanced Materials*, 22(35):3906–3924, 2010.
- [179] Hummers, W.S. and Offeman, R.E. Preparation of graphitic oxide. *Journal of the American Chemical Society*, 80(6):1339–1339, 1958.
- [180] Li, D., Müller, M.B., Gilje, S., Kaner, R.B., and Wallace, G.G. Processable aqueous dispersions of graphene nanosheets. *Nature Nanotechnology*, 3(2):101–105, 2008.
- [181] Stankovich, S., Dikin, D.A., Piner, R.D., et al. Synthesis of graphene-based nanosheets via chemical reduction of exfoliated graphite oxide. *Carbon*, 45(7):1558–1565, 2007.
- [182] Yang, D., Velamakanni, A., Bozoklu, G., et al. Chemical analysis of graphene oxide films after heat and chemical treatments by X-ray photoelectron and Micro-Raman spectroscopy. *Carbon*, 47(1):145–152, 2009.
- [183] Barinov, A., Malcioglu, O.B., Fabris, S., et al. Initial stages of oxidation on graphitic surfaces: Photoemission study and density functional theory calculations. *The Journal of Physical Chemistry C*, 113(21):9009–9013, 2009.
- [184] Hossain, M.Z., Johns, J.E., Bevan, K.H., et al. Chemically homogeneous and thermally reversible oxidation of epitaxial graphene. *Nature Chemistry*, 4(4):305–309, 2012.
- [185] Marsden, A.J., Brommer, P., Mudd, J.J., et al. Effect of oxygen and nitrogen functionalization on the physical and electronic structure of graphene. *Nano Research*, 8(8):1–16, 2015.
- [186] Leconte, N., Moser, J., Ordejón, P., et al. Damaging graphene with ozone treatment: A chemically tunable metal-insulator transition. *ACS Nano*, 4(7):4033–4038, 2010.
- [187] Yuan, J., Ma, L.P., Pei, S., et al. Tuning the electrical and optical properties of graphene by ozone treatment for patterning monolithic transparent electrodes. *ACS Nano*, 7(5):4233–4241, 2013.
- [188] McEvoy, N., Nolan, H., Ashok Kumar, N., Hallam, T., and Duesberg, G.S. Functionalisation of graphene surfaces with downstream plasma treatments. *Carbon*, 54(1):283–290, 2013.

- [189] Kuila, T., Bose, S., Mishra, A.K., et al. Chemical functionalization of graphene and its applications. *Progress in Materials Science*, 57(7):1061–1105, 2012.
- [190] Kim, H., Abdala, A.A., and Macosko, C.W. Graphene/polymer nanocomposites. *Macromolecules*, 43(16):6515–6530, 2010.
- [191] Yang, X., Li, L., Shang, S., and Tao, X.M. Synthesis and characterization of layer-aligned poly(vinyl alcohol)/graphene nanocomposites. *Polymer*, 51(15):3431–3435, 2010.
- [192] Potts, J.R., Dreyer, D.R., Bielawski, C.W., and Ruoff, R.S. Graphene-based polymer nanocomposites. *Polymer*, 52(1):5–25, 2011.
- [193] Head Graphne XT Tennis Racquets. <http://www.head.com/en/sports/tennis/technology/graphene-xt/>. Accessed 2016-07-28.
- [194] Vittoria Graphene Enhanced Bicycle Wheels. <https://www.vittoria.com/graphene-evidence/>. Accessed 2016-07-28.
- [195] Ramanathan, T., Abdala, A.A., Stankovich, S., et al. Functionalized graphene sheets for polymer nanocomposites. *Nature Nanotechnology*, 3(6):327–331, 2008.
- [196] Pokharel, P., Pant, B., Pokhrel, K., et al. Effects of functional groups on the graphene sheet for improving the thermomechanical properties of polyurethane nanocomposites. *Composites Part B: Engineering*, 78:192–201, 2015.
- [197] Nair, R.R., Wu, H.A., Jayaram, P.N., Grigorieva, I.V., and Geim, A.K. Unimpeded permeation of water through helium-leak-tight graphene-based membranes. *Science*, 335(6067):442–444, 2012.
- [198] Scharfenberg, S., Rocklin, D.Z., Chialvo, C., et al. Probing the mechanical properties of graphene using a corrugated elastic substrate. *Applied Physics Letters*, 98(9):1–3, 2011.
- [199] Frank, I.W., Tanenbaum, D.M., van der Zande, A.M., and McEuen, P.L. Mechanical properties of suspended graphene sheets. *Journal of Vacuum Science & Technology B*, 25(6):2558, 2007.
- [200] Poot, M. and Van Der Zant, H.S.J. Nanomechanical properties of few-layer graphene membranes. *Applied Physics Letters*, 92(6):1–4, 2008.

- [201] Komaragiri, U., Begley, M.R., and Simmonds, J.G. The mechanical response of freestanding circular elastic films under point and pressure loads. *Journal of Applied Mechanics*, 72(2):203–212, 2005.
- [202] Wan, K.T., Guo, S., and Dillard, D.A. A theoretical and numerical study of a thin clamped circular film under an external load in the presence of a tensile residual stress. *Thin Solid Films*, 425(1-2):150–162, 2003.
- [203] Al-Jishi, R. and Dresselhaus, G. Lattice-dynamical model for graphite. *Physical Review B*, 26(8):4514–4522, 1982.
- [204] Blakslee, O.L., Proctor, D.G., Seldin, E.J., Spence, G.B., and Weng, T. Elastic constants of compression-annealed pyrolytic graphite. *Journal of Applied Physics*, 41(8):3373–3382, 1970.
- [205] Rasool, H.I., Ophus, C., Klug, W.S., Zettl, A., and Gimzewski, J.K. Measurement of the intrinsic strength of crystalline and polycrystalline graphene. *Nature Communications*, 4:2811–2817, 2013.
- [206] Zandiatashbar, A., Lee, G.H., An, S.J., et al. Effect of defects on the intrinsic strength and stiffness of graphene. *Nature Communications*, 5:3186, 2014.
- [207] Suk, J.W., Piner, R.D., An, J., and Ruoff, R.S. Mechanical Properties of Monolayer Graphene Oxide. *ACS Nano*, 4(11):6557–6564, 2010.
- [208] Cao, C., Daly, M., Singh, C.V., Sun, Y., and Filleter, T. High strength measurement of monolayer graphene oxide. *Carbon*, 81(1):497–504, 2015.
- [209] Wilson, N.R., Marsden, A.J., Saghir, M., et al. Weak mismatch epitaxy and structural feedback in graphene growth on copper foil. *Nano Research*, 6(2):99–112, 2013.
- [210] Zhang, B., Lee, W.H., Piner, R., et al. Low-temperature chemical vapor deposition growth of graphene from toluene on electropolished copper foils. *ACS Nano*, 6(3):2471–2476, 2012.
- [211] Hirata, M., Gotou, T., Horiuchi, S., Fujiwara, M., and Ohba, M. Thin-film particles of graphite oxide 1: High-yield synthesis and flexibility of the particles. *Carbon*, 42(14):2929–2937, 2004.
- [212] Wilson, N.R., Pandey, P.A., Beanland, R., et al. Graphene oxide: Structural analysis and application as a highly transparent support for electron Microscopy. *ACS Nano*, 3(9):2547–2556, 2009.

- [213] Ruiz-Vargas, C.S., Zhuang, H.L., Huang, P.Y., et al. Softened elastic response and unzipping in chemical vapor deposition graphene membranes. *Nano Letters*, 11(6):2259–2263, 2011.
- [214] Lee, G.H., Cooper, R.C., An, S.J., et al. High-strength chemical-vapor-deposited graphene and grain boundaries. *Science*, 340(6136):1073–1076, 2013.
- [215] Chen, S., Brown, L., Levendorf, M., et al. Oxidation resistance of graphene-coated Cu and Cu Ni alloy. *ACS Nano*, 5(2):1321–1327, 2011.
- [216] Marsden, A.J., Skilbeck, M.S., Healey, M., et al. From graphene to graphene oxide: the evolution of the atomic structure. *Unpublished*, 2016.
- [217] Rourke, J.P., Pandey, P.A., Moore, J.J., et al. The real graphene oxide revealed: Stripping the oxidative debris from the graphene-like sheets. *Angewandte Chemie - International Edition*, 50(14):3173–3177, 2011.
- [218] Ferrari, A.C., Meyer, J.C., Scardaci, V., et al. Raman spectrum of graphene and graphene layers. *Physical Review Letters*, 97(18):187401, 2006.
- [219] Ferrari, A.C. Raman spectroscopy of graphene and graphite: Disorder, electron-phonon coupling, doping and nonadiabatic effects. *Solid State Communications*, 143(1-2):47–57, 2007.
- [220] Pandey, D., Reifengerger, R., and Piner, R. Scanning probe microscopy study of exfoliated oxidized graphene sheets. *Surface Science*, 602(9):1607–1613, 2008.
- [221] Xu, Y., Bai, H., Lu, G., Li, C., and Shi, G. Flexible graphene films via the filtration of water-soluble noncovalent functionalized graphene sheets. *Journal of the American Chemical Society*, 130(18):5856–5857, 2008.
- [222] Georgakilas, V., Otyepka, M., Bourlinos, A.B., et al. Functionalization of graphene: covalent and non-covalent approaches, derivatives and applications. *Chemical Reviews*, 112(11):6156–6214, 2012.
- [223] Boldrin, L., Scarpa, F., Chowdhury, R., and Adhikari, S. Effective mechanical properties of hexagonal boron nitride nanosheets. *Nanotechnology*, 22(50):505702, 2011.
- [224] Peng, Q., Ji, W., and De, S. Mechanical properties of the hexagonal boron nitride monolayer: Ab initio study. *Computational Materials Science*, 56:11–17, 2012.

- [225] Song, L., Ci, L., Lu, H., et al. Large scale growth and characterization of atomic hexagonal boron nitride layers. *Nano Letters*, 10(8):3209–3215, 2010.
- [226] Mas-Ballesté, R., Gómez-Navarro, C., Gómez-Herrero, J., and Zamora, F. 2D materials: to graphene and beyond. *Nanoscale*, 3(1):20–30, 2011.
- [227] Tang, Q. and Zhou, Z. Graphene-analogous low-dimensional materials. *Progress in Materials Science*, 58(8):1244–1315, 2013.
- [228] Bhimanapati, G.R., Lin, Z., Meunier, V., et al. Recent advances in two-dimensional materials beyond graphene. *ACS Nano*, 9(12):11509–11539, 2015.
- [229] Kolosov, O. and Yamanaka, K. Nonlinear detection of ultrasonic vibrations in an atomic force microscope. *Japanese Journal of Applied Physics*, 32(Part 2, No. 8A):L1095–L1098, 1993.
- [230] Rabe, U. and Arnold, W. Acoustic microscopy by atomic force microscopy. *Applied Physics Letters*, 64(12):1493–1495, 1994.
- [231] Yamanaka, K., Ogiso, H., and Kolosov, O.V. Ultrasonic force microscopy for nanometer resolution subsurface imaging. *Applied Physics Letters*, 64(2):178–180, 1994.
- [232] Yamanaka, K. and Nakano, S. Ultrasonic atomic force microscope with overtone excitation of cantilever. *Japanese Journal of Applied Physics*, 35(Part 1, No. 6B):3787–3792, 1996.
- [233] Inagaki, K., Kolosov, O.V., Briggs, G.A.D., and Wright, O.B. Waveguide ultrasonic force microscopy at 60 MHz. *Applied Physics Letters*, 76(14):1836–1838, 2000.
- [234] Cuberes, M.T., Stegemann, B., Kaiser, B., and Rademann, K. Ultrasonic force microscopy on strained antimony nanoparticles. *Ultramicroscopy*, 107(10-11):1053–1060, 2007.
- [235] Kolosov, O.V., Castell, M.R., Marsh, C.D., et al. Imaging the elastic nanostructure of Ge islands by ultrasonic force microscopy. *Physical Review Letters*, 81(5):1046–1049, 1998.
- [236] Geer, R.E., Kolosov, O.V., Briggs, G.A.D., and Shekhawat, G.S. Nanometer-scale mechanical imaging of aluminum damascene interconnect structures in a low-dielectric-constant polymer. *Journal of Applied Physics*, 91(7):4549–4555, 2002.

- [237] Bosse, J.L., Grishin, I., Huey, B.D., and Kolosov, O.V. Nanomechanical morphology of amorphous, transition, and crystalline domains in phase change memory thin films. *Applied Surface Science*, 314:151–157, 2014.
- [238] Dinelli, F. and Assender, H.E. Elastic mapping of heterogeneous nanostructures with ultrasonic force microscopy (UFM). *Surface and Interface Analysis*, 27(5-6):562–567, 1999.
- [239] Porfyrakis, K., Kolosov, O.V., and Assender, H.E. AFM and UFM surface characterization of rubber-toughened poly(methyl methacrylate) samples. *Journal of Applied Polymer Science*, 82(11):2790–2798, 2001.
- [240] Dinelli, F., Castell, M.R., Ritchie, D.A., et al. Mapping surface elastic properties of stiff and compliant materials on the nanoscale using ultrasonic force microscopy. *Philosophical Magazine A*, 80(10):2299–2323, 2000.
- [241] Yamanaka, K. UFM observation of lattice defects in highly oriented pyrolytic graphite. *Thin Solid Films*, 273(1-2):116–121, 1996.
- [242] García, R. Dynamic atomic force microscopy methods. *Surface Science Reports*, 47(6-8):197–301, 2002.
- [243] Tamayo, J. and García, R. Deformation, contact time, and phase contrast in tapping mode scanning force microscopy. *Langmuir*, 12(18):4430–4435, 1996.
- [244] James, P.J., Antognozzi, M., Tamayo, J., et al. Interpretation of contrast in tapping mode AFM and shear force microscopy. A study of Nafion. *Langmuir*, 17(2):349–360, 2001.
- [245] Hurley, D.C., Kopycinska-Müller, M., and Kos, A.B. Mapping mechanical properties on the nanoscale using atomic-force acoustic microscopy. *JOM*, 59(1):23–29, 2007.
- [246] Killgore, J.P., Yablon, D.G., Tsou, A.H., et al. Viscoelastic property mapping with contact resonance force microscopy. *Langmuir*, 27(23):13983–13987, 2011.
- [247] Turner, J.A., Hirsekorn, S., Rabe, U., and Arnold, W. High-frequency response of atomic-force microscope cantilevers. *Journal of Applied Physics*, 82(3):966–979, 1997.
- [248] Matsuda, O., Terada, T., Inagaki, K., and Wright, O.B. Cantilever dynamics in ultrasonic force microscopy. *Japanese Journal of Applied Physics*, 41(Part 1, No. 5B):3545–3546, 2002.

- [249] Briggs, A. and Kolosov, O. *Acoustic Microscopy*, 2nd edition. Oxford University Press, 2009.
- [250] Huey, B.D. AFM and acoustics: Fast, quantitative nanomechanical mapping. *Annual Review of Materials Research*, 37(1):351–385, 2007.
- [251] Dinelli, F., Biswas, S.K., Briggs, G.A.D., and Kolosov, O.V. Ultrasound induced lubricity in microscopic contact. *Applied Physics Letters*, 71(9):1177–1179, 1997.
- [252] Hesjedal, T. and Behme, G. The origin of ultrasound-induced friction reduction in microscopic mechanical contacts. *IEEE Transactions on Ultrasonics, Ferroelectrics, and Frequency Control*, 49(3):356–364, 2002.
- [253] Robinson, B.J., Kay, N.D., and Kolosov, O.V. Nanoscale interfacial interactions of graphene with polar and nonpolar liquids. *Langmuir*, 29(25):7735–7742, 2013.
- [254] Inagaki, K., Kolosov, O.V., Briggs, G.A.D., et al. Ultrasonic force microscopy in waveguide mode up to 100 MHz. *Proceedings of the 1998 IEEE Ultrasonics Symposium. Proceedings*, 2:1255–1260, 1998.
- [255] Cuberes, M.T., Assender, H.E., Briggs, G.A.D., and Kolosov, O.V. Heterodyne force microscopy of PMMA/rubber nanocomposites: nanomapping of viscoelastic response at ultrasonic frequencies. *Journal of Physics D: Applied Physics*, 33:2347–2355, 2000.
- [256] Edgeworth, J.P., Wilson, N.R., and Macpherson, J.V. Controlled growth and characterization of two-dimensional single-walled carbon-nanotube networks for electrical applications. *Small*, 3(5):860–870, 2007.
- [257] Bosse, J.L., Tovee, P.D., Huey, B.D., and Kolosov, O.V. Physical mechanisms of megahertz vibrations and nonlinear detection in ultrasonic force and related microscopies. *Journal of Applied Physics*, 115(14):144304, 2014.
- [258] Wortman, J.J. and Evans, R.A. Young’s modulus, shear modulus, and poisson’s ratio in silicon and germanium. *Journal of Applied Physics*, 36(1):153–156, 1965.
- [259] Hopcroft, M.A., Nix, W.D., and Kenny, T.W. What is the Young’s modulus of silicon? *Journal of Microelectromechanical Systems*, 19(2):229–238, 2010.
- [260] Kelly, P. *Properties of Materials*. CRC Press, 2014.

- [261] Savvides, N. and Bell, T.J. Microhardness and Young's modulus of diamond and diamondlike carbon films. *Journal of Applied Physics*, 72(7):2791–2796, 1992.
- [262] Scherer, V., Bhushan, B., Rabe, U., and Arnold, W. Local elasticity and lubrication measurements using atomic force and friction force microscopy at ultrasonic frequencies. *IEEE Transactions on Magnetics*, 33(5):4077–4079, 1997.
- [263] Cuberes, M.T. and Martinez, J.J. Mechanical-diode mode ultrasonic friction force microscopy. *Journal of Physics: Conference Series*, 61(1):224–228, 2007.
- [264] Mate, C.M., McClelland, G.M., Erlandsson, R., and Chiang, S. Atomic-scale friction of a tungsten tip on a graphite surface. *Physical Review Letters*, 59(17):1942–1945, 1987.
- [265] Kerssemakers, J. and De Hosson, J.T.M. A quantitative analysis of surface deformation by stick/slip atomic force microscopy. *Journal of Applied Physics*, 82(8):3763, 1997.
- [266] Sirghi, L. Transport mechanisms in capillary condensation of water at a single-asperity nanoscopic contact. *Langmuir*, 28(5):2558–2566, 2012.
- [267] Robinson, B., Rabot, C., Mazzocco, R., et al. Nanomechanical mapping of graphene layers and interfaces in suspended graphene nanostructures grown via carbon diffusion. *Thin Solid Films*, 550:472–479, 2014.
- [268] Cho, J., Luo, J.J., and Daniel, I.M. Mechanical characterization of graphite/epoxy nanocomposites by multi-scale analysis. *Composites Science and Technology*, 67(11-12):2399–2407, 2007.
- [269] Marsden, A.J., Phillips, M., and Wilson, N.R. Friction force microscopy: a simple technique for identifying graphene on rough substrates and mapping the orientation of graphene grains on copper. *Nanotechnology*, 24(25):255704, 2013.
- [270] Park, S., Vosguerichian, M., and Bao, Z. A review of fabrication and applications of carbon nanotube film-based flexible electronics. *Nanoscale*, 5(5):1727–52, 2013.
- [271] Snow, E.S., Perkins, F.K., and Robinson, J.A. Chemical vapor detection using single-walled carbon nanotubes. *Chemical Society reviews*, 35(9):790–798, 2006.

- [272] Nirmalraj, P.N., Lyons, P.E., De, S., Coleman, J.N., and Boland, J.J. Electrical connectivity in single-walled carbon nanotube networks. *Nano Letters*, 9(11):3890–3895, 2009.
- [273] Stadermann, M., Papadakis, S.J., Falvo, M.R., et al. Nanoscale study of conduction through carbon nanotube networks. *Physical Review B*, 69(20):201402, 2004.
- [274] Cease, H., Derwent, P.F., Diehl, H.T., Fast, J., and Finley, D. Measurement of mechanical properties of three epoxy adhesives at cryogenic temperatures for CCD construction. *Fermilab Technical Report*, Fermilab-T:1–19, 2006.
- [275] Kuilla, T., Bhadra, S., Yao, D.H., et al. Recent advances in graphene based polymer composites. *Progress in Polymer Science*, 35(11):1350–1375, 2010.
- [276] Qian, H., Greenhalgh, E.S., Shaffer, M.S.P., and Bismarck, A. Carbon nanotube-based hierarchical composites: a review. *Journal of Materials Chemistry*, 20(23):4751–4762, 2010.
- [277] Young, R.J., Kinloch, I.A., Gong, L., and Novoselov, K.S. The mechanics of graphene nanocomposites: A review. *Composites Science and Technology*, 72(12):1459–1476, 2012.
- [278] Raoux, S., Welnic, W., and Ielmini, D. Phase change materials and their application to nonvolatile memories. *Chemical Reviews*, 110(1):240–267, 2010.
- [279] Bray, D.E. and McBride, D. *Nondestructive Testing Techniques*. John Wiley & Sons, 1992.
- [280] Cartz, L. *Nondestructive Testing*. ASM International, 1995.
- [281] Halmshaw, R. *Non-destructive Testing*. Edward Arnold, 1987.
- [282] Sposito, G., Ward, C., Cawley, P., Nagy, P.B., and Scruby, C. A review of non-destructive techniques for the detection of creep damage in power plant steels. *NDT & E International*, 43(7):555–567, 2010.
- [283] Garland, P.J. The importance of non-destructive testing and inspection of pipelines. In *10th European Conference on Non-Destructive Testing*, pages 1–10, Moscow, 2010.
- [284] Petcher, P.A., Potter, M.D.G., and Dixon, S. A new electromagnetic acoustic transducer (EMAT) design for operation on rail. *NDT & E International*, 65:1–7, 2014.

- [285] Eric, H. Real-time detection of developing cracks in jet engine rotors. In *2000 IEEE Aerospace Conference. Proceedings*, volume 6, pages 173–183. IEEE, 2000.
- [286] Balageas, D., Fritzen, C.P., and Güemes, A. *Structural Health Monitoring*. ISTE Ltd, 2006.
- [287] McCann, D. and Forde, M. Review of NDT methods in the assessment of concrete and masonry structures. *NDT & E International*, 34(2):71–84, 2001.
- [288] Hull, B. and John, V. *Non-Destructive Testing*. Macmillan Education UK, 1988.
- [289] McEvily, A.J. Failures in inspection procedures: Case studies. *Engineering Failure Analysis*, 11(2):167–176, 2004.
- [290] Morreyjr, W. Penetrant testing in the quality control of nuclear power plant construction. *NDT International*, 10(1):9–12, 1977.
- [291] Liao, T. and Ni, J. An automated radiographic NDT system for weld inspection: Part I – Weld extraction. *NDT & E International*, 29(3):157–162, 1996.
- [292] Babot, D., Berodias, G., and Peix, G. Detection and sizing by X-ray Compton scattering of near-surface cracks under weld deposited cladding. *NDT & E International*, 24(5):247–251, 1991.
- [293] Holt, R.S., Cooper, M.J., and Jackson, D.F. Gamma-ray scattering techniques for non-destructive testing and imaging. *Nuclear Instruments and Methods in Physics Research*, 221:98–104, 1984.
- [294] Loveman, R., Bendahan, J., Gozani, T., and Stevenson, J. Time of flight fast neutron radiography. *Nuclear Instruments and Methods in Physics Research Section B: Beam Interactions with Materials and Atoms*, 99(1-4):765–768, 1995.
- [295] Hanke, R., Fuchs, T., and Uhlmann, N. X-ray based methods for non-destructive testing and material characterization. *Nuclear Instruments and Methods in Physics Research, Section A: Accelerators, Spectrometers, Detectors and Associated Equipment*, 591(1):14–18, 2008.

- [296] Brenizer, J.S., Hosticka, B., Berger, H., and Gillies, G.T. The use of contrast agents to enhance crack detection via neutron radiography. *NDT & E International*, 32(1):37–42, 1999.
- [297] Rossi, M., Casali, F., Bettuzzi, M., et al. Experimental micro-CT system for x-ray NDT. In Bonse, U., editor, *Developments in X-Ray Tomography III*, volume 4503, pages 338–348, 2002.
- [298] Doering, E.R., Basart, J.P., and Gray, J.N. Three-dimensional flaw reconstruction and dimensional analysis using a real-time X-ray imaging system. *NDT & E International*, 26(1):7–17, 1993.
- [299] Balaskó, M., Kuba, A., Nagy, A., et al. Neutron-, gamma- and X-ray three-dimensional computed tomography at the Budapest research reactor site. *Nuclear Instruments and Methods in Physics Research A*, 542(1-3):22–27, 2005.
- [300] Saguy, H. and Rittel, D. Flaw detection in metals by the ACPD technique: Theory and experiments. *NDT & E International*, 40(7):505–509, 2007.
- [301] Sophian, A., Tian, G.Y., Taylor, D., and Rudlin, J. Electromagnetic and eddy current NDT: A review. *Insight: Non-Destructive Testing and Condition Monitoring*, 43(5):302–306, 2001.
- [302] García-Martín, J., Gómez-Gil, J., and Vázquez-Sánchez, E. Non-destructive techniques based on eddy current testing. *Sensors*, 11(12):2525–2565, 2011.
- [303] Hall, E.H. On a new action of the magnet on electric currents. *American Journal of Mathematics*, 2(3):287–292, 1879.
- [304] Baibich, M.N., Broto, J.M., Fert, A., et al. Giant magnetoresistance of (001)Fe/(001)Cr magnetic superlattices. *Physical Review Letters*, 61(21):2472–2475, 1988.
- [305] Binasch, G., Grünberg, P., Saurenbach, F., and Zinn, W. Enhanced magnetoresistance in layered magnetic structures with antiferromagnetic interlayer exchange. *Physical Review B*, 39(7):4828–4830, 1989.
- [306] Lebrun, B., Jayet, Y., and Baboux, J.C. Pulsed eddy current signal analysis: application to the experimental detection and characterization of deep flaws in highly conductive materials. *NDT & E International*, 30(3):163–170, 1997.

- [307] Sophian, A., Tian, G.Y., Taylor, D., and Rudlin, J. A feature extraction technique based on principal component analysis for pulsed eddy current NDT. *NDT & E International*, 36(1):37–41, 2003.
- [308] Förster, F. New findings in the field of non-destructive magnetic leakage field inspection. *NDT International*, 19(1):3–14, 1986.
- [309] Inagaki, T., Ishii, T., and Iwamoto, T. On the NDT and E for the diagnosis of defects using infrared thermography. *NDT & E International*, 32(5):247–257, 1999.
- [310] Filipczyński, L., Pawłowski, Z., and Wehr, J. *Ultrasonic Methods of Testing Materials*. Butterworths, 1966.
- [311] Gooberman, G.L. *Ultrasonics: Theory and Application*. Hart Publishing Company, 1969.
- [312] Silk, M.G. *Ultrasonic Transducers for Nondestructive Testing*. Taylor & Francis, 1984.
- [313] Clough, A.R. and Edwards, R.S. Lamb wave near field enhancements for surface breaking defects in plates. *Journal of Applied Physics*, 111(10):104906, 2012.
- [314] Capineri, L., Tattersall, H.G., Silk, M.G., and Temple, J.A.G. Time-of-flight diffraction tomography for NDT applications. *Ultrasonics*, 30(5):275–288, 1992.
- [315] Silk, M.G. The transfer of ultrasonic energy in the diffraction technique for crack sizing. *Ultrasonics*, 17(3):113–121, 1979.
- [316] Silk, M.G. and Lidington, B.H. An evaluation of single probe bulk-wave time-delay techniques in sizing cracks in steel. *NDT International*, 10(3):129–134, 1977.
- [317] Dewhurst, R.J., Edwards, C., McKie, A.D.W., and Palmer, S.B. Estimation of the thickness of thin metal sheet using laser generated ultrasound. *Applied Physics Letters*, 51(14):1066–1068, 1987.
- [318] Smith, R.T. Third-order elastic moduli of polycrystalline metals from ultrasonic velocity measurements. *The Journal of the Acoustical Society of America*, 40(5):1002–1008, 1966.

- [319] Leamy, H.J., Gibson, E.D., and Kayser, F.X. The elastic stiffness coefficients of iron-aluminum alloys—I experimental results and thermodynamic analysis. *Acta Metallurgica*, 15(12):1827–1838, 1967.
- [320] Aussel, J.D. and Monchalin, J.P. Precision laser-ultrasonic velocity measurement and elastic constant determination. *Ultrasonics*, 27(3):165–177, 1989.
- [321] Hirao, M. Texture of polycrystalline metals characterized by ultrasonic velocity measurements. *The Journal of the Acoustical Society of America*, 81(5):1434, 1987.
- [322] MacDonald, D.E. On determining stress and strain and texture using ultrasonic velocity measurements. *IEEE Transactions on Sonics and Ultrasonics*, 28(2):75–78, 1981.
- [323] Potter, M.D.G., Dixon, S., and Davis, C. Development of an automated non-contact ultrasonic texture measurement system for sheet metal. *Measurement Science and Technology*, 15(7):1303–1308, 2004.
- [324] Sharples, S.D., Clark, M., and Somekh, M.G. Spatially resolved acoustic spectroscopy for fast noncontact imaging of material microstructure. *Optics Express*, 14(22):10435–10440, 2006.
- [325] Smith, R., Sharples, S., Li, W., Clark, M., and Somekh, M. Orientation imaging using spatially resolved acoustic spectroscopy. *Journal of Physics: Conference Series*, 353:012003, 2012.
- [326] Smith, R.J., Li, W., Coulson, J., et al. Spatially resolved acoustic spectroscopy for rapid imaging of material microstructure and grain orientation. *Measurement Science and Technology*, 25(5):055902, 2014.
- [327] Kažys, R., Voleišis, A., and Voleišienė, B. High temperature ultrasonic transducers: review. *Ultrasound*, 63(2):7–17, 2008.
- [328] Baba, A., Searfass, C.T., and Tittmann, B.R. High temperature ultrasonic transducer up to 1000°C using lithium niobate single crystal. *Applied Physics Letters*, 97(23):232901, 2010.
- [329] Drinkwater, B.W. and Wilcox, P.D. Ultrasonic arrays for non-destructive evaluation: A review. *NDT & E International*, 39(7):525–541, 2006.

- [330] Cai, J., Shi, L., Yuan, S., and Shao, Z. High spatial resolution imaging for structural health monitoring based on virtual time reversal. *Smart Materials and Structures*, 20(5):055018, 2011.
- [331] Simonetti, F. Multiple scattering: The key to unravel the subwavelength world from the far- field pattern of a scattered wave. *Physical Review E*, 73(3):1–13, 2006.
- [332] Fan, C., Caleap, M., Pan, M., and Drinkwater, B.W. A comparison between ultrasonic array beamforming and super resolution imaging algorithms for non-destructive evaluation. *Ultrasonics*, 54(7):1842–1850, 2014.
- [333] Bristow, J.R. Microcracks, and the static and dynamic elastic constants of annealed and heavily cold-worked metals. *British Journal of Applied Physics*, 11(2):81–85, 1960.
- [334] Evans, A. and Fu, Y. Some effects of microcracks on the mechanical properties of brittle solids—II. Microcrack toughening. *Acta Metallurgica*, 33(8):1525–1531, 1985.
- [335] Fu, Y. and Evans, A.G. Some effects of microcracks on the mechanical properties of brittle solids—I. Stress, strain relations. *Acta Metallurgica*, 33(8):1515–1523, 1985.
- [336] Hironobu, N. and Ken-Ichi, T. Significance of initiation, propagation and closure of microcracks in high cycle fatigue of ductile metals. *Engineering Fracture Mechanics*, 15(3-4):445–456, 1981.
- [337] Cannon, R., Dagleish, B., Dauskardt, R., Oh, T., and Ritchie, R. Cyclic fatigue-crack propagation along ceramic/metal interfaces. *Acta Metallurgica et Materialia*, 39(9):2145–2156, 1991.
- [338] Gardner, R.N., Pollock, T.C., and Wilsdorf, H.G.F. Crack initiation at dislocation cell boundaries in the ductile fracture of metals. *Materials Science and Engineering*, 29(2):169–174, 1977.
- [339] Ortiz, M. Microcrack coalescence and macroscopic crack growth initiation in brittle solids. *International Journal of Solids and Structures*, 24(3):231–250, 1988.
- [340] Guidici, D.C. Microcrack detection in silicon crystals with an ultrasonic sonoprobe. *Microelectronics Journal*, 11(1):37–40, 1980.

- [341] Abdelhamid, M., Singh, R., and Omar, M. Review of microcrack detection techniques for silicon solar cells. *IEEE Journal of Photovoltaics*, 4(1):514–524, 2014.
- [342] Kozhushko, V.V. and Hess, P. Nondestructive evaluation of microcracks by laser-induced focused ultrasound. *Applied Physics Letters*, 91(22):3–5, 2007.
- [343] Edwards, R., Dixon, S., and Jian, X. Characterisation of defects in the railhead using ultrasonic surface waves. *NDT & E International*, 39(6):468–475, 2006.
- [344] Jian, X., Dixon, S., and Edwards, R.S. Optimising ultrasonic wideband Rayleigh wave generation by pulsed electromagnetic coils. *Nondestructive Testing and Evaluation*, 20(1):43–62, 2005.
- [345] Dixon, S., Burrows, S.E., Dutton, B., and Fan, Y. Detection of cracks in metal sheets using pulsed laser generated ultrasound and EMAT detection. *Ultrasonics*, 51(1):7–16, 2011.
- [346] Butt, H.J. and Jaschke, M. Calculation of thermal noise in atomic force microscopy. *Nanotechnology*, 6:1–7, 1995.
- [347] Hrabina, J., Lazar, J., Holá, M., and Číp, O. Frequency noise properties of lasers for interferometry in nanometrology. *Sensors*, 13(2):2206–2219, 2013.
- [348] Monchalín, J.P. Optical detection of ultrasound. *IEEE Transactions on Ultrasonics, Ferroelectrics and Frequency Control*, 33(5):485–499, 1986.
- [349] Zhou, Q., Lau, S., Wu, D., and Kirk Shung, K. Piezoelectric films for high frequency ultrasonic transducers in biomedical applications. *Progress in Materials Science*, 56(2):139–174, 2014.
- [350] Ito, H., Furuta, T., Kodama, S., and Ishibashi, T. InP/InGaAs uni-travelling-carrier photodiode with 310 GHz bandwidth. *Electronics Letters*, 36(21):1809–1810, 2000.
- [351] Wang, S.Y., Bloom, D.M., and Collins, D.M. 20-GHz bandwidth GaAs photodiode. *Applied Physics Letters*, 42(2):190–192, 1983.
- [352] Martínez, A., Rayas, J.A., Meneses-Fabián, C., and Anguiano-Morales, M. Simultaneous measurement with one-capture of the two in-plane components of displacement by electronic speckle pattern interferometry. *Optics Communications*, 281(17):4291–4296, 2008.

- [353] Arai, Y. Development of in-plane and out-of-plane deformation simultaneous measurement method by using only two speckle patterns. In Harding, K.G. and Yoshizawa, T., editors, *Proceedings of SPIE*, volume 9110, page 911008, 2014.
- [354] Tyrer, J.R. and Petzing, J.N. In-plane electronic speckle pattern shearing interferometry. *Optics and Lasers in Engineering*, 26(4-5):395–406, 1997.
- [355] Monchalín, J.P., Aussel, J.D., Héon, R., et al. Measurement of in-plane and out-of-plane ultrasonic displacements by optical heterodyne interferometry. *Journal of Nondestructive Evaluation*, 8(2):121–133, 1989.
- [356] Blackshire, J.L. and Sathish, S. Near-field ultrasonic scattering from surface-breaking cracks. *Applied Physics Letters*, 80(18):3442–3444, 2002.
- [357] Clough, A.R. *A Study on the Near-Field Interactions of Ultrasonic Surface Waves with Surface-Breaking Defects*. Phd thesis, University of Warwick, 2013.
- [358] Dixon, S., Cann, B., Carroll, D.L., Fan, Y., and Edwards, R.S. Non-linear enhancement of laser generated ultrasonic Rayleigh waves by cracks. *Nondestructive Testing and Evaluation*, 23(1):25–34, 2008.
- [359] López-Polín, G., Gómez-Navarro, C., Parente, V., et al. Increasing the elastic modulus of graphene by controlled defect creation. *Nature Physics*, 11(1):26–31, 2014.
- [360] Bunch, J.S., van der Zande, A.M., Verbridge, S.S., et al. Electromechanical resonators from graphene sheets. *Science*, 315(5811):490–493, 2007.
- [361] Chen, C., Rosenblatt, S., Bolotin, K.I., et al. Performance of monolayer graphene nanomechanical resonators with electrical readout. *Nature Nanotechnology*, 4(12):861–867, 2009.
- [362] van der Zande, A.M., Barton, R.A., Alden, J.S., et al. Large-scale arrays of single-layer graphene resonators. *Nano Letters*, 10(12):4869–4873, 2010.
- [363] Barton, R.A., Ilic, B., van der Zande, A.M., et al. High, size-dependent quality factor in an array of graphene mechanical resonators. *Nano Letters*, 11(3):1232–1236, 2011.
- [364] Skilbeck, M.S., Marsden, A.J., Cao, G., et al. Multimodal microscopy using ‘half and half’ contact mode and ultrasonic force microscopy. *Nanotechnology*, 25(33):335708, 2014.